Universidad Autónoma de Madrid

Quantum Electrodynamics with Quantum Dots in Microcavities

Thesis

Elena del Valle Reboul

Advisor

Prof. Carlos Tejedor

Jury

Prof. Luis Viña..... UAM Madrid, Spain
Prof. Alexey Kavokin..... Univ. of Southampton, UK
Prof. Maurice Skolnick..... Univ. of Sheffield, UK
Dr. Antonio Badolato..... .....ETH Zurich, Switzerland
Dr. Francesca Marchetti..... UAM Madrid, Spain

February 2009

Quantum Electrodynamics with Quantum Dots in Microcavities

Elena del Valle Reboul

February 9, 2009

Cover picture: "*Abstracción con sedas*", by Inma Reboul.

The author can be contacted at: elena.delvalle.reboul@gmail.com.
This thesis can be found in the web: http://delvalle.laussy.org/elena

We must never cease from exploration. And the end of all our exploring will be to arrive where we began and to know the place for the first time.
T. S. Eliot

Basta mirar algo con atención para que se vuelva interesante.
E. D'Ors

Sigue, sigue adelante y no regreses,
Fiel hasta el fin del camino y tu vida,
No eches de menos un destino más fácil,
Tus pies sobre la tierra antes no hollada,
Tus ojos frente a lo antes nunca visto.
L. Cernuda

Toma la verdad y llévala por el mundo.
E. Bose

Prefacio

Excribir la tésis es una de esas cosas que una *hace* una sola vez en la vida. Otras cosas uni-ocasionales *se le hacen a una*, sin comerlo ni beberlo, como nacer o morir. De hecho no se me ocurren muchas más cosas fruto de la voluntad que no se repetirán (el eterno no retorno), tal vez el parto de un hijo único o la boda con la media naranja. En cualquier caso, un poco del uno y del otro ejemplo tiene escribir la tésis. De lo primero, porque escribir la tésis es una catarsis. Uno se explaya, se desaloja, se vacía todo lo que puede y "pare" un monstruo de 200 hojas, que posiblemente solo le parezca absolutamente maravilloso a una (de ahí la similitud con el ejemplo segundo). Incluso cuando siempre una tenderá a creer que pudo hacer más y mejor, el amor de un doctorando por su tésis recién parida es súbito. Después de los sudores del parto, e incluso en los casos desafortunados en los que se reniega del contenido (¿por qué no?, se ha dado más de un caso), la visión primera de esas verdades tan bien encuadernadas nos llena de gozo. Con este texto, mato dos pájaros de un tiro y ya solo me queda plantar un árbol.

Mi tésis comenzó a gestarse allá en la adolescencia, cuando el gusto por las matemáticas tomó un tinte personal: las matemáticas y yo. Cierta Rosa me enseñó a deshojar las funciones y ya no pude quitarme desde entonces. Ahí empezé a *divertirme* de una manera muy especial, distinta a otras que competían. Tan distinta que ganó por pura curiosidad de ver si esa emoción indescriptible, ansiosa, que me invadía al ir desentrañando los misterios de los numeros complejos o las exponenciales, sería más intenso según se fueran complicando los problemas. Y no puedo negar que, a ratos, como todo, en la carrera que elegí he podido sentir esa emoción, ese hilo motivador de mi vida, y ese sentimiento de saturación de belleza abstracta (sin aplicación) que lo envuelve todo en un instante de comprensión profunda. Gracias a ese hilo mágico, que me conecta con la imagen de mí misma que siempre proyecté, de la que a veces dudé y a la que siempre volví, estoy aquí hoy, luchando por darle vida esta carne de mi carne a las 4 y cuarto de la mañana.

Y no se trató nunca de la Física, ni de la Ciencia (ni de otras grandes cosas con mayúsculas), ni siquiera de la admiración por los grandes científicos o los grandes proyectos. Siempre se trató de algo íntimo, raramente compartible, como una tarde a la soledad de mi mesa con un problema o una ecuación. Pido nada más que eso, pero eso cada día. Siendo yo poco (o tan) exigente, no siempre ha sido fácil…

No siempre ha sido fácil seguirle la pista al hilo adorado. Durante mucho tiempo pareció haberme abandonado. Las pasiones, incluso las cotidianas, a veces se nos revelan y no hay que culparse. Como una espectadora, me veía extraña, actuando por costumbre donde siempre me guió el instinto. Capacidad, voluntad, futuro, fueron palabras que durante ese tiempo se me escapaban. No hay que menospreciar la crisis del doctorando, es toda una institución mental: la carcel de

las ilusiones perdidas. Casi no valió la pena seguir en los momentos más duros de estos cuatro años y medio. Pero, como en toda historia con final feliz, lo humano se impone sobre los constructos, el cariño sobre las apariencias y la fé nos devuelve a la lucha, ciega a toda evidencia que vaticine derrota. Cuando tanta gente en la que tú crees (ver the Agradecimientos) cree en ti, tienes dudas de tus dudas. Y eso te puede salvar. A mí me salvó, al margen de que decidiera no abandonar la tésis.

Con todo, es un largo camino el que me ha traído hasta aquí. La tésis es una etapa, para los que nos damos a la vida académica, como el colegio, el instituto, la carrera. El eslabón más duro que no te asegura el cielo pero te da cierta altura. Es duro porque estás a solas con la ignorancia, por primera vez, sin red ni armas. Ya no te puedes esconder en los libros manoseados y los ejercicios mil veces repetidos por generaciones. Ya no puedes correr al sabio profesor para que corrija tus torpezas. Los sabios cercanos ya no existen mientras que los sabios lejanos e inaccesibles se multiplican. Los problemas más minúsculos, tan minúsculos que al principio te dan risa (¡¡¿diagonalizar una matriz?!!), te ponen constantemente en evidencia frente a un público mundial que te ignora por defecto. Ya no te codeas con las grandes teorías de la humanidad cada día, pero cualquier integral del camino amenaza con no tener solución, y eso te paraliza. ¡Qué absurdo desamparo!

Como si se tratara de una teoría que ya no aplica y empieza a dar divergencias, la tésis te obliga a cambiar de modelo. Hay que *decidir* (sin pararse a pensar) que todo el mundo empieza a andar con los pañales, a pasos ridículos y titubeantes. Solo hace falta que te den la mano para no caer y para comprobar también son numerosos los titubeos de los otros. La felicidad mayor de doctorando es la del niño, poder jugar sin miedo, sin nisiquiera concebir la idea de aquivocarse. Los errores no existen. Claro. Lo único que debe quitarme el sueño es no tener suficiente madeja para mi hilo. Solo cuando abracé en plenitud esta idea, solo cuando los sabios abstractos cayerón de su pedestal lejano, pude volver a subirles a uno más cercano y verdadero, más a mi altura, recién conquistada por decisión propia. Y las cosas parecen tranquilizarse. Nada es tan fácil como me atormentaba pensando ni tan difícil como acabé creyendo. Solo tuve que empezar a andar.

Es andando que me cruzé con la *gente*. Al final siempre se trata de la gente. “Que la ciencia nos haga más humanos” decía aquella, pero primero tenemos que hacer nosotros a la ciencia completamente humana. Ponerle caras, gestos, miedos e ilusiones. Despojarnos de las excusas serias para poder hacer cosas interesantes en serio. Disfrutar con la física requiere que nunca se ponga por encima de nadie ni sea lo más importante o algo sagrado. La física ha de ser algo plástico, modelable, que no se escandaliza ni sabe de apariencias y subterfugios. Un refugio para la humanidad de sus subjetividades, donde lo que es verdadero y de calidad lleva la batuta. Lejos de los tópicos, creo que prefiero el cálido varemo

de la lógica al frío critero de los intereses personales. Sí, sé que esa ciencia, concebida con los ideales con la que mi padres me llenaban la cabeza de pequeña, no existe, pero me gusta pensar que es a la que aspiramos.

Agradecimientos

La gente está al principio y al final de todo, también de la física: La *Física*, que al fin y al cabo se enorgullece de servir a la humanidad, y la *física*, que cada día hago con, para, por y gracias a mucha gente.

Si se trata de hacer listas, quiero empezar por darles las gracias a mis compañeros de despacho: Pilar y José Manuel, que me hacían reir como nadie y convirtieron el departamento el lugar donde quería trabajar; Miguel, que tanto me ayudó a combatir los pesares del doctorando (¡y a escuchar buena música!); y las últimas adquisiciones del C-V 505, Stefan y Alejandro.

Es ineludible dar las gracias a los miembros del gran coro del ICMM, con José Antonio (y ahora Maria) a la cabeza, que aceleraba el paso de la semana con un buen empujón las tardes de los lunes y me ha prestado una contra-alto y un tenor para el tribunal de esta tésis.

El buen ambiente en el C-V tengo que agradecerlo a todos sus miembros en masa, en especial a los que se fueron dejando gran huella (como Miriam), a los que empezaron y siguen a mi lado (como Laura, con su alegría contagiosa) y tantos y tantos otros... Pero entre todos ellos tiene su lugar irremplazable Antonio, mi amigo inseparable desde el primer día de carrera. A él, que le encanta leer los agradecimientos de la tésis, le doy las gracias por infinitas cosas: su sobrevaloración y fé en mis capacidades, el privilegio de su amistad serena, me sujetaron a la tierra cuando todo se tambaleaba. Antonio pone inspiración en la confusión con sus juicios lúcidos y su humor subrealista.

Durante la tésis también he podido viajar y trabajar con personas fuera del departamento, gracias a las cuales se ha configurado mi visión de la física y el mundo, ambas dos entrelazadas. Las colaboraciones has resultado, no solo la mejor manera de aprender y hacer física, sino también el mejor antídoto contra la desidia y el pesimismo que acechan en su soledad al físico teórico: Filippo (en Módena), Ivan y Fabricio (en Brasilia), Giovanna y Stefano (en Barcelona), Iacopo, Frank, Misha, Alexey... (¡en dondequiera que nos encontráramos!).

Y, como no, la ciencia que he podido hacer estos años es la ciencia del que ha sido mi grupo en la UAM. Con Carlos, mi director y guía, Luis, Alberto, Dario, Daniele y Fabrice, hemos vivido interminables reuniones, a veces divertidas, a veces reveladoras, y hasta hemos alcanzado sueños, a golpe de discusiones, de comidas y de conferencias. Y en este punto, antes de que Daniele piense que se la he jugado con la lista, le agradezco a él y solo a él (un pequeño privilegio para

un gran amigo) el dinamismo y la locura con que ha impregnado nuestro grupo y a mí.

Amigos, amigos, amigos. Tantos amigos a los que agradecer su apoyo y tan buenos. Algunos parece que les picó la espina de mi mismo Rosal, literalmente fue el caso de Carlos y Jose (¡con los que me enorgullezco de haber compartido el camino por más de 12 años!) y algo más figurado en el caso de Javi, Bea y Joss. Los compañeros de mi generación ± 1 han sido mi universo en todos los sentidos. Y seguimos: Ana, David, Juanjo, Paula, Miriam, Paco, Jacobo, José Mi, Alfonso, Adolfo, Dani, Dani, Eva, Álvaro... Hay amigos también que no saben de física, claro, sino de cosas más útiles, pero tienen que tener un lugar en estos agradecimientos: mi querida Elena, Santi, Marta y Noe.

Mi familia, mis tíos, mis abuelas son los responsables de que esta tésis exista por extensión. Mi padre, con su arte profundo, me enseñó lo que es la ciencia. Mi madre, con su ciencia profunda, me enseñó lo que es el arte. Entre los dos conforman el ideal de equilibrio entre rigor e imaginación, entre orden y caos, que como poco me guía en la investigación. Con la conciencia tranquila, solo me atribuyo parte de la culpa si mi hermano (por ahora es una amenaza) crea una saga de físicos en la familia.

Por mucho que me haya quejado en estos años y que me queje en lo que me queda, tengo que agradecer a la ciencia la oportunidad de ver mundo y el flujo constante de amigos que me proporciona. Me ha regalado con el encuentro de algunas de las personas, y una muy, muy en particular, más importantes de mi vida.

¡Lo que la ciencia une, que no lo separe el hombre!

Para Fabrice, mi hilo dorado,
que lo cambió todo para siempre.

Contents

List of Figures

Abstract (*Presentación*)

Spanish *(Castellano)*

Esta tésis describe, en el marco de la teoría de Electrodinámica Cuántica en Cavidades, la interacción de luz y materia bajo un bombeo continuo e incoherente. Como tal, describe sistemas físicos como es un punto cuántico—que provee de excitones (materia)—dentro de una cavidad semiconductora—que provee de fotones (luz).

Considero dos modelos para describir su interacción: el modelo lineal (para excitones bosónicos) y el modelo de Jaynes-Cummings (para excitones fermiónicos). En el llamado regimen de *acoplo fuerte*, fotones y excitones interactúan fuertemente, perdiendo su identidad y dando lugar a nuevas partículas, los *polaritones* 0-dimensionales.

La física de polaritones se ve gravemente afectada por la decoherencia, que describo mediante términos Lindblad en una ecuación maestra. Las dos fuentes principales de decoherencia en semiconductores son la disipación (pérdida de partículas) y el esquema cw de excitación fuera de resonancia (injección continua de partículas). Aunque el efecto del decaimiento ha sido estudiado desde los comienzos de cQED, el efecto del bombeo incoherente has sido ignorado. Aquí muestro como el efecto conjunto de bombeo y decaimiento puede impedir o favorecer la formación de polaritones.

El modelo bosónico se resuelve exactamente mostrando las consecuencias cualitativas y cuantitativas que el bombeo tiene en los experimentos, en particular, en medidas espectroscópicas de fotoluminescencia. El problema fermiónico se resuelve semi-analíticamente, y se propone como una herramienta de laboratorio para estudiar la transición del régimen cuántico al clásico.

La observaciónde polaritones en los espectros de emisión depende crucialmente del bombeo y de la naturaleza de los excitones (bonónica o fermiónica), como muestro en el texto. Otras propiedades de estos sistemas como correlaciones de primer y segundo orden, ganancia de uno o dos fotones, lasing y entanglement son también discutidas.

English *(Inglés)*

This thesis describes, in the framework of cavity Quantum Electrodynamics, the interaction of light with matter under an incoherent continuous pumping. As such, it describes physical systems like a quantum dot—that provides excitons (matter)—inside of a semiconductor microcavity—that provides photons (light).

I consider two models to describe their interaction: the linear model (for bosonic excitons) and the Jaynes-Cummings model (for fermionic excitons). In the so-called *Strong Coupling* regime, photons and excitons interact strongly, loosing their identity and giving birth to new particles, called (0D) *polaritons*.

Polariton physics is greatly affected by decoherence. I describe it with Lindblad terms in a master equation. The two main sources of decoherence in semiconductors are dissipation (losses of particles) and the off-resonant continuous wave scheme of excitation (continuous injection of particles). Although the effect of decay has been studied since the early days of cQED, the effect of incoherent pumping has been largely overlooked. I show how the interplay of pump and decay can hinder or favour the formation of polaritons.

The boson model is solved exactly and shows the qualitative and quantitative consequences that pumping bears in experiments, in particular in spectroscopic measurements of photoluminescence. The fermion problem is solved semi-analytically, and advocated as a laboratory tool to study the transition from quantum to classical regimes.

Observation of polaritons in the actual spectra of emission depends on the pumping and the nature of the excitons (bosonic or fermionic) in a crucial way that I unravel in this text. Other properties of these systems like first and second order correlations, one and two photon gain, lasing and entanglement are also discussed.

Notations

We set $\hbar = 1$ in the text, to remove the distinction between energy and frequency. The energy (time) unit will be the coupling constant g (inverse $1/g$), if not otherwise specified.

List of acronyms

This is a list of the acronyms used in the text.

1R(P) one-photon (resonance)

2LS two-level system

2R(P) two-photon (resonance)

BEC Bose-Einstein Condensate (or Condensation)

cQED Cavity Quantum Electrodynamics (see also QED)

HO harmonic oscillator

JC(M) Jaynes-Cummings (model)

LM linear model

PL Photoluminescence

QD Quantum Dot

QED Quantum Electrodynamics (see also cQED)

QW Quantum Well

SC Stronc Coupling (see also WC)

SE Spontaneous Emission

SS Steady State

VRS Vacuum Rabi Splitting

WC Weak Coupling (see also SC)

Chapter 1

Introduction

Contents

In this introductory Chapter, I will discuss, at the level of general physics, the theory of spontaneous emission (QED). Then, I will revisit this phenomenon in the context of cavity QED and of semiconductor physics, giving an overview of the state of the art. This introduction is part of a Review, in preparation.

1.1 Quantum Electrodynamics (QED)

Quantum Electrodynamics (QED) is the relativistic quantum field-theory that describes the interaction of light with matter.

It is the most successful theory ever conceived by man. The so-called *fine structure constant* α—the coupling strength of the interaction between electrons and photons—brings together some of the most important fundamental constants of physics:[1] $\alpha = e^2/(4\pi\varepsilon_0\hbar c)$. The numerical value of this constant embeds both the impressive achievements of science and its limitations. On the one hand, the theory has proven exact in predicting phenomena of light-matter couplings with an accuracy better than one part in a billion. On the other hand, there is no fundamental (or mathematical) explanation of its value, it has to be determined empirically.

[1] The charge of the electron e, the vacuum permittivity ε_0, the reduced Planck constant $\hbar$ and the speed of light in vacuum c

As a consequence, the best of our theories provides a very fine description of natural phenomena, but ultimately relying on what is essentially a fitting parameter.

The small value of the fine structure constant before 1, $\alpha \approx 1/137$, allows to recourse to the techniques of perturbation theory, vividly expressed in terms of Feynman diagrams. QED is sometimes described as the perturbative theory of the electromagnetic quantum vacuum, and this is indeed this particular aspect that most books on that topic actually study. In this text, we shall contemplate a rather different angle at the same time as we focus on but a very particular confine of the general theory, namely, to that which is known as *quantum optics*. It fits in the general picture as QED in the Coulomb gauge. We shall in particular discard relativity completely and rely on classical Schrödinger equation, but we will on the opposite reach to the nonperturbative regime, and go deeper into the quantum world.

Schrödinger immortalized his worries about one of the tenets of quantum theory—the principle of superposition—with his namesake cat that he imagined in a quantum superposition of alive and dead. Nowadays, there is no mysticism about the meaning nor doubt about the existence of such "cat states". One of the most important physical object that we will deal with throughout this text (we introduce it in next Section)—the *polariton*—is specifically of this nature.[2]

By studying the equilibrium properties of a gas of photons in a cavity, Einstein deduced the fundamental mechanisms of interactions of light with matter:

i Spontaneous Emission (SE)
ii Stimulated Emission

(Absorption is here regarded as a particular case of the stimulated process) The first mechanism refers to the return towards the ground (or an intermediate) state: when an atom has been excited and raised to an energy state higher than its ground state (with one electron having undergone a transition from its orbital to one of higher energy), it will ultimately recover its ground state by emitting a photon which carries away the energy of the transition. This decay of the excited state is spontaneous: it occurs randomly. Einstein derived and quantified it with the so-called A coefficient.

The second mechanism seems more mysterious at first, it describes emission in presence of another photon: if the excited atom as above is in presence of a photon similar to one that would be emitted spontaneously (of about the same energy), then the atom decays towards its ground state emitting a clone photon of

[2] In quantum dots. I use here a terminology that I shall define more precisely later. The main arena for polaritons is currently in quantum wells, where their quantum character is more disputable. However the term is gaining wide acceptance to describe superposition of light and matter, specifically in a quantum context. It is now even used in the atomic literature.

the original one, leaving two identical copies in the final state. Einstein termed it the B coefficient. They are still known as such nowadays.

A and B coefficients arise from Einstein's rate equations to fit the Planck distribution. The first important conceptual difference between the two is that despite the seemingly natural character of SE, it is actually of a deeper microscopic origin. The nature of the B process is at the heart of the bose statistics, responsible for lasing and Bose-Einstein Condensation (BEC). Bose statistics follows from a requirement of symmetry of the wavefunction. In that respect, it arises naturally from elementary quantum mechanics (in the first quantization). The B coefficient arises straightforwardly from perturbation theory, with the original photon playing the role of the perturbating field. The origin of the A coefficient cannot be traced at this level: an excited state without any perturbation acting on it should remain as it is. Of course, phenomenologically, one can introduce a decay rate, and this is the procedure Einstein used to fit the observed data. In this sense the temptation is great to think of this decay time as an intrinsic property of the atom, its lifetime.

Already in the so-called "old quantum theory", it was felt by Bohr that SE was of a nonclassical character: the atom makes a quantum jump which is probabilistic and without a cause. Dirac (1927) was the first to study the microscopic origin of the A coefficient, in the framework of the quantum theory of radiation, that would flourish in its wake as QED (he was the first to use that term). Dirac's extension of Schrödinger equation to include relativity still found, remarkably, an exact solution to the problem of the hydrogen atom. This most abundant of atomic elements therefore provides a complete, exact and self-contained picture of special relativity and quantum mechanics working together. One consequence of this theory was that states with the same n and j but different l quantum numbers are degenerate. In a cleverly set up experiment to challenge this prediction, Lamb Jr. & Retherford (1947) evidenced the contrary with what is now known as the *Lamb shift*, between the states $2s_{1/2}$ ($(n,l,j) = (2,0,1/2)$) and $2p_{1/2}$ ($(n,l,j) = (2,1,1/2)$). This showed that even a relativistic quantum description of the hydrogen atom was not, after all, complete! This caused a great turmoil at the time, specifically during the first Shelter Island Conference on the Foundations of Quantum Mechanics in 1947. Bethe (1947) quickly worked out a non-relativistic argument involving vacuum fluctuations that showed how a good numerical estimate could be obtained. In this attempt, he had to deal more directly than ever before with the famous problem of divergences that plague Dirac's quantum theory of radiation, the resolution of which—initiated at the Shelter Island conference that also attended Schwinger and Feynman—led to the full-fledged QED.

Back to the late 20s, Weisskopf, then a student in Göttingen, addressed the problem of the emission of one excited state to a stable (ground) state in the wake

of Dirac's theory. He did not encounter divergences[3] as he neglected most of the relativistic features but his treatment was nevertheless directly inspired by Dirac's treatment of the radiation field. Franck proposed Weisskopf to investigate the case of transitions between two excited states, that, however, he could not solve by himself (he once said that if he had had the proper mathematical training, he would have calculated the Lamb shift even before it was found). He put the question to a visiting Wigner who worked it out with him on the spot. Agreeably surprised by the outcome, Weisskopf & Wigner (1930) wrote a joint paper, now famous.[4] The outcome that pleased them both was the way the final linewidth built up from broadenings of the various states involved in the transition. The problem does not occur when the transition is from an excited state to the ground-state, which is not broadened. This is this case that the young Weisskopf solved by himself, and which is the one most frequently reported as Weisskopf-Wigner theory (sometimes with more than was there in the first place, like calculation of the Lamb shift). Interestingly, we shall see in my formulation of the problem that the Weisskopf-Wigner concerns revive in my treatment that includes the excitation, because with a pumping term, the ground state gets broadened too, and this bears some interesting consequences on the problem. But rather than considering any source of excitation, Weisskopf and Wigner considered the SE of the initial state $|1,0_{\mathbf{k}}\rangle$, where the atom is in its excited states and all modes of a continuous radiation field are devoid of photons.[5] They computed with the Dirac equation (that is in fact the Schrödinger equation in their approximations) the time evolution of the amplitude for $|1,0_{\mathbf{k}}\rangle$ and states $|0,1_{\mathbf{k}}\rangle$ for the various $\mathbf{k}$ that could have received the emitted photon. Even in this simplified picture, the problem is short of trivial. In this succinct introductory material, we shall not go through its derivation in details, but consider an approximation for the rate of transition from the initial state to the bulk of photon modes, grounded in Fermi's golden rule:

$$w_{1\to 0} = \frac{2\pi}{\hbar} |\langle 0,1_{\mathbf{k}}| H_{\text{int}} |1,0_{\mathbf{k}}\rangle|^2 \rho(\hbar\omega_{\mathbf{k}}), \tag{1.1}$$

where H_{int} is the light-matter coupling $\mu \cdot \mathbf{E}$ and $\rho(\hbar\omega_{\mathbf{k}})$ the density of optical

[3] They would resurface much later when his work would be scrutinized by early quantum field theorists such as Low (1952) or quantum opticians such as Louisell (1973).

[4] The historical background of this important theory is delightfully consigned in the Interview of Weisskopf by T.S. Kuhn and J.L. Heilbron on July 10, 1965, Niels Bohr Library & Archives, American Institute of Physics. Weisskopf's humility brought him to conclude that he was the first author of the paper with Wigner only for reasons of alphabetical order, even with such odds, at which point he resolved to author all his papers and books in this way. Sadly, the theory is now more frequently referred to as "Wigner-Weisskopf" theory.

[5] Here we must quote again Low (1952) who, in his three complaints against the Weisskopf-Wigner theory, starts with the problem of the excitation scheme that is approximated as a mere initial condition. The divergency I mentionned before was his second complaint.

modes. The exact Weisskopf-Wigner result obtains an exponential decay of the excited initial state, at a rate given by eqn (1.1) and that their procedure links to the value previously given by Dirac; in that sense, the main value of their approach, at least in their view, was an alternative microscopic derivation of the mechanism of SE in quantum theory. Although the Schrödinger equation is reversible, the Weisskopf-Wigner model devised an insightful picture mechanism—with a coupling of a single mode (the excited atom) to a continuum (the empty radiation field)—whereby irreversibility emerge from an Hamiltonian (cyclic) dynamics. This mechanism predates the modern description of it in terms of reservoirs, a formalism that I will review briefly in §2.

The modern QED picture accounts for the Lamb shift, with the accuracy evoked previously, by summing-up various contributions (various Feynman diagrams) of opposite tendencies (like the anomalous magnetic moment, and the vacuum polarization). But the most important effect is the one captured by Weisskopf and Wigner's mechanism and advanced by Bethe, that of the renormalization of the electron mass by its interaction with the electromagnetic field (in vacuum). This was further studied by Welton (1948), who also suggested that fluctuations of the vacuum were responsible for spontaneous emission. In Dirac's interpretation, this was attributed to QED radiaction reaction, but, as was later realized by Milonni et al. (1973), this is essentially the same with some reordering of operators.

Another important name of the field, Jaynes, was also thinking in terms of back-action of the electromagnetic field on the atom, but with the view that quantization of the field was not necessary, at least not to explain the Lamb shift, SE or any related phenomena. He accepted the challenge that he could demonstrate the Lamb shift from these grounds (without photon field quantization) in within 10 years! He could indeed reproduce, with great efforts from himself and his students, the result qualitatively, but he failed to match the same accuracy that QED was providing so elegantly.[6] Ironically, the model Jaynes & Cummings (1963) developed as a support of Jaynes' so-called neoclassical theory, against field quantization, is now the drosophilia of quantum optics and cQED. The celebrated *Jaynes-Cummings* (**JC!**) model provides the fundamental picture of light-matter interactions at the ultimate quantum level: when only one mode of light a is interacting with only one mode of matter σ, and single quanta are mediating

[6] Stroud remembers the whole sequence of events in "*The Jaynes-Franken Bet*" §30 of "*A Jewel In The Crown*", Meliora Press, (2004). Jaynes' efforts have naturally been pursued long time after him, see for instance the attempts by Barut & Huele (1996), whose claims have been, naturally, further disputed. I will leave aside further questions on to which extent is the full-field quantization necessary, holding to the mainstream view that it is and that both the Lamb shift and SE are two fundamentally quantum phenomena.

the interactions. Its hamiltonian reads:

$$H = \omega_a a^\dagger a + \omega_\sigma \sigma^\dagger \sigma + g(a^\dagger \sigma + a\sigma^\dagger)\,. \tag{1.2}$$

Here, $\omega_{a,\sigma}$ are the free energies for the modes and g is their coupling strength. The physics of this system is to be investigated in specially prepared conditions, where these single modes have been properly selected and isolated. This is the topic of next Section.

1.2 Cavity Quantum Electrodynamics (cQED)

Cavity QED (cQED) rests on the realization above that the lifetime of an atom is not a property of the atom itself but of the coupled atom-radiation field system. If one would be able to alter the radiation field in some sense, such as for instance in suppressing its fluctuations (including those of the vacuum!) or modifying its density of states, this would alter the lifetime of an excited state, as suggested by Eq. (1.1) if $\rho(\omega)$ is changed.

The effect was first put to use by Purcell (1946) in nuclear magnetic resonance for the practical purpose of thermalizing spins at radio frequencies, by bringing down their relaxation time from $\approx 10^{21}$s to a few minutes. Interestingly, this seminal achievement in tailoring what was widely regarded before (since Einstein's theory of spontaneous emission) as an intrinsic property of matter, did not impress much Purcell himself or his contemporaries, despite the good timing (Purcell did not attend the Shelter Island conference, but Rabi, his then hierarchic superior, did). The effect of tailoring lifetime through the density of optical modes is nevertheless now known as the *Purcell effect*. Similar concepts were investigated from a more fundamental and direct angle by Casimir (1948), for instance demonstrating the attraction between two conducting plates close enough for—in the words of Casimir—"*the zero point pressure of electromagnetic waves*" being reduced between the plates. With regard to SE, the problem was considered again for its own sake by Kleppner (1981). In his initial proposal, he considered it in the opposite sense than Purcell, namely, to increase the lifetime of the excited state, by decoupling it from the optical field (and therefore also from its vacuum fluctuations). Soon after, Goy et al. (1983), from the Haroche group, reported the first experimental observation of Purcell enhancement.[7] The authors concluded their paper setting the goal for an higher milestone of cavity QED: when spontaneous emission is enhanced so much that absorption—which is equal to it from Einstein's theory—or more specifically, since we have only one emitter, *reabsorption* of the photon by its own emitter, becomes dominant over the leakage of the photon

[7] Of sodium atoms, with an increase to $8 \times 10^4 \mathrm{s}^{-1}$ from the free-space value of $150\mathrm{s}^{-1}$.

out of the cavity, then the perturbative—so-called *Weak Coupling* (WC)—regime breaks down and instead *Strong Coupling* (SC) takes place. In this case, emitted photons entail a whole sequence of absorptions and emissions, known as *Rabi oscillations*, until their ultimate decay out of the cavity. This regime is of greater interest, as it gives rise to new quantum states of the light-matter coupled system, sometimes referred to as *dressed states*, especially in atomic physics and as *polaritons* in solid-state physics. Experimentally, SC is more difficult to reach, as it requires a fine control of the quantum coupling between the bare modes and in particular to reduce as much as possible all the sources of dissipation.

Haroche's group in their first report of tuning the SE, placed this higher goal only "*a tenfold increase in Q*" away. Shortly after, they reported, with Kaluzny et al. (1983), the first observations of Rabi oscillations. However, rather than increasing the Q, they had used N atoms, thereby enhancing the coupling strength by a factor $\sqrt{N}$. Unfortunately, my thesis will stop short of the so-called Dicke Hamiltonian (cf. my conclusions) that explains this enhancement in its full generality. However we shall see its manifestation in the particular case of $N = 2$. Haroche & Kleppner (1989) have written an authoritative review on the early cQED experimental achievements. [8]

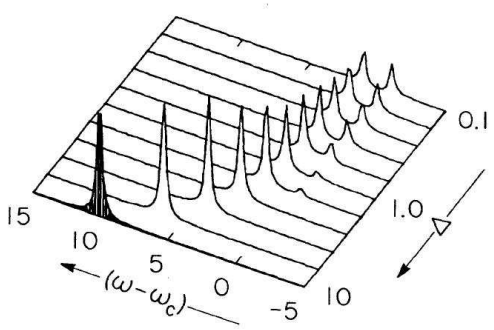

Figure 1.1: The first theoretical computation of the cQED lineshape of the spontaneous emission of a system in strong coupling, as detuned is varied, by Sanchez-Mondragon et al. (1983).

On the theoretical side, Sanchez-Mondragon et al. (1983) were the first to address the fundamental problem of the lineshape of the SE in cQED.[9] They met with the difficulty of the definition of the optical spectrum, which had otherwise found an acceptable solution for the physics community with the mathematical

[8]This much quoted paper is nowadays of interest mainly for its historical content. Better reviews for the modern reader are given by Vahala (2003).

[9]The brevity and clarity of the full abstract of their text is exemplar and will fit comfortably in this footnote: "*The spontaneous-emission spectrum of an atom in an ideal cavity is calculated.*" This work was part of the Ph. D. thesis of José Javier Sánchez Mondragón.

work of Wiener (1930) and Khinchin, even in the cases of non-stationary signals. However, under the guidance of Eberly, they recursed to the rigorous Eberly & Wódkiewicz (1977)'s time-dependent physical spectrum instead:

$$\mathscr{R}(t,\omega_f) = \Gamma_f^2 \int_{-\infty}^{t}\int_{-\infty}^{t} e^{-(\Gamma_f - i\omega_f)(t-t_1)} e^{-(\Gamma_f + i\omega_f)(t-t_2)} \langle a(t_1)^\dagger a(t_2)\rangle dt_1 dt_2\,. \quad (1.3)$$

This expression is derived from physical (rather than mathematical) grounds, computing probabilities of measuring a photon by absorption from a detector, that introduces its linewidth Γ into the problem. The rest of their treatment was otherwise the most standard possible. Their Hamiltonian was JC's hamiltonian and they considered as initial conditions the excited state of an atom in an empty cavity (case of Fig. 1.1) or in a cavity prepared in a coherent state, in which case they observed the transition from a Rabi doublet to a Mollow triplet with the intensity of the cavity. This first description however suffered from serious limitations, the most important of which being the absence of dissipation: they considered an infinite lifetime atom in a lossless cavity (whence the "ideal" cavity). This is another value of Eberly and Wódkiewicz's approach that it takes into account the linewidth of the detector, thereby rescuing the result with well-behaved spectral-shapes rather than δ singularities. The doublet they obtained as a result of this modelisation consists in exactly two Lorentzian lines. They could observe, however, the *vacuum Rabi splitting* and the anticrossing at resonance, but their result actually relates to the Hamiltonian structure of the coupling, artificially broadened. Their description is lacking in particular the most important feature of SE, as should be clear from our previous discussion, namely, irreversibility.

If only for reasons of self-consistency, cavity decay should be included to describe any luminescence experiment, since photons should leak out from the cavity to be detected, as duly noted by Agarwal & Puri (1986), who added this ingredient κ in a master equation for the coupled light-matter system:

$$\partial_t \rho = -i[H,\rho] - \kappa(a^\dagger a\rho - 2a\rho a^\dagger + \rho a^\dagger a)\,. \quad (1.4)$$

(note that here and also in Fig. 1.2, κ is the *cavity* decay rate, in possible conflict with other notations.) H is still JC's hamiltonian, eqn (5.9), although, in the linear case, the linear model where both fields obey Bose algebra, would give the same result (a simplification that we shall take advantage of in §3). Also, as we shall prove later, in the case of SE, the Lindblad form is not necessary to compute correlator functions and a much more straightforward treatment is obtained by including dissipation as an imaginary part to the energy. Interestingly, they used the same Eberly and Wódkiewicz' physical spectrum, eqn (1.3). Agarwal & Puri also considered transmission and absorption as well as SE, but I will not discuss this aspect of their work which is not relevant to my description (where I will compute only photoluminescence).

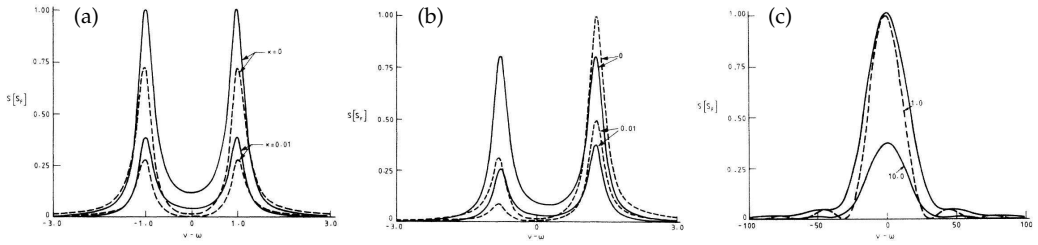

Figure 1.2: Lineshapes of a coupled light-matter system with cavity dissipation, as computed by Agarwal & Puri (1986). Solid lines are cavity emission and dashed lines direct atomic emission. Detector linewidth was taken as $g/5$. (a) at resonance for no cavity decay (upper lines) and small cavity decay (lower lines). (b) same as (a) but for a detuning of $g/2$. (c) Bad-cavity case with disappearance of the doublet.

The most complete quantum optical calculation, supported by the most insightful discussion, was brought by Carmichael et al. (1989), who consider the most general case with both types of decay:

$$\begin{aligned}\partial_t \rho = &-i[H,\rho] + \kappa(2\sigma\rho\sigma^\dagger - \sigma^\dagger\sigma\rho - \rho\sigma^\dagger\sigma) \\ &+(\gamma/2)(a^\dagger a\rho - 2a\rho a^\dagger + \rho a^\dagger a)\,. \end{aligned} \tag{1.5}$$

(Note that in Carmichael et al.'s notations, κ is now the atom decay rate and γ the cavity decay rate). As before, the authors consider the SE of the initial state $|+\rangle|0\rangle$ (excited state, no photon in the cavity) and can solve the problem exactly since in this picture it self truncates in the Hilbert space spanned by the initial condition and $|-\rangle|1\rangle$, $|-\rangle|0\rangle$.

In rupture with the two previous approaches, the luminescence spectrum is here computed with the formula:

$$2\pi S(\omega) = \frac{\int_0^\infty \int_0^\infty e^{-i(\omega-\omega_0)(t-t')} C_s(t,t')}{\int_0^\infty C_s(t,t)}\,, \tag{1.6}$$

which is the expression we shall later adopt in the case of time-dependent dynamics (case of SE). There are various reasons to do so that I want to discuss at once: the main one is that the description of luminescence of the coupled light-matter system by Carmichael et al. is the most achieved at this level of description and I regard the formulation of this problem for semiconductors, that I have proposed with Laussy et al. (2008), as an extension of Carmichael's treatment. Another reason is that it frees us from the detector's linewidth, which, if the needs should be felt to include it, can be considered at a refinement of the fundamental spectrum (by the usual procedure of convolution) but that otherwise does not need to enter

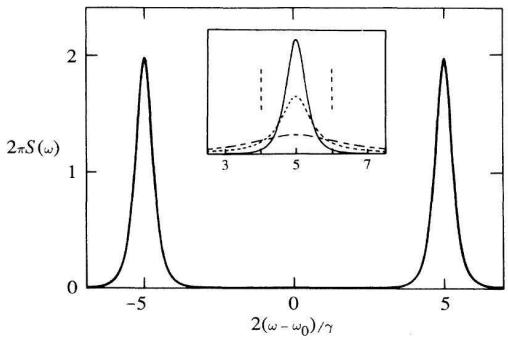

Figure 1.3: Lineshapes of a coupled light-matter system with both cavity and emitter dissipation, as computed by Carmichael et al. (1989), showing the subnatural linewidht averaging. Parameters are $\kappa \gg \gamma/2$ and $2g/\gamma = 5$. In inset, zoom on one peak comparing the SE (dashed), free-space fluorescence (broader line, dot-dashed) and fluorescence (solid).

the picture at the chief level, as it did in the two previous descriptions. Finally, in my generalized treatment to the case of a steady state, formula (1.6) will be shown to a more relevant limiting case of the Wiener-Khinchin formula that I use for the stationary fields, this time in full rigor. This, a posteriori, justifies the choice of formula (1.6) over its counterpart (1.3), whose extraneous parameter Γ, physically relevant and important, deserved the theoretical description of SC.

Before closing this Section of the seminal experimental and theoretical efforts in cQED that are the most relevant for our subsequent discussion, I want to comment on the feature that are missing from Carmichael et al.'s description, and that I will provide in next Chapter. Those are the arbitrary initial condition, and the atom emission. In their partial pictures, both Sanchez-Mondragon et al. and Agarwal & Puri had addressed these questions to some extent (but still far from full generality). The former had considered various coherent states of the optical field, and the former had computed both the photon and exciton emission. I want to comment quickly on the necessity of these extensions, though we shall discuss them at greater length when I address the problem. It is clear that the initial condition strongly influences the optical spectrum, as can be seen by considering as initial states the excited state of the two-level system, $|\psi_{\rm ex}\rangle\,(t=0) = |0,1\rangle$, or $\left|\psi_{\rm ph}\right\rangle(t=0) = |1,0\rangle$ on the one hand, and an eigenstate of the Hamiltonian, eqn (5.9), $\left|\psi_{\rm eig}\right\rangle(t=0) = (|1,0\rangle \pm |0,1\rangle)/\sqrt{2}$ on the other hand. These will normally produce, respectively, a Rabi doublet and a single peak, which are quantitatively very different. It is may be less obvious that $|\psi_{\rm ex}\rangle$ and $\left|\psi_{\rm ph}\right\rangle$, also differ, and in some case also quantitatively. In particular cases, one initial state will produce a doublet while the other will produce a single line (in fact a doublet which splitting is too small to be resolved as such). These considerations, that in this context

might appear as mere gratuitous and/or academic generalization, will become a natural, and in fact, compulsory, requirement in the semiconductor treatment, to which I now turn.

1.3 Semiconductor cQED

The physics of cQED has naturally attracted the attention of the semiconductor community, if only in view of the possible technological applications. Semiconductor heterostructures are the state of the art arena for this purpose. They allow to engineer, with an ever rising control, the solid state counterpart of the atomic system to match or isolate their excitation spectra and thus control their behavior.

At the most basic level of description, an heterostructure is a man-made, microscopic edifice of different semiconductors. A typical heterostructure is the alternating sequence of fine semiconducting slabs with different refractive index, such as gallium arsenide (GaAs), the compound of gallium and arsenic, and aluminium arsenide, AlAs, with almost the same lattice constant as GaAs but a wider bandgap. A pile of typically twenty such pairs produce a microscopic mirror for light, because of Bragg's reflection in this periodic crystal (such a structure is called a "Bragg mirror", or a "distributed Bragg mirror"). Two such mirrors face to face produce a microcavity.

The different bandgaps result in energy band offsets that produce potentials for the carriers. In effect, this can be used to confine the semiconductor excitations, namely, electrons and holes, or their bound state, called an *exciton*. Confinement can thus be achieved in a plane when, e.g., a slab of semiconductor is sandwiched between two others with a wider bandgap, giving rise to a so-called Quantum Well (QW), for instance again with GaAs and AlAs, used above to build a mirror. Confinement can also be achieved in 1D with Quantum Wires, and, more importantly for our discussion, full confinement in all dimensions can be achieved in so-called Quantum Dots (QDs). A QD, for that reason, is sometimes referred to as an "artificial atom", because the full space quantization means that its excitations consists in discrete excited states, much like in the Bohr (and modern) picture of the atom. Placing a QD in a microcavity, by growing a sequence of alternating layers to produce a first mirror, then growing a QD, and finally toping it off with another sequence of alternating layers to produce another mirror, completing the cavity, yields a micron-scale cQED system, opening the way forward to *microcavity QED*.

For historical purposes, and to give the proper background to microcavity QED, one must start with QWs as the active element,[10] not QDs. I will give only

[10] "Active" in this context means the part that provides the electronic excitations, the excitons. A

the most elementary overview of this huge field. Excellent reviews have been written on that topic, for instance by Skolnick et al. (1998), Khitrova et al. (1999) or, for the most recent developments, by Kavokin (2007); see also the textbook by Kavokin & Malpuech (2003) for a dedicated coverage of QWs polaritons and the collection of texts edited by Deveaud (2007) for the views of some of the leading experts of these questions. Kavokin et al. (2007)'s textbook is addressing these questions in a larger context and will be a useful companion to this introduction for bridging between dimensions.

For the same reason that atomic physics found it hard to achieve SC with a single atom, it was not at the reach of technology to yield strong exciton-photon coupling until the year 2004 (interestingly, at the same year than the experiment by Boca et al. (2004) in atomic cQED, that, by retaining one and the same atom, provides the closest counterpart to the QD cQED case). QWs are more easily grown and controlled, multiple QWs can be placed inside the cavity and the antinodes of the field (where it is maximum) to achieve the best coupling.

The most significant finding in this field has been the observation by Weisbuch et al. (1992) of anticrossing in absorption of a planar heterostructure,[11] whose schema is shown on the left part of Fig 1.4. The stack explicated above is here spelt out; the QWs also involve Indium. The anticrossing itself is shown on the right: at resonance, two symmetric dips show a splitting of the structure's modes. This splitting is universally called the Rabi splitting. We pose to provide the proper context to this terminology.

Weisbuch et al. described their seminal finding as a "*solid state QED effect*" and linked it to the vacuum Rabi splitting (VRS) with many references to the atomic QED achievements. They were well aware, however, of the alternative, "*more classical*" picture. Which one should be favored has been a topic of debates, that is still not completely settled to this day. Khitrova et al. (2006), in their review of SC with QDs in microcavities, speak of a "genuine" or "real" SC, to distinguish it from the 2D-polaritons SC what they would prefer to be called "normal mode coupling" (a term that we find in the original Weisbuch et al.'s paper along with VRS, but that has been completely ignored by the polariton community thereafter). Normal mode coupling essentially refers to a fully classical analog to the phenomenon of anticrossing that, because it evokes mode repulsion, is often favourably understood as quantum in origin. Instead, the mere appearance of new modes in coupled (classical) oscillators, is an exact depiction of the phenomenon without the need to recourse to quantum physics. This point has been made very

cavity without QWs or QDs between the two Bragg mirrors is an empty cavity, a passive element described by classical linear optics.

[11]There has been, prior to Weisbuch's line-splitting, reports of Purcell effect in planar cavities (e.g., fromYokoyama et al. (1990) and Björk et al. (1991)), but I will not discuss these because they are of interests in the context of 2D polaritons only. We shall focus on the QD case later.

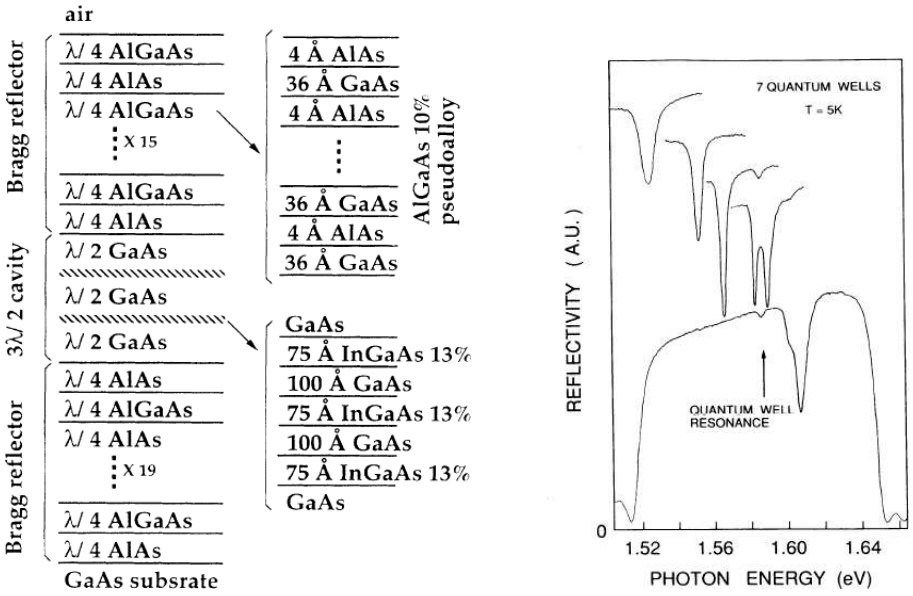

Figure 1.4: Schema of a semiconductor heterostructure, by Houdré et al. (1994), and its observed anticrossing, by Weisbuch et al. (1992), launching the field of microcavity-polaritons physics.

clear by Zhu et al. (1990), who insist that their Rabi splitting stems from classical physics. The main issue against 2D-polaritons to perform cQED physics is the vast number of excitations involved, as opposed to QDs where the physics can be brought to the quantum limit, in the sense of involving a few quanta, one—or none if there is a way to evidence effects of the quantum vacuum—in a regime where one quantum more or less changes the behaviour of the system. In the 2D case, the idea of VRS goes with that of linear response, but not with that of field quantization. The most elaborate and accurate descriptions of these systems have been in terms of continuous fields. Also, in the atomic QED problem, interaction is between two modes only (in this sense it is zero-dimensional), but with 2D-polaritons, although there is still a one-to-one matching between a photon and an exciton, this extends over a whole range of in-plane wavevectors.[12] This provides polaritons with a rich dynamics of scattering, but in a fundamental picture, this brings complications and somewhat blurs the picture.

This is not to say that quantum physics should be excluded as a whole from these systems. Probably the second strongest input to the polariton field was the report by Savvidis et al. (2000) of stimulated scattering of polaritons. This evi-

[12] Often, the $k = 0$ mode is considered separately from the higher modes and some arguments of 0D cQED reappear in this particular context. Here neither this polariton ground-state can be put on a par with the single mode of a real 0D system.

denced bosonic statistics in the system, and opened the way to that the field of BECs of polaritons, with a recent claim to this breakthrough by Kasprzak et al. (2006). One of the most actively sought after signature of the quantum degeneracy of 2D-polaritons is currently being looked for with manifestation of superfluidity, and some preliminary experimental evidence have been reported by Amo, Sanvitto, Laussy, Ballarini, del Valle, Martin, Lemaître, Bloch, Krizhanovskii, Skolnick, Tejedor & Viña (2009) and Amo, Lefrere, Pigeon, Adrados, Ciuti, Carusotto, Houdre, Giacobino & Bramati (2009). In any case, those are still manifestations of macroscopic coherence where large numbers of microscopic particles exhibit the behaviour of a continuous field (classical or not). At the ultimate quantum limits where single polaritons matter in a quantum way, there is still some activity but not with quite the same attention. Let us mention however the pioneering proposal of Ciuti (2004)[13] to generate entangled photons from 2D polaritons, or the investigations of vacuum radiations, that he proposed with De Liberato et al. (2007). In a cleverly designed "triple cavity", Diederichs & Tignon (2005) have proposed another promising mechanism for generating entangled pairs, later announced by Diederichs et al. (2006). Finally, Savasta et al. (2005) have also discussed the genuine quantum nature of polaritons. However, those results have elicited a limited interest (as compared to their significance) and their recognition is unclear. There is not as yet an explicit demonstration of full-field quantization such as violation of some Bell inequalities. The opposition between macroscopic quantum phenomena versus nonlinear classical optics is still important, and the necessity of the quantum picture at the one-quantum limit for 2D-polaritons is even more debatable.

A better of single quanta in the QD picture was foreseeable. Brunner et al. (1992) were already able to measure the PL of single dots, a feat repeated by Marzin et al. (1994) with self-organized (or self-assembled) QDs. Placing them in a cavity would seem to lead to an easy, direct and explicit manifestation of full-field quantization. I take over the historical progresses with this approach, ultimately the system that we shall devote the best of our attention to.

To be in SC with the single-mode QD, the cavity should also sustain an isolated single mode, otherwise the mechanism of Weisskopf of non-reversible leakage of the excitation into the many cavity modes would lead to exponential decay rather than Rabi oscillations. There are various but mainly three types of designs to achieve this goal of a zero-dimensional semiconductor microcavity. Figure 1.7 shows a stunning view of so-called *pillar cavities*. These are obtained from etching a conventional planar stack of Bragg mirrors. The lateral confinement is then

[13] Ciuti et al. (2000) had already pioneered the theory of OPO in 2D microcavities, that has been so far the system of choice for tracking polariton superfluidity, in a theoretical context that he also put to the front with Carusotto (Carusotto & Ciuti 2004).

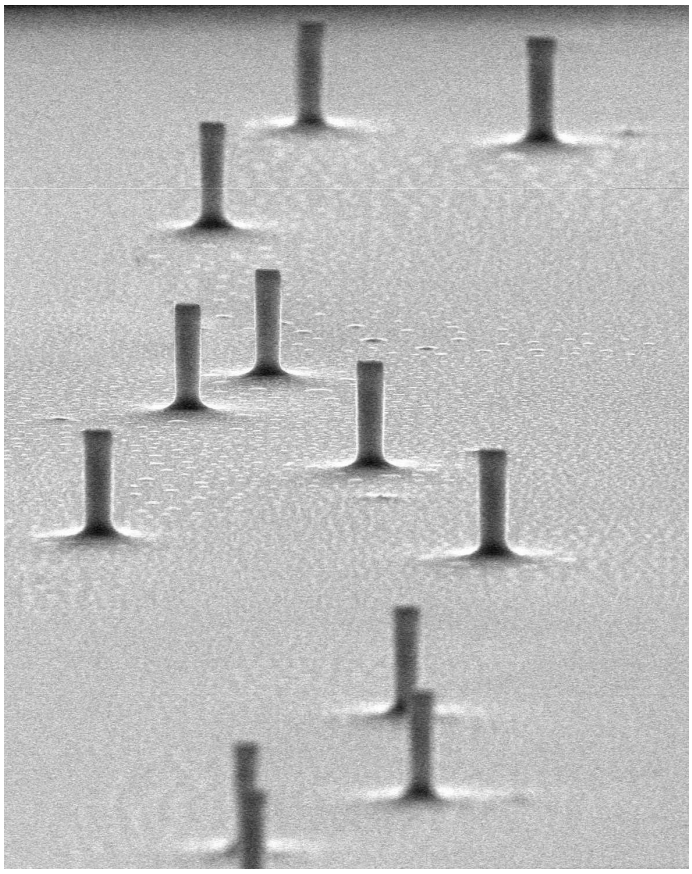

Figure 1.5: SEM image of pillar microcavities, from the LPN laboratory in Paris. Each pillar is about 10μm of height.

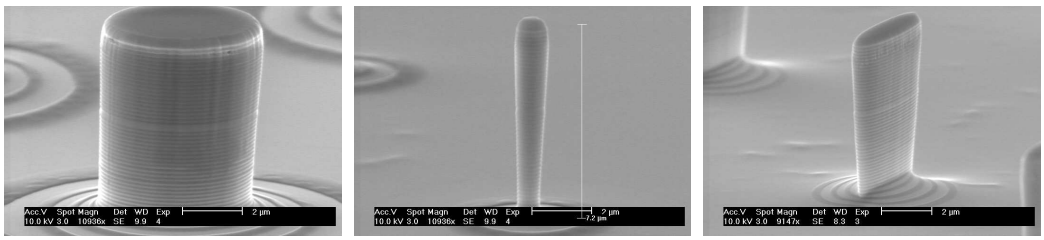

Figure 1.6: Various pillars as grown by the University of Sheffield, demonstrating the great control of shapes and sizes that can be obtained. Ellipticity of the right pillar is used to control polarization of the emitted light, as discussed by Whittaker et al. (2007).

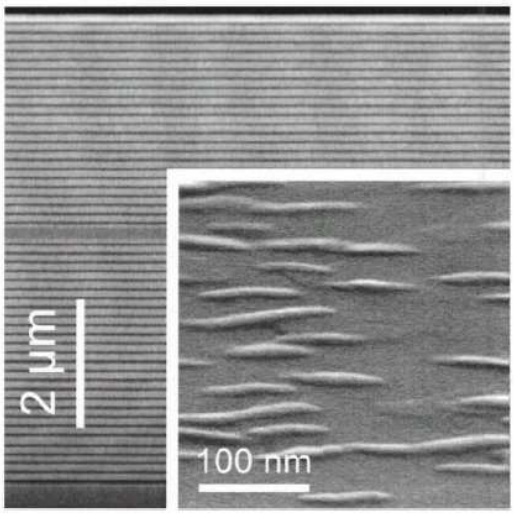

Figure 1.7: SEM image from Löffler et al. (2005) of the two Bragg mirrors, forming the microcavity (that can be seen near the center) and of the QDs that are embedded inside.

provided by the refractive index. The pillars would typically be selected one by one, until a system evidences a sufficient interest. Chance has it that, as of today, many and probably most of these pillars do not present a single QD in SC. There is therefore a strong element of choice in isolating an interesting system. To the best of my knowledge, there is however no quantitative estimate for this factor. I shall discuss this question in more details later. Figure 1.6 shows close-up views of pillars, this time grown in Sheffield. There is an impressive control in the size and shapes with which to shape these structures. Sanvitto et al. (2005) have reported high values of Q with such structures,[14] but could not observe SC. I will propose a tentative explanation for this shortcoming. In Fig. 1.7, finally, we get the closest view on the pillar system, with an image from Würsburg, where are shown both a close view of the Bragg mirror (compare with the schematic view of Fig. 1.4) as well as the particular QDs that have been used in this work. I shall describe this aspect in more details later when I come back to the theoretical description of these dots, as the pillar structure is the one to which I will devote more direct attention.

Another important realization of a single microcavity mode is the photonic crystal. The concept has been put to technological use only recently, after the topic was itself brought to the limelight by Yablonovitch (1987) and John (1987) (in two consecutive letters to the Physical Review). The principle is based on

[14] Of the order of $\sim 3 \times 10^4$. Same figures are also reported by Muller et al. (2006), and more recently, of 1.65×10^5 for radius size of 4μm by Reitzenstein et al. (2007).

the same physics that leads to bandgaps in semiconductors:[15] the propagation of photons in the periodic structure is forbidden for regions of wavelengths because of destructive interferences of the same type as those of Bragg physics. These regions form bands that can be separated by a photonic bandgap.

Yablonovitch et al. (1991) reported the first 3D PC. By drilling holes in a slab at three different angles, they could create a complex PC with a full bandgap in the microwave range. Krauss et al. (1996) reported a 2D PC near the optical spectrum. We shall be more interested in this case, that has in fact attracted more attention, if only because of the much easier fabrication (drilling holes on a plane rather than inside a volume). The crystal is directly etched into a slab of semiconductor. Noda et al. (2000) demonstrated that a cunningly introduced defect in the 2D crystal structure, was forming a cavity for photons (that were injected through a lateral waveguide close to the cavity). The Q of the cavity thus formed was then of about 400. They then realized that much better confinement was possible if the cavity itself, rather than a mere defect in the crystal, would be engineered to allow the electric field distribution to vary slowly, ideally as a Gaussian. This is realized "merely" by shifting the position and reducing the radius of neighboring holes to the one that has been skipped to form the cavity. Now, Q factors of more than 2.5×10^6 have been reported by Takahashi et al. (2007) and Tanaka et al. (2008) speculate on designs that promises figures up to 10^9. A review of PC structures is given by Noda et al. (2007)

Finally, a last structure prone to rich cQED, is the so-called microdisk, where light is trapped in whispering gallery modes. An example system is shown on Fig. 1.9. A review of microdisks is given by Nosich et al. (2007).[16]

Embedding the dots in a pillar cavity, Gérard & Gayral (1999) reported the Purcell effect of shortening, or lengthening, of the lifetime in the SE problem, with a Purcell factor of 5 and there since have been a considerable number of similar observations in various systems (e.g., Solomon et al. (2001) and Bennett et al. (2007) also in pillars, Kiraz et al. (2001) in microdisks, Chang et al. (2006) in PC, etc...) On Fig. 1.10, Purcell effect is nicely demonstrated by Chang et al. (2006) who observe the time-resolved observation of the luminescence of a dot in a bulk semiconductor (with a lifetime of $\tau \approx 0.65$ns). When a similar dot is place inside the photonic bandgap of this semiconductor, its lifetime is extended to 2.52ns, while still another dot, this time in resonance with a cavity mode etched into the semiconductor, the lifetime drops to 0.21ns. Another experiment with the Pucell effect that I want to highlight is that of Bayer et al. (2001), in a pillar

[15] Yablonovitch (2001) himself dub them "semiconductors of light" in a personal recount of the early experimental efforts to the Scientific American, and is generally keen to relate the two systems in his academic discussions. Yablanovitch is one of the surest future Nobel laureate one can envision for the near future.

[16] Oddly, the SC issue is addressed but not quoted in this review.

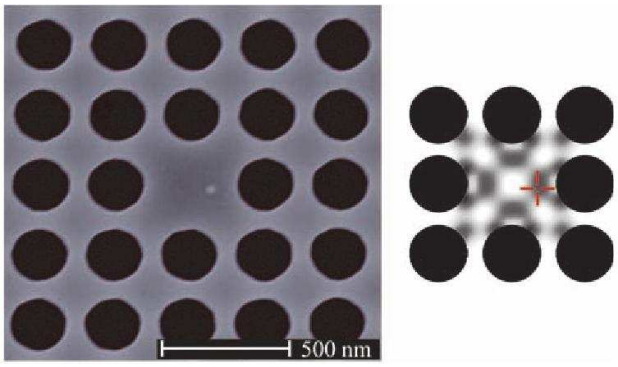

Figure 1.8: SEM image of a Noda cavity formed in a photonic crystal by "removing one hole" in the periodic structure, by Badolato et al. (2005). On the right, calculated electric field, with maximum in dark. Remarkably, Badolato et al. can place a single QD at a location of their choice, so they could put it at precisely one of these maxima, namely at the point marked by the red cross. The dot is indeed visible on the SEM picture!

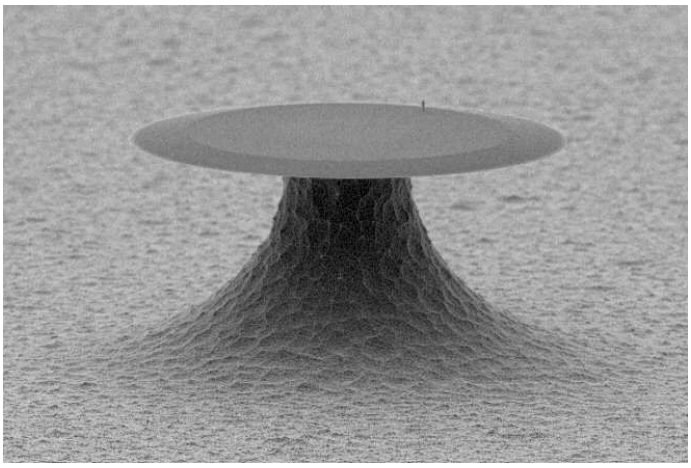

Figure 1.9: SEM image of a microdisk, from Kippenberg et al. (2006), sitting on a Si post erected on the silicon wafer. The silica microdisk cavity is 30μm in radius. The wedge has been etched intentionally to push the whispering gallery modes inward, to protect them from scattering-induced cavity boundaries. See also the discussion by Armani et al. (2003).

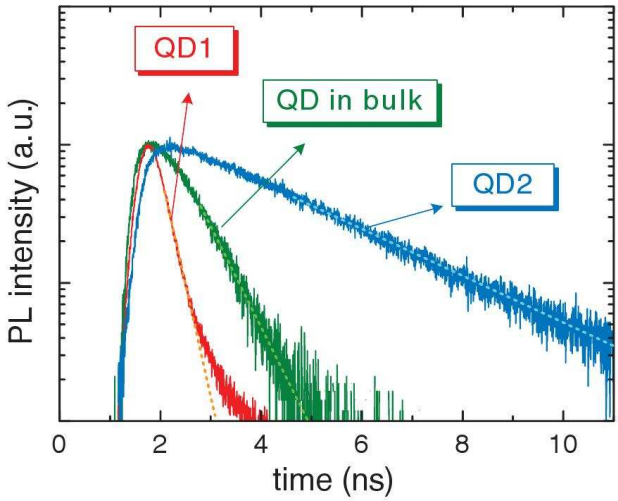

Figure 1.10: Purcell effect, as observed by Chang et al. (2006) with a QD (1) in resonance with a single mode of a PC, suffering enhancement of its decay, a QD (2) out of resonance, slowing down its SE and a QD in bulk, setting up the scale of "normal" decay.

whose sides had been coated or not, demonstrating the impact of leaky emission on the Purcell effect. In subsequent chapters, I will discuss at length its role in the physics Strong-Coupling.

A continuous progress has been made towards a better quantum coupling with dots in 0D MC, as well as towards its external control. The inclusion in the cavity of QDs lowers the quality factor, but prowesses have been achieved in the engineering of the heterostructure, allowing to deterministically position a QD inside a photonic crystal to within 25nm accuracy, and thus place the dot at a maxima of the light intensity, along with an etching technique of the holes of the photonic crystal to match spectrally the QD and cavity mode emission (see Fig. 1.8). At the same time, the density of self-assembled QDs in the active medium has been successfully reduced over the years, with figures of 10^{10}cm^{-2}, and the possibility to grow large dots (with lens shape of $\approx$ 30nm) so as to provide a large oscillator strength. With microdisk resonators, the whispering gallery modes of a thin disk supported by a column provide the high Q modes of the cavity. Nevertheless, reaching the SC has been painful and long, and the number of reports has not been overwhelming ever since. Anyway, in late 2004, in two consecutive letters to Nature, Yoshie et al. (2004) and Reithmaier et al. (2004), report SC of QDs with a single-mode microcavity, in a PC and a pillar, respectively. At about the same time, but published later, Peter et al. (2005) report SC in microdisks. Their results are shown on Fig. 1.11

In stark contrast with my outrageous overview of the situation with Purcell

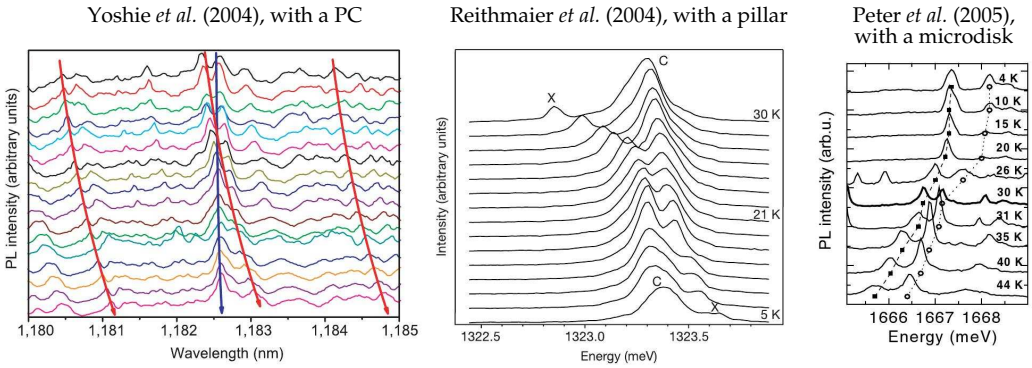

Figure 1.11: The seminal observations of SC of a QD with a single-mode of light, by Yoshie et al. (2004), Reithmaier et al. (2004) and Peter et al. (2005). All observe a clear anticrossing of the modes as they are brought to resonance by tuning the temperature. Because the data of Reithmaier et al. appeared the cleanest to us, we decided to focus on this particular experiment.

effect, I shall attempt to list an exhaustive list of reports of SC (not counting multiple publication of the same experiment) following the three above mentionned. We shall see that there is ample room for them even in this short introduction. They are displayed in Fig. 1.12.

Despite the steady progresses made in all areas relevant to SC physics, the reports of SC are conspicuously rare. The latest one, from Laucht et al. (2008), comes with an interesting setup. They authors have realized an electrically controlled device, shown on Fig. 1.13, that is operated with a mere bias voltage, using the quantum confined Stark effect to detune the dots in SC with the mode of a L3 photonic crystal.[17] They excited the system with an off-resonant laser pulse, and observed the SE. on a fully integrated (at the exception of the pumping) chip, allowing for quick, convenient and reversible control. Their work opens the road towards on-chip control of SC.

The SC reported by Hennessy et al. (2007) comes with a strangely non conventional feature, namely, the appearance of a triplet at resonance! The authors motivate the scenario that the triplet is in fact the superposition of a normal Rabi doublet of SC on top of a single line of the system in WC, and that the system is either in WC or SC depending of some irrelevant microscopic detail.[18] After all, the emission is collected from millions of realizations of SC, and if a fraction of them does not succeed but remain in WC, the net impression will be that of this

[17] "L3" means that three holes in the PC patterns have been skipped to produce the defect region that serves as the microcavity. The PC in Fig. 1.8 is therefore L1.

[18] In their case, they suspect the effect of a charged carrier; see their manuscript for more precisions.

Press *et al.* (2007), Pillar

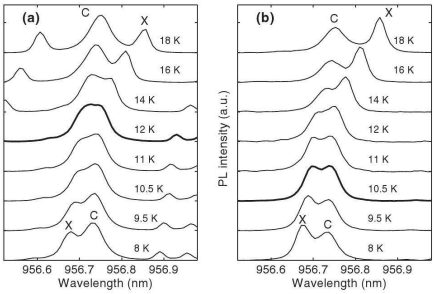

Hennessy *et al.* (2008), PC

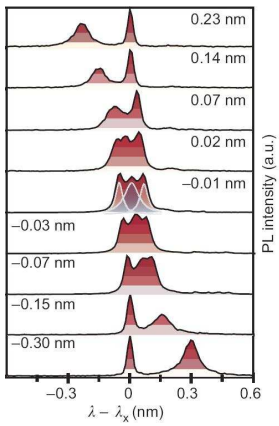

Laucht *et al.* (2008), PC

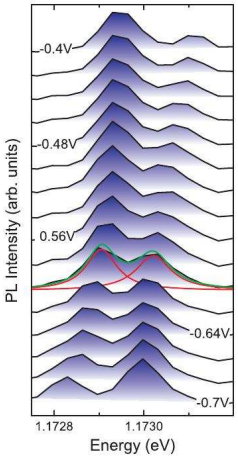

Nomura *et al.* (2008), PC

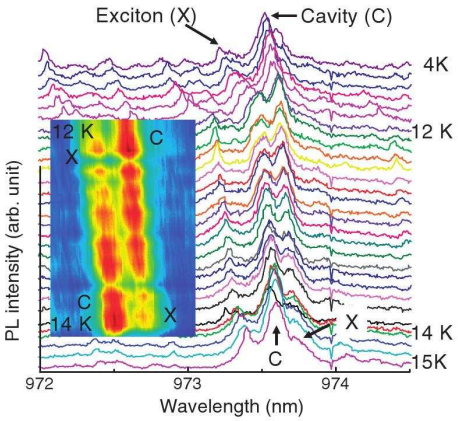

Figure 1.12: Later reports of SC in 0D semiconductor microcavities after the seminal breakthroughs of Fig. 1.11: by Hennessy et al. (2007), Press et al. (2007), Laucht et al. (2008) and Nomura et al. (2008).

odd triplet structure. In this sense their SC is not robust to its environment, but this is still better than no SC at all. The main value of this work was, anyway, not so much in this spectral line, but in its photon-counting statistics. Measuring $g^{(2)}$ (I shall explain its exact meaning in next Chapter), they could support the double result that: *i*) the middle peak was indeed not correlated with the doublet, showing that it is just an addition, plausibly indeed an irrelevant one (but the exact nature of which is not completely certain), and *ii*) that the two peaks of the doublet are antibunched. This second result is the most important one. It is possibly the first tangible argument to support full field-quantization of the QD-MC system, that we have discussed previously. This result has been confirmed by Press et al. (2007). This is not completely conclusive, however, as although it proves that the dynamics involves a single quantum of excitation between two isolated modes (by itself

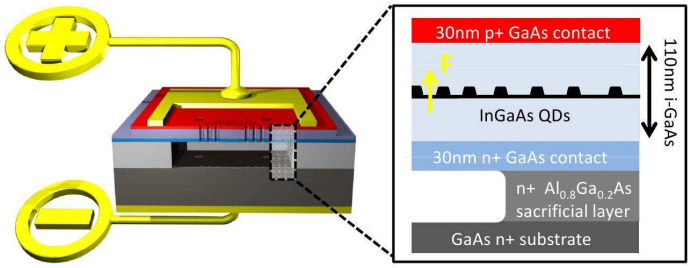

Figure 1.13: Laucht et al. (2008)'s on-chip device, controlled by an applied bias-voltage, opening the road towards fully-integrated cavity QED devices.

already a considerable achievement), it does not instruct on the modes themselves (consider the vacuum Rabi problem of two harmonic oscillators, that gives the same result). After all, dimming classical light until single photons remain, would exhibit antibunching, but this says nothing about the emitter itself.[19]

A genuine, or quantum, SC, should culminate with a direct, explicit demonstration of quantization, with one quantum more or less changing the behaviour of the system. In the ideal picture where the QD system can be described accurately by a 2LS (that the QD accommodates exact fermions), the JC physics should apply.[20] Such a quantum sensitivity would then be strongly manifest, as is well known from its Hamiltonian structure (Shore & Knight (1993) have given an authoritative review of this textbook system.) In particular, the so-called *Jaynes-Cummings ladder*, built up from the light and matter states dressed by their strong interaction, would provide such a direct, unarguable proof of cQED regime at its full pace. Such nonlinearities have been more or less directly observed by Brune et al. (1996) and Meekhof et al. (1996) in atomic cQEC. Recently, direct spectroscopic evidence has been reported for atoms and superconducting circuits, in elaborate experiments by Schuster et al. (2008) and Fink et al. (2008) that remind the heroic efforts of Lamb to reveal the splitting of the orbitals of hydrogen. Even

[19] Which is ultimately quantum anyway; if the photons are coming from the sun, for instance, they all originate independently from the spontaneous emission of an atom, or to much lower probability, from stimulated emission. If this seems like a moot statement, let us remember from the atomic QED case the controversy that arise anytime that field quantization is deduced. Did not Lamb Jr. (1995) himself support the view that "there is no such thing as a photon"? Such controversies can be settled completely only with a direct, explicit demonstration of field quantization, rather than one of its many possible logical consequence.

[20] Laussy, Shelykh, Malpuech & Kavokin (2006) have considered QDs that would exhibit an intermediate case between bosons and fermions, but their approach does not lend itself to an exact computation of the luminescence lines. They have resorted to a Lorentzian approximation, following a rather standard—but as I will show in the rest of the text—also sloppy, practise.

more recently, very clear transitions from up to the fifth step of the ladder have been unambiguously observed in circuit QED in very strong-coupling, with the Rabi splitting more than 260 times the vacuum linewidth (Bishop et al. 2009)!

To the best of my knowledge, no such nonlinear features have been reported in microcavity QED. The panorama laid down by Figs. 1.11 and 1.12 show that observation of the VRS is already a difficult task. In this work, I shall endeavour to take up the situation where it has been left by Carmichael et al. (1989) with regard to the theoretical description of the lineshapes of the SC system. My principal theme will be that the semiconductor case differs in at least one fundamental respect with the paradigm set up by atomic cQED. Namely, in its excitation scheme. In the canonical semiconductor case, a steady state is established by the presence of an incoherent pumping. This pumping itself is quite different in character than the coherent excitation that is typically used in the atomic or circuit QED case, where it enters in the Hamiltonian. Extending the previous description and solving the system, we will be rewarded by a beautiful generalization of the SE problem. As far as concrete, experimental physics is concerned, I will show that my considerations bear huge importances for understanding the data. In particular, it could explain why SC reports have been so scarce, and if the description is right, it would greatly help to correct this shortcoming and to benefit from a quantiative description of the result. As far as the problem of full-field quantization is concerned, I will propose that, despite figures of merit much lower in semiconductors than other systems (atomic and circuit QED), clear qualitative features could still be observed, but still thanks to the same proper understanding of the excitation scheme. I will show that, indeed, merely increasing the pump intensity in the hope of probing nonlinearities, could more likely bring the regime to the classical realm.

1.4 Summary of contents

The rest of this text will be organized as follows:

In Chapter 2, I introduce the two basic elements of all the theoretical light-matter models we discuss in this thesis: the harmonic oscillator (HO) and the two-level system (2LS). This comes along with the definition of fundamental concepts. I lay down in full details the Hamiltonians that describe the coupling of light and excitonic modes, the linear model (LM) and the Jaynes-Cummings model (JCM) and the formalism of the density matrix and master equation, to include decoherence (dissipation and incoherent continuous excitation). I develop in its most general form the method we will use to compute time correlators and the spectra of emission of a dissipative system, the quantum regression formula (QRF).

In Chapter 3, I address light-matter coupling of bosonic excitons (adequate

for large QDs or one polariton mode) with the LM, that also describes the linear regime of vanishing excitation. I will show how this model successfully describes one of the first experimental realizations of strong coupling with a single QD in a microcavity. The incoherent continuous pump, both electronic and photonic, is a key element to tune between the coupling regimes enhancing or hindering the visibility of the dressed modes (a Rabi doublet vs. singlet).

In Chapter 4, I present the case of two coupled 2LSs, interesting because it interpolates between the LM and the JCM of coupled modes with the advantage of being fully solvable analytically. I dedicate one chapter to it for its fundamental interest and because it brings us one step closer to unravelling the JCM, shedding light on the more complex mechanisms that manifest at a larger scale there. New regimes of coupling appear for this model due to the interplay between pump and decay, giving rise to more exotic lineshapes (quadruplet and triplet structures that result in distorted doublets and singlets).

In Chapter 5, I describe light-matter coupling with models that take into account some excitonic nonlinearities, appearing when the excitation is powerful enough to probe the system out of the linear regime. Such nonlinearities stem from the Coulomb repulsion experienced by the excitons if their wavefunctions overlap in the QD and also from the fermionic nature of the underlying electrons and holes. The study of the first effect is done considering excitons as weakly interacting bosons, described by an anharmonic oscillator (AO). The starting point is the analytic results of LM in Chapter 3 and a separate analysis of the AO physics. The second effect of saturation is studied with the Jaynes-Cummings model, the most important and fundamental model of cavity-quantum electrodynamics. We unravel in this section a surprising complexity with fractal structures, that suggest a transition from the quantum to the classical realm. In all cases, the spectra has a multiplet structure, better resolved in the quantum regime, that can turn into broad singlets (AO) and Mollow triplets (JC) in the lasing regime, all depending on the competition with decoherence.

In Chapter 6, I go through different properties of three element systems. A natural extension of the previous chapters is the study of two QDs, or one QD that can guest up to two excitons (a biexciton), in a microcavity. The description of this configuration requires putting together two JC Hamiltonians, it is the simplest case of the Dicke model of superradiance (two 2LS coupled to an HO). I speak here of their properties of emission, this time distinguishing between one- and two-photon emission and lasing. The finding of a scheme of incoherent excitation that generates entanglement between the QDs, leads us to the proposal of a transport experiment with three QDs.

Chapter 2

Theoretical Background

Contents

In this Chapter we introduce the basic concepts and formulas that we will use in the rest of the Chapters: Bosons, fermions, strong coupling, decoherence, spectra of emission and other fundamental ideas are defined.

What is contained here can be found in various books: Gerry & Knight (2005) and S. Haroche (2006) for basic quantum optics and light matter interaction; Carmichael (2002), Gardiner (1991) or Schlosshauer & Schlosshauer-Selbach (2007), more focused on the treatment of decoherence; Yamamoto & Ĭmamog̅lu (1999) and Kavokin et al. (2007), on quantum and classical optics of semiconductor systems.

2.1 The harmonic oscillator: bosonic states

The *quantum harmonic oscillator* (HO) is the most natural description for field excitations. Basically, it consists in the endless possibility to create particles through a creation or ladder operator $a^\dagger$. It is then the perfect match for *bosons*. Bosons are particles, quasi-particles or composite particles that have an integer total spin and can occupy the same state. The electromagnetic field, composed of photons, is perfectly modelled by an HO. Also matter excitations, such as excitons in semiconductors, that are composite bosons in the regime $a_{\mathrm{B}}^D \rho_D \ll 1$, can be well represented in this basic picture when the density is very low. Then, their energy levels are far from saturated and the Pauli effects arising from the fermionic components (electrons and holes) are negligible. We will see in Sec. 2.2 how to deal with matter excitations when fermionic effects are important.

Let us now go quickly through the HO basic properties and possible realizations. To begin with, a state with one particle is simply defined as the application of a creation operator $a^\dagger$ on the vacuum, $|1\rangle = a^\dagger |0\rangle$. The n-particle state is obtained through recursive creation:

$$|n\rangle = \frac{(a^\dagger)^n}{\sqrt{n!}} |0\rangle \,. \tag{2.1}$$

except for the normalization prefactor $1/\sqrt{n!}$ which depends on the state of the field. Operators a and $a^\dagger$ annihilate and create respectively a particle,

$$a|n\rangle = \sqrt{n}\,|n-1\rangle \,, \tag{2.2a}$$

$$a^\dagger |n\rangle = \sqrt{n+1}\,|n+1\rangle \,, \tag{2.2b}$$

$$a^\dagger a |n\rangle = n|n\rangle \,. \tag{2.2c}$$

With this definitions, $a^\dagger a$ is the number operator. The Hamiltonian of the free field finds its most compact expression in such terms as

$$H_a = \omega_a a^\dagger a \,, \tag{2.3}$$

where ω_a is the frequency of the monomodal field. In this section, we work in Schrödinger representation where states carry the temporal dynamics and operators are time-independent. Heisenberg picture, where operators and not states can evolve with time, will be more suitable later on when we deal with two-time correlations. In this picture, from the commutation rules of bosons, $[a, a^\dagger] = 1$, other relations follow, for example, those related to normal ordering of the operators (which requires to move all creation operators to the left):

$$a{a^\dagger}^n = {a^\dagger}^n a + n{a^\dagger}^{n-1} \tag{2.4a}$$

$$a^n a^\dagger = a^\dagger a^n + n a^{n-1} \tag{2.4b}$$

In order to further investigate interesting states of the HO, one can imagine an ideal detector that absorbs field particles of all frequencies one by one. A measurement means removing one particle from the initial field state to get $a|i\rangle$. As described by Glauber (1963b), the probability per unit time to detect a particle whatever the final state, $|f\rangle$, is given by

$$\text{Probability}(1) = \sum_f |\langle f|a|i\rangle|^2, \tag{2.5}$$

which is equal to the mean number of particles $\langle n_a\rangle = \langle i|a^\dagger a|i\rangle$. Therefore, the intensity of the field is proportional to the probability of counting a particle per unit time and can be measured by these means. In is possible to generalise this idea to the probability of counting M photons at the same time

$$\text{Probability}(M) = \sum_f |\langle f|a^M|i\rangle|^2 = \langle i|a^{\dagger M}a^M|i\rangle\,. \tag{2.6}$$

Here, we see the importance of normal order and is linked to observable quantities in photon counting experiments. The most celebrated of those, are the two-particle coincidence experiments developed for the first time by Hanbury Brown & Twiss (1956) with photons. Taken at zero delay (we will see more general two-time expressions in Sec. 2.7), they provide information about the particle statistics of the state of the field. A widely used example is the *degree of second-order coherence* (or, equivalently, *second-order correlation function* at zero delay)

$$g^{(2)} = \frac{\langle a^\dagger a^\dagger a a\rangle}{\langle a^\dagger a\rangle^2} \tag{2.7}$$

is linked to the variance (or second *cumulant*) $\Delta n_a^2 = \langle (n_a - \langle n_a\rangle)^2\rangle$ of the distribution of particles

$$g^{(2)} = 1 + \frac{\Delta n_a^2 - \langle n_a\rangle}{\langle n_a\rangle}\,. \tag{2.8}$$

More generally, the *degree of Mth-order coherence* reads

$$g^{(M)} = \frac{\langle a^{\dagger M}a^M\rangle}{\langle a^\dagger a\rangle^M} = \frac{\langle n_a(n_a-1)(n_a-2)\ldots(n_a-M+1)\rangle}{\langle n_a\rangle^M}\,. \tag{2.9}$$

The *number state* or *Fock state* that we already introduced has zero variance around the mean number of particles n, that is completely determined. This results in $g^{(2)} = 1 - 1/n$—which jumps from 0 to $1/2$ at $n = 2$, as it corresponds to a two-photon observable—remaining always bellow 1. This feature of $g^{(2)} < 1$ is linked to some kind of quantum behavior. $|n\rangle$ is a very "quantum" state, in the sense

that it can only be understood if we consider the propagating field as composed of particles whose change in number has some impact. If one photon is detected from an initial state $|i\rangle = |1\rangle$, no second photon can be expected as it gets projected into vacuum $|f\rangle = |0\rangle$ when measuring the first photon. For the number states, the probability of emission decreases after each emission. At high numbers, one particle more or one particle less does not make much difference ($n \approx n \pm 1$). A classical description and understanding of the state start to be valid and $g^{(2)}$ tends to 1. Similar behavior is found for higher orders of coherence:

$$g^{(M)} = \frac{n!}{(n-M)!\, n^M}\,. \tag{2.10}$$

The probability of having p particles in the field can be written as a Kronecker delta $\mathscr{P}_p = |\langle p|n\rangle|^2 = \delta_{n,p}$.

Another interesting state is the *coherent state* $|\alpha\rangle$, derived by E. Schrödinger for the first time in 1926 but only fully developed by Glauber (1963a). It is characterized by being the eigenstate of the destructor operator

$$a\,|\alpha\rangle = \alpha\,|\alpha\rangle \tag{2.11}$$

with eigenvalue a complex number $\alpha = |\alpha| e^{i\phi}$. Eq. (2.11) shows that removing one particle does not change the coherent state. This is an essentially classical property where all detections are statistically independent, as opposed to case of the number state. Therefore, coherent state is a good approximation for a classical monochromatic wave of particles. Let us take as an illustration of this point, one mode of a transversal free electromagnetic field. The electric field operator E is composed of photons, which are bosons and at some point of space can be written (skipping constants) as a sum of two contributions

$$E = E^{(+)} + E^{(-)} = \frac{1}{2}(a e^{-i\omega_a t} + a^\dagger e^{i\omega_a t})\,. \tag{2.12}$$

This can be also considered the expression a general bosonic field. In a coherent state, the expectation value of the electric field, the intensity operator and the field variance, respectively, are given by

$$\langle E\rangle = \langle\alpha|E\,|\alpha\rangle = |\alpha|\cos(\omega_a t - \phi)\,, \tag{2.13}$$

$$\langle E^2\rangle = \langle\alpha|E^2\,|\alpha\rangle = \langle E\rangle^2\,, \tag{2.14}$$

$$\Delta E^2 = \langle E^2\rangle - \langle E\rangle^2 = \frac{1}{4}\,, \tag{2.15}$$

which basically means that the quantum fluctuations of the field ΔE are independent of its intensity $\langle E\rangle$ and become negligible at large $|\alpha|$. This is the regime

where the coherent state can well be considered a classical wave. On the other hand, for number states the situation is radically different

$$\langle E \rangle = 0\,, \tag{2.16}$$

$$\langle E^2 \rangle = \frac{1}{2}\left(\frac{1}{2}+n\right), \tag{2.17}$$

$$\Delta E^2 = \langle E^2 \rangle\,, \tag{2.18}$$

having no electric in average but quantum fluctuations even in the vacuum.

Back in the basis of number states, the variance of the particle number distribution is the same as the mean number

$$\langle n_a \rangle = \Delta n_a^2 = |\alpha|^2\,. \tag{2.19}$$

In fact, all cumulants of the distribution converge to this value and the state is *coherent* at all orders (in Glauber's sense): $g^{(M)} = 1$ for all M.

One can double check this by obtaining the explicit expression of the coherent state in terms of number states

$$|\alpha\rangle = e^{-|\alpha|^2/2} \sum_{n=0}^{\infty} \frac{\alpha^n}{\sqrt{n!}} |n\rangle \tag{2.20}$$

and analyzing the particle number distribution

$$\mathscr{P}_p = |\langle p|\,\alpha\rangle|^2 = e^{-\langle n_a\rangle} \frac{\langle n_a\rangle^p}{p!}\,. \tag{2.21}$$

Such distribution is called *Poissonian* as it was discovered by S. D. Poisson in 1838. Any distribution with $g^{(2)} < 1$, such as that of the number state, is called *sub-Poissonian* and with $g^{(2)} > 1$, *super-Poissonian*.

States like $|n\rangle$ and $|\alpha\rangle$ that are completely described with a wave function (one ket) are known as *pure* states. They can be a good description for a field in some limiting cases where it is very well isolated from the environment, and it experiences only *coherent dynamics* given by a Hamiltonian. For example, the evolution of $|\alpha\rangle$ through the free Hamiltonian (2.3) (a phase rotation in its complex parameter) remains always perfectly determined by a wavefunction $\left|e^{-i\omega_a t}\alpha\right\rangle$. However, in general one should consider the contamination of this dynamics with others originated by the field being in contact with the exterior world. In principle one could model all possible interactions with environment with a more comprehensive Hamiltonian that includes all processes affecting the field a. This is an impossible task if one takes it seriously (having to model the whole universe!), and quite a difficult one even with some approximations. One cannot and does not

want to keep track of all the degrees of freedom affecting the field. This lack of interest on the external world results in *decoherence* for our system.

In the previous example of the evolution of a coherent state, one can imagine that the field a is affected by an *incoherent process* that interrupts its coherent free evolution (like a measurement that randomizes its phase). We are not interested in this process by itself and therefore only know its effect on our field, the rate at which the perturbation happens. After some time t_e, when the probability that a first event has happened is $\mathscr{P}_e$ we cannot say anymore that the state of the system is defined by $\left|e^{-i\omega_a t_e}\alpha\right\rangle$. We only know that this is so with a probability $1-\mathscr{P}_e$ and that the state of the system is $|\alpha\rangle$ with a probability P_e. Therefore we need a *mixture* of two wave functions and not only one, like for the pure state, for our description. Following this idea, the dynamics of the system can be understood as a succession of coherent periods and incoherent random (from our ignorant point of view) events that project the wave function into a given state. Those are the so-called *quantum jumps*. One can guess that after some time and a complicated mixture of *quantum trajectories*, we loose track completely of the phase of the state. This means that the steady state (SS) of this system is a mixture of coherent states where all possible phases have the same probability $\mathscr{P}(\phi)d\phi = 1/(2\pi)$.

A consistent way to express this situation, and the most general state of the system, is through the *density matrix* operator ρ. In general, the density matrix of a system can always be put in its diagonal form as the following combination of projectors

$$\rho = \sum_i \mathscr{P}_i \left|\Psi_i\right\rangle \left\langle\Psi_i\right| . \tag{2.22}$$

$\mathscr{P}_i$ are the probabilities for the field to be in a given basis $\{|\Psi_i\rangle\}$ of its Hilbert space. The pure state is a particular case where $\rho = |\Psi_1\rangle\langle\Psi_1|$ and all eigenvalues of ρ are zero but one ($\mathscr{P}_1 = 1$ and $\mathscr{P}_{i\neq 1} = 0$). In this case, it is straightforward to see that $\rho^2 = \rho$. On the other hand, a mixture is characterized by $\rho^2 \neq \rho$, which yields $\mathrm{Tr}\rho^2 < \mathrm{Tr}\rho = 1$. These properties are independent of the basis of states and so are others such as $\mathrm{Tr}\rho = 1$ (normalization) or $\rho = \rho^\dagger$ (hermiticity). In any other basis than that of eigenstates, ρ will have off-diagonal elements that give an account of the interplay or *coherence* between two pure states of the basis. For example, the density matrix of a coherent state,

$$\rho^a_\alpha = |\alpha\rangle\langle\alpha| = e^{-|\alpha|^2} \sum_{m,n} \frac{\alpha^m \alpha^{*n}}{\sqrt{m!\,n!}} |m\rangle\langle n| , \tag{2.23}$$

has all off-diagonal terms in the number state basis. On the other hand, in our previous example of a mixture of coherent states with a random phase, the SS density matrix can be constructed as

$$\rho^a_{|\alpha|} = \int d\phi \frac{1}{2\pi} \left|\,|\alpha|e^{i\phi}\right\rangle \left\langle |\alpha|e^{i\phi}\,\right| . \tag{2.24}$$

from which follows that

$$\rho^a_{|\alpha|} = e^{-|\alpha|^2} \sum_n \frac{|\alpha|^{2n}}{n!} |n\rangle \langle n| \,. \tag{2.25}$$

In each basis we can see two aspects of the decoherence that the coherent state of Eq. (2.23) suffered. In the first one, the most direct consequence of the phase randomization manifests in the lack of off-diagonal elements between states with different phases. The second basis evidences that the particle number distribution is still Poissonian but also that the off-diagonal elements between number states have been washed out. As it is the case for any mixture diagonal in the number state basis, the average of the field is zero, $\langle E \rangle = 0$, and its intensity is time independent,

$$\langle E^2 \rangle = \frac{1}{2}\big(\frac{1}{2} + \langle n_a \rangle\big) \,. \tag{2.26}$$

These results are closer to those of a number state (2.16) than of a coherent one (2.13), for purely statistical reasons. The state is still coherent at all orders.

The next important state to discuss is the *thermal mixture*. It is the state whose bosonic excitations, the particles of the field, are thermally spread among the energy levels. We will see in Sec. 2.4 that this is the result of the interaction with a reservoir of particles at a given temperature T. The density matrix for a given mode ω_a can be derived from the *Bose-Einstein statistics* as

$$\rho^a_{\text{th}} = \frac{e^{-\frac{H}{K_B T}}}{\text{Tr}(e^{-\frac{H}{k_B T}})} = \frac{e^{-\frac{\omega_a a^\dagger a}{k_B T}}}{1/\big(1 - e^{-\frac{\omega_a}{k_B T}}\big)} \tag{2.27}$$

where k_B is the Boltzmann constant and the denominator is the partition function. The thermal density matrix is also a diagonal in the number basis

$$\rho^a_{\text{th}} = \sum_n \frac{\langle n_a \rangle^n}{(1 + \langle n_a \rangle)^{1+n}} |n\rangle \langle n| \tag{2.28}$$

with the average occupation being the *Bose-Einstein distribution*,

$$\langle n_a \rangle = \frac{1}{e^{\frac{\omega_a}{k_B T}} - 1} \,. \tag{2.29}$$

This formula was guessed by M. Planck in 1900 to fit the experiments on Black body radiation and later derived by Bose from statistical principles for photons. As the system is in thermal equilibrium with a bosonic bath, their average occupation at the frequency ω_a are the same:

$$\langle n_a \rangle = \bar{n}_T \tag{2.30}$$

We can analyze the process that leads to the thermal equilibrium. We suppose that the reservoir population is not influenced by the interaction with our system (approximation discussed in Sec. 2.4). The system does evolve from vacuum into the SS of thermal equilibrium and the mean value depends on time $\langle n_a(t)\rangle$. The total rate of incoming particles from reservoir to the system is given by $\kappa_a \bar{n}_T[1+\langle n_a(t)\rangle]$. The effective rate of excitation of the system (analog for the *Einstein B-coefficient* for bosons), is

$$P_a = \kappa_a \bar{n}_T \,. \tag{2.31}$$

It vanishes at $T = 0$. Similarly, the transfer rate in the opposite sense is given by $\kappa_a(1+\bar{n}_T)\langle n_a(t)\rangle$. The system is loosing excitations with effective rate

$$\gamma_a = \kappa_a(1+\bar{n}_T)\,. \tag{2.32}$$

The new parameter κ_a is the *spontaneous emission* (SE) rate at $T = 0$, analog of the *Einstein A-coefficient*. In terms of the effective parameters, γ_a, P_a, the *rate equations* for the system dynamics reads

$$\frac{d\langle n_a(t)\rangle}{dt} = -\gamma_a\langle n_a(t)\rangle + P_a[1+\langle n_a(t)\rangle] \tag{2.33}$$

and leads in the SS to Eq. (2.30), now

$$n_a^{\mathrm{SS}} = \frac{P_a}{\gamma_a - P_a}\,. \tag{2.34}$$

At very high temperatures, as the effective income approaches the outcome, $P_a \approx \gamma_a$, the number of particles grows as $n_a^{\mathrm{SS}}\ k_B T/\omega_a$ but it is never diverges because $P_a < \gamma_a$. As long as $\gamma_a \neq 0$, any combination of parameters γ_a, P_a corresponds to a physical thermal bath (with $\kappa_a = \gamma_a - P_a$ and $T > 0$).

Logically, given its origin, the thermal state does not exhibit any coherence properties at any order (other than the first),

$$g^{(M)} = M!\,, \tag{2.35}$$

and in particular $g^{(2)} = 2$. This means that the particle distribution in Eq. (2.28) is super-Poissonian with fluctuations

$$\Delta n_a^2 = \langle n_a\rangle^2 + \langle n_a\rangle \tag{2.36}$$

that exceed those of the Poissonian distribution by $\langle n_a\rangle^2$.

In the following chapters and sections, we will study different configurations and processes which generate the states that we just described. Very rarely, the state of the system is completely thermal, or coherent, or has a purely Poissonian

statistics. In most of the cases, the bosonic field (of light or matter) is a convolution of different states. For example, a *cothermal state*, the superposition of a coherent and a thermal state, first explored by Lachs (1965), has a distribution of particles

$$\langle n|\,\rho^{a}_{\mathrm{coth}}\,|n\rangle = \mathscr{P}_{\mathrm{coth}}(n) = e^{-\frac{n_{\mathrm{c}}}{1+n_{\mathrm{t}}}}\frac{n_{\mathrm{t}}^{n}}{(1+n_{\mathrm{t}})^{n+1}}L_n[-\frac{n_{\mathrm{c}}/n_{\mathrm{t}}}{1+n_{\mathrm{t}}}] \tag{2.37}$$

where L_n are the Laguerre polynomial. Together with the total mean value $\langle n_a\rangle = n_{\mathrm{c}} + n_{\mathrm{t}}$, this state is defined by the fraction of coherent particles $\chi = n_{\mathrm{c}}/\langle n_a\rangle$. With this definition, the thermal fraction is $n_{\mathrm{t}} = \langle n_a\rangle(1-\chi)$. This distribution interpolates between a thermal (at $\chi = 0$) and a Poissonian one (at $\chi = 1$). The variance is the sum of that of both components, Eq. (2.19) and Eq. (2.36), plus an "interference term"

$$\Delta n^2 = n_{\mathrm{c}} + n_{\mathrm{t}}^2 + n_{\mathrm{t}} + 2n_{\mathrm{c}}n_{\mathrm{t}}\,. \tag{2.38}$$

The total density matrix takes a simple expression in the *P representation*, that is, in the basis of coherent states, as the convolution of the coherent and thermal P functions (a delta function and a Gaussian respectively).

2.2 The two level system: fermionic states

Excitons cannot be described in all regimes as an HO. When density is high enough to push together more than one electron or hole in the same state, the *Pauli Exclusion Principle* should be taken into account in the model. This is the case also of atoms, whose excitations are electronic and therefore saturable. In all these examples, the system can only populate with a maximum of one excitation a finite number of levels. The most suitable description is in terms of the projector operators

$$|i\rangle\langle i| \tag{2.39}$$

for each level (with corresponding energy ω_i) and their ladder counterparts,

$$\sigma^{\dagger}_{ij} = |j\rangle\langle i|\,, \tag{2.40}$$

the rising (if $\omega_i < \omega_j$) and lowering (if $\omega_i > \omega_j$) operators. Eq. (2.40) describes the promotion from state i to $j \neq i$ by creating an excitation of the matter field in the same way as $a^{\dagger}$ does of the bosonic mode. The difference is that $\sigma^{\dagger}_{ij}$ cannot be applied twice because only one excitation is allowed in each level ($\langle i|j\rangle = \delta_{ij}$). Operator $a^{\dagger}$ had implicit this possibility in its expression

$$a^{\dagger} = \sum_n \sqrt{n+1}\,|n+1\rangle\langle n|\,. \tag{2.41}$$

The free Hamiltonian of these levels is simply

$$H_{\text{levels}} = \sum_i \omega_i |i\rangle \langle i| \,. \tag{2.42}$$

Let us consider only two of these levels with energy difference ω_σ and operators of creation and destruction $\sigma^\dagger$ and σ respectively. This *two-level system* (2LS) already covers a great deal of physical situations, as we will see, and, most importantly, it constitutes the paradigm for the study of light-matter interaction. For what concerns us, it is a reasonable approximation for an exciton in a small quantum dot. The two levels involved are the ground state $|0\rangle$, in the absence of exciton, and excited state $|1\rangle = \sigma^\dagger |0\rangle$, in its presence. The σ-operators

$$\{\sigma^\dagger = |1\rangle\langle 0|\,, \sigma = |0\rangle\langle 1|\,, \sigma^\dagger\sigma = |1\rangle\langle 1|\,, \sigma\sigma^\dagger = |0\rangle\langle 0|\} \tag{2.43}$$

can be put in terms of the *pseudo-spin* operators or *Pauli matrices*, $\{s_x, s_y, s_z\}$

$$\begin{aligned} s_z &= \frac{1}{2}(\sigma^\dagger\sigma - \sigma\sigma^\dagger) = \frac{1}{2}[\sigma^\dagger, \sigma]\,, & (2.44)\\ s_x &= \sigma^\dagger + \sigma\,, & (2.45)\\ s_y &= -i(\sigma^\dagger - \sigma)\,, & (2.46) \end{aligned}$$

used for the $1/2$-spin dynamics. The anti-commutation rules

$$[\sigma, \sigma^\dagger]_+ = 1 \tag{2.47}$$

sums up the fermionic properties of the 2LS algebra. The Hamiltonian in Eq. (2.42) can be written as

$$H_\sigma = \omega_\sigma \sigma^\dagger\sigma\,. \tag{2.48}$$

A general state is described by the 2-dimensional density matrix. It characterized by two numbers, the probability of having an excitation, which is also the average occupation $\mathscr{P}_1 = \langle\sigma^\dagger\sigma\rangle = \langle n_\sigma\rangle$, and the coherence between the two levels, ρ^σ_{01},

$$\rho^\sigma = \begin{pmatrix} 1-\langle n_\sigma\rangle & \rho^\sigma_{01} \\ (\rho^\sigma_{01})^* & \langle n_\sigma\rangle \end{pmatrix}. \tag{2.49}$$

In case of a pure state of the form $\sqrt{1-\langle n_\sigma\rangle}\,|0\rangle + e^{i\phi_1}\sqrt{\langle n_\sigma\rangle}\,|1\rangle$, we have $\rho^\sigma_{01} = \sqrt{\langle n_\sigma\rangle(1-\langle n_\sigma\rangle)}e^{-i\phi}$. On the other hand, if the system is in thermal equilibrium with some bath at temperature T, we have a thermal mixture as it was the case with bosons. The density matrix of Eq. (2.27) should be computed now taking into account the *Fermi-Dirac statistics*

$$\rho^\sigma_{\text{th}} = \frac{e^{-\frac{\omega_\sigma \sigma^\dagger\sigma}{k_B T}}}{1+e^{-\frac{\omega_\sigma}{k_B T}}} = (1-\langle n_\sigma\rangle)\,|0\rangle\langle 0| + \langle n_\sigma\rangle\,|1\rangle\langle 1| \tag{2.50}$$

where $\langle n_\sigma \rangle$ is the *Fermi-Dirac distribution*,

$$\langle n_\sigma \rangle = \frac{1}{e^{\frac{\omega_\sigma}{k_B T}} + 1}\,. \tag{2.51}$$

The maximum value that this probability can take, when the temperature is infinitely high, is $1/2$. It is therefore, not possible to saturate the 2LS, that is, to invert its population, only with a thermal bath. We will see in Sec. 2.4 how this can change when more than one bath is considered.

The thermal equilibrium for the mean value $\langle n_\sigma(t) \rangle$ is driven by the interplay of outgoing particles into reservoir, with rate given by $\kappa_\sigma(1+\bar{n}_T)\langle n_\sigma(t)\rangle$ (κ_σ is the *Einstein A-coefficient*), and incoming particles, given by $\kappa_\sigma \bar{n}_T[1-\langle n_\sigma(t)\rangle]$. The incoming rate is, in contrast with the bosonic case, proportional to the subtraction $1-\langle n_\sigma(t)\rangle$, which is the probability of the system being in the ground state and therefore available for excitation. This provides the saturation effect, as now, with the same definition for the effective parameters as in the previous section, $\gamma_\sigma = \kappa_\sigma(1+\bar{n}_T)$ and $P_\sigma = \kappa_\sigma \bar{n}_T$ (the *Einstein B-coefficient*), we have that the rate equations read

$$\frac{d\langle n_\sigma(t)\rangle}{dt} = -\gamma_\sigma \langle n_\sigma(t)\rangle + P_\sigma[1-\langle n_\sigma(t)\rangle]\,. \tag{2.52}$$

The SS of Eq. (2.51) can be also written as

$$n_\sigma^{\mathrm{SS}} = \frac{P_\sigma}{\gamma_\sigma + P_\sigma} = \frac{\bar{n}_T}{2\bar{n}_T + 1}\,. \tag{2.53}$$

At very high temperatures, as the total income approaches the outcome, $P_\sigma \approx \gamma_\sigma$, we obtain the half saturation. In this case, the 2LS cannot have the same occupation number as the reservoir, which is bosonic, but of both correspond to the same temperature. Also in contrast with the bosonic case, not any combination of parameters γ_σ, P_σ correspond to a physical thermal bath where $\gamma_\sigma > P_\sigma$. In this text, we will study the most general case of pumping and decay where it is possible that $P_\sigma > \gamma_\sigma$ and therefore to completely saturate the 2LS, $n_\sigma^{\mathrm{SS}} = 1$. We will see in Sec. 2.4 how this is possible in the actual experiments.

It is interesting to note that the 2LS dynamics is symmetric under the exchange of pump and decay ($\gamma_\sigma \leftrightarrow P_\sigma$) if we also exchange the ground and the excited states. Saturation can occur in two senses, in the ground state when the decay is large, and in the excited state when the pump is large. The equivalence between pump and decay for the 2LS is in contrast with the totally different nature that they bear in the HO, where the pump can put up to infinite excitations (when $P_a \to \gamma_a$) but the decay can only "saturate" the system in the ground state.

2.3 Coherent coupling

Coherent processes are those that can be written as a Hamiltonian H (always hermitian) and included in the Schrödinger equation

$$\frac{d\rho}{dt} = i[\rho, H]\,. \tag{2.54}$$

We already wrote the free evolution of the bosonic and fermionic fields in Eq. (2.3) and (2.48). Two fields a and b in the same point of space can interact linearly with a Hamiltonian that is of the form

$$H_{ab} = g(ab^\dagger + a^\dagger b)\,. \tag{2.55}$$

If the detuning between the modes,

$$\Delta = \omega_a - \omega_b\,, \tag{2.56}$$

is small as compared to the coupling, during the dynamics of H_{ab}, an a-particle becomes b and vice-versa. The frequencies are assumed much larger than the coupling and detuning between the modes, $\omega_{a,b} \ll g, \Delta$, so that the *Rotating Wave Approximation* holds. Terms with only destruction ab and creation $a^\dagger b^\dagger$ of particles can be neglected as they do not conserve energy. The Hamiltonian $H = H_a + H_b + H_{ab}$ does not conserve the number of particles a and b separately, as they experience a mutual conversion usually known as *Rabi oscillations*. The particles whose number is conserved are the eigenstates of H. But in order to diagonalize H we must specify the nature of the fields.

In this text, field a will be always the electromagnetic field inside a cavity, where one mode with frequency ω_a can be selected. Depending on the model for the material excitation, b is described by, typically, another HO (*linear model* (LM) developed by Hopfield (1958)) or a 2LS (the so-called *Jaynes-Cummings model* (JCM) developed by Jaynes & Cummings (1963)). Those are the most fundamental cases as they describe material fields with Bose and Fermi statistics, respectively. Possible extensions are a collection of HOs as done by Rudin & Reinecke (1999) and more recently by Averkiev et al. (2008) or of 2LS like in the work of Dicke (1954), a three-level system as Bienert et al. (2004) did, etc.

The parameter g depends on both the properties of the cavity and the emitters: $g \sim (f/V)^{-1/2}$, where V is the effective cavity volume and f the oscillator strength of the emitter. Therefore, in order to achieve strong coupling experimentally, the cavity must have a high quality factor Q ($\gamma_a \sim Q^{-1}$) and a small effective volume V. The emitters must be placed close to the anti-node of the electric field in the cavity, have transition frequencies close to resonance with the cavity mode and exhibit high oscillator strengths.

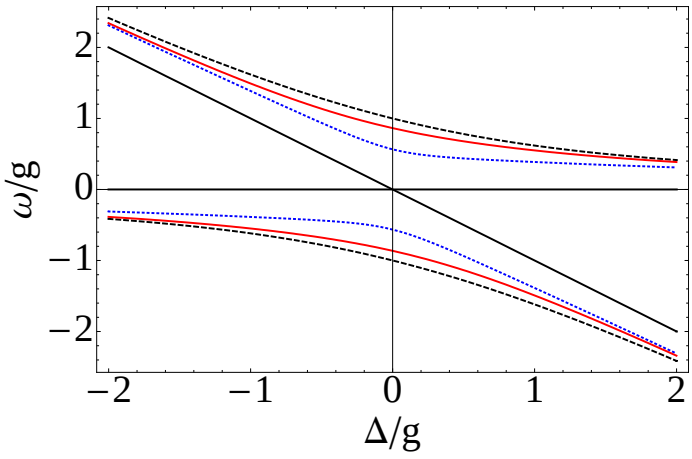

Figure 2.1: Solid black: Bare energies of the cavity photon (horizontal line) and of the exciton (tilted) as a function of detuning $\Delta = \omega_a - \omega_b$. Dashed black: Eigenenergies of the total system Hamiltonian, without dissipation nor pumping [Eq. (2.57a)]. The exciton-like state at large negative Δ has become a photon-like state at large positive Δ, and vice-versa. Around $\Delta = 0$, both modes are an admixture of exciton and photon. Dotted blue: Correction of the eigenenergies when pump and decay are taken into account in Chapter 3 (for parameters of point (c) in Fig. 3.8). Solid red: Actual position of the observed peaks in the photoluminescence spectra for the same parameters. For these parameters, the three descriptions of SC give the same qualitative results.

The linear model (discussed in Chapter 3) corresponds to the coupling of two bosonic modes, a and b. The Hamiltonian H can be straightforwardly diagonalized, giving

$$H = \omega_{\mathrm{U}} u^\dagger u + \omega_{\mathrm{L}} l^\dagger l\,, \tag{2.57a}$$

$$\omega_{\substack{\mathrm{U}\\\mathrm{L}}} = \frac{\omega_a + \omega_b}{2} \pm \mathscr{R}\,, \tag{2.57b}$$

$$\mathscr{R} = \sqrt{g^2 + \left(\frac{\Delta}{2}\right)^2}\,, \tag{2.57c}$$

with new Bose operators $u = \cos\theta\, a + \sin\theta\, b$ and $l = -\sin\theta\, a + \cos\theta\, b$, determined by the *mixing angle*,

$$\theta = \arctan\left(\frac{g}{\frac{\Delta}{2} + \mathscr{R}}\right) \tag{2.58}$$

These new modes are the *polaritons* (or *dressed states*) with $||\,1,0\rangle\rangle = u^\dagger\,|0\rangle$ and $||\,0,1\rangle\rangle = l^\dagger\,|0\rangle$, where $|0\rangle$ is the vacuum, $|m,n\rangle$ is the Fock state of in the bare basis and $||\,m,n\rangle\rangle$ the Fock state in the dressed basis.

The energies defined by Eq. (2.57b) are displayed in Fig. 2.1 with dashed lines, on top of that of the bare modes, with thick lines, as detuning is varied by changing

the energy of the emitter and keeping that of the cavity constant. The *anticrossing* always keeps the upper mode U higher in energy than the lower L one, strongly ad mixing the light and matter character of both particles. If the system is initially prepared as a bare state—which is the natural picture when reaching the SC from the excited state of an emitter—the dynamics is that of an oscillatory transfer of energy between light and matter. In an empty cavity, the time evolution of the probability to have an exciton when there was one at $t = 0$, is given by:

$$\mathscr{P}_{\text{exc}} = |\langle 0,1| e^{-iHt} |0,1\rangle|^2 = \sin^4\theta + \cos^4\theta + 2\sin^2\theta\cos^2\theta\cos(2\mathscr{R}t)\,, \quad (2.59)$$

which results in oscillations between the bare modes at the so-called *Rabi frequency*, given by $2\mathscr{R}$. At resonance this oscillations reach their maximal amplitude $\mathscr{P}_{\text{exc}} = \cos^2(\mathscr{R}t)$ making possible a complete photon conversion. In this text, we will refer to $\mathscr{R}$ directly as the Rabi frequency for simplicity, keeping in mind that there is a factor 2 that links it to the oscillations.

On the other hand, when the coupled modes are far from resonance $\Delta \gg g$, they affect perturbatively each other as we can see in Fig. 2.1. In this regime, the small difference in energy between the coupled and bare modes is known as the *Stark shift*. The Rabi frequency, when $g/\Delta \to 0$ is $\mathscr{R} \to |\Delta|/2 + g^2/|\Delta|$ so that the Stark shift of each mode amounts to the same quantity

$$s_b^a = \pm\frac{g^2}{\Delta}\,. \quad (2.60)$$

The second interesting possibility is when the matter field is a 2LS. We will denote it by σ for clarity and discuss it in more details in Chapters 5 and 6. The Jaynes-Cummings Hamiltonian $H = H_a + H_\sigma + H_{a\sigma}$ can be diagonalized in a given *manifold* with a fixed number of excitation $n = \langle n_a\rangle + \langle n_\sigma\rangle > 0$: $\mathscr{M}_n = \{|n,0\rangle, |n-1,1\rangle\}$. Rewriting the Hamiltonian as a sum of all manifold's contribution,

$$H = \sum_n H_n = \sum_n \Big[n\omega_a |n,0\rangle\langle n,0| + \Big((n-1)\omega_a + \omega_\sigma\Big)|n-1,1\rangle\langle n-1,1| \quad (2.61)$$

$$+ g\sqrt{n}\Big(|n-1,1\rangle\langle n,0| + |n,0\rangle\langle n-1,1|\Big)\Big] \quad (2.62)$$

it can be diagonalized in each subspace as

$$H = \sum_n \Big[\omega_{\text{U}}^n \,||\, 1_n,0\rangle\rangle\langle\langle 1_n,0\,|| + \omega_{\text{L}}^n \,||\, 0,1_n\rangle\rangle\langle\langle 0,1_n\,||\Big]\,. \quad (2.63)$$

The eigenstates and eigenenergies are n-dependent

$$\omega_{\text{U}\atop\text{L}}^n = \frac{n\omega_a + \omega_\sigma}{2} \pm \mathscr{R}_n \quad (2.64)$$

as so it is the (half) Rabi frequency

$$\mathscr{R}_n = \sqrt{(\sqrt{n}g)^2 + (\frac{\Delta}{2})^2}. \tag{2.65}$$

Only the 2LS Stark shift depends on the manifold

$$s_a = \frac{g^2}{\Delta} \tag{2.66}$$

$$s_\sigma = -(2n-1)\frac{g^2}{\Delta} \tag{2.67}$$

The manifold structure is the fundamental difference between the coupling of mode a with a bosonic of fermionic mode. The n-manifold in the first linear case, is composed by the $n+1$ states $\{|n-m,m\rangle\}$ with $m = 0,\ldots,n$. The Hamiltonian can be also written in these terms, in the bare or polariton basis,

$$\begin{aligned} H = \sum_n \Big\{ & \sum_{m=0}^{n} \Big[(n-m)\omega_a + m\omega_b\Big] |n-m,m\rangle \langle n-m,m| + \\ & + g \sum_{m=0}^{n-1} \sqrt{m(n-m+1)}\Big(|n-m-1,m+1\rangle \langle n-m,m| + \text{h.c.}\Big)\Big\} \\ = \sum_n & \sum_{p=0}^{n} \Big[(n-p)\omega_{\mathrm{U}} + p\omega_{\mathrm{L}}\Big] \,||\, n-p,p\rangle\rangle\langle\langle n-p,p \,||\,, \end{aligned} \tag{2.68}$$

which makes it explicit that the energy of an excitation, $\omega_{\mathrm{U,L}}$, is independent of the manifold. We will see in Chapter 3 that if we consider the excitonic particle-particle interactions with a Hamiltonian with nonlinear terms in n_b,

$$H_{\text{int}} = \frac{U}{2} b^\dagger b^\dagger b b = \frac{U}{2} n_b(n_b-1)\,. \tag{2.69}$$

this indistinguishability is broken. The energy U accounts for the strength of the interactions and is positive in the case of the weakly repulsive excitons. A linear simplification of the total Hamiltonian, as in Eq. (2.57a) and (2.68) is no longer possible as the eigenenergies depend on the manifold,

$$H_{\text{int}} = \frac{U}{2} \sum_n n(n-1)\,|n\rangle \langle n|\,. \tag{2.70}$$

All these cases are indistinguishable when the excitation is very low and the system only probes up to the first manifold, as it is not until a second excitation arrives that interactions or fermionic effects enter the picture. It is one of the

goals of this text to explore the differences arising between the different models and physical systems when $n \geq 1$.

A last interesting point to discuss is the coherent excitation of a mode via coupling to a monochromatic laser. For instance, the cavity field can be excited directly with a classical electromagnetic field $F(t) = \langle E(t) \rangle$ (in a coherent state) with frequency ω_{L}, like that of Eq. (2.13). This Hamiltonian,

$$H_{\mathrm{L}} = \varepsilon F(t)(a^{\dagger} + a) \approx \frac{\varepsilon}{2}(e^{-i\omega_{\mathrm{L}}t}a + e^{i\omega_{\mathrm{L}}t}a^{\dagger}), \tag{2.71}$$

drives the cavity field into a coherent state $\alpha = e^{i\omega_{\mathrm{L}}t}\varepsilon/(2\omega_a)$. The same can happen with the excitonic field, changing a operators with the b or σ. If the excitation intensity is strong, it may result in the appearance of new eigenstates in the system and Rabi oscillations with proportional magnitude. On the other hand, if it is weak, it can be used to probe the system structure without altering it, as we will see in Sec. 2.5.

2.4 Incoherent processes: Master equation Lindblad terms

The correct description of the system dynamics must include the decoherence processes, as we explained in Section 2.1. The first element to take into account is dissipation. The excitations (photons, excitons or polaritons) will eventually leak out of the system (the cavity in our case) and become part of the environment. Apart from the consequent decoherence induced in the system, these excitations can be detected from the outside and provide valuable information of the light-matter coupling. Therefore, at zero temperature, we already introduced when studying the thermal equilibrium states, photons and excitons in the cavity have a finite lifetime (κ). At $T \neq 0$, not only the dissipation rate is now given by Eq. (2.32), but also there is an intrinsic particle income from the environment with rate given by Eq. (2.31). In order to take this into account, the model is upgraded from a Hamiltonian [Eq. 2.54)] to a *Liouvillian description* with a quantum dissipative *master equation* for the density matrix of the system ρ:

$$\frac{d\rho}{dt} = i[\rho, H] + \mathscr{B}_T^a \rho + \mathscr{B}_T^b \rho\,. \tag{2.72}$$

Each superoperator $\mathscr{B}_T^c$ ($c = a, b$) is composed of two *Lindblad terms* [Lindblad (1976)], representing the outcoming and incoming particles respectively,

$$\mathscr{B}_T^c \rho = \frac{\kappa_c(1+\bar{n}_T)}{2}(2c\rho c^{\dagger} - c^{\dagger}c\rho - \rho c^{\dagger}c) + \frac{\kappa_c \bar{n}_T}{2}(2c^{\dagger}\rho c - cc^{\dagger}\rho - \rho cc^{\dagger})\,. \tag{2.73}$$

Mainly, there are two possible complementary derivations of these terms in the literature. The first one, is the microscopic approach, described by Carmichael (2002) or Gardiner (1991) in their books. It consists in considering dissipation as a coupling to a bath of oscillators and taking the following steps:

1. In the interaction picture, we apply second order perturbation theory on the coupling constants.

2. *Born approximation*: we assume that the coupling is so weak that system and reservoir are separable at all times and that the bath is too large to be affected by the system dynamics.

3. We consider a *Markovian environment*: the interactions with the system take place at a longer timescale than the environment's internal dynamics and, therefore, any correlations induced in the environment by such interactions are quickly lost.

4. We trace out the reservoir degrees of freedom making use of their bosonic statistics in thermal equilibrium.

5. We change back to the Schrödinger picture.

In this frame, the escape of the cavity photons is accounted for by the coupling to a reservoir of exterior photons in thermal equilibrium. The κ_a parameter is inversely proportional to the cavity quality factor Q: $\kappa_a = \omega_a/Q$ as (see Khitrova et al. (2006) for a review). The spontaneous decay of the QD excited states into other modes than that of the cavity cannot be avoid. It follows from the coupling with all possible modes, even when inside the cavity they are kept in the vacuum state (at zero temperature). Non-radiative de-excitation also takes place due coupling to photons and other particles of the solid state environment. The total QD decay rate, κ_b, is typically much smaller than the cavity emission rate κ_a but still they can induce significant deviations from the ideal case and should be included. The environment also induces *pure dephasing* on the light-matter coupling, causing the off-diagonal terms of the density matrix, linked to light-matter coupling, to decay . We do not consider this effect for simplicity and because in general it only contributes to destroying the coherence and its role is well understood.

The last essential ingredient is the excitation of the system. As we over-viewed in Sec. 1, experiments usually excite, optically or with electrical injection, the electronic levels far above resonance. Then, a reservoir of electron-hole pairs is created in the *wetting layer* with further relaxation to the exciton level. A detailed microscopic analysis of carrier capture in QDs has been developed by Nielsen et al. (2004) taking into account semiconductor many-body physics. It

showed that the Coulomb scattering of electrons and holes, in delocalized states of the wetting layer, can provide efficient transitions into the discrete localized QD states. Also LO-phonons can be an important mechanism responsible for such a relaxation. In this work, the pumping terms will represent only carrier capture due to phonons, processes where a fully correlated electron-hole pair is created in the QD. Our aim, therefore, is not to make a systematic analysis of all the relaxation processes which are taking place in the system. Rather, it is to develop an heuristic model where one can investigate the impact of the pumping mechanism. The pumping is modelled by a coupling to a reservoir of electron-hole pairs and phonons. However, some conceptual changes are needed in the microscopic derivation of these terms that we described above. The case of electronic pumping, for instance, is similar to the process of laser gain: the medium requires an inversion of electron-hole population, something that cannot be achieved by means of a simple HO heat bath. The actual process of gaining an exciton in the QD involves the annihilation of an electron-hole pair in an external reservoir out of equilibrium and the emission of a phonon, that carries the excess of energy, to another one (which can be in thermal equilibrium). A simple effective description of this non-equilibrium process can be made by an inverted HO with levels $E_p = -\omega_{\mathrm{p}}(p+1/2)$ maintained at a *negative temperature* as explained by Gardiner (1991). Since the raising operator for the energy decreases the number of quanta of this oscillator, the role of creation and destruction operators is indeed reversed with respect to the usual case of damping. Effectively, this results in new Lindblad of incoming particles, like those in the last term of Eq. (2.73) but that can be controlled externally and independently. An other approach with a microscopic derivation of the pumping mechanism has been recently investigated by Averkiev et al. (2008) This mechanism of direct excitation of the excitonic degree of freedom is sketched in the right side of Fig. 2.2. Here, we see the QD under study, represented by its two levels, placed in the cavity and interacting with one of the photonic modes.

We also consider another type of pumping, that offers a counterpart for the cavity by injecting photons incoherently. The major factor to account for such a term is the presence of many other QDs, that have been grown along with the one of interest. Those only interact weakly with the cavity. In most experimental situations so far, it is indeed difficult to find one dot with a sufficient coupling to enter the non-perturbative regime. When this is the case, all the other dots that remain in *weak coupling* (WC) become "spectators" of the *strong coupling* (SC) physics between the interesting dot and the cavity, and their presence is noticed by weak emission lines in the luminescence spectrum and an increased cavity emission. They are also excited by the electronic pumping that is imposed by the experimentalist, but instead of undergoing SC, they relax their energy into the cavity by *Purcell enhancement* or inhibition, depending on their proximity with

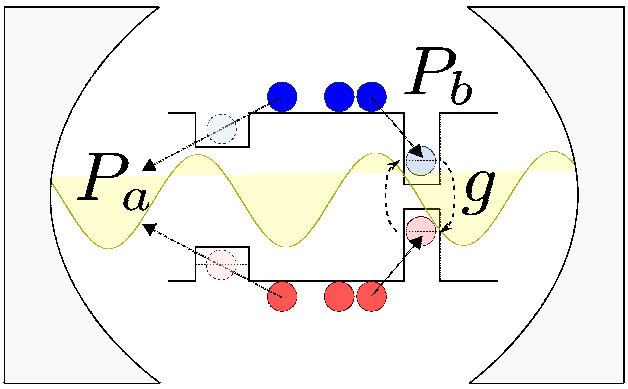

Figure 2.2: Schema of our system for the SS case: self-assembled QDs in a semiconductor microcavity. The QD sketched on the right is in *strong coupling* with the cavity mode with coupling strength g, while the one of the left is in *weak coupling*. The electron-hole pairs created by the incoherent pumping of the structure provide an effective electronic pumping, of the dot of interest, while the pumping of the assemble of dot around results in an effective cavity pumping through rapid conversion of the excitons into cavity photons.

the cavity mode. This, in turn, results in an effective pumping of the cavity as was also pointed out by Keldysh et al. (2006).

The second possible procedure to derive the Lindblad terms is based on Monte Carlo methods and quantum jumps. In the books by Gerry & Knight (2005) and S. Haroche (2006) this approach is preferred as it is closer to quantum information and measurement theories. The time evolution of a system is conceived as a succession of coherent periods of the Hamiltonian dynamics (inside a manifold) and incoherent events (between manifolds), taking place with some probability, which force the collapse of the wave function into a given realization. In this image, the microscopic origin of the incoherent processes is overlooked and they are just assumed to exist with a given probability and give rise to random flows of incoming and outcoming particles. Once we have analyzed the most relevant processes leading to incoherent dissipation and pumping, we adopt this point of view, as it goes better with the spirit of our study. We can define the Liouvillian $\mathscr{L}^c$ that acts in the density matrix through the *jump operator* c as $\mathscr{L}^c = 2c\rho c^\dagger - c^\dagger c\rho - \rho c^\dagger c$ and consider the general master equation

$$\frac{d\rho}{dt} = i[\rho, H] + \frac{\gamma_a}{2}\mathscr{L}^a\rho + \frac{\gamma_b}{2}\mathscr{L}^b\rho + \frac{P_a}{2}\mathscr{L}^{a^\dagger}\rho + \frac{P_b}{2}\mathscr{L}^{b^\dagger}\rho\,, \tag{2.74}$$

which includes the total rates for decay γ and pump P for both modes a, b. All together, these elements can be put in the form the total superoperator $\mathscr{L}$ and write the master equation as $d\rho/dt = \mathscr{L}\rho$. In what follows, we consider that these parameters can take all possible values as long as they drive the system to some SS (with non-divergent populations). We will not be concerned with the exact

experimental situation that leads to such parameters. They could well correspond to the action of one or more thermal baths, with positive of negative temperatures, etc.

It is interesting to look at the difference between the bosonic b and fermionic σ density matrices for SS of the free particles under pump and decay. For bosons, solving the master equation for the general term $\rho^b_{n,p} = \langle n| \rho^b |p\rangle$,

$$\begin{aligned} \frac{d}{dt}\rho^b_{n,p} &= -[i\omega_b(n-p) + (\gamma+P)\frac{n+p}{2} + P]\,\rho^b_{n,p} && (2.75)\\ &\quad +\gamma\sqrt{(n+1)(p+1)}\,\rho^b_{n+1,p+1} + \gamma\sqrt{np}\,\rho^b_{n-1,p-1}\,, && (2.76)\end{aligned}$$

leads, as we know, to the thermal mixture with average number give by Eq. (2.34): $\rho^b_{n,n} = (\frac{P}{\gamma})^n(1-\frac{P}{\gamma})$. The fermionic master equation,

$$\begin{aligned} \frac{d}{dt}\rho^\sigma_{0,0} &= -P\rho^\sigma_{0,0} + \gamma\rho^\sigma_{1,1}\,, && (2.77)\\ \frac{d}{dt}\rho^\sigma_{1,1} &= -\gamma\rho^\sigma_{1,1} + P\rho^\sigma_{0,0}\,, && (2.78)\\ \frac{d}{dt}\rho^\sigma_{0,1} &= i\omega\,\rho^\sigma_{0,1} - \frac{\gamma+P}{2}\rho^\sigma_{0,1}\,, && (2.79)\end{aligned}$$

leads to the counterpart, $\rho^\sigma_{n,n} = (\frac{P}{\gamma})^n(1+\frac{P}{\gamma})^{-1}$ (with only $n = 0,1$). They converge at low pump $P/\gamma \ll 1$ when the population grows linearly $\rho_{1,1} \approx P/\gamma$. At the limit $P \to \gamma$, the excitation is equally shared between all the manifolds. In the fermionic system this just means $\rho^\sigma_{n,n} = 1/2$, but in the bosonic case where there are infinite manifolds available, it implies $\rho^b_{n,n} \approx 1 - P/\gamma \to 0$, and the divergence of the average $\langle n\rangle$. The inversion of population is not possible for bosons where always $\rho^b_{n,n} > \rho^b_{n+1,n+1}$ but it is achieved for the 2LS when $P > \gamma$.

In the master equation of the 2LS, we note again the equivalence between pump and decay from the symmetry under exchange $\gamma \leftrightarrow P$ and $0 \leftrightarrow 1$. Mathematically, this it is inherited from the simplicity of the 2LS operators, $\sigma^\dagger = |E\rangle\langle G|$, that makes equivalent the Lindblad terms for pump and decay.

In the case of two bosonic modes (exciton-photon) or two fermionic modes (two QDs), we will consider also the possibility that the pumping or decay affects directly the polaritons. With pump and decay it is impossible to define anymore eigenstates of the system, as the dynamics is not given by a Hamiltonian anymore. However, in the case where the coupling is strong enough, the evolution can still be interpreted in terms of manifolds and polaritons. Lindblad terms for polariton decay $\mathscr{L}^u, \mathscr{L}^l$ and pump $\mathscr{L}^{u^\dagger}, \mathscr{L}^{l^\dagger}$ can be included in Eq. (2.74) with parameters $\gamma_{\rm U}, \gamma_{\rm L}$ and $P_{\rm U}, P_{\rm L}$ respectively. The total master equation in terms of the photon and exciton operators will include crossed Lindblad terms defined as

$$\mathscr{L}^{c+d} = 2c\rho d^\dagger - d^\dagger c\rho - \rho d^\dagger c\,. \qquad (2.80)$$

Many other Lindblad terms have been considered in literature to describe incoherent transfer of population between levels. A very interesting case are those used by Holland et al. (1996) to describe the evaporative cooling and later by Porras & Tejedor (2003) or Laussy et al. (2004) in their models of polariton condensation, in order to account for polariton-polariton and photon-polariton scattering. It represents the scattering process of two particles at level 1 into another two at levels $0, 2$ (assuming energy and momentum conservation) when level 2 is adiabatically eliminated. The jump operator describing this event is ${a^\dagger}_0 a_1^2$. In the same way, the operator for polariton relaxation down its dispersion, from level 1 to 0, by phonon emission (with energy $\omega_1 - \omega_0$), is ${a^\dagger}_0 a_1$. These few-body Lindblad terms couple the modes involved growing entanglement between the different populations even if the dynamics are incoherent.

2.5 First order coherence function and the power spectrum

Studying light-matter interaction in a given system, means probing the Hamiltonian structure described in Sec. 2.3. For that purpose, the $n > 0$ manifolds need to be excited and the cavity mirrors must let particles leak out so that we can measure them. In a naive picture, that we call the *manifold picture*, these particles carry the difference in energies between the eigenstates in the initial manifold n and those in the final one $n-1$. The probabilities of each transition, which are proportional to the intensity of the emission, are given by Eq. (2.5). This method was used, and proven useful as a first approach to the emission properties, by Laussy, Glazov, Kavokin, Whittaker & Malpuech (2006) and in some of our works, del Valle et al. (2008). However, as we know, emission (and excitation if is incoherent) comes with the price of decoherence which will change the underlying manifold structure. Pumping and decay makes the physics of light-matter coupling richer, even bringing the system into new regimes where it is no longer dominant, as we will see in the following Chapters.

In order to minimize the effects on decoherence and keep the SC physics as ”pure” as possible, several experimental options are available, as explained for example by Agarwal & Puri (1986). The excitation can be of the kind of Eq. (2.71). As I explained in Chapter 1, in atomic physics, a coherent continuous pumping *cw* standing for *continuous wave*), in the form of a monochromatic laser shined on the atom, is used to probe (if weak) or drive (if strong) the system inside the cavity in the SS. In semiconductors, this excitation process corresponds to optical resonant excitation of the quantum dot or well. In this case, the direction of excitation and collection of the emission is the same. Exciting resonantly, it is difficult to distin-

guish the light emitted by the system from that reflected from the sample as they have also similar frequencies. That is why the experiments are usually done with non-resonant excitation. However, in last few years, some experiments have been carried out where clever configurations allowed to resonantly drive a single self assembled QDs. Muller et al. (2007) used a wavelight as the excitation channel to separate it from the emitted light, reporting the first measurement of *resonant fluorescence* in this system.

A quantity that can be measured under the coherent cw, is the amplitude of the field *scattered* by the driven atom, $\langle a \rangle$, given that the output is a coherent state of cavity photons. The intensity of the scattered field $I(\omega_{\rm L}) = |\langle a \rangle|^2$ is a function of the external radiation frequency $\omega_{\rm L}$. If the laser intensity is weak, the resonances of this function are related to the Rabi frequency of the atom coupling with the cavity mode, renormalized by dissipation, the only source of decoherence. Similarly, one can look at the average rate of absorption of energy, the *absorption spectrum* $W(\omega_{\rm L})$, proportional to the atomic field $\langle b \rangle$, or $\langle \sigma \rangle$ depending on the matter model, with the same resonances. With a weak probe, the spectral features of $I(\omega_{\rm L})$ and $W(\omega_{\rm L})$ can be similarly found by assuming that the atom-photon system decays from a given initial state without any driving source. This is even closer to the experimental situation of pulse excitation as the result is to put the system in a given state from which it decays. Instead of looking at the SS imposed by the Hamiltonian in Eq. (2.71), we will prefer to study the SE of the system. This will allow us to compare our results of incoherent pump with the physics under coherent excitation where the pump does not play a role further than putting particles.

Strong laser driving fields, as those of Muller et al. (2007), serve not only as the excitation source but also as the coupling field that induces the Rabi oscillations. This method allows to put more and more particles, going up the manifold ladder, without adding any extra decoherence. There is a point where the regime of the *Mollow triplet*, studied by Mollow (1969), is entered. It consists in driving the 2LS into the very high manifolds of excitations where $n+1 \approx n$. In this case, at resonance, the two eigenenergies of the system [Eq. (2.64)] in both manifolds are just $n\omega_\sigma \pm \sqrt{n}g$. The four possible transitions correspond to only three frequencies ω_σ and $\pm 2\sqrt{n}g$ giving rise to a triplet resonance. This is an interesting configuration and we will come back to it and its possibilities under incoherent excitation in Chapter 5.

Finally, the case we want to analyze in depth is that of a SS driven by incoherent pumping. As we explained in the Introduction chapter and the previous section, this is the most common way of exciting the system in semiconductor physics. We will look into how this kind of excitation can drastically modify the Hamiltonian manifold picture depending on the character of the particle, bosonic of fermionic. But, in the same way that dissipation allows for the investigation

of the cavity output, incoherent excitation does not only contribute hindering SC features, but also bringing them out depending on the configuration. We will compare our results with the SE from a general initial state for illustration of this and other points.

In the SS under incoherent exchange with the environment, quantities as $\langle a\rangle$ or $\langle\sigma\rangle$ decay with combinations of γ and P rates until they vanish. Therefore they cannot be used to characterize the Rabi oscillations, completely washed out from the averaged one-time quantities by the probabilistic uncertainty. The most interesting and straightforward quantity to measure and study then is the *luminescence spectrum* $s(\omega)$. It is defined as the mean number of a-particles in the system with frequency ω

$$s(\omega) = \langle a^\dagger(\omega)a(\omega)\rangle\,. \tag{2.81}$$

This is proportional to the intensity of particles emitted by the system at this frequency. It is convenient to define as well the normalized spectra

$$S(\omega) = s(\omega)\Big/\int_0^\infty \langle a^\dagger a\rangle(t)dt\,, \tag{2.82}$$

so that Eq. (2.82) is now the density of probability that a photon emitted by the system has frequency ω. This is independent of the detection time, in the same way as $\langle a^\dagger a\rangle(t)$ in Eq. (2.5) was the probability of emission of a photons disregarding their frequency. The Fourier transform of $a(\omega) = \int_0^\infty e^{i\omega t}a(t)dt/\sqrt{2\pi}$ relates the emission spectrum to a two-time correlator

$$S(\omega) = \frac{1}{2\pi}\frac{1}{\int_0^\infty\langle a^\dagger a\rangle(t)dt}\iint_0^\infty \langle a^\dagger(t_1)a(t_2)\rangle e^{i\omega(t_2-t_1)}dt_1dt_2\,. \tag{2.83}$$

After a change of variables, $S(\omega)$ can be expressed in terms of the so-called *first-order correlation function*

$$G^{(1)}(t,\tau) = \langle a^\dagger(t)a(t+\tau)\rangle \tag{2.84}$$

at positive time delays $\tau = t_2 - t_1 > 0$. All put together, this yields the usual Fourier-pair relationship between the power spectrum and the correlation function:

$$S(\omega) = \frac{1}{\pi\int_0^\infty\langle a^\dagger a\rangle(t)dt}\Re\int_0^\infty\int_0^\infty G^{(1)}(t,\tau)e^{i\omega\tau}\,d\tau dt\,. \tag{2.85}$$

In the SS case, care must be taken with cancellation of infinities brought by the ever-increasing time t. Both the numerator and the denominator become infinite quantities. Their ratio, however, produces a finite quantity, which recovers the well-established and rigorously derived Wiener-Khintchine formula (see Mandel & Wolf's (1995)) that reads:

$$S^{\rm SS}(\omega) = \frac{1}{\pi}\frac{1}{n_a^{\rm SS}}\Re\int_0^\infty G^{(1)}_{\rm SS}(\tau)e^{i\omega\tau}d\tau\,. \tag{2.86}$$

Note that this formula is, strictly speaking, an arcane mathematical result in the theory of stochastic processes. There, $S(\omega)$ is a measurement of the strength of the fluctuations of the Fourier component at frequency ω. It has no strict connection with a physical signal, as both infinite negative and positive times are required for its demonstration, which violates causality among other things. For a rigorous and extended discussion of a physical optical spectrum, see the discussion by Eberly & Wódkiewicz's (1977). From the general Eq. (2.81) to the SS, Eq. (2.86), there is the cancellation of the diverging quantities by obtaining the final result as a limit of the time-integrated spectrum. The population and the correlator can be decomposed as a transient (TR) and steady-state (SS) values:

$$\langle a^\dagger a\rangle(t) = \langle a^\dagger a\rangle^{\mathrm{TR}}(t) + \lim_{t\to\infty}\langle a^\dagger a\rangle(t)\,, \tag{2.87a}$$

$$G^{(1)}(t,\tau) = \langle a^\dagger(t)a(t+\tau)\rangle^{\mathrm{TR}} + \lim_{t\to\infty}\langle a^\dagger(t)a(t+\tau)\rangle\,, \tag{2.87b}$$

where $\lim_{t\to\infty}\langle a^\dagger a\rangle(t) = n_a^{\mathrm{SS}}$. We rewrite Eq. (2.85) as the time integration of the Fourier transform until time T, that is left to increase without bounds:

$$S(\omega) = \lim_{T\to\infty}\frac{1}{\pi\int_0^T\langle a^\dagger a\rangle(t)dt}\Re\int_{t=0}^{T}\int_{\tau=0}^{\infty}G^{(1)}(t,\tau)e^{i\omega\tau}\,d\tau dt\,. \tag{2.88}$$

Substituting Eq. (2.87) in this expression, we can keep track of the terms that cancel (one can check, from the explicit results of the text, the convergence of the quantities $N \equiv \int_0^\infty \langle a^\dagger a\rangle^{\mathrm{TR}}(t)dt$ and $M_\tau = \int_0^\infty \langle a^\dagger(t)a(t+\tau)\rangle^{\mathrm{TR}}e^{i\omega\tau}\,dt$, for all $\tau > 0$):

$$S^{\mathrm{SS}}(\omega) = \frac{1}{\pi}\lim_{T\to\infty}\frac{1}{N+Tn_a^{\mathrm{SS}}}\Re\int_{\tau=0}^{\infty}\left[M_\tau + T\lim_{t\to\infty}\langle a^\dagger(t)a(t+\tau)\rangle\right]e^{i\omega\tau}d\tau\,. \tag{2.89}$$

Since the norm of the Fourier transform of M_τ is also bounded (that, again, can be checked from the explicit result), the limit in T yields Eq. (2.86).

2.5.1 Basic examples

Before going further with the details on how to compute the two-time correlator and the power spectrum for a general system described by the master Eq. (2.74), we can try to learn on the basic structure and properties of these quantities through some basic examples. For the isolated modes, the two-time correlator can be obtained by solving the *Heisenberg equations*

$$\frac{dc}{dt} = i[H,c] \tag{2.90}$$

for the creation/annihilation operators of the fields $c = a, b, \sigma$. A free mode ($H = H_c = \omega_c c^\dagger c$), propagates like $c(t) = e^{-i\omega_c t} c(0)$ and therefore $\langle c^\dagger(t) c(t+\tau)\rangle = e^{-i\omega_c \tau}\langle n_c\rangle$. $\langle n_c\rangle$ is conserved and equal to the initial average number of particles. The spectrum is just a delta function, $S(\omega) = \delta(\omega - \omega_c)$, with the pole at the energy of the mode ω_c. We can think of the spectrum of the Hamiltonian as the probability of emission when almost nothing is allowed to exit. The time uncertainty is very large, as we must wait a long time to detect a particle. The resonant energies are, therefore, exactly defined. They are given by the energy difference between eigenenergies of two consecutive manifolds. The *emission spectrum* is nothing else than the *energy spectrum*. We can see this is another example. If we add interactions in the bosonic case, with the Hamiltonian in Eq. (2.69), $H = H_b + H_{\text{int}}$, then the operator $b(t)$ depends on the manifold,

$$b(t) = e^{-i(\omega_b + U n_b)t} b(0)\,, \tag{2.91}$$

as well as the correlator

$$\langle b^\dagger(t) b(t+\tau)\rangle = e^{-i\omega_b \tau}\langle b^\dagger(0) e^{-iU n_b \tau} b(0)\rangle = e^{-i\omega_b \tau}\sum_n n\rho_{n,n} e^{-iU(n-1)\tau}\,. \tag{2.92}$$

Note that $[n_b, H] = 0$ and therefore n_b is a constant of motion. This yields to a spectrum for the b operator,

$$S(\omega) = \frac{1}{\langle n_b\rangle}\sum_n n\rho_{n,n}\delta\big(\omega - [\omega_b + U(n-1)]\big) \tag{2.93}$$

which simply weights with the occupation, the resonances that corresponds to each pair of manifolds $\langle n|\,H\,|n\rangle - \langle n-1|\,H\,|n-1\rangle$.

When the lifetime of the particles in the system is not infinite, the uncertainty in the energy of the emitted particle increases. This corresponds to changing the delta functions by a broader function, which allows for some *linewidth*. One can think naively and simply break the conservation of particles by adding some exponential decay to the operators $c(t) = e^{-i\omega_c t} e^{-\frac{\gamma_c}{2}t} c(0)$ which results in the expected decay of particles $\langle n_c\rangle(t) = e^{-\gamma_c t}\langle n_c\rangle(0)$. This corresponds, and it is often found in the literature, to adding an imaginary part to the energy

$$\omega_c \to \omega_c - i\frac{\gamma_c}{2} \tag{2.94}$$

in the free Hamiltonian H_c and solving the equation $dc/dt = -i\omega_c c - \gamma_c/2 c$. This procedure is in general incorrect, as it is nicely explained for instance by Yamamoto & Ĭmamoḡlu (1999). It leads to unphysical results like the decay of the bosonic commutation relation: $[a(t), a^\dagger(t)] = e^{-\gamma t}$. Dissipation not only empties

the system but also induces quantum noise due to fluctuations in the reservoir. A more elaborated method is needed like the master equation and Lindblad terms we presented in Sec. 2.4. Equivalently, the Heisenberg equations for the operators $dc/dt = -i\omega_c c$ can be upgraded to the *quantum Langevin equations*,

$$\frac{dc}{dt} = -i\omega_c c - \frac{\gamma_c}{2}c - \sqrt{\gamma_c}R(t)\,, \tag{2.95}$$

where the quantum white *noise operator* $R(t)$ is introduced. This operator is determined by the state of the bath. The average value of its commutation relations carries the statistic information which leads to the expected physical results. However, depending on the system, solving the Heisenberg equations with decay introduced as an imaginary frequency, can give rise to the same results as solving the Langevin equations. For example, in the case of averaged quantities like $\langle n_c\rangle$ or the two-time correlator, $\langle c^\dagger(t)c(t+\tau)\rangle = e^{-\gamma_c t}e^{-i\omega_c\tau}e^{-\gamma\tau/2}\langle c^\dagger(0)c(0)\rangle$, the correct expression is obtained. Before we derive them using the proper methods, let us just write the spectrum this yields:

$$S(\omega) = \frac{1}{\pi}\frac{\frac{\gamma_c}{2}}{\left(\frac{\gamma_c}{2}\right)^2 + (\omega-\omega_c)^2}\,, \tag{2.96}$$

where we used

$$\int_0^\infty e^{i(\omega-\omega_c)\tau}e^{-\frac{\gamma_c}{2}\tau}d\tau = \frac{\frac{\gamma_c}{2} + i(\omega-\omega_c)}{(\frac{\gamma_c}{2})^2 + (\omega-\omega_c)^2}\,. \tag{2.97}$$

This is the *Cauchy-Lorentz distribution* with a full width at half its maximum (*FWHM*) given by γ_c, which is also the inverse lifetime of the particles in the system. This shape is the most commonly found in spectroscopy as it appears when the mechanisms causing the broadening of the line affects homogeneously all the emitters.

2.5.2 The manifold approach

From the previous examples, we can generalize an approximate expression for the spectrum of emission that can give valuable and intuitive insights into the system under study. The spectra, in general, consist of a sum of peaks, at least one for each transition allowed in the system between energy levels. The peaks are given by the lineshape, position, linewidth and weight. In Eq. (2.93) we can see that, for the case of Hamiltonian (2.69), the lineshape for each peak n is a Delta function (with no broadening), positioned at $\omega_b + U(n-1)$. Its weight in the total spectra is given by the product of the population of state $|n\rangle$, $\rho_{n,n}$, times the probability of

emission of such state into the lower one $|n-1\rangle$, $I^n = |\langle n-1|\, a\, |n\rangle|^2 = n$, that is also the intensity of this transition [Eq. (2.5)]. If decay is considered, the lineshape becomes a Lorentzian, like in Eq. (2.96), or other functions depending on the interferences that take place between the different transitions. In what follows we will consider Lorentzian lineshapes for simplicity.

The extension of these ideas for a general system is what we call the *manifold method*. It has been applied, for instance, by Laussy, Glazov, Kavokin, Whittaker & Malpuech (2006) and derived more rigorously by Vera et al. (2008) or Averkiev et al. (2008) from the exact expression for the spectra in Eq. (2.86). We assume that the total number of excitations is conserved by the Hamiltonian (the Hamiltonian dynamics take place inside each manifold independently), that the decay processes remove particles jumping between manifolds, and that the excitation mechanism does not change the energy structure. The method, based on the quantum jump approach, to obtain the elements of the approximate expression for the spectra

$$s(\omega) = \sum_p I^p \rho^p \frac{1}{\pi} \frac{\gamma_p/2}{(\gamma_p/2)^2 + (\omega - \omega_p)^2}\,, \tag{2.98}$$

consists in the following steps:

1. Constructing a non-Hermitian Hamiltonian of the form (2.94) that includes the decay of the modes in a complex frequency $\omega - i\gamma/2$.

2. Obtaining eigenenergies $\{E_i^k\}$ and eigenstates $\{\mathbf{e}_i^k\}$ of this Hamiltonian in a given manifold k. We suppose that the system, in its coherent evolution, is in a mixture of these states.

3. The positions ($\omega_{i,j}^k$) and broadenings ($\gamma_{i,j}^k/2$) of the lines corresponding to each possible transition are given by, respectively, the imaginary and real parts of

$$i[E_i^k - (E_j^{k-1})^*]\,. \tag{2.99}$$

   This is simply because the positions are given by the difference in energy between the levels but the broadening of each line is given by the sum of the broadenings associated to them, as the uncertainty must increase.

4. Obtaining the amplitudes of probabilities of loosing an excitation from a given manifold to the neighboring one counting one excitation less. This is computed for each pair of states through the corresponding jump operator (a in the case of photon emission):

$$I_{i,j}^{k\to k-1} = |\langle k-1, j|\, a\, |k, i\rangle|^2\,. \tag{2.100}$$

5. Obtaining ρ_i^k, the average population of each state $|k,i\rangle$, for example by solving the master equation.

6. Summing in Eq. (2.98) all the contributions $p \to \{k,i,j\}$.

The resulting spectra is qualitatively similar to the exact results from Eq. (2.86) in the sense that it gives the good number of peaks and their positions in general. However, it is inaccurate in the broadenings and weights that are oversimplified here. The whole picture breaks when the incoherent pump is comparable to the decay, as this is a strong source of decoherence, or when there are interferences between the different resonances and channels of emission of the system, as each transition is considered independently here. Therefore, although this method provides a good physical insight into the system and its spectra, as we will see in Chapter 5, we must also find a way to compute it exactly. This is the goal of the next Section.

2.6 The Quantum Regression Formula

The *quantum regression formula* (QRF) found by Lax (1967) provides a method to compute any two-time correlator from a master equation of the form $d\rho/dt = \mathscr{L}\rho$ [Eq. (2.74)] (for system interacting with Markovian reservoirs). As explained in the book by Carmichael (2002), once one has found a set of operators $C_{\{\eta\}}$ that satisfy

$$\mathrm{Tr}(C_{\{\eta\}}\mathscr{L}\Omega_1) = \sum_{\{\lambda\}} M_{\{\eta\lambda\}}\mathrm{Tr}(C_{\{\lambda\}}\Omega_1) \tag{2.101}$$

for the general operator Ω_1, and the corresponding matrix elements $M_{\{\alpha\beta\}}$, then, the equations of motion for the two-time correlators read (for $\tau \geq 0$)

$$\frac{d}{d\tau}\langle\Omega_1(t)C_{\{\eta\}}(t+\tau)\rangle = \sum_{\{\lambda\}} M_{\{\eta\lambda\}}\langle\Omega_1(t)C_{\{\lambda\}}(t+\tau)\rangle\,. \tag{2.102}$$

The Hilbert space of correlators is separated in *manifolds*, just as the Hilbert state of states is separated in manifolds of excitations. The order of the manifold k is the minimum number of particles that should be in the system (regardless of the regression matrix) so that the correlator is nonzero. Equivalently, it is the minimum manifold of excitations that should be probed in the dynamics. We will refer to the two-time and one-time correlator manifolds as $\mathscr{N}_k$ and $\tilde{\mathscr{N}_k}$, respectively.

The first step is to find the set of operators that are need to compute the correlator of interest. For example, in the case of bosons, in order to set the equations where $\langle a^\dagger(t)a(t+\tau)\rangle$ can be obtained, we consider $\Omega_1 = a^\dagger$. If this is the only field involved in the dynamics, the most general set of operators in normal order

can be written as $\{C_{\{m,n\}} = a^{\dagger m} a^n\}$. For the simple problem of a thermal bath, it is enough to consider only $C_1 = a$. The only matrix element is $M_{1,1} = -i\omega_a - \frac{\gamma_a - P_a}{2}$ and the correlator can be trivially integrated taking as the initial state the SS value $n_a^{\rm SS}$: $\langle a^\dagger(t) a(t+\tau)\rangle = e^{-i\omega_a \tau} e^{-(\gamma_a - P_a)/2\tau} n_a^{\rm SS}$. The spectra is again a Lorentzian

$$S(\omega) = \frac{1}{\pi} \frac{\frac{\Gamma_a}{2}}{\left(\frac{\Gamma_a}{2}\right)^2 + (\omega - \omega_a)^2}\,, \tag{2.103}$$

this time broadened by a renormalized bosonic decay rate

$$\Gamma_a = \gamma_a - P_a = \frac{\gamma_a}{1 + n_a^{\rm SS}}\,. \tag{2.104}$$

In this case, in order to have a physical SS (finite populations and correlations which decay with time) we know that the parameters γ_a and P_a correspond to a given thermal bath. This implies that $n_a^{\rm SS} = \bar{n}_T$ and $\Gamma_a = \kappa_a$. On the other hand, if we deal with a free 2LS and we want to compute $\langle \sigma^\dagger(t)\sigma(t+\tau)\rangle$, the equivalent procedure yields to an effective broadening

$$\Gamma_\sigma = \gamma_\sigma + P_\sigma = \frac{\gamma_\sigma}{1 - n_\sigma^{\rm SS}} \tag{2.105}$$

which is different from the decay rate in vacuum κ_σ. We can also distinguish the nature of the particles in the appearance of the bosonic $(1+n_a)$ or the fermionic $(1-n_\sigma)$ factors in the dependence of the effective decays with the average occupation. The narrowing (broadening) of the linewidth with pump, as the number of particles increases, is a bosonic (fermionic) effect.

In more complicated systems, the correlator of interest will depend on others giving rise to a set of coupled equations of the form of Eq. (2.102). The initial values at $\tau = 0$ must also be found in the SS or a general time t for the SE case. The equations for $\langle \Omega_1(t) C_{\{\eta\}}(t)\rangle$ can be equally found applying the same QRF with $\tilde{\Omega}_1 = 1$ and a new set of operators $C_{\{\tilde{\eta}\}}$ where $\Omega_1 C_{\{\eta\}}$ is included:

$$\frac{d}{d\tau}\langle C_{\{\tilde{\eta}\}}(t+\tau)\rangle = \sum_{\{\tilde{\lambda}\}} M_{\{\tilde{\eta}\tilde{\lambda}\}} \langle C_{\{\tilde{\lambda}\}}(t+\tau)\rangle\,. \tag{2.106}$$

In the SE case, the running variable is τ with $t = 0$. The initial state of these differential equations is the initial value of the correlators $\langle C_{\{\tilde{\eta}\}}(0)\rangle$. In the SS case, the equations are set to zero and solved as a linear system to find $\langle C_{\{\tilde{\eta}\}}\rangle^{\rm SS}$. The one-time mean values can also be obtained from the density matrix resulting from the master equation by applying the general relation $\langle C_{\{\tilde{\eta}\}}(t)\rangle = {\rm Tr}[C_{\{\tilde{\eta}\}}\rho(t)]$.

In the general problem of two coupled modes, a, b, we refer with the label $\{\eta\} = (m,n,\mu,\nu)$ to the two-time correlator $\langle \Omega_1(t) C_{\{\eta\}}(t+\tau)\rangle$ with $C_{\{\eta\}} =$

$a^{\dagger m}a^n b^{\dagger\mu}b^\nu$, regardless Ω_1. This is the most general form for the correlators, grouped in manifolds $\mathscr{N}_k$. The emission of particles a (b) corresponds to $\Omega_1 = a^\dagger$ ($= b^\dagger$). Each two-time correlator will have as initial condition ($\tau = 0$) the one-time correlator $\langle C_{\{m+1,n,\mu,\nu\}}\rangle$ ($\langle C_{\{m,n,\mu+1,\nu\}}\rangle$) that belongs to the corresponding manifold of the same order $\tilde{\mathscr{N}}_k$. The QRF for them, with $\tilde{\Omega}_1 = 1$, applies in a new set of operators $\{\tilde{\eta}\} = (m+1,n,\mu,\nu)$ ($\{\tilde{\eta}\} = (m,n,\mu+1,\nu)$). The final result for the correlator of interest, $\langle C_{\rm i}(t,\tau)\rangle$, will be, as we will see in the following Chapters, always of the form

$$\langle C_{\rm i}(t,\tau)\rangle = \sum_p (l_p(t) + ik_p(t))e^{-i\omega_p\tau}e^{-\frac{\gamma_p}{2}\tau}\,, \tag{2.107}$$

where all the new parameters, the weights l_p, k_p, the frequencies ω_p and the effective decay rates γ_p, are real. The values l_p and k_p depend on the one-time mean-values $\langle C_{\{\tilde{\eta}\}}(t)\rangle$, either in the SS or in time t, depending on the case. In the SS, they are already constants and can be normalized $L_p^{\rm SS} = l_p^{\rm SS}/\langle C_{\rm i}\rangle^{\rm SS}$, $K_p^{\rm SS} = k_p^{\rm SS}/\langle C_{\rm i}\rangle^{\rm SS}$. In the SE, they have to be integrated and normalized accordingly: $L_p^{\rm SE} = \int_0^\infty l_p^{\rm SE}(t)dt/\int_0^\infty \langle C_{\rm i}(t,0)\rangle dt$ and $K_p^{\rm SE} = \int_0^\infty k_p^{\rm SE}(t)dt/\int_0^\infty \langle C_{\rm i}(t,0)\rangle dt$. From here, Eq. (2.97) leads to the spectrum,

$$S_{\rm i}(\omega) = \frac{1}{\pi}\sum_{p=1}\left[L_p\frac{\frac{\gamma_p}{2}}{\left(\frac{\gamma_p}{2}\right)^2 + (\omega-\omega_p)^2} - K_p\frac{\omega-\omega_p}{\left(\frac{\gamma_p}{2}\right)^2 + (\omega-\omega_p)^2}\right], \tag{2.108}$$

which is in general a sum of many peaks labelled with p, with two type of contributions. The first one is the already introduced Lorentzian shape, which is the only contribution for free fields. The second contribution appears when the system in its evolution is able of developing correlations between the energetic levels, due to coupling to other modes or some dependence on the manifold. The second term in Eq. (2.108) is a sort of *dispersive* line shape that breaks the symmetry of the Lorentzian around the frequency ω_p. This is due to the interference between nearby resonances.

This way of computing the spectra, in which we take the Fourier transform explicitly, gives us the structure of the lines in a transparent way. ω_p and γ_p are the line positions and broadenings. They originate from the energy levels structure and uncertainties, whose skeleton is the Hamiltonian eigenstates but that can be greatly distorted by decoherence. As such, they are independent of the channel of detection (cavity or direct exciton emission) and independent of time. Coefficients L_p^c and K_p^c depend on the one time correlators and, therefore, they are different in the SS or the SE cases. They determine which lines actually appear in the spectra, and with which intensity depending on the channel of emission and the quantum state in the system.

Most of the authors, like Savage (1989), Clemens et al. (2004), Porras & Tejedor (2003) or Perea et al. (2004), compute the spectrum with completely numerical methods from the density matrix and master equation. Their results are blind to the underlying individual lines and, therefore, miss all the information on the manifold structure that the spectra contains. This is a very dramatic loss if one is interested in quantum features or the crossover from quantum to classical regime, like is the case in this thesis. However, the lack of this information is not so important when the system is essentially classical or in the classical regime, where there is no quantized manifold structure. We will prefer this kind of "blind" methods then. In this direction and taking advantage of the SS properties, it is possible to go from the density matrix to the spectra without any need to compute the correlator. This method is described by Mølmer (1996) in his notes:

First, we choose a basis of states $\{|i\rangle\}$, ordered in a given way and labelled with the index $i = 1, ...N$. Then, we obtain the density matrix, in its $N \times N$ matrix form $\rho_{ij} = \langle i|\,\rho\,|j\rangle$, in the SS. That is, we solve the master equation

$$\frac{d}{dt}\rho_{ij} = \sum_{k,l} \mathscr{M}_{ij,kl}\rho_{kl} = 0 \tag{2.109}$$

where $\mathscr{M}_{ij,kl}$ is a supermatrix $N^2 \times N^2$. The spectral function can be defined in terms of the two operators A, B which constitute the two-time correlator of interest, $C_{\rm i}(t,\tau) = A(t)B(t+\tau)$, as

$$s_{AB}(\omega) = \frac{1}{\pi}\Re\int_0^\infty \langle A(t)B(t+\tau)\rangle e^{i\omega\tau}d\tau\,. \tag{2.110}$$

By means of the QRF, the spectrum can be put in terms of the matrix form of the operators A_{ij} $(= \langle i|A|j\rangle)$ and B_{ij} and the SS density matrix:

$$s_{AB}(\omega) = -\frac{1}{\pi}\Re\sum_{i,j,k,l,m}[(\mathscr{M} + i\omega I)^{-1}]_{ij,kl}\rho^{\rm SS}_{km}A_{ml}B_{ji}\,. \tag{2.111}$$

I is the $N^2 \times N^2$ identity matrix. This formula is valid as long as $\langle A\rangle = 0$ in the SS. It is useful when the Hilbert space is not very large as it requires the inversion of a $N^2 \times N^2$ matrix for each point ω of the spectra.

2.7 Second order correlation function and the noise spectrum

The power spectrum can only provide information on probabilities for single particles, being the Fourier transform of the first-order correlation function $G^{(1)}(t,\tau)$.

To investigate the statistics in a system, we must go further in the order of the correlation functions. We already discussed the degree of second order coherence of a distribution, $g^{(2)}$ in Eq. (2.7). Now we can generalize it to a arbitrary delay and define the two-time *second-order correlation function*

$$G^{(2)}(t,\tau) = \langle a^\dagger(t)a^\dagger(t+\tau)a(t+\tau)a(t)\rangle \tag{2.112}$$

and the normalized version for stationary states, $g^{(2)}(t,\tau) = G^{(2)}(t,\tau)/\langle a^\dagger(t)a(t)\rangle^2$. $G^{(2)}(t,\tau)$ is related to the probability to emit two particles one after the other, at times t and $t+\tau$, and it can also be identified with intensity correlations. Let us from now on consider that $t \to \infty$ and write expressions for the SS only, as this will be the most relevant case. As in the time domain, in order to fully describe the correlations between two particles emitted at different frequencies ω_1, ω_2, one would have to compute $S^{(2)}(\omega_1,\omega_2) = \langle a^\dagger(\omega_1)a^\dagger(\omega_2)a(\omega_2)a(\omega_1)\rangle/(n_a^{\rm SS})^2$. This quantity requires three-time correlators and is technically involved. Therefore, as a first approximation to the problem, we will simply analyze $S^{(2)}(\omega) \propto \int_{-\infty}^{\infty} s^{(2)}(\omega_1+\omega_a, \omega-\omega_1+\omega_a)d\omega_1$. It corresponds to the Fourier transform

$$S^{(2)}(\omega) = \frac{1}{\pi}\Re\int_0^\infty (g^{(2)}_{\rm SS}(\tau)-1)e^{i\omega\tau}d\tau\,, \tag{2.113}$$

so it can be considered the intensity fluctuation spectrum or *noise spectrum*, in analogy with the power spectrum. $S^{(2)}(\omega)$ can also be interpreted as the joint density of probability that two particles in the system have frequencies whose fluctuations around the bare reference frequency (ω_a) sum up to ω. Still in this simplified version of $s^{(2)}$, the two-particle frequency correlations are to be found in the difference between $S^{(2)}(\omega)$ and the convolution of individual densities of probability:

$$S^{(2)}_{\rm corr}(\omega) = S^{(2)}(\omega) - \int_{-\infty}^{\infty} S(\omega_1+\omega_a)S(\omega-\omega_1+\omega_a)d\omega_1 \tag{2.114}$$

The correlator $\langle a^\dagger(t)a^\dagger(t+\tau)a(t+\tau)a(t)\rangle$ needed here, can again be computed thanks to the QRF. Once Eqs. (2.101) is satisfied for some set of operators $C_{\{\eta\}}$, not only Eq. (2.102) holds, but also the relation

$$\frac{d}{d\tau}\langle C_{\{\eta\}}(t+\tau)\Omega_2(t)\rangle = \sum_{\{\lambda\}} M_{\{\eta\lambda\}}\langle C_{\{\lambda\}}(t+\tau)\Omega_2(t)\rangle\,, \tag{2.115}$$

is true for any general operator Ω_2 and the same regression matrix. From this, another useful equation involving two operators can be derived

$$\frac{d}{d\tau}\langle \Omega_1(t)C_{\{\eta\}}(t+\tau)\Omega_2(t)\rangle = \sum_{\{\lambda\}} M_{\{\eta\lambda\}}\langle \Omega_1(t)C_{\{\lambda\}}(t+\tau)\Omega_2(t)\rangle\,. \tag{2.116}$$

In the present case, we need to take $\Omega_1 = a^\dagger$ and $\Omega_2 = a$, and find the set $C_{\{\eta\}}$ that includes the operator $a^\dagger a$. It is interesting to note that the matrix of regression $M_{\{\eta\lambda\}}$ and set of correlators $C_{\{\eta\}}$ involved in the computation of $G^{(2)}(t,\tau)$ are the same as those involved in the computation of the one-time average value n_a.

For the simple example of a thermal bosonic field, only the operators $C_0 = 1$ and $C_1 = a^\dagger a$ are needed with $M_{1,1} = -\Gamma_a$ and $M_{1,0} = P_a$. The result in the SS is $g^{(2)}(\tau) = 1 + e^{-\Gamma_a \tau}$, that decays from 2 (as it corresponds to the thermal SS) to the general infinite delay value of 1 (two uncorrelated emissions). Thermal or chaotic sources correspond to the case where each emission event is independent and:

$$g^{(2)}(\tau) = 1 + |g^{(1)}(\tau)|^2, \quad S^{(2)}_{\text{corr}}(\omega) = 0\,. \tag{2.117}$$

Chapter 3

One quantum dot in a microcavity: the linear model

Contents

In this Chapter, we solve the exciton-cavity photon coupling analytically with the linear model and analyze its properties of emission in the presence of decoherence (dissipation and incoherent pump). The results presented here have been published in the references 4, 8 and 9 of the list of my publications, in page 225.

3.1 Introduction

Light-matter coupling is described by the Hamiltonian that we already introduced in Chapter 2:

$$H = \omega_a a^\dagger a + \omega_b b^\dagger b + g(a^\dagger b + a b^\dagger) \tag{3.1}$$

where a and b are the cavity photon and material excitation field operators, respectively, with bare mode energies ω_a and ω_b, coupled linearly with strength g. In the *linear model* (LM), both the photon and exciton operators are Bose operators, satisfying the usual commutation rule $[a, a^\dagger] = 1$, $[b, b^\dagger] = 1$. This is an important case for two reasons. The first one is that in many relevant cases, the matter-field is indeed bosonic, such as the case of quantum wells, or large quantum dots, at low density of excitations. The second reason is that this case provides the limit for vanishing excitations (*linear limit*) of all the other cases, and is fully solvable analytically. In Chapter 5, we investigate the case of fermionic behavior at large pumping, more relevant when dealing with small QDs that confine excitations, and more prone to involve genuine quantum mechanics as one quantum of excitation can alter the system's response.

The master equation in the absence of pump and at zero temperature,

$$\frac{d\rho}{dt} = i[\rho, H] + \sum_{c=a,b} \frac{\gamma_c}{2}(2c\rho c^\dagger - c^\dagger c\rho - \rho c^\dagger c)\,, \tag{3.2}$$

has been extensively studied. However, the typical restrictions have been to consider the case of resonance, $\omega_a = \omega_b$, with only one particular initial condition, namely, the excited state of the emitter in an empty cavity, and to detect the emission of the emitter itself. All together, they describe the spontaneous emission of an emitter placed into a cavity with which it enters into SC. This has been the topical case for decades as this was the case of experimental interest with atoms in cavities.

With the advent of SC in other systems, other configurations start to be of interest. With a QD in a microcavity, the detuning Δ between the modes, Eq. (2.56), is a crucial experimental parameter, as it can be easily tuned and to a great extent, for instance by applying a magnetic field or changing the temperature. Also in this case, the detection is in the optical mode of the cavity, rather than the direct emission of the exciton emission, because the latter is awkward for various technical reasons of a more or less fundamental character (an example of a fundamental complication is that the emission is enhanced in the cavity mode and suppressed otherwise, and the exciton lifetime is typically much longer, so the exciton emission is much weaker; an example of a petty technical complication is that the exciton detection should be made at an angle and, practically, a lot of samples are grown on the same substrate. Both the substrates and other samples

hinder the lateral access to one given sample, whereas all are equally accessible from above). If both modes are bosonic, symmetry allows to focus on the cavity emission without loss of generality, as we can obtain the leaky excitonic emission by simply exchanging indexes a, b (the spectrum could also have photon-exciton crossed terms that could be computed in a similar way).

Regarding the initial condition, more general quantum states can now be realized, at least in principle, by coherent control, pulse shaping or similar techniques. Additionally and more importantly, the type of excitation of a cavity-emitter system in a semiconductor is typically of an incoherent nature and brings many fundamental changes into the problem that go beyond the mere generalization of Eq. (3.2). Pure states do not correspond to the experimental reality. Instead, the system is maintained in a mixed state with probabilities $p(n)$ to realize the nth excited state. In all cases, a steady state is imposed by the interplay of pumping and decay. Explicitly, the complete master equation (2.74) reads:

$$\frac{d\rho}{dt} = i[\rho, H] + \sum_{c=a,b} \frac{\gamma_c}{2}(2c\rho c^\dagger - c^\dagger c\rho - \rho c^\dagger c) + \sum_{c=a,b} \frac{P_c}{2}(2c^\dagger \rho c - cc^\dagger \rho - \rho cc^\dagger)\,. \tag{3.3}$$

The Rabi oscillations of the populations are always washed out, regardless of the photon-like, exciton-like or polariton-like (eigenstate) character of the density matrix.

There has been naturally many efforts and a large output in the literature to describe theoretically light-matter coupling in semiconductors. A huge majority of them address the Spontaneous Emission case, partly because of the precedent set up by the atomic case. Andreani et al. (1999) in their paper, which seems to be the most highly quoted on that question, apply the atomic theory of Carmichael et al. (1989), that was already restricted to the first manifold of excitation. This work's major contribution was the analysis of the coupling strength g and the prediction of QDs in microcavities as successful candidates for SC physics. Unfortunately, the expression for the luminescence spectrum that was taken straight from the atomic literature concerns the configuration of direct exciton emission, which is not the canonical case of a semiconductor microcavity where photons are detected through their leakage in the cavity mode (in the growth axis). Pau et al. (1995) had used a similar scheme to describe the spectra of microcavity polaritons in the very strong coupling regime (in a Lorentzian limit). Let us also mention, among the numerous recent works on the SE of an excited state in a cavity, Cui & Raymer (2006), who applied the Weisskopf-Wigner approximation to compute the spectra and put strong emphasis to the forward and side emission, Auffèves et al. (2008) and Inoue et al. (2008), who gave an insightful description in particular of the *Fano resonance* on which we shall comment thoroughly below, and Yamaguchi et al. (2008), who studied the influence of pure dephasing in the spectra, providing

a possible explanation for the anomalously large cavity intensity found by Reithmaier et al. (2004), that we also discuss. In the appropriate limits, we recover the results of these papers, that corresponds to the spontaneous emission of one excitation.

In this Chapter, we address both the emission spectra obtained in a configuration of spontaneous emission (SE)—where an initial state is prepared and left to decay—under its most general setting, and the case of luminescence emission under the action of a continuous and incoherent pumping that establishes a steady state (SS). We bring all results under a common and unified formalism and show how none of the cases fully encompasses the other. We focus especially on the continuous pumping case which endows the problem with self-consistency in view of its initial state. The rest of the Chapter is organized as follows. In Section 3.2, we analyze the single-time dynamics. In Section 3.3, we obtain fully analytically the main results in both of the cases explicated above, this time focusing more on the two-time dynamics, which Fourier transform gives the luminescence spectra. In Section 3.4, we discuss the mathematical results derived in the two previous sections, accentuating the physical picture and relying on particular cases for illustration. In this Section, we consider specifically the case of resonance, where all the concepts manifest more clearly. In Section 3.5 we show how the expressions obtained for the SS spectra allow for a successful global fitting of the semiconductor experimental data of Reithmaier et al. (2004) providing an estimation for the system parameters and the pumping conditions. In Section 3.6 we briefly look into the second order correlation function. Finally, in Section 3.7, we give a summary of the main results and provide an index of all the important formulas and key figures of this Chapter.

3.2 Mean values

Let us start by introducing some notation that will be useful in the general description of SE and SS emission. The *effective broadenings* reduce to the decay rates in the SE case but get renormalized by the pumping rate in the SS case:

$$\Gamma_{a,b} = \gamma_{a,b}\,, \qquad \text{(SE case)} \tag{3.4a}$$

$$\Gamma_{a,b} = \gamma_{a,b} - P_{a,b}\,. \qquad \text{(SS case)} \tag{3.4b}$$

We shall also use thoroughly the combinations:

$$\gamma_{\pm} = \frac{\gamma_a \pm \gamma_b}{4} \quad \text{and} \quad \Gamma_{\pm} = \frac{\Gamma_a \pm \Gamma_b}{4}\,. \tag{3.5}$$

Thanks to the general relations $\langle C\rangle = \mathrm{Tr}(C\rho)$ and $d\langle C\rangle/dt = \mathrm{Tr}(Cd\rho/dt) = \mathrm{Tr}(C\mathscr{L}\rho)$, we can obtain from Eq. (3.3) the single-time mean values of interest

for this problem, by solving the equation of motion of the coupled system:

$$\frac{d\mathbf{u}(t)}{dt} = -\mathbf{M}_0\mathbf{u}(t) + \mathbf{p} \tag{3.6}$$

with

$$\mathbf{u} = \begin{pmatrix} n_a \\ n_b \\ n_{ab} \\ n_{ba} \end{pmatrix}, \quad \mathbf{p} = \begin{pmatrix} P_a \\ P_b \\ 0 \\ 0 \end{pmatrix}, \quad \mathbf{M}_0 = \begin{pmatrix} \Gamma_a & 0 & ig & -ig \\ 0 & \Gamma_b & -ig & ig \\ ig & -ig & 0 & -i\Delta + 2\Gamma_+ \\ -ig & ig & i\Delta + 2\Gamma_+ & 0 \end{pmatrix}, \tag{3.7}$$

where $n_c = \langle c^\dagger c \rangle \in \mathbb{R}$ (for $c = a, b$) and $n_{ab} = \langle a^\dagger b \rangle = n_{ba}^* \in \mathbb{C}$. The SE case corresponds to setting $P_{a,b} = 0$ and providing the initial conditions, $\mathbf{u}(0)$, with:

$$n_a^0 \equiv n_a(0), \quad n_b^0 \equiv n_b(0), \quad \text{and} \quad n_{ab}^0 \equiv n_{ab}(0)\,. \tag{3.8}$$

The solution,

$$\mathbf{u}^{\mathrm{SE}}(t) = e^{-\mathbf{M}_0 t}\mathbf{u}(0)\,, \tag{3.9}$$

gives the cavity population:

$$\begin{aligned} n_a(t) = e^{-2\gamma_+ t}\Bigg\{ & \left[\cos(R_{\mathrm{r}}t) + \cosh(R_{\mathrm{i}}t)\right]\frac{n_a^0}{2} \\ & - \left[\cos(R_{\mathrm{r}}t) - \cosh(R_{\mathrm{r}}t)\right]\frac{(\frac{\Delta^2}{4} + \gamma_-^2)n_a^0 + g^2 n_b^0 + g\Delta\Re n_{ab}^0 - 2g\gamma_-\Im n_{ab}^0}{2|R|^2} \\ & + \left[\frac{\sin(R_{\mathrm{r}}t)}{R_{\mathrm{r}}} + \frac{\sinh(R_{\mathrm{i}}t)}{R_{\mathrm{i}}}\right]\left(g\Im n_{ab}^0 - \gamma_- n_a^0\right) \\ & + \left[\frac{\sin(R_{\mathrm{r}}t)}{R_{\mathrm{r}}} - \frac{\sinh(R_{\mathrm{i}}t)}{R_{\mathrm{i}}}\right]\frac{\gamma_-(\frac{\Delta^2}{4} + \gamma_-^2 - g^2)n_a^0 + g\Delta\gamma_-\Re n_{ab}^0 + g(\frac{\Delta^2}{4} - \gamma_-^2 + g^2)\Im n_{ab}^0}{|R|^2} \Bigg\}. \end{aligned} \tag{3.10}$$

The expression for $n_b(t)$ follows from $a \leftrightarrow b$. The crossed mean value that

reflects the coherent coupling reads:

$$
\begin{aligned}
n_{ab}(t) = e^{-2\gamma_+ t}\Bigg\{ & \left[\cos(R_{\rm r}t)+\cosh(R_{\rm i}t)\right]\frac{n^0_{ab}}{2} \\
-&\left[\cos(R_{\rm r}t)-\cosh(R_{\rm i}t)\right]\frac{g(\frac{\Delta}{2}+i\gamma_-)n^0_a - g(\frac{\Delta}{2}-i\gamma_-)n^0_b - (\frac{\Delta^2}{4}+\gamma_-^2)n^0_{ab} + g^2(n^0_{ab})^*}{2|R|^2} \\
+&\left[\frac{\sin(R_{\rm r}t)}{R_{\rm r}}+\frac{\sinh(R_{\rm i}t)}{R_{\rm i}}\right]\frac{i(\Delta n^0_{ab} - g(n^0_a - n^0_b))}{2} \\
+&\left[\frac{\sin(R_{\rm r}t)}{R_{\rm r}}-\frac{\sinh(R_{\rm i}t)}{R_{\rm i}}\right]\times \\
&\frac{g(\Delta\gamma_- - i(\frac{\Delta}{2}+g^2-\gamma_-^2))n^0_a + g(\Delta\gamma_- + i(\frac{\Delta}{2}+g^2-\gamma_-^2))n^0_b + i\Delta(\frac{\Delta^2}{4}+\gamma_-^2+g^2)n^0_{ab}}{2|R|^2}\Bigg\}
\end{aligned}
\tag{3.11}
$$

where we have defined the *complex (half) Rabi frequency*:

$$
R = \sqrt{g^2 - \left(\Gamma_- + i\frac{\Delta}{2}\right)^2}, \tag{3.12}
$$

that arises as a direct extension of the dissipationless case, Eq. (2.57c). $R_{\rm r,i}$ are its real and imaginary parts respectively, $R = R_{\rm r} + iR_{\rm i}$. Note that in the SE case $\Gamma_- \to \gamma_-$ in R, that we define now in general. It is clear from Eqs. (3.10)–(3.11) that $R_{\rm r}$ is responsible of the oscillations and $R_{\rm i}$, together with γ_+, of the damping.

It is interest to note that Eqs. (3.10)–(3.11) are reproduced by introducing decay as an imaginary part to the energies in the Heisenberg picture, i.e., substituting $\omega_{a,b}$ by $\omega_{a,b} - i\gamma_{a,b}/2$ and solving directly in a full Hamiltonian picture the operator equations of motion: $dc(t)/dt = i[H, c(t)]$ with $c = a, b$. This method in the manifold picture, in principle incorrect (as we explained in the previous Chapter), provides the right average quantities, such as the correlator $\langle a^\dagger(t)a(t+\tau)\rangle$ and therefore leads also to the correct expression for the SE spectra.

On the other hand, the SS case corresponds to setting the time derivative on the left hand side of Eq. (3.6) to zero, and solving the resulting set of linear equations. The solution

$$
\mathbf{u}^{\rm SS} = \mathbf{M}_0^{-1}\mathbf{p} \tag{3.13}
$$

explicitly yields:

$$n_a^{\mathrm{SS}} = \frac{g^2\Gamma_+(P_a+P_b)+P_a\Gamma_b(\Gamma_+^2+(\frac{\Delta}{2})^2)}{4g^2\Gamma_+^2+\Gamma_a\Gamma_b(\Gamma_+^2+(\frac{\Delta}{2})^2)}\,, \tag{3.14a}$$

$$n_b^{\mathrm{SS}} = \frac{g^2\Gamma_+(P_a+P_b)+P_b\Gamma_a(\Gamma_+^2+(\frac{\Delta}{2})^2)}{4g^2\Gamma_+^2+\Gamma_a\Gamma_b(\Gamma_+^2+(\frac{\Delta}{2})^2)}\,, \tag{3.14b}$$

$$n_{ab}^{\mathrm{SS}} = \frac{\frac{g}{2}(\gamma_a P_b-\gamma_b P_a)(i\Gamma_+-\frac{\Delta}{2})}{4g^2\Gamma_+^2+\Gamma_a\Gamma_b(\Gamma_+^2+(\frac{\Delta}{2})^2)}\,. \tag{3.14c}$$

Both photonic and excitonic reduced density matrices are diagonal. They correspond to thermal distributions of particles with the above mean numbers:

$$\rho^{\mathrm{a}}_{n,p} = \sum_m \rho_{n,m;\,p,m} = \delta_{n,p}\frac{(n_a^{\mathrm{SS}})^n}{(1+n_a^{\mathrm{SS}})^{n+1}}\,, \tag{3.15a}$$

$$\rho^{\mathrm{b}}_{m,q} = \sum_n \rho_{n,m;\,n,q} = \delta_{m,q}\frac{(n_b^{\mathrm{SS}})^m}{(1+n_b^{\mathrm{SS}})^{m+1}}\,. \tag{3.15b}$$

Behind their forbidding appearance, Eqs. (3.14) enjoy a transparent physical meaning, that they inherit from the semi-classical—and therefore intuitive—picture of rate equations. When the coupling strength between the two modes, g, vanishes, the solutions are those of thermal equilibrium for a and b [Eqs. (2.34) and (2.53)]. In the general case where $g \neq 0$, the mean numbers can also be written in the same form:

$$n_a^{\mathrm{SS}} = \frac{P_a^{\mathrm{eff}}}{\gamma_a^{\mathrm{eff}}-P_a^{\mathrm{eff}}}\,, \tag{3.16}$$

(Id. for mode b throughout by exchanging indexes $a \leftrightarrow b$), in terms of effective pump and decay rates:

$$P_a^{\mathrm{eff}} = P_a + \frac{Q_a}{\Gamma_a+\Gamma_b}(P_a+P_b)\,, \tag{3.17a}$$

$$\gamma_a^{\mathrm{eff}} = \gamma_a + \frac{Q_a}{\Gamma_a+\Gamma_b}(\gamma_a+\gamma_b)\,, \tag{3.17b}$$

with Q_a the rate at which mode a exchanges particles with mode b:

$$Q_a = \frac{4(g^{\mathrm{eff}})^2}{\Gamma_b}\,, \tag{3.18}$$

in terms of the effective coupling strength at nonzero detuning:

$$g^{\mathrm{eff}} = \frac{g}{\sqrt{1+\left(\frac{\Delta/2}{\Gamma_+}\right)^2}}\,. \tag{3.19}$$

Q_a is a generalization of the *Purcell rate* $\gamma_a^{\mathrm{P}} = 4g^2/\gamma_b$, which is the rate at which the population $n_a(t)$, [cf. Eq. (3.10)], decays in weak coupling when $\gamma_b, \gamma_a^{\mathrm{P}} \gg \gamma_a$. From the point of view of mode a, the coupling with mode b is both adding particles, contributing to P_a^{eff}, and removing them, contributing to γ_a^{eff}. The total effective decay is:

$$\Gamma_a^{\mathrm{eff}} = \gamma_a^{\mathrm{eff}} - P_a^{\mathrm{eff}} = \Gamma_a + Q_a \tag{3.20}$$

Note that the generalized Purcell rate Q_a appears in the same way in both effective parameters in Eqs. (3.17), due to the "bidirectionality" of the coupling (the coupling both brings in and removes excitations).

The mean value of the coherence can also be expressed in terms of these quantities:

$$n_{ab}^{\mathrm{SS}} = \frac{2g^{\mathrm{eff}}}{\Gamma_a^{\mathrm{eff}} + \Gamma_b^{\mathrm{eff}}} \frac{\gamma_a P_b - \gamma_b P_a}{\Gamma_a \Gamma_b} e^{i\phi} \tag{3.21}$$

where $\phi = \arctan\left(\frac{\Gamma_+}{\Delta/2}\right)$.

The quantities defined in Eqs. (3.17) and Eq. (3.20) are all positive when $\Gamma_b > 0$ ($Q_a > 0$) and all negative when $\Gamma_b < 0$ (if there exists a solution for the steady state). The conditions for the pumping terms P_a, P_b to yield a physical state (a steady state), are therefore those for which the mean values $n_{a,b}^{\mathrm{SS}}$ are positive and finite, implying:

$$\Gamma_+ > 0\,, \tag{3.22a}$$

$$4(g^{\mathrm{eff}})^2 > -\Gamma_a \Gamma_b\,. \tag{3.22b}$$

The first condition requires that pumps P_a, P_b are not *simultaneously* larger than their respective decay rates γ_a, γ_b. The second condition only represents a restriction when one of the effective parameters, either Γ_a or Γ_b, is negative. Then, it reads explicitly $4(g^{\mathrm{eff}})^2 > |\Gamma_a \Gamma_b|$. Note that, out of resonance, the pumping rates appear both in g^{eff} and Γ_a, Γ_b and therefore the explicit range of physical values for them needs to be found self-consistently.

From now on, we shall refer with "SE" and "SS" to the expressions that apply specifically to the spontaneous emission and to the steady state, respectively, leaving free of index those that are of general validity. In some cases, as for instance in Eq. (3.4), no index is required if it is understood that $P_{a/b}$ are defined and equal to zero in the SE case. For that reason, we shall leave Γ free of the SE/SS redundant index.

3.3 First order correlation function and power spectrum

We now turn to the luminescence spectrum of the system $S(\omega)$ given by Eq. (2.82). The equations for the two-time correlator $\langle a^\dagger(t)a(t+\tau)\rangle$ follow from the quantum regression formula. The most general set of correlators we can construct is $\{C_{\{mn\mu\nu\}} = a^{\dagger m}a^n b^{\dagger\mu}b^\nu\}$, which satisfy Eq. (2.101) for any operator Ω_1 through the most general regression matrix for the linear problem given by

$$M_{\substack{mn\mu\nu\\mn\mu\nu}} = i\omega_a(m-n) + i\omega_b(\mu-\nu) - (m+n)\frac{\gamma_a - P_a}{2} - (\mu+\nu)\frac{\gamma_b - P_b}{2}, \quad (3.23a)$$

$$M_{\substack{mn\mu\nu\\m-1,n-1,\mu\nu}} = P_a mn\,, \quad M_{\substack{mn\mu\nu\\mn\mu-1,\nu-1}} = P_b\mu\nu \quad (3.23b)$$

$$M_{\substack{mn\mu\nu\\mn-1,\mu\nu+1}} = -ign\,, \quad M_{\substack{mn\mu\nu\\m+1,n,\mu-1,\nu}} = ig\mu \quad (3.23c)$$

$$M_{\substack{mn\mu\nu\\m-1,n\mu+1,\nu}} = igm\,, \quad M_{\substack{mn\mu\nu\\mn+1,\mu\nu-1}} = -ig\nu\,. \quad (3.23d)$$

However in order to compute $\langle\Omega_1(t)a(t+\tau)\rangle$, we only need the subset of correlators $\{C_{\{0n0\nu\}} = a^n b^\mu\}$, which satisfies Eq. (2.101) with a regression matrix M defined only by

$$M_{\substack{n\nu\\n\nu}} = -i(n\omega_a + \nu\omega_b) - n\frac{\Gamma_a}{2} - \nu\frac{\Gamma_b}{2}\,, \quad (3.24a)$$

$$M_{\substack{n\nu\\n+1,\nu-1}} = M_{\substack{\nu,n\\\nu-1,n+1}} = -ig\nu\,, \quad (3.24b)$$

and zero everywhere else. Furthermore, for the computation of the optical spectrum, it is enough to consider the subset $\{a,b\}$ and $\Omega_1 = a^\dagger$. In Fig. 3.1 we can see a scheme of this finite set of correlators (left) and mean values (right), labelled with the indices $\{\eta\} = \{m,n,\mu,\nu\}$. The coherent (through g) and incoherent (through $P_{a,b}$) links between the various correlators, given by the regression matrix, are shown with arrows (see a detailed explanation of the figure in the caption). This simple graph complicates slightly for two coupled two-level systems, extending no further than the second manifold (see Fig. 4.2 in Chapter 4), but it becomes infinite for the Jaynes-Cummings model (see Fig. 5.11 in Chapter 5).

Thanks to the linearity of the problem, we obtain a simple equation,

$$\frac{\mathbf{v}(t,t+\tau)}{d\tau} = -\mathbf{M}_1\mathbf{v}(t,t+\tau)\,, \quad (3.25)$$

for the two-time correlators

$$\mathbf{v}(t,t+\tau) = \begin{pmatrix}\langle a^\dagger(t)a(t+\tau)\rangle\\ \langle a^\dagger(t)b(t+\tau)\rangle\end{pmatrix} \quad (3.26)$$

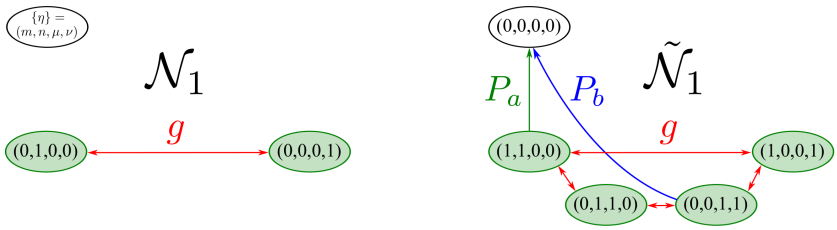

Figure 3.1: Chain of correlators—indexed by $\{\eta\} = (m,n,\mu,\nu)$—linked by the Hamiltonian dynamics with pump and decay for two coupled harmonic oscillators. On the left (resp., right), the set $\mathscr{N}_1$ (resp., $\tilde{\mathscr{N}_1}$) involved in the equations of the two-time (resp., single-time) correlators. In this and similar figures throughout the manuscript (Figs. 4.2 and 5.11), in green is shown the first manifold, the only one needed to compute the spectrum in the linear model. The equation of motion $\langle a^\dagger(t) C_{\{\eta\}}(t+\tau)\rangle$ with $\eta \in \mathscr{N}_1$ requires for its initial value the correlator $\langle C_{\{\tilde{\eta}\}}\rangle$ with $\{\tilde{\eta}\} \in \tilde{\mathscr{N}_1}$ defined from $\{\eta\} = (m,n,\mu,\nu)$ by $\{\tilde{\eta}\} = (m+1,n,\mu,\nu)$, as seen on the diagram. The thick red arrows indicate which elements are linked by the coherent (SC) dynamics, through the coupling strenght g, while the green/blue thin arrows show the connections due to the incoherent cavity/QD pumpings. The sense of the arrows indicates which element is "calling" which in its equations. The self-coupling of each node to itself is not shown. This is where $\omega_{a,b}$ and $\Gamma_{a,b}$ enter. These links are obtained from the rules in Eq. (3.23), that result in the matrices of regression $\mathbf{M}_1$ and $\mathbf{M}_0$. Higher manifolds $\mathscr{N}_k$ and $\tilde{\mathscr{N}_k}$ (not plotted), that include higher order correlators, increase their dimension as $k(k+1)$ and $(k+1)^2$, respectively. A manifold k is only linked directly to $k-1$ in this model. For example, when computing $g^{(2)}$ in Sec. 3.6, only manifolds $\tilde{\mathscr{N}}_{k\leq 2}$ will be involved.

where

$$\mathbf{M}_1 = -\begin{pmatrix} M_{10}^{10} & M_{10}^{01} \\ M_{01}^{10} & M_{01}^{01} \end{pmatrix} = \begin{pmatrix} i\omega_a + \frac{\Gamma_a}{2} & ig \\ ig & i\omega_b + \frac{\Gamma_b}{2} \end{pmatrix}. \tag{3.27}$$

The formal solution follows straightforwardly from $\mathbf{v}(t,t+\tau) = e^{-\mathbf{M}_1\tau}\mathbf{v}(t,t)$. The initial vector $\mathbf{v}(t,t)$ is that of the mean values that we computed in Sec. 3.2 for the SE and SS case. They can also be found through the quantum regression formula, applied on the set of correlators $\tilde{\mathscr{N}_1}$ (see Fig. 3.1) with $\Omega_1 = 1$ and the regression matrix $\mathbf{M}_0$. In terms of these average one-time quantities, the correlator of interest reads explicitly (for positive τ):

$$\begin{aligned}\langle a^\dagger(t)a(t+\tau)\rangle = \frac{1}{2R} e^{-\Gamma_+\tau} e^{-i(\omega_a - \frac{\Delta}{2})\tau} \\ \times \Big\{ e^{iR\tau}[(R + i\Gamma_- - \Delta/2)n_a(t) - g\, n_{ab}(t)] \\ + e^{-iR\tau}[(R - i\Gamma_- + \Delta/2)n_a(t) + g\, n_{ab}(t)] \Big\}\end{aligned} \tag{3.28}$$

in terms of the complex (half) Rabi frequency that we defined in Eq. (3.12). Out of resonance, the Rabi frequency is a complex number with both nonzero real,

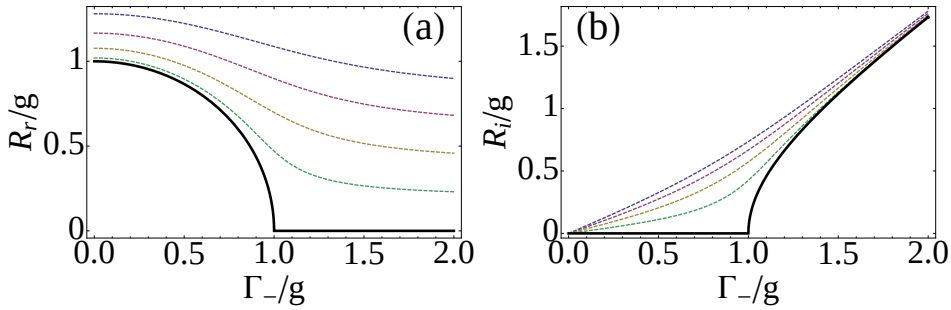

Figure 3.2: Complex Rabi R/g, separated in its real (a) and imaginary (b) parts, as a function of the decoherence parameter Γ_-/g for various detunings (Δ/g from -1.6, up, to 0, bottom, by steps of 0.4). Solid black lines correspond to resonance.

$R = R_\mathrm{r}$, and imaginary, R_i, parts. The absolute value of these frequencies can be written as:

$$|R_{\mathrm{r,i}}| = \frac{1}{\sqrt{2}}\sqrt{|R|^2 \pm (g^2 - \Gamma_-^2 + \frac{\Delta^2}{4})}\,. \tag{3.29}$$

For parameters Γ_- and g which result in SC at resonance ($g > |\Gamma_-|$), this can be further simplified into

$$|R_{\mathrm{r,i}}| = \frac{|R|}{\sqrt{2}}\sqrt{1 \pm \sqrt{1 - \left(\frac{\Gamma_-\Delta}{|R|^2}\right)^2}}\,. \tag{3.30}$$

At resonance, R is either pure imaginary (in the WC regime), either pure real (in the SC one). For this latter case, it is worth defining a new quantity:

$$R_0 = R(\Delta = 0) = \sqrt{g^2 - \Gamma_-^2}\,. \tag{3.31}$$

The real and imaginary parts of R are plotted in Fig. 3.2 as a function of Γ_-/g for various negative detunings. The invariance of R under exchange of indexes $a \leftrightarrow b$ results in the property $R(-\Delta,\Gamma_-) = R(\Delta,-\Gamma_-) = R^*(\Delta,\Gamma_-)$. From this follows the results of R_r and R_i for the combinations of $\Delta \neq 0$ and Γ_- that are not plotted in the figure:

$$R_\mathrm{r}(-\Delta,\Gamma_-) = R_\mathrm{r}(\Delta,-\Gamma_-) = R_\mathrm{r}(-\Delta,-\Gamma_-) = R_\mathrm{r}(\Delta,\Gamma_-)\,, \tag{3.32a}$$

$$R_\mathrm{i}(-\Delta,\Gamma_-) = R_\mathrm{i}(\Delta,-\Gamma_-) = -R_\mathrm{i}(-\Delta,-\Gamma_-) = -R_\mathrm{i}(\Delta,\Gamma_-)\,. \tag{3.32b}$$

In the limit of high detuning, $|\Delta| \gg g$, $|\Gamma_-|$, regardless of WC or SC, the real part becomes independent of the dissipation (decay and pumping), $R_\mathrm{r} \approx |\Delta|/2$, and the imaginary part becomes $R_\mathrm{i} \approx \mp\Gamma_-$. We can see in Fig. 3.2 that this sets an upper bound for R_i:

$$|R_\mathrm{i}| < |\Gamma_-| \tag{3.33}$$

Once again, for the steady state case, we can obtain a range of physical combinations of pumping intensities, P_a, P_b, by ensuring that the correlator of Eq. (3.28) converges to zero when $\tau \to \infty$. Here, the condition follows from having a positive total decay rate:

$$\Gamma_+ - |R_\mathrm{i}| \quad > \quad 0\,. \tag{3.34}$$

The first consequence of this condition is simply that Γ_+ must be positive, as we already found with the analysis of the mean values and wrote in Eq. (3.22a). With $\Gamma_+ > 0$, the other decay rate appearing in Eq. (3.28) is automatically fulfilled ($\Gamma_+ + |R_\mathrm{i}| > 0$). On the one hand, if Γ_a, $\Gamma_b > 0$, Eq. (3.34) is always true, as we know that $|R_\mathrm{i}| < |\Gamma_-| < \Gamma_+$ [from Eq. (3.33)]. This includes the spontaneous emission case where there is no restriction in the parameters. On the other hand, if either Γ_a or Γ_b is negative, Eq. (3.34) represents a further limitation for the pumping parameters. One can check that it is again exactly equivalent to the condition we already found in Eq. (3.22b). Therefore, the condition that the correlators are well behaved are exactly the same as those that the populations are positive and a physical steady state exists.

Using the result of Eq. (3.28) into the definition of Eq. (2.85), we obtain the formal structure of the emission spectrum:

$$S(\omega) = \frac{1}{2}(\mathscr{L}^1 + \mathscr{L}^2) - \Im\{W\}(\mathscr{L}^1 - \mathscr{L}^2) - \Re\{W\}(\mathscr{A}^1 - \mathscr{A}^2) \tag{3.35}$$

with $\mathscr{L}(\omega)$ and $\mathscr{A}(\omega)$ some Lorentzian and dispersive functions whose features (position and broadening) are entirely specified by the complex Rabi frequency [Eq. (3.12)], Γ_+ [Eq. (3.5)] and the detuning Δ:

$$\mathscr{L}^{1,2}(\omega) = \frac{1}{\pi}\frac{\Gamma_+ \pm R_\mathrm{i}}{(\Gamma_+ \pm R_\mathrm{i})^2 + (\omega - (\omega_a - \frac{\Delta}{2} \mp R_\mathrm{r}))^2}\,, \tag{3.36a}$$

$$\mathscr{A}^{1,2}(\omega) = \frac{1}{\pi}\frac{\omega - (\omega_a - \frac{\Delta}{2} \mp R_\mathrm{r})}{(\Gamma_+ \pm R_\mathrm{i})^2 + (\omega - (\omega_a - \frac{\Delta}{2} \mp R_\mathrm{r}))^2}\,. \tag{3.36b}$$

We also introduced the weight W, a complex coefficient given by

$$W = \frac{\Gamma_- + i(\frac{\Delta}{2} + gD)}{2R}\,, \tag{3.37}$$

that we define in terms of still another parameter, D:

$$D = \frac{\displaystyle\int_0^\infty \langle a^\dagger b\rangle(t)\,dt}{\displaystyle\int_0^\infty \langle a^\dagger a\rangle(t)\,dt}\,. \tag{3.38}$$

Written in this form, Eqs. (3.35)–(3.38) assume a transparent physical meaning with a clear origin for each term. The spectrum consists of two peaks (that we label 1 and 2), as is well known qualitatively for the SC regime. These are composed of a Lorentzian $\mathscr{L}$ and a dispersive $\mathscr{A}$ part. We already introduced the Lorentzian as the fundamental lineshape for a system with a lifetime, and in the expression above, it inherits most of how the dissipation gets distributed in the coupled system, including the so-called *subnatural linewidth averaging* that sees the broadening at resonance below the cavity mode width, as pointed out by Carmichael et al. (1989). The dispersive part originates from the coupling as in the Lorentz (driven) oscillator. In our system, it stems from the driving of one mode by the other, because of the coupling. This decomposition of each peak in such terms is therefore entirely clear and expected. More quantitatively, the first peak, (e.g.,) is placed at $\omega_a - \frac{\Delta}{2} - R_\mathrm{r}$ and has Half-Width at Half Maximum (HWHM) of $\Gamma_+ + R_\mathrm{i}$. As $R_\mathrm{r} > 0$, this peak corresponds to the lower branch "L". The limit of bare modes at energies ω_a and $\omega_b = \omega_a - \Delta$ broadened with the bare parameters $\Gamma_{a/b}$ (FWHM), is recovered at large detunings. The bare cavity mode will be taken as a reference for the energy scales in the rest of the text (we set $\omega_a = 0$). Again, we find that the real (resp. imaginary) part of the complex Rabi frequency, R_r (R_i), contributes to the oscillations (damping) in the correlator and therefore, to the positions (broadenings) in the spectrum.

The normalized first order correlation function can also be written in terms of the new parameters, from Eq. (3.28), as:

$$g^{(1)}(t,t+\tau) = e^{-\Gamma_+\tau} e^{-i(\omega_a - \frac{\Delta}{2})\tau} \left[e^{iR\tau}(\frac{1}{2} + iW) + e^{-iR\tau}(\frac{1}{2} - iW) \right]. \qquad (3.39)$$

So far, all the results hold for both cases of SE and SS. This shows that the qualitative depiction of SC is robust. This made it possible to pursue it in a given experimental system with the parameters of the theoretical models fit for another. This has indeed been the situation with semiconductor results explained in terms of the formalism built for atomic systems.

To be complete, the solution now only requires the boundary conditions that are given by the quantum state of the system. They will affect the parameter D, Eq. (3.38), that is therefore the bridging parameter between the two cases. In the next two sections, we address the two cases and their specificities.

3.3.1 Spontaneous Emission

In the case of Spontaneous Emission, where the system decays from an initial state, the boundary conditions are supplied for $\tau = 0$ by the initial values $\mathbf{v}(t,t)$, i.e., the cavity population, $n_a(t) = \langle a^\dagger a \rangle(t)$ and the coherence element $n_{ab}(t) = \langle a^\dagger b \rangle(t)$. In turn, those are completely defined by the initial conditions, Eqs. (3.8).

Although the analytical expression for these mean values as a function of time are cumbersome [cf. Eqs. (3.10)-(3.11)] the D coefficient, Eq. (3.38), that determines quantitatively the lineshape, assumes a (relatively) simpler expression:

$$D^{\mathrm{SE}} = \frac{[\frac{g}{2}(\gamma_a n_b^0 - \gamma_b n_a^0) - 2in_{ab}^0(\gamma_+^2 - \gamma_-^2)](i\gamma_+ - \frac{\Delta}{2}) + 2g^2\gamma_+ \Re n_{ab}^0}{g^2\gamma_+(n_a^0 + n_b^0) + n_a^0\gamma_b(\gamma_+^2 + (\frac{\Delta}{2})^2) + g\gamma_b(\frac{\Delta}{2}\Re n_{ab}^0 + \gamma_+ \Im n_{ab}^0)}\,. \tag{3.40}$$

To prepare the analogy with the SS case in the next section, we also write the particular case when $n_{ab}^0 = 0$:

$$D^{\mathrm{SE}} = \frac{\frac{g}{2}(\gamma_a n_b^0 - \gamma_b n_a^0)(i\gamma_+ - \frac{\Delta}{2})}{g^2\gamma_+(n_a^0 + n_b^0) + n_a^0\gamma_b(\gamma_+^2 + (\frac{\Delta}{2})^2)}\,. \tag{3.41}$$

This is an important case as it is realized whenever the initial population of one of the modes is zero, which is the typical experimental situation. Note that in this case, D^{SE}, and therefore also the normalized spectra, does not depend on the two populations independently but on their ratio only:

$$\alpha = \frac{n_a^0}{n_b^0}\,. \tag{3.42}$$

3.3.2 Steady State under continuous incoherent pumping

In the case where the system is excited by a continuous, incoherent pumping, a steady state is reached and the boundary conditions are given by the stationary limit, as time tends to infinity, of the dynamical equation (whose solution is unique). The D parameter, Eq. (3.38), is defined in this case as:

$$D^{\mathrm{SS}} = \frac{n_{ab}^{\mathrm{SS}}}{n_a^{\mathrm{SS}}} = \frac{\frac{g}{2}(\gamma_a P_b - \gamma_b P_a)(i\Gamma_+ - \frac{\Delta}{2})}{g^2\Gamma_+(P_a + P_b) + P_a\Gamma_b(\Gamma_+^2 + (\frac{\Delta}{2})^2)}\,. \tag{3.43}$$

There is a clear analogy between Eq. (3.43)—that corresponds to the SS—and Eq. (3.41)—that corresponds to SE when $n_{ab}^0 = 0$. In this case, the spectrum can also be written in terms of the ratio, counterpart of Eq. (3.42),

$$\alpha = \frac{P_a}{P_b}\,, \tag{3.44}$$

in which case Eqs. (3.41) and (3.43) assume the same expression, keeping in mind the definition of Eqs. (3.4). Table 3.1 displays this common expression of D in terms of α. The limiting cases when $\alpha \to 0$ or ∞ are also given. They correspond to only photons or excitons as the initial state for the SE, or to the presence of only one kind of incoherent pumping for the SS case.

The analogy and differences between D^{SE} and D^{SS} reflect in the spectra S^{SE} and S^{SS}. For the same α, they become identical when the pumping rates are negligible as compared to the decays, $P_{a,b} \ll \gamma_{a,b}$. In this case, where $\Gamma_{\pm,a,b} \approx \gamma_{\pm,a,b}$, the SS system indeed behaves like that of the SE of particles that decay independently and that are, at each emission, either a photon or an exciton, with probabilities in the ratio α.

However, in the most general case, D^{SS} depends on more parameters than D^{SE}. Moreover, the pumping rates $P_{a,b}$ affect S^{SS} not only through α and D^{SS}, but also in the position and broadening of the peaks (given by $\Gamma_{\pm}$ and R). Therefore, the SS is a more general case, from which the SE with $n^0_{ab} = 0$ can be obtained, but not the other way around. On the other hand, as seen in Table 3.1, the SS case cannot recover the SE case when $n^0_{ab} \neq 0$. Further similarities could be found if cross Lindblad pumping terms like those in Eq. (2.80) were introduced in Eq. (3.3) with parameters P_{ab} in analogy to the cross initial mean value n^0_{ab}, but this describes a different system where polaritons can also be directly excited. In the present one, none of the SE and SS cases comprises all the possibilities of the other.

Anyhow, an important fact for the semiconductor community is that a SS with non-vanishing pumping rates is out of reach of the SE of any initial state, which has been the case studied by Carmichael et al. (1989) and Andreani et al. (1999), and that even in this limiting case, the effective quantum state obtained in the SS should still be resolved self-consistently, rather than assuming for α the particular case 0 or ∞.

$\alpha = \dfrac{n^0_a}{n^0_b} = \dfrac{P_a}{P_b}$	D
0	$\dfrac{-\frac{g}{2}(i\Gamma_+ - \frac{\Delta}{2})\gamma_b}{g^2\Gamma_+ + \Gamma_b(\Gamma_+^2 + (\frac{\Delta}{2})^2))}$
$0 < \alpha < \infty$	$\dfrac{\frac{g}{2}(i\Gamma_+ - \frac{\Delta}{2})(\gamma_a - \gamma_b\alpha)}{g^2\Gamma_+(1+\alpha) + \alpha\Gamma_b(\Gamma_+^2 + (\frac{\Delta}{2})^2))}$
∞	$\dfrac{(i\Gamma_+ - \frac{\Delta}{2})\gamma_a}{2g\Gamma_+}$

Table 3.1: Expression of D, Eq. (3.38), as a function of α, Eqs. (3.42) and (3.44), in the SE (with $\Gamma_{\pm,a,b} \to \gamma_{\pm,a,b}$ and $n^0_{ab} = 0$) and SS cases. D embodies in the luminescence spectrum the influence of the quantum state of the system. The latter is specified by the initial condition in SE, or the pumping/decay interplay in the SS.

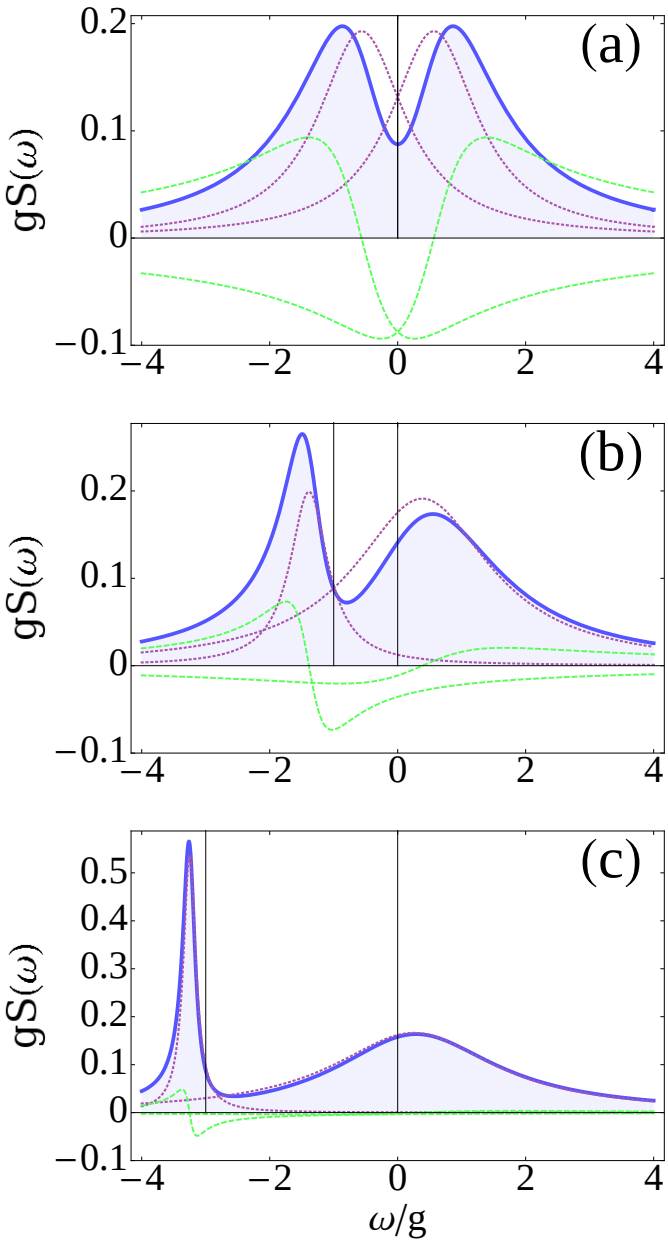

Figure 3.3: Strong coupling SS spectra (blue solid line) and their decomposition into Lorentzian (dotted purple) and dispersive parts (dashed green) for various detunings ($\Delta/g = 0, 1, 3$) with parameters of point (c) of Fig. 3.8: $\gamma_a = 3.8g$, $\gamma_b = 0.1g$, $P_a = 0.5g$, $P_b = 0.1g$. The vertical black lines mark the positions of the bare modes (cavity at $\omega_a = 0$ and exciton at $\omega_b = -\Delta$), showing the "level repulsion" of SC.

3.3.3 Discussion

With this exposition of the analytical expressions of the luminescence spectra, and the discussion of their similarity and distinctions that we have just given, the coverage of the problem is complete. For instance, Fig. 3.3 shows the SS spectra and their mathematical decompositions into Lorentzian and dispersive parts, as detuning is varied. Figs. (b) and (c) are obtained using Eq. (3.35–3.38), and in this particular case, the expression (3.43) for D. In order to give a more physical picture of these abstract results, we shall in the rest of this Chapter illustrate their implications in practical terms. For this purpose, we will now concentrate on the resonant case, which is the pillar of the SC physics. The main output of the out-of-resonance case is to help identify or to characterize the resonance, for instance by localizing it in an anticrossing or by providing useful additional constrains with only one more free parameter in a global fitting. Even a slight detuning brings features of WC into the SC system and ultimately, when $|\Delta| \gg g$, the complex Rabi frequency converges into the same expression for both regimes (as showed in Fig. 3.2). This is why we now consider the SC problem in its purest form: when the coupling between the modes is optimum.

3.4 Strong and Weak Coupling at resonance

Strong coupling is most marked at resonance, and this is where its signature is experimentally ascertained, in the form of an anticrossing. Fundamentally, there is another reason why resonance stands out as predominant; this is where a criterion for SC can be defined unambiguously in presence of dissipation:

WC and SC are formally defined as the regime where the complex Rabi frequency at resonance, Eq. (3.31), is pure imaginary (WC) or real (SC).

This definition, that takes into account dissipation and pumping, generalizes the classification found in the literature. The reason for this definition is mainly to be found in the behavior of the time autocorrelator, Eq. (3.28), that is respectively damped or oscillatory as a result. The exponential damping is the usual manifestation of dissipation, that decays the correlations in the field, even when a steady state is maintained. On the other hand, in the same situation of steady averages (no dynamics) but now in SC, oscillations with τ are the mark of a coherent exchange between the bare fields (the photon field and exciton field).

In the literature, one sometimes encounters the confusion that SC is linked to a periodic transfer of energy or of population between the photon and exciton field, or that it follows from a chain of emissions and absorptions. This is an in-

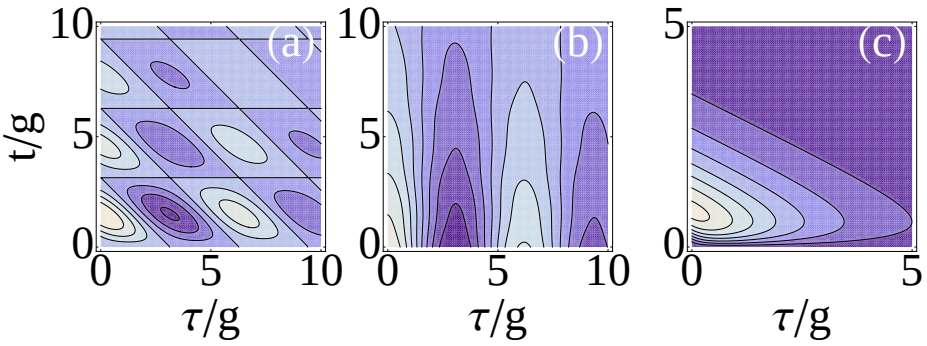

Figure 3.4: Time dynamics of the correlator $\Re\langle a^\dagger(t)a(t+\tau)\rangle^{\mathrm{SE}}$, cf. Eq. (3.28). Only the pattern of oscillations is of interest here (lighter blues correspond to higher values). In all cases, both the t and τ dynamics tend to zero. Figures (a) and (b) show the SE of an exciton and of an upper polariton, respectively, in a very strongly coupled system ($\gamma_a = 0.2g$ and $\gamma_b = 0.1g$). Fig. (c) shows the SE of an exciton in weak coupling ($\gamma_a = 5.9g$). The oscillations in τ, rather than in t, are the mark of SC.

correct general association as one can explicit cases with apparent oscillations of populations that correspond to weak coupling, or on the contrary, cases with no oscillations of populations that are in SC. The two concepts are therefore unrelated in the sense that none implies the other. This is illustrated for the SE case in Figs. 3.4(a), 3.4(b) and 3.5 on the one hand, where the system is in SC, and in Fig. 3.4(c) and 3.6 on the other hand, where it is in WC. In SS, there is no t dynamics in any case, so oscillations of populations are clearly unrelated to weak or strong coupling. In SE, the distinction is clearly seen in Fig. 3.4 where both the t and τ dynamics are shown in a contour-plot in the case where the system is initially prepared as an exciton, (a) and (c), or as a polariton, (b). In the polariton case, the dynamics in t is simply decaying (because of the lifetime), while it is clearly oscillating in τ, were the proper manifestation of SC is to be found. The t decay is not exactly exponential because in the presence of dissipation, the polariton is not anymore an ideal eigenstate (the larger the dissipation, the more the departure). However this effect in SC is so small that it only consists in a small "wobbling" of the τ contour lines. On the other hand, the exciton, (a), that is not an eigenstate, features oscillations both in the t dynamics (the one often but unduly regarded as the signature of SC), as well as the τ dynamics. In stark contrast, the exciton in WC, (c), bounces with t. This, that might appear as an oscillation, is not, as it happens only once and is damped in the long-time values. This behavior is shown quantitatively in Fig. 3.5 for SC and Fig. 3.6 for WC, where the population $n_a(t)$ is displayed for the SE of an exciton (blue solid), a photon (purple dashed) and an upper polariton (brown dotted), respectively, along with the luminescence spectrum that they produce (detected in the cavity emission). Here

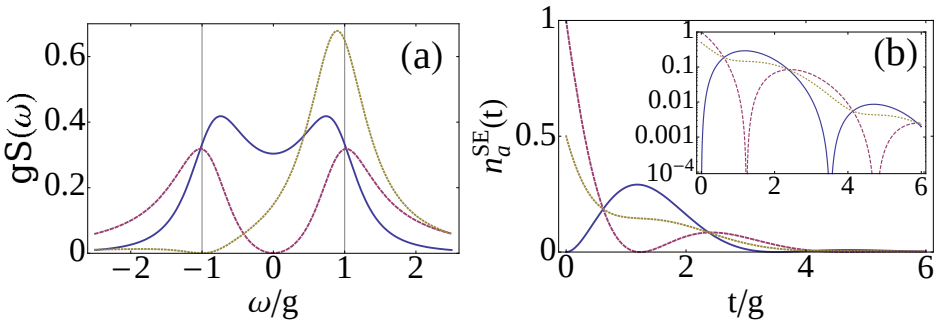

Figure 3.5: (a) SC spectra $S_0^{\mathrm{SE}}(\omega)$ and (b) its corresponding mean number dynamics $n_a^{\mathrm{SE}}(t)$ for the SE of three different initial states: In blue solid, one exciton; in purple dashed, one photon and in brown dotted, one upper polariton. Parameters are $\gamma_a = 1.9g$ and $\gamma_b = 0.1g$. Inset of (b) is the same in log-scale.

it is better seen how, for instance, the polariton-decay is wobbling as a result of the dissipation, that perturbs its eigenstate-character and leaks some population to the lower polariton. More importantly, note how very different the spectra are, depending on whether the initial state is a photon or an exciton, despite the fact that the dynamics is similar in both cases (see the inset in log-scale of their respective populations). The PL spectrum observed in the cavity emission is much better resolved when the system is initially in a photon state, than it is when the system is initially in an exciton state. The splitting is larger and the overlap of the peaks smaller in the former case. This will find an important counterpart in the SS case. In Fig. 3.6, the corresponding case of WC is shown for clarity, with a decay of populations and possible oscillations.

Figure 3.7 shows the τ dynamics in the SS (when the t dynamics has converged and is steady), for five cases of interest to be discussed later (in Fig. 3.8). A first look at the dynamics would seem to gather together a group of two curves that decay exponentially to good approximation (and remain positive as a result), and another group of three that assume a local minimum. The correct classification is the most counter-intuitive in this regard, as it puts together the dashed lines on the one hand and the solid on the other, i.e., scrambling them together. The mathematical reason for this classification is revealed in the inset, where the same dynamics is plotted in log-scale. The dashed (resp. solid) lines correspond to parameters where the system is in WC (resp. SC) according to the definition, i.e., to values of R that are imaginary on the one hand and real on the other. In log-scale, this corresponds respectively to a damping of the correlator, against oscillations with an infinite number of local minima. Note that the blue dashed line features one local minimum, which does not correspond to an oscillatory—or coherent-exchange—behavior of the fields, but rather to a jolt in the damping.

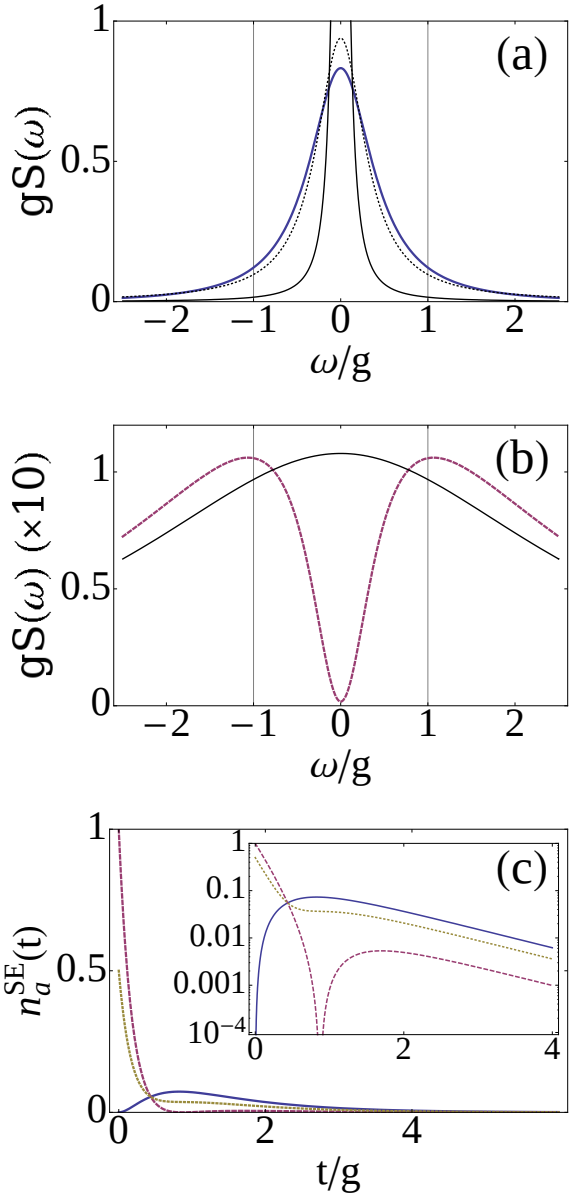

Figure 3.6: (a)-(b) Weak-coupling spectra $S_0^{\mathrm{SE}}(\omega)$ and (c) its corresponding mean number dynamics $n_a^{\mathrm{SE}}(t)$ for the SE of an exciton (a) and a photon (b) as the initial condition. In all figures, solid blue corresponds to the decay of an exciton; dashed purple to the decay of a photon and dotted brown to the decay of an upper polariton. For comparison, we plotted in (a) and (b), with solid black lines, the very different bare emission ($g = 0$) of an exciton and photon respectively. Also in (a), in dashed black, that of an exciton decaying with the Purcell rate $\gamma_b^{\mathrm{P}} = 4g^2/\gamma_a$. Parameters are $\gamma_a = 1.9g$ and $\gamma_b = 0.1g$. Inset of (c) is the same in log-scale.

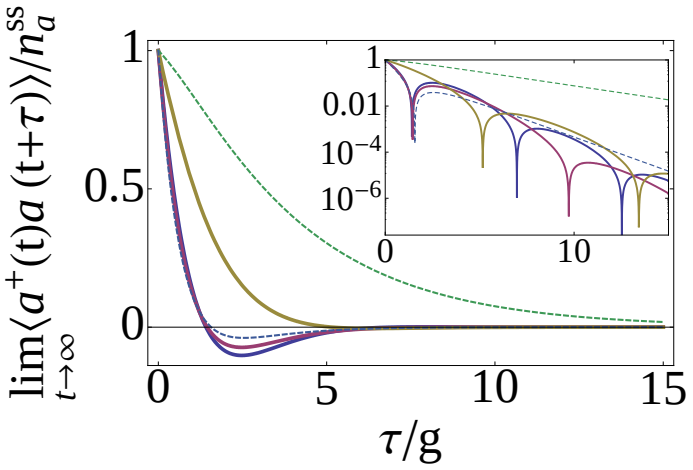

Figure 3.7: Dynamics of $\lim_{t\to\infty}\langle a^\dagger(t)a(t+\tau)\rangle/n_a^{\rm SS}$, Eq. (3.28) and (3.14a), for the SS corresponding to the points (a)–(e) in Fig. 3.8. In inset, the same in log-scale. Solid lines (b, blue; c, purple and d, brown) of SC feature oscillations of the correlator, as the mark of SC. Dashed lines (a, green and e, blue) correspond to WC. Note that although the blue dashed line (e) appears to be similar to other SC lines, it does not oscillate in the log-scale, where it only features a single local minimum. In the same way, the brown line (d) that seems not to oscillate actually features an infinite set of local minima, as is revealed in the log scale.

These considerations that may appear abstract at this level will later turn out to show up as the actual emergence of split (dressed) states or not in the emitted spectrum.

We now return to the general (SE/SS) expression for the spectra, Eq. (3.35), that, at resonance in SC, simplifies to:

$$S_0(\omega)=\frac{1}{2}(\mathscr{L}_{\rm s}^1+\mathscr{L}_{\rm s}^2)-\frac{g\Re\{D_0\}}{2R_0}(\mathscr{L}_{\rm s}^1-\mathscr{L}_{\rm s}^2)+\frac{g\Im\{D_0\}-\Gamma_-}{2R_0}(\mathscr{A}_{\rm s}^1-\mathscr{A}_{\rm s}^1) \tag{3.45}$$

where we used the definition for the (half) Rabi frequency at resonance, Eq. (3.31), and

$$\mathscr{L}_{\rm s}^{1,2}(\omega)=\frac{1}{\pi}\frac{\Gamma_+}{\Gamma_+^2+(\omega\pm R_0)^2}\,, \tag{3.46a}$$

$$\mathscr{A}_{\rm s}^{1,2}(\omega)=\frac{1}{\pi}\frac{\omega\pm R_0}{\Gamma_+^2+(\omega\pm R_0)^2}\,. \tag{3.46b}$$

In the weak coupling regime, with R_0 pure imaginary ($g<|\Gamma_-|$), the positions of the two peaks collapse onto the center, $\omega_a=\omega_b=0$. Defining $iR_{\rm w}=R_0$, with

$R_{\rm w} = \sqrt{\Gamma_-^2 - g^2}$ a real number, the general expression for the spectra rewrites as:

$$\begin{aligned} S_0^{\rm w}(\omega) = &\left(\frac{1}{2} + \frac{\Gamma_- - g\Im\{D_0\}}{2R_{\rm w}}\right)\mathscr{L}_{\rm w}^1 \\ &+ \left(\frac{1}{2} - \frac{\Gamma_- - g\Im\{D_0\}}{2R_{\rm w}}\right)\mathscr{L}_{\rm w}^2 \\ &- \frac{g\Re\{D_0\}}{2R_{\rm w}}(\mathscr{A}_{\rm w}^1 - \mathscr{A}_{\rm w}^2)\,, \end{aligned} \tag{3.47}$$

with the Lorentzian and dispersive contributions now given by:

$$\mathscr{L}_{\rm w}^{1,2}(\omega) = \frac{1}{\pi}\frac{\Gamma_+ \pm R_{\rm w}}{(\Gamma_+ \pm R_{\rm w})^2 + \omega^2} \tag{3.48a}$$

$$\mathscr{A}_{\rm w}^{1,2}(\omega) = \frac{1}{\pi}\frac{\omega}{(\Gamma_+ \pm R_{\rm w})^2 + \omega^2}\,. \tag{3.48b}$$

Before addressing the specifics of the SE and SS cases, it is important to note that, at resonance, the Lorentzian and dispersive parts [Eqs. (3.46) and (3.48)] are invariant under the exchange of indexes $a \leftrightarrow b$. Therefore, the photon and the exciton spectrum are composed of the same lineshapes differing in the prefactor that weights them in Eq. (3.45).

3.4.1 Spontaneous Emission

In the most general case of SE, the $D^{\rm SE}$ coefficient at resonance, $D_0^{\rm SE}$, is a complex number. If the initial condition further fulfils $\Re n_{ab}^0 = 0$, it becomes pure imaginary. Usually [see the work by Carmichael et al. (1989), Andreani et al. (1999)], the initial states considered are independent states of photons or excitons (not a quantum superposition), where indeed $n_{ab}^0 = 0$. In these cases,

$$D_0^{\rm SE} = i\frac{\frac{g}{2}(\gamma_a n_b^0 - \gamma_b n_a^0)}{g^2(n_a^0 + n_b^0) + n_a^0\gamma_b\gamma_+}\,, \tag{3.49}$$

which yields the following expression for the spectrum:

$$S_0^{\rm SE}(\omega) = \frac{1}{\pi}\frac{\frac{\gamma_a+\gamma_b}{2}(g^2 + \frac{\gamma_a\gamma_b}{4})(g^2 n_b^0 + \frac{n_a^0\gamma_b^2}{4} + n_a^0)}{\left(\omega^4 + \omega^2(\frac{\gamma_a^2+\gamma_b^2}{4} - 2g^2) + (g^2 + \frac{\gamma_a\gamma_b}{4})^2\right)\left(g^2(n_a^0 + n_b^0) + n_a^0\gamma_b\frac{\gamma_a+\gamma_b}{4}\right)}\,. \tag{3.50}$$

The SE spectrum of exciton observed in the leaky modes is obtained from Eq. (3.50) by exchanging the indexes $a \leftrightarrow b$. We illustrate this with the two particular cases that follow.

The typical detection geometry for the spontaneous emission of an atom in a cavity consists in having the atom in its excited state as the initial condition, and observing its direct emission spectrum. In this case the role of the cavity is merely to affect the dynamics of its relaxation, that is oscillatory with the light-field in the case of SC. This case corresponds to $n_b^0 = 1$ and $n_a^0 = n_{ab}^0 = 0$ in Eq. (3.50) with $a \leftrightarrow b$. This gives:

$$S_0^{\mathrm{SE}}(\omega) = \frac{1}{\pi} \frac{\frac{\gamma_a+\gamma_b}{2}(g^2 + \frac{\gamma_a\gamma_b}{4})(\frac{\gamma_a^2}{4} + \omega^2)}{\omega^4 + \omega^2(\frac{\gamma_a^2+\gamma_b^2}{4} - 2g^2) + (g^2 + \gamma_a\frac{\gamma_a+\gamma_b}{4})(g^2 + \frac{\gamma_a\gamma_b}{4})^2}\,. \tag{3.51}$$

In the semiconductor case, one would typically still have in mind the excited state of the exciton as the initial condition, but this time, this is the cavity emission that is probed. The initial condition is therefore the same as before but without interchanging a and b in Eq. (3.50), which reads in this case:

$$S_0^{\mathrm{SE}}(\omega) = \frac{1}{\pi} \frac{2(\gamma_a+\gamma_b)(4g^2 + \gamma_a\gamma_b)}{16\omega^4 - 4\omega^2(8g^2 - \gamma_a^2 - \gamma_b^2) + (4g^2 + \gamma_a\gamma_b)^2}\,. \tag{3.52}$$

The difference in the lineshape due to the initial quantum state is seen in Fig. 3.5. The visibility of the line-splitting is much reduced in the case of an exciton in SC which SE is detected through the cavity emission, than in the case of a photon. With a polariton as an initial state, only one line is produced.

Again, by symmetry, interchanging $a \leftrightarrow b$ in Eqs. (3.51) and (3.52), correspond to the SE of the system prepared as a photon at the initial time and detected in, respectively, the cavity emission on the one hand (Eq. (3.51), $a \leftrightarrow b$), and in the leaky mode emission on the other hand [Eq. (3.52)]. In the latter case, the spectrum is invariant under the exchange $a \leftrightarrow b$. Fig. 3.5 also hints to the changes brought by the detection channel (direct emission of the exciton or through the cavity mode).

If $n_a^0 = 0$ or $n_b^0 = 0$ (in which case $n_{ab}^0 = 0$), the normalized spectra do not depend on the nonzero value n_b^0 or n_a^0. That is, one cannot distinguish in the lineshape, the decay of one exciton from that of two, or more. In the more general case, when $n_{ab}^0 \neq 0$, the peaks can be differently weighted. For instance, starting with an upper polariton $|\mathrm{U}\rangle = (|1,0\rangle + |0,1\rangle)/\sqrt{2}$ ($n_a^0 = n_b^0 = n_{ab}^0 = 1/2$) gives rise to a dominant upper-polariton peak (labelled 2 in the above equations, as seen in the brown dotted line in Fig. 3.5). One can classify the possible lineshapes obtained for various initial states. For instance, as we have just mentioned, the normalized spectrum of $|0,n\rangle$ as an initial state, is the same whatever the nonzero n, which is not unexpected from a linear model. From the previous statement, the same spectrum is also obtained for a coherent state or a thermal state of photons, or indeed any quantum state, as long as the exciton population remains zero. In

the same way, the PL spectrum of the product of coherent states in the photon and exciton fields, $|z\rangle\,|z'\rangle$ with $z = z' \in \mathbb{C}^*$, is the same as that of a polariton state $|\mathrm{U}\rangle$, although both are very different in character: a classical state on the one hand and a maximally entangled quantum state on the other.

3.4.2 Steady State under continuous incoherent pumping

In the SS, at resonance, D_0^{SS} is pure imaginary:

$$D_0^{\mathrm{SS}} = i\frac{\frac{g}{2}(\gamma_a P_b - \gamma_b P_a)}{g^2(P_a+P_b)+P_a\Gamma_b\Gamma_+}\,, \tag{3.53}$$

and the term that consists in the difference of Lorentzians in Eq. (3.35) disappears: $\Im\{W\} = 0$. As a result, the two peaks are equally weighted for any combination of parameters:

$$S_0^{\mathrm{SS}}(\omega) = \frac{1}{2}(\mathscr{L}_{\mathrm{s}}^1 + \mathscr{L}_{\mathrm{s}}^2) + \frac{g\Im\{D_0^{\mathrm{SS}}\} - \Gamma_-}{2R_0}(\mathscr{A}_{\mathrm{s}}^1 - \mathscr{A}_{\mathrm{s}}^2)\,. \tag{3.54}$$

The only way to weight more one of the peaks than the other in the SS of an incoherent pumping, would be to pump directly the polariton (dressed) states, as is the case in higher-dimensional systems were polaritons states with nonzero momentum relax into the ground state or in 0D case when cross pumping is considered. In our present model, however, such terms are excluded. The two peaks of the Rabi doublet, composed of a Lorentzian and a dispersive part, are both symmetric with respect to $\omega_a = \omega_b = 0$. Only if $\Im\{D_0^{\mathrm{SS}}\} = \Gamma_-/g$, the spectrum of Eq. (3.54) consists exclusively of two Lorentzians. The parameters that correspond to this case are those fulfilling either $g^2 = \frac{P_a}{P_b - P_a}\Gamma_b\Gamma_-$ or $\Gamma_+ = 0$. The second case corresponds to the limiting case of diverging populations, where the SC becomes arbitrarily good. Note that this spectra, composed of Lorentzians only, is the same in the exciton or photon channel of emission due to the invariance under the exchange $a \leftrightarrow b$. In the most general case, the dispersive part will contribute to the fine quantitative structure of the spectrum, bringing closer or further apart the maxima and thus altering the apparent magnitude of the Rabi splitting. In some extreme cases, as we shall discuss, it even contrives to blur the resolution of the two peaks and a single peak results, even though the modes split in energy. As for the weak coupling formula, it simplifies to:

$$\begin{aligned} S_0^{\mathrm{w}}(\omega) = &\left(\frac{1}{2} + \frac{\Gamma_- - g\Im\{D_0\}}{2R_{\mathrm{w}}}\right)\mathscr{L}_{\mathrm{w}}^1 \\ &+ \left(\frac{1}{2} - \frac{\Gamma_- - g\Im\{D_0\}}{2R_{\mathrm{w}}}\right)\mathscr{L}_{\mathrm{w}}^2\,, \end{aligned} \tag{3.55}$$

losing completely the dispersive contribution. Both decompositions, Eqs. (3.54) and (3.55), have been given to spell-out the structure of the spectra in both regimes. The unified expression that covers them both reads explicitly:

$$S_0^{\mathrm{SS}}(\omega) = \frac{1}{\pi n_a^{\mathrm{SS}}} \frac{8g^2 P_b + 2P_a(4\omega^2 + \Gamma_b^2)}{16\omega^4 - 4\omega^2(8g^2 - \Gamma_a^2 - \Gamma_b^2) + (4g^2 + \Gamma_a\Gamma_b)^2}\,. \tag{3.56}$$

It is the counterpart for SS of Eq. (3.50), for SE. The case of excitonic emission can also be obtained, as for SE, exchanging the indexes $a \leftrightarrow b$.

3.4.3 Discussion

Although the spectra in the semiconductor case that are probed at negligible electronic pumping ($P_b \ll 1$) with no cavity pumping at all ($P_a = 0$), are in principle described by the same expression as that of the SE case used in the atomic model, in practise, however, both of these conditions can be easily violated. The renormalization of γ_b with P_b brings significant corrections well in the regime where n_a, $n_b \ll 1$ and one could think that the pump is negligible. For instance, for parameters of point (c) in Fig. 3.8 with $P_a = 0$, the rate P_b that is needed to bring a 100% correction to γ_b yields, according to Eqs. (3.14a) and (3.14b), average populations much below unity, namely, $n_a^{\mathrm{SS}} \approx 0.026$ and $n_b^{\mathrm{SS}} \approx 0.121$. By the time n_b reaches unity, with n_a still one fourth smaller, the correction on the effective decay rate has became 400%. Because of thermal fluctuations in the particle numbers, for these average values, the results are already irreconcilable with a SE emission case. They are, as we shall see in the next Chapter, also irreconcilable with a Fermion model. As this is n_a which is proportional to the signal detected in the laboratory, the electronic pumping must be kept very small so that corrections to the effective linewidth can be safely neglected. As regimes with high occupation numbers are reached, the renormalized Γs become very different from the bare γs in this model.

Second, even in the vanishing electronic pumping limit, it must be held true that P_a is zero. Even if only an electronic pumping is supplied externally by the experiment, the pumping rates of the model are the effective excitation rates of the cavity and exciton field inside the cavity, and it is clear that photons get injected in the cavity in structures that consists of numerous spectator dots surrounding the one in SC (cf. Fig. 2.2). Although most of these dots are in WC and out of resonance with the cavity, they affect the dynamics of the SC QD by pouring cavity photons in the system. In the steady state, following our previous discussion, this corresponds to changing the effective quantum state for the emission of the strongly coupled QD. As we shall see in more detail in what follows, this bears huge consequences on the appearance of the emitted doublet, especially on its visibility.

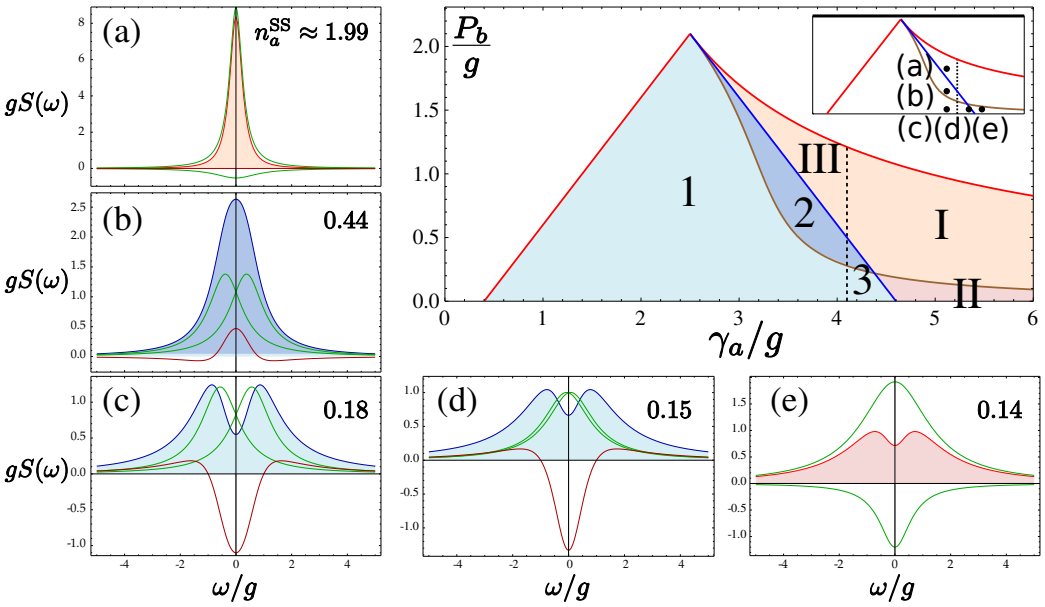

Figure 3.8: Phase space of the SS strong/weak coupling as a function of P_b/g and γ_a/g for the parameters $\gamma_b = 0.1g$ and $P_a = 0.5g$. The red lines delimit the region where there is a steady state [Eqs. (3.60)–(3.61)]. The blue line, Eq. (3.62), separates the strong (in shades of blue) from the weak (shades of red) coupling regions. The dotted black line, Eq. (3.63), separates SC and WC regions in the absence of pumping. The brown line, Eq. (3.64), separates the regions where one (dark blue) or two (light blue) peaks can be resolved in the luminescence spectra. This defines three areas in the SC region: (1) two peaks are resolved in the spectra, (2) the two peaks cannot be resolved and effectively merge into one, albeit in SC, and (3) SC is achieved thanks to the pump P_a (with one or two peaks visible depending of the overlap with the light or dark area) despite the large dissipation that predicts WC according to Eq. (3.57). In the same way we can distinguish three regions in weak coupling: (I) standard WC, (II) SC with a two peaked spectrum and (III) WC due to pumping P_b. The surrounding figures (a) to (e) show spectra (filled) from these regions and their decomposition into, Lorentzian (green) and dispersive (brown) parts. Parameters correspond to the points in the inset: (a) $\gamma_a = 3.8g$ and $P_b = g$, (b) $\gamma_a = 3.8g$ and $P_b = 0.5g$, (c) $\gamma_a = 3.8g$ and $P_b = 0.1g$, (d) $\gamma_a = 4.49g$ and $P_b = 0.1g$, (e) $\gamma_a = 4.8g$ and $P_b = 0.1g$. Observe how, in SC, two eigenstates have emerged, even in the cases—like in (b)—where they are not seen in the total spectrum. In the same way, in WC, all the emission emanates from the origin, although a two-peak structure can arise as a result of a resonance, also centered at the origin.

To fully appreciate the importance and deep consequences of these two provisions made by the SS case on its SE counterpart, we devote the rest of this Section to a vivid representation in the space of pumping and decay rates. Now that it has been made clear what is the relationship between the SE and the SS cases, we shall focus on the latter that is the adequate, general formalism to describe SC of QDs in microcavities.

In presence of a continuous, incoherent pumping, the criterion for SC—from the requirement of energy splitting and oscillations in the τ dynamics that we have discussed above—gets upgraded from its usual expression found in the literature:

$$g > |\gamma_-|\,, \tag{3.57}$$

to the more general condition:

$$g > |\Gamma_-|\,. \tag{3.58}$$

The quantitative and qualitative implications and their extent are shown in Fig. 3.8, where we have fixed the parameters $\gamma_b = 0.1g$ and $P_a = 0.5g$, and outlined the various regions of interest as P_b and γ_a are varied (central panel). This choice of representation allows us to investigate configurations that can be easily imprinted experimentally in the system: by tuning P_b in cavities that have different quality factors (inversely proportional to γ_a).

The red lines enclosing the filled regions in the central plot, delimit a frontier above which the pump is so high that populations diverge (there is no steady state). This is is given by the equivalent conditions that we derived in two different ways, Eqs. (3.22) and (3.34). At resonance, they simplify to

$$\Gamma_+ > 0\,, \tag{3.59a}$$

$$4g^2 > -\Gamma_a\Gamma_b\,. \tag{3.59b}$$

In the SC regime, the first condition is sufficient: $R_\mathrm{i} = 0$ and the total decay rate for the system is given only by Γ_+ (condition (3.59b) is therefore automatically fulfilled). The equation for the border of the physical region in SC reads:

$$P_b = \gamma_a + \gamma_b - P_a \qquad \text{(boundary of SC)}. \tag{3.60}$$

In the WC regime, condition (3.59b) becomes restrictive and the limiting value for P_b reads:

$$P_b = \gamma_b + Q_b = \gamma_b + \frac{4g^2}{\gamma_a - P_a}\,, \qquad \text{(boundary of WC)}, \tag{3.61}$$

and can be interpreted as the point where the effective decay rate for mode b (direct losses plus its Purcell emission through mode a) is exactly counterbalanced by the effective pump [$\Gamma_b^\mathrm{eff} = 0$, from Eq. (3.20)].

The main separation inside that region where a SS exists, is that between SC (in shades of blue, inside the triangle) and WC (in shades of red, on its right elbow). The blue solid line that marks this boundary, is specified by $g = |\Gamma_-|$, i.e., by

$$P_b = 4g - \gamma_a + \gamma_b + P_a\,, \qquad \text{(SS transition between SC and WC).} \tag{3.62}$$

The dashed vertical black line, is specified by $g = |\gamma_-|$, i.e., by

$$\gamma_a = 4g + \gamma_b\,, \qquad \text{(SE transition between SC and WC),} \tag{3.63}$$

corresponds to the standard criterion of SC (without incoherent pumping).

The light-blue region, labelled 1 in Fig. 3.8, corresponds to SC as it is generally understood. The luminescence spectrum shows a clear splitting of the lines. The dark-blue region, labelled 2, corresponds to SC, according to the requisite that R_0 be real, but with a broadening of the lines so large that in the luminescence spectrum, Eq. (3.54), only one peak is resolved. This region is delimited by the brown line, which is the solution of the equation $d^2S(\omega)/d\omega^2|_{\omega=0} = 0$, i.e., no concavity of the spectral line at the origin. From this condition follows the implicit equation:

$$(3\Gamma_+ - \Gamma_-)g^2 + (\Gamma_- - \Gamma_+)^3 + g|D_0|(g^2 - \Gamma_-^2 + 3\Gamma_+^2) = 0 \tag{3.64}$$

that yields two solutions, only one of which is physical. The other one is placed on the red line $\Gamma_+ = 0$, where the system diverges and the Rabi peaks become delta functions $\delta(\omega \pm g)$. Note that this line extends into the WC region, as we shall discuss promptly. The distinction between line-splitting, as it results from the emergence of new dressed states in the SC, and the observation of two peaks in the spectrum, is seen clearly in Fig. 3.9, where the two are superimposed and seen to differ greatly even at a qualitative level for most of the range of parameters, coinciding only in a narrow region. The doublet, as observed in the luminescence spectrum, collapses much before SC is lost. Any estimation of system parameters, such as the coupling strength, from a naive interpretation of the peak separation in the PL spectrum, will most likely be off by a large amount.

The last region of SC, labelled 3, is that specified by $4g + \gamma_b < \gamma_a < 4g + \gamma_b + P_a - P_b$, i.e., that which satisfies Eq. (3.58) but violates Eq. (3.57), thereby being in SC according to the more general definition that takes into account the effect of the incoherent pumping, but that, according to the conventional criterion, is in WC. For this reason, we refer to this region as of *pump-aided strong coupling*. This is a region of strong qualitative modification of the system, that should be in WC according to the intrinsic system parameters (γ_a, γ_b, g), but that restores SC thanks to the cavity photons forced into the system.

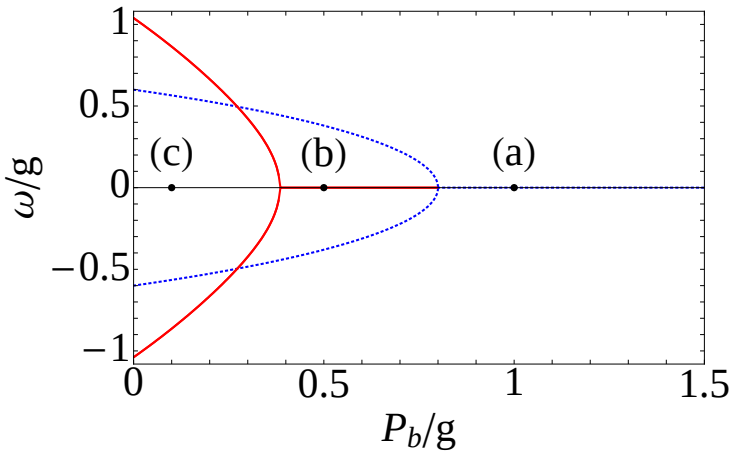

Figure 3.9: Rabi slitting at resonance (dotted blue) given by $\pm R_0$, Eq. (3.31), and the observed position of the peaks in the PL spectra (solid red) as a function of P_b/g. Parameters are those of the line of points (a), (b) and (c) of Fig. 3.8: $\gamma_a = 3.8g$, $\gamma_b = 0.1g$, $P_a = 0.5g$. The corresponding P_b are marked for those points.

We now consider the other side of the blue line, that displays the counterpart behavior in the WC. Region I is that of WC in its most natural expression. Region II, in light, is the extension into WC of featuring two maxima in the emission spectrum. In this case, this does not correspond to a line-splitting in the sense of SC where each peak is assigned to a renormalized (dressed) state, but rather to a resonance of the Fano type that is carving a hole in the single line of the weakly coupled system. In this region, one needs to be cautious not to read SC after the presence of two peaks at resonance. Finally, region III is the counterpart of region 3, in the sense that, according to the conventional criterion for the system parameters [Eq. (3.57)], this region is in SC when in reality the too-high electronic pumping has bleached it.

In the inset of Fig. 3.8-central panel, we reproduce the diagram to position the five points (a)–(e) in the various regions discussed, for which the luminescence spectra are displayed and decomposed into their Lorentzian (green lines) and dispersive (brown) contributions, Eqs. (3.46) and (3.48). Case (c), at the lower-left angle, corresponds to SC without any pathology nor surprise: the doublet in the luminescence spectrum—although displaced in position as shown in Fig. 3.9—is a faithful representation of the underlying Rabi-splitting. Increasing pumping brings the system into region 2 where, albeit still in SC, it does not feature a doublet anymore. The reason why, is clear on the corresponding decomposition of the spectrum, Fig. 3.8(b), with a broadening of the dressed states (in green) too large as compared to their splitting. Further increasing the pump brings it out of the SC

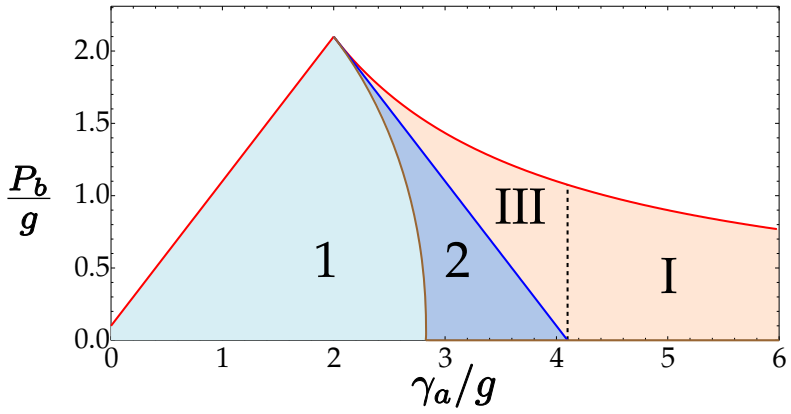

Figure 3.10: The same phase space of SC/WC as in Fig. 3.8 as a function of P_b/g and γ_a/g, only with P_a now set to zero (no cavity pumping). The triangle of SC is displaced, and the regions of one peak spectra (regions 2 of SC and I of WC) are enlarged, following Eq. (3.64). As a result regions 3 and II have disappeared.

region to reach point (a), where the two Lorentzians have collapsed on top of each other. This degeneracy of the mode emission means that the coupling only affects perturbatively each mode. As a result, the dispersive correction has vanished, and the spectrum now decomposes into two new Lorentzians centered at zero, with opposite signs [Eq. (3.55)].

Back to point (c), now keeping the pump constant and increasing γ_a, we reach point (d). It is still in SC, although the cavity dissipation is very large (more than four times the coupling strength) for the small value of γ_b considered. Its spectrum of emission shows, however, a clear line-splitting that is made neatly visible thanks to the cavity (residual) pumping P_a. Note that the actual separations of the two peaks is much larger than that of the dressed states. Increasing further the dissipation eventually brings the system into WC, but in region II where, again due to $P_a \neq 0$, the spectrum remains a doublet. In Fig. (e), one can see, however, that there is no Rabi splitting, and that the two peaks arise as a result of a subtraction of the two Lorentzians centered at $\omega_a = 0$ [see the WC spectrum decomposition in Eq. (3.48) and (3.55)]. Varying detuning for the system of point (e), even leads to an apparent anticrossing. There is no need to display a spectrum from region I, as in this case it does not show any qualitative difference as compared to that of (a). Note that the transition from SC to WC is always smooth in the observed spectra, although it is an abrupt transition in terms of apparition or disappearance of dressed states (due to a change of sign in a radical in the underlying mathematical formalism).

The scheme in Fig. 3.8, constructed through Eqs. (3.60)–(3.64), contains all the physics of the system. In the following, we shall look at variations of this

representation to clarify or illustrate those aspects that have been amply discussed before.

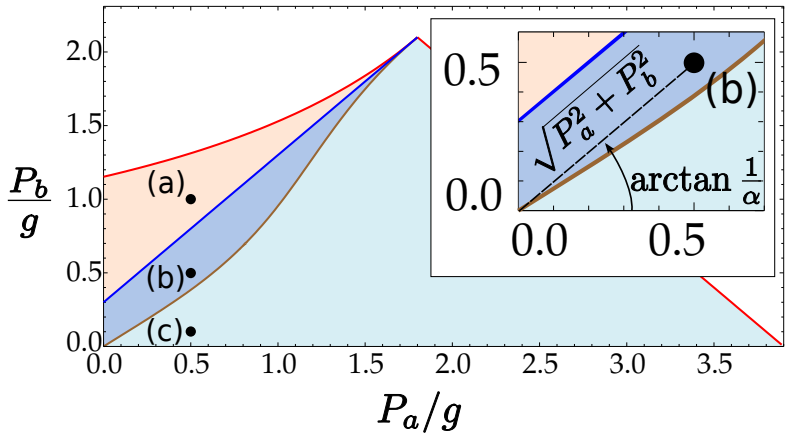

Figure 3.11: Phase space of SC/WC as a function of the pumps P_b/g and P_a/g for fixed decay parameters $\gamma_a = 3.8g$ and $\gamma_b = 0.1g$. As in Fig. 3.8, the red lines mark the physical regions and the blue one the SC (blue shades)/WC (red shades) transition, with the same regions 1 and 2 of SC and III of WC, also with the points (a), (b) and (c), of Fig. 3.8. In inset, zoom of the low-pump region, showing the importance of both the angle, $\arctan(1/\alpha)$, and the magnitude, $\sqrt{P_a^2 + P_b^2}$, of a given point in the diagram.

Fig. 3.10 shows the same diagram as that of Fig. 3.8, only with P_a now set to zero, i.e., corresponding to the case of a very clean sample with no spurious QDs other than the SC coupled one, that experiences only an electronic pumping. Observe how, as a consequence, region 3 of SC and II of WC have disappeared. The former was indeed the result of the residual cavity photons helping SC. The "pathology" in WC of featuring two peaks at resonance has also disappeared, but most importantly, see how region 2 has considerably increased inside the "triangle" of SC, meaning that the parameters required so that the line-splitting can still be resolved in the luminescence spectrum now put much higher demands on the quality of the structure. This difficulty, especially in the region where $P_b \ll g$ follows from the "effective quantum state in the steady state", that we have already discussed. The presence of a cavity pumping, even if it is so small that no field-intensity effects are accounted for, can favor SC by making it visible, indeed by merely providing a photon-like character to the quantum state. This is the manifestation in a SS of the same influence that was observed in the SE: the luminescence spectrum of a photon as an initial state of the coupled system, is more visible than that of an exciton, keeping all parameters otherwise the same (see Fig. 3.5). Another useful picture to highlight this last point, is that where the various regions are plotted in terms of the pumping rates, P_a and P_b (see Fig. 3.11, for the line (a)–(c) with $\gamma_a = 3.8g$ in Fig. 3.8). The angle of a given point with the

horizontal, linked to $\alpha^{-1} = P_b/P_a$, defines the exciton-like or photon-like character of the SS established in the system, and thus determines the visibility of the double-peak structure of SC. This is, at low pumpings, independent of the magnitude $\sqrt{P_a^2 + P_b^2}$, as the brown line defined by Eq. (3.64) is approximately linear in this region. This shows the importance of a careful determination of the quantum state that is established in the SS by the interplay of the pumping and decay rates, through Eq. (3.6). The magnitude $\sqrt{P_a^2 + P_b^2}$, on the other hand, affects the splitting $2R_0$, and the linewidth $2\Gamma_+$. In order to have a noticeable renormalization, the pumps must be comparable to the decays. On the one hand, the Rabi frequency can be affected in different ways by the pumpings, depending on the parameters. If $\Gamma_a = \Gamma_b$, there is, in general, no effect of decoherence on the splitting of the dressed states, showing that in this case there is a perfect symmetric coupling of the modes into the new eigenstates (although the broadening can be large and spoil the resolution of the Rabi splitting anyway). If they are different, for example in the common situation that $\gamma_a - \gamma_b > P_a - P_b$, the Rabi increases with increasing $P_a - P_b$. On the other hand, the linewidth $2\Gamma_+ = (\gamma_a + \gamma_b - P_a - P_b)/2$ presents clear bosonic characteristics: it increases with the decays but narrows with pumping. The intensity of the pumps also affects the total intensity of the spectra, that is proportional to n_a^{SS} through γ_a and the integration time of the apparatus. Here, however, we have focused on the normalized spectra (i.e., the lineshape).

3.5 Fitting of the experimental data

The most striking feature of strong coupling is the splitting of the spectral shape when the system is at resonance: the line of the cavity and that of the emitter, both at the same frequency, do not superimpose but anticross with a splitting related to the coupling strength. In Fig. 3.12 we can see the central result of Reithmaier et al.'s (2004) work. Here, it is claimed that the doublet found at 21K, when the two modes are expected to be resonant, demonstrates SC. However, this claim and the coupling strenght g extracted, are based on the SE picture and a Lorentzian fitting of the spectra.

First, let us try to analyze this experimental data with the general SE expressions we obtained, Eqs. (3.35) and (3.40). In Fig. 3.13, we can see four examples of anticrossing with detuning. The first row correspond to the cavity emission and the second to the exciton direct emission. Cases (a), (c) correspond to the decay of an exciton and (b), (d) of a photon. An exciton decay detected in the SE of the exciton, plot (c), is the situation most commonly considered in the literature (e.g. Carmichael et al. 1989, Andreani et al. 1999), although, it does not correspond to the experimental reality. Instead, in what concerns Reithmaier et al.'s

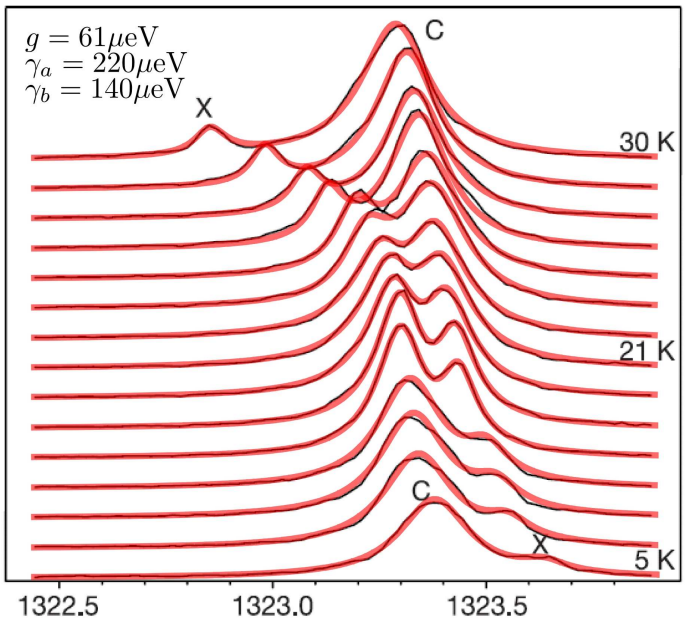

Figure 3.12: Anticrossing of the the cavity (C) and exciton (X) photoluminescence lines as reported by Reithmaier *et al.* in Nature (2004), demonstrating SC in their system. Energies are given in meV. The red lines are our superimposed fits with the best global fit parameters in the top left corner. Such a good agreement cannot be obtained neglecting the pump-induced decoherence.

experiments, we prefer to consider the cavity emission only. Changing the channel of detection provides results qualitatively different, contrary to what one could naively think. This is because, although the system is in strong coupling and photons and excitons should convert into each other rather quickly making all the cases equivalent, γ_a, γ_b are still quite different. This becomes even more obvious out of resonance. Given that $\gamma_a - \gamma_b$, if, for instance, the initial state is an exciton [see (a) and (c)], the polaritons realised in the system and the emission have always a stronger excitonic character. On the other hand, the bare cavity mode only survives resonance when photons are detected through the cavity emission. The two cases of detection of one mode through the opposite channel [(a) and (d)], result in the same spectra by symmetry. The anticrossing (b) is the closest to the experimental one in Fig. 3.12, showing a more intense cavity mode out of resonance. Still, a global fitting of the data with these formulas is very poor. The resemblance between Fig. 3.12 and Fig. 3.13(b) is only a hint about the state realised in the system, that seems to be more photonic in character. Finally, it is illustrative to see in Figs. 3.13(e) how misleading is to reduce the spectra to the Lorentzian contribution (plotted in blue filling). At resonance, this part of the spectral shapes is common to the four cases (because $n^0_{ab} = 0$), which anyway are

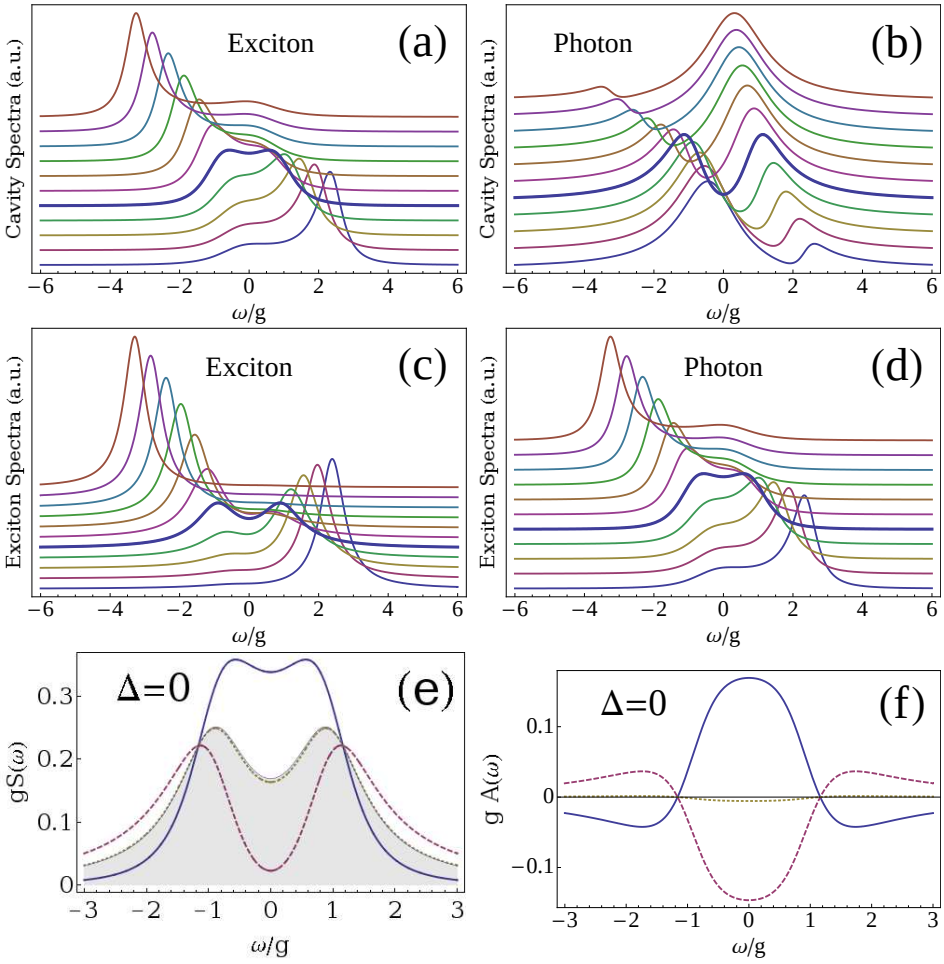

Figure 3.13: Theoretical SE spectra: anticrossing of the the cavity ($\omega_a = 0$) and exciton ($\omega_b = -\Delta$) modes varying detuning from $-2g$ to $3g$. The first row corresponds to the cavity emission $S_a^{\mathrm{SE}}(\omega)$ for the SE of (a) one exciton and (b) one photon. The second row corresponds to the lateral excitonic direct emission $S_b^{\mathrm{SE}}(\omega)$ for the SE of (c) one exciton and (d) one photon. The parameters are those reported in Reithmaier et al.'s (2004) experiments: $g = 80\mu$ eV, $\gamma_a = 180\mu\mathrm{eV} = 2.25g$, $\gamma_b = 50\mu\mathrm{eV} = 0.625g$. In (e) we put together the four cases at resonance [in solid-blue (a) and (d), dashed-purple (b) and dotted-brown (c)], and their common Lorentzian contribution (blue filling). The different dispersive contributions are plotted in (f) with the same code of colors.

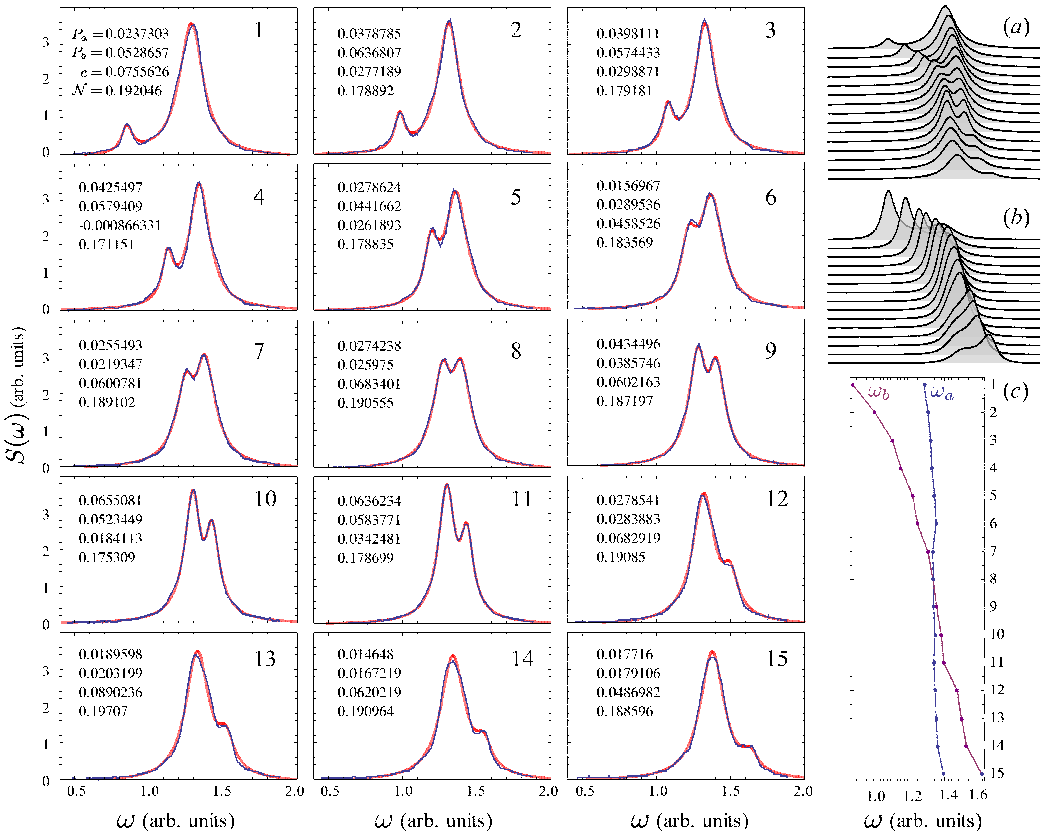

Figure 3.14: Theoretical fit (in semi-transparent red) of the data digitized from Reithmaier et al. (2004) (blue). The data has been fitted on rescaled axes for numerical stability by a Levenberg–Marquardt method with $\mathcal{N}S(\omega) - c$, with $\mathcal{N}$ and c to account for the normalization and the background. Beside these two necessary parameters regardless of the model, each panel only has $P_{a/b}$ and $\omega_{a/b}$ (c) as fitting parameters. g and $\gamma_{a/b}$ have been optimized globally, with best fits for $g = 61\mu$eV, $\gamma_a = 220\mu$eV and $\gamma_b = 140\mu$eV. (a) shows again the anticrossing from theoretical curves 1–15 put together. (b) keeps all fitting parameters the same but with $P_a = 0$ and vanishing P_b. The dot emission now dominates and no anticrossing is observed, although the system is still in strong-coupling.

very different from each other thanks to the dispersive part, plotted in (f). The quantum interference between the modes can result in closing the Rabi doublet, cases (a) and (d) in solid-blue, or in separating the peaks, case (b) in dashed-purple. It can also contribute very little as in case (c), in dotted-brown. In any case, it is an indispensable element.

Now, we will turn to our SS model under incoherent continuous pump, that is closer to the semiconductor experimental reality, and see that is can successfully reproduce Reithmaier et al.'s curves. In this experiments, both large QDs and low excitations were used, so a Fermionic model is less appropriate than the present

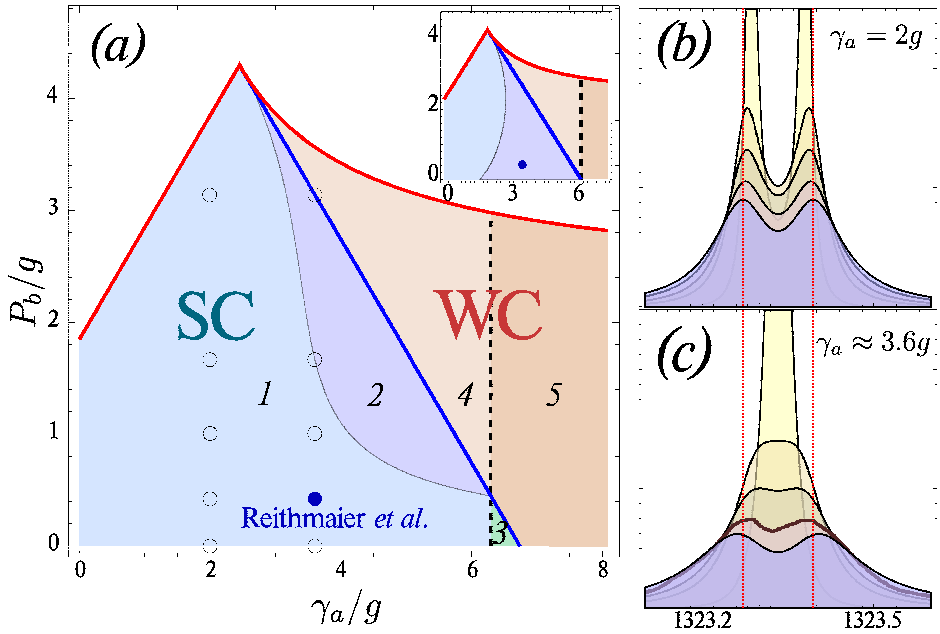

Figure 3.15: The same phase space of SC/WC as in Fig. 3.8 with $\gamma_b \approx 2.3g$ and $P_a \approx 0.44g$ fitting the experiment of Reithmaier *et al.* Reithmaier et al.'s (2004), marked by a plain blue point ($\gamma_a \approx 3.6g$, $P_b \approx 0.42g$). In inset, the same phase space but for $P_a = 0$, in which case the line-splitting of Reithmaier et al.'s (2004) would not be resolved. (b) and (c): Spectra of emission with increasing exciton pumping P_b marked by the hollow points in panel (a). For $\gamma_a = 2g$ in (b), SC is retained throughout and made more visible. For the best fit parameter, $\gamma_a \approx 3.6g$ in (c), line-splitting is lost increasing pumping, first because it is not resolved and then because the system goes into WC.

bosonic picture. In Fig. 3.13 and in the more detailed Fig. 3.14, we show in red the results of optimizing the *global* nonlinear fit of the experimental data (in black) with Eqs. (3.35) and (3.43). That is, the detuning (ω_a and ω_b) and pumping rates (P_a and P_b) are the fitting parameter from one curve to the other, while g and $\gamma_{a,b}$ have been optimized but kept constant for all curves. We find an excellent overall agreement, that instructs on many hidden details of the experiment.

First, the model provides more reliable estimations of the fitting parameters than a direct reading of the line-splitting at resonance or of the linewidths far from resonance: The best-fitting coupling constant is $g = 61\mu$eV. The value for $\gamma_a = 220\mu$eV is consistent with the experiment (the authors place it at 180μeV but from a Lorentzian fit of the 5K curve in the assumption that the system is not strongly-coupled here, where our model shows this to be a poor approximation), and the value for γ_b, that is the most difficult to estimate experimentally, is reasonable in the assumption of large QDs, as is the case of those that have been used to benefit from their large coupling strength. The point here is not to conduct an accurate

statistical analysis of this particular work but to show the excellent agreement that is afforded by our model with one of the paradigmatic experiment in the field. Such a good global fit cannot be obtained without taking into account the effect of pumping, even when it is small. More interestingly, it is necessary to include both the exciton pumping P_b (expected from the experimental configuration) but also the cavity pumping P_a. The latter requirement confirms the idea that the photonic contribution is important in the system that we could extract from the comparison with the SE. Experimentally, we already discussed in Chapter 2 that there are numerous QDs weakly-coupled to the cavity in addition of the one that undergoes SC. Beyond this QD of interest, a whole population of "spectator" dots contributes an effective cavity pumping, which looms up in the model as a nonzero P_a. The fitting pumping rates (Fig. 3.14) vary slightly with detuning, as can be explained by the change in the effective coupling of both the strongly-coupled dot with the cavity (pumping tends to increase out of resonance) and the spectator QDs that drift in energy with detuning. We find as best fit parameters at resonance $P_a \approx 0.44\underline{g} = 0.12\gamma_a$ and $P_b \approx 0.42g = 0.18\gamma_b$ (the mean over all curves is $\bar{P_a} \approx 0.15\gamma_a$ and $\bar{P_b} \approx 0.28\gamma_b$ with rms deviations of $\approx 10\%$). The existence of P_a in an experiment with electronic pumping is supported by the authors of Reithmaier et al.'s (2004) who observed a strong cavity emission with no QD at resonance. We shall see in the following the considerable importance of this fact to explain the success of their experiment.

The position where we estimate the result of Ref. Reithmaier et al. (2004) in the SC-WC diagram (Fig. 3.15) for this system, validates that SC has indeed been observed in this experiment. In inset, however, one sees that in the case where the cavity pumping P_a is set to zero keeping all other parameters the same, the point falls in the dark region 2 where, although still in SC, the line-splitting cannot be resolved. Even if it is possible in principle to demonstrate SC through a finer analysis of the crossing of the lines [see Fig. 3.14(b)], it is obviously less appealing than a demonstration of their anticrossing. This is despite the fact that the case of $P_a = 0$ is equally, if not more, relevant as far as SC is concerned, as it corresponds to the case where only the QD is excited, whereas in the case of Fig. 3.12, it also relies on cavity photons. With the populations involved in the case of the best fit parameters that we propose—$n_a \approx 0.15$—one can still read in Reithmaier *et al.*'s experiment a good *vacuum* Rabi splitting, so the appearance of the line-splitting with P_a is not due to the photon-field intensity. Rather, the system is maintained in a quantum state that is more photon-like in character, which is more prone to display line splitting in the cavity emission, as we already discussed. In this sense, there is indeed an element of chance involved in the SC observation, as one sample can fall in or out of region 2 depending on whether or not the pumping scheme is forcing photon-like states. Understanding the excitation scheme drastically reduces this element of hazard. The shortcoming

of downplaying the importance of the quantum state that is realized in the system owing to pumping, has as its worst consequence a misunderstanding of the results, the most likely being the qualification of weak-coupling (WC) for a system in SC that cannot be spectrally resolved because of decoherence-induced broadening of the lines.

A natural experiment to build upon our results is to tune pumping. In our interpretation, it is straightforward experimentally to change P_b, but it is not clear how P_a would then be affected, as it is due to the influence of the crowd of spectator QDs, not directly involved in SC. In Fig. 3.15(c), we hold P_a to its best fit parameters and vary P_b in the best fit case $\gamma_a = 3.6g$ on panel (c), then for a better cavity with $\gamma_a = 2g$ on panel (b), where the system is in SC for all possible values of P_b. Spectra are displayed for the values of P_b marked by the points in (a). Two very different behaviors are observed for two systems varying slightly only in γ_a. In one case (b), strong renormalization of the linewidths and splitting results from Bose effects in a system that retains SC throughout. In the other (c), line-splitting is lost and transition towards WC then follows. At very high pumping, the model breaks down. A careful study of pump-dependent PL can tell much about the underlying statistics of the excitons and the precise location of one experiment in the SC diagram.

The confrontation of the theory with the experimental data is an illustration only, as the raw experimental data was not available by the time of our investigation. We have therefore digitized the data, what forbids an in-depth statistical analysis, since the experimental points are required rather than the interpolated curves published, if only to know the number of degrees of freedom. Note that one expects better still results as our procedure added noise. We found the best agreements near resonance, which might be due to the exciton that, when it is less-strongly coupled at larger detunings, may go below the resolution of the detector, resulting in an apparently broader line. All these limitations can be circumvented with a careful statistical analysis (and treatment of the data to reconstruct linewidths below the experimental resolution). This is a standard procedure to validate a theoretical model over another by statistical analysis of the experiment. I would also provide a meaningful and quantitative comparison between the various implementations (micropillars, microdisks and photonic crystals). Lacking the full experimental data, we have merely been unable to provide a confidence interval to our most-likelihoods estimators. Doing so, progress will be meaningfully quantified, and claims—rather than ranging between likely and convincing—will become unambiguously proven (within their interval of confidence).

3.6 Second order correlation function

The correlator $\langle a^\dagger(t)a^\dagger(t+\tau)a(t+\tau)a(t)\rangle$ needed to compute $g^{(2)}(\tau)$, requires to apply the quantum regression formula in Eq. (2.116) for the general set of operators $C_{\{m,n,\mu,\nu\}} = a^{\dagger m}a^n b^{\dagger\mu}b^\nu$ (that includes $a^\dagger a$) with $\Omega_1 = a^\dagger$ and $\Omega_2 = a$. As we noted in Sec. 2.7, the quantum regression formula is the same as that used to compute the mean values of Sec. 3.2. The set of correlators $C_{\{m,n,\mu,\nu\}}$ is again reduced to $\tilde{\mathscr{N}_1}$ (see Fig. 3.1). We write explicitly these four correlators, linked to $G^{(2)}(\tau)$, in the form $\langle a^\dagger(t)C_{\{m,n,\mu,\nu\}}(t+\tau)a(t)\rangle$ and construct the vector

$$\mathbf{w}(t,t+\tau) = \begin{pmatrix} \langle a^\dagger(t)(a^\dagger a)(t+\tau)a(t)\rangle \\ \langle a^\dagger(t)(b^\dagger b)(t+\tau)a(t)\rangle \\ \langle a^\dagger(t)(a^\dagger b)(t+\tau)a(t)\rangle \\ \langle a^\dagger(t)(ab^\dagger)(t+\tau)a(t)\rangle \end{pmatrix}. \tag{3.65}$$

The equation we must solve reads

$$\frac{d\mathbf{w}(t,t+\tau)}{d\tau} = -\mathbf{M}_0\mathbf{w}(t,t+\tau) + \mathbf{p}n_a(t)\,, \tag{3.66}$$

with the same matrix $\mathbf{M}_0$ and pumping vector $\mathbf{p}$ [Eqs. (3.7)] that already appeared in Eq. (3.6) for the mean values. If we concentrate on the SS case, the initial conditions $\mathbf{w}(t,t)$ are given by the SS values,

$$\mathbf{w}^{\rm SS} = \begin{pmatrix} \langle a^\dagger a^\dagger aa\rangle^{\rm SS} \\ \langle a^\dagger b^\dagger ba\rangle^{\rm SS} \\ \langle a^\dagger a^\dagger ba\rangle^{\rm SS} \\ \langle a^\dagger ab^\dagger a\rangle^{\rm SS} \end{pmatrix}, \tag{3.67}$$

and $n_a(t) \to n_a^{\rm SS}$. These new four average quantities can be obtained by applying once more the quantum regression formula, in the same way we did to obtain $\mathbf{v}(t,t)$, having in mind the scheme on the right of Fig. 3.1. However, the quantities in $\mathbf{w}^{\rm SS}$ correspond to $C_{\{\tilde{\eta}\}}$ in the second manifold, $\{\tilde{\eta}\} \in \tilde{\mathscr{N}_2}$ (not plotted in Fig. 3.1). We need to obtain all correlators in $\tilde{\mathscr{N}_2}$:

$$\{1,1,1,1\}\,, \tag{3.68a}$$
$$\{2,2,0,0\}\,,\{2,1,0,1\}\,,\{1,2,1,0\}\,, \tag{3.68b}$$
$$\{0,0,2,2\}\,,\{1,0,2,1\}\,,\{1,0,1,2\}\,, \tag{3.68c}$$
$$\{2,0,0,2\}\,,\{0,2,2,0\}\,. \tag{3.68d}$$

The new set of equations link these elements among themselves and to those in the first manifold, that we already computed. Now that we know how to obtain $\mathbf{w}^{\rm SS}$, we can write the solution of Eq. (3.66) as:

$$\mathbf{w}(\tau) = e^{-\mathbf{M}_0\tau}\mathbf{w}^{\rm SS} - \mathbf{M}_0^{-1}(e^{-\mathbf{M}_0\tau}-1)\mathbf{p}n_a^{\rm SS}\,. \tag{3.69}$$

Remembering from Sec. 3.2 that $\mathbf{M}_0^{-1}\mathbf{p} = \mathbf{u}^{\mathrm{SS}}$, the solution can be further simplified into:

$$\mathbf{w}(\tau) = \mathbf{u}^{\mathrm{SS}} n_a^{\mathrm{SS}} + e^{-\mathbf{M}_0\tau}\left(\mathbf{w}^{\mathrm{SS}} - \mathbf{u}^{\mathrm{SS}} n_a^{\mathrm{SS}}\right). \tag{3.70}$$

If we define the SS fluctuation vector,

$$\mathbf{f}^{\mathrm{SS}} = \mathbf{w}^{\mathrm{SS}} - \mathbf{u}^{\mathrm{SS}} n_a^{\mathrm{SS}} = (n_a^{\mathrm{SS}})^2 \begin{pmatrix} (g^{(2)})^{\mathrm{SS}} - 1 \\ \frac{\langle a^\dagger a b^\dagger b\rangle^{\mathrm{SS}}}{(n_a^{\mathrm{SS}})^2} - \frac{n_b^{\mathrm{SS}}}{n_a^{\mathrm{SS}}} \\ \frac{\langle a^\dagger a^\dagger b a\rangle^{\mathrm{SS}}}{(n_a^{\mathrm{SS}})^2} - D^{\mathrm{SS}} \\ \left(\frac{\langle a^\dagger a^\dagger b a\rangle^{\mathrm{SS}}}{(n_a^{\mathrm{SS}})^2} - D^{\mathrm{SS}}\right)^* \end{pmatrix}, \tag{3.71}$$

we can write a general expression for $g^{(2)}(\tau)$ (with $\tau > 0$):

$$g^{(2)}(\tau) = \frac{[\mathbf{w}(\tau)]_1}{(n_a^{\mathrm{SS}})^2} = 1 + \frac{[e^{-\mathbf{M}_0\tau}\mathbf{f}^{\mathrm{SS}}]_1}{(n_a^{\mathrm{SS}})^2}, \tag{3.72}$$

where $[\mathbf{x}]_1$ means that we take the first element of the vector $\mathbf{x}$. Note that for the present system, $(g^{(2)})^{\mathrm{SS}} = 2$ and

$$\langle a^\dagger a b^\dagger b\rangle^{\mathrm{SS}} = 2 n_a^{\mathrm{SS}} n_b^{\mathrm{SS}} - \frac{n_a^{\mathrm{SS}} P_b + n_b^{\mathrm{SS}} P_a}{\Gamma_a + \Gamma_b}. \tag{3.73}$$

A more explicit expression of $g^{(2)}(\tau)$ in terms of the system parameters, can be obtained by analogy with the solution for $\mathbf{u}^{\mathrm{SE}}(t)$ in Eq. (3.9), by exchanging t for τ and the elements in $\mathbf{u}(0)$ for those in $\mathbf{f}^{\mathrm{SS}}/(n_a^{\mathrm{SS}})^2$. However, $g^{(2)}(\tau)$ can be more straight forwardly obtained from the relation $g^{(2)}(\tau) = 1 + |g^{(1)}(\tau)|^2$, that applies for thermal photons (Eq. 2.117). Two emission events are independent from each other in this case, where we also have $S^{(2)}_{\mathrm{corr}}(\omega) = 0$. For the sake of completeness, we can write the explicit expressions in the SS for $g^{(2)}(\tau)$ and $S^{(2)}(\omega)$:

$$g^{(2)}(\tau) = 1 + e^{-2\Gamma_+\tau}\left\{\frac{1}{2} + 2|W|^2 + \Re[e^{iR\tau}(\frac{1}{2} - 2|W|^2 + 2i\,\Re W)]\right\}, \tag{3.74a}$$

$$\begin{aligned} S^{(2)}(\omega) = {} & (\frac{1}{4} - |W|^2)\Big[\frac{2}{\pi}\frac{2\Gamma_+}{(2\Gamma_+)^2 + \omega^2} \\ & + \frac{1}{\pi}\frac{2\Gamma_+ + 2R_{\mathrm{i}}}{(2\Gamma_+ + 2R_{\mathrm{i}})^2 + (\omega + 2R_{\mathrm{r}})^2} + \frac{1}{\pi}\frac{2\Gamma_+ - 2R_{\mathrm{i}}}{(2\Gamma_+ - 2R_{\mathrm{i}})^2 + (\omega - 2R_{\mathrm{r}})^2}\Big] \\ & + \Re(W)\Big[\frac{1}{\pi}\frac{\omega + 2R_{\mathrm{r}}}{(2\Gamma_+ + 2R_{\mathrm{i}})^2 + (\omega + 2R_{\mathrm{r}})^2} - \frac{1}{\pi}\frac{\omega - 2R_{\mathrm{r}}}{(2\Gamma_+ - 2R_{\mathrm{i}})^2 + (\omega - 2R_{\mathrm{r}})^2}\Big], \end{aligned} \tag{3.74b}$$

with the definitions of Eq. (3.37) and (3.12). As it corresponds to bosons, the emission presents *bunching*, that is, the second photon prefers to be emitted together with the first one, $g^{(2)}(0) > g^{(2)}(\tau)$. The $g^{(2)}(\tau)$ goes from its steady state

value, 2, towars the infinite delay value, 1, with damped oscillations in SC and exponential decay in the WC. In all cases, the transient in τ happens at twice the speed of $g^{(1)}(\tau)$, given also in terms of R and Γ_+. The noise spectrum consists of three peaks, one centered at zero and the other two at $\pm 2R_{\rm r}$.

The full dynamics of the general one-time average values in $\mathbf{u}(t)$, that we computed in Sec. 3.2 only for the SS or in the absence of pump, can be obtained now for the same price by simple analogy with Eq. (3.70):

$$\mathbf{u}(t) = e^{-\mathbf{M}_0 t}\mathbf{u}(0) + (1 - e^{-\mathbf{M}_0 t})\mathbf{u}^{\rm SS}. \tag{3.75}$$

The transient part of the dynamics, $\mathbf{u}^{\rm TR}(t) = e^{-\mathbf{M}_0 t}(\mathbf{u}(0) - \mathbf{u}^{\rm SS})$, has the same mathematical expression as $\mathbf{u}^{\rm SE}(t)$, making the substitutions ($\gamma_{a,b} \to \Gamma_{a,b}$), ($\gamma_\pm \to \Gamma_\pm$) and $\mathbf{u}(0) \to (\mathbf{u}(0) - \mathbf{u}^{\rm SS})$. Therefore, the frequency/damping of the oscillations in the transient is also given by real/imaginary part of R.

3.7 Conclusions

In this Chapter I have presented a unified formalism for the zero-dimensional light-matter interaction between bosons (the linear model), both in the WC and SC regimes, for the two cases of SE of an initial state, and emission in the SS maintained by an incoherent continuous pumping. The general theory provided here is suitable to describe not only the traditional cavity quantum electrodynamics (direct SE of the excited atom in a cavity), but also the more recent semiconductor version with quantum dots in microcavities.

I have emphasized how a proper consideration of the incoherent pumping scheme is needed to describe the effective quantum state realized in the system, and how this bears consequences on the spectral lineshapes, in particular on the ability to resolve a Rabi doublet when the splitting to broadening ratio is small.

The main results of this Chapter are to be found in Eqs. (3.35)–(3.38) that provide the analytical expression for the cavity emission spectra of a system whose specificities—such as whether it corresponds to SE or the SS established by an incoherent continuous pumping—are provided by a single parameter D. These formulas, that allow for an arbitrary detuning between the bare modes, reduce to more self-contained expressions at resonance, namely Eq. (3.50) for SE and Eq. (3.56) for SS. The resonance case allows an unambiguous definition of SC, depending on whether the complex Rabi frequency, Eq. (3.12), is pure imaginary (WC) or real (SC) which means the existence bare or dressed modes respectively in the system. However, there is no one-to-one mapping of the eigenenergies of the system with the lines observed in the luminescence spectrum. All cases can arise: one or two peaks can be observed at resonance both in WC and SC. For that reason, an understanding of the general picture is required to be able to position a

particular experiment in the space of parameters, as was done in Figs. 3.15, rather than to rely on a qualitative effect of anticrossing at resonance. Figure 3.9 shows how loosely related are the observed line-splitting in the luminescence spectrum and the actual energy splitting of the polariton modes.

Chapter 4

Two coupled quantum dots

Contents

In this Chapter, we solve analytically the direct coupling of two two-level systems (quantum dots) and analyze its properties of emission in the presence of decoherence (dissipation and incoherent pump). The results presented here belong to the references 12 and 13 of the list of my publications, Page 225, in preparation and submitted for publication respectively.

4.1 Introduction

The Hamiltonian for two coupled two-level systems (2LS) reads

$$H = \omega_{E1}\sigma_1^\dagger\sigma_1 + \omega_{E2}\sigma_2^\dagger\sigma_2 + g(\sigma_1^\dagger\sigma_2 + \sigma_2^\dagger\sigma_1)\,, \tag{4.1}$$

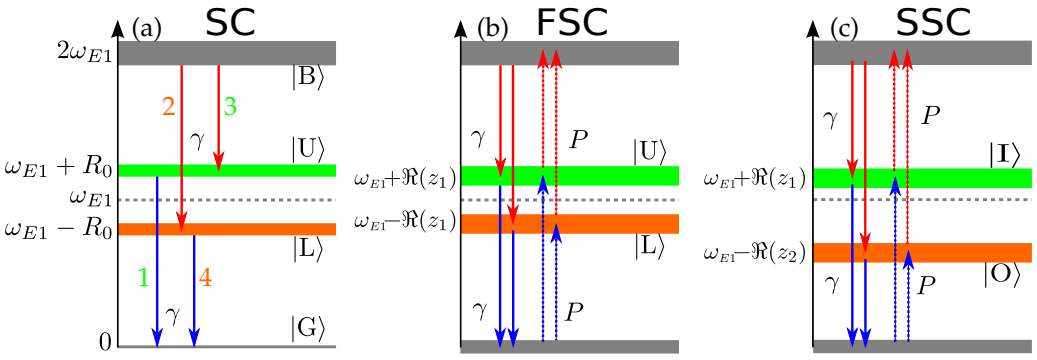

Figure 4.1: Energy levels for the coupled QDs system described by Hamiltonian (4.1), that remain a good picture in SC. As we will see in Sec. 4.3.2, the SC regime in the absence of pump (a) separates in two regions when pump is turned on, FSC (b) and SSC (c). The dressed states $|U,L\rangle$ of SC and FSC, change in SSC into a new set $|I,O\rangle$ that are not symmetrically splitted. The thickness of the lines represents the uncertainty in energy due to (a) the decay and (b,c) both the pump and the decay. Transitions labelled 1 and 4 (in blue) are those involving $|G\rangle$ and transitions 2 and 3 (in red), those involving $|B\rangle$. The energy and total decay rate of transitions 1 and 3 (involving $|U\rangle$ or $|I\rangle$, in green) depend on z_1, while 2 and 4 (involving $|L\rangle$ or $|O\rangle$, in orange) depend on z_2. The same color code is used in the rest of the figures for the decomposition of the spectra of emission.

where $\sigma_{1,2}$ are the lowering operators of the 2LSs, with bare energies $\omega_{E1,E2}$, that are coupled linearly with strength g. The Hilbert space consists only of three manifolds with zero ($|G\rangle = |g,g\rangle$), one ($|E1\rangle = |e,g\rangle$, $|E2\rangle = |g,e\rangle$) and two ($|B\rangle = |e,e\rangle$) excitations. The letters g and e mean the ground or exciton states in the dot. In Fig. 4.1 we can see in a scheme how the intermediate levels, $|E1\rangle$, $|E2\rangle$, form two dressed states, $|U\rangle$ and $|L\rangle$, with the same splitting and structure found for the harmonic oscillators (HOs) [Eqs. (2.57a)–(2.58)]. This equivalence breaks in the manifold with two excitations where the statistical nature of the particles reveals. The master equation in Eq. (2.74) can be exactly solved in this finite Hilbert space. If the pump is strong, the dots are brought to saturation in the SS, quenching the system emission and effectively decoupling the dots, but also avoiding the divergences that appeared in the LM due to bosonic accumulation. The fermionic character of both *effective broadenings*

$$\Gamma_1 = \gamma_{E1} + P_{E1}\,, \quad \Gamma_2 = \gamma_{E2} + P_{E2}\,, \tag{4.2}$$

results in qualitative differences that can be directly contrasted with the completely bosonic case. For later convenience, we also define the parameters:

$$\Gamma_\pm = \frac{\Gamma_1 \pm \Gamma_2}{4}\,, \quad \gamma_\pm = \frac{\gamma_{E1} \pm \gamma_{E2}}{4}\,. \tag{4.3}$$

4.2 First order correlation function and power spectrum

The luminescence spectrum of the system through the emission of one of the dots, $S_1(\omega)$, requires the correlator $\langle\sigma_1^\dagger(t)\sigma_1(t+\tau)\rangle$ in Eq. (2.82). Let us write the quantum regression formula for the most general set of operators $\{C_{\{m,n,\mu,\nu\}} = \sigma^{\dagger m}_1\sigma_1^n\sigma^{\dagger\mu}_2\sigma_2^\nu\}$, with m, n, μ, $\nu \in \{0,1\}$. The regression matrix M is defined by

$$M_{\substack{mn\mu\nu\\mn\mu\nu}} = i\omega_{E1}(m-n) + i\omega_{E2}(\mu-\nu) - \frac{\Gamma_1}{2}(m+n) - \frac{\Gamma_2}{2}(\mu+\nu)\,, \tag{4.4a}$$

$$M_{\substack{mn\mu\nu\\1-m,1-n,\mu\nu}} = P_{E1}mn\,, \quad M_{\substack{mn\mu\nu\\mn,1-\mu,1-\nu}} = P_{E2}\mu\nu\,, \tag{4.4b}$$

$$M_{\substack{mn\mu\nu\\m,1-n,1-\mu,\nu}} = 2ig(\nu-\mu)(1-n)(1-\mu)\,, \tag{4.4c}$$

$$M_{\substack{mn\mu\nu\\1-m,n,\mu,1-\nu}} = 2ig(n-\mu)(1-\nu)(1-m)\,, \tag{4.4d}$$

$$M_{\substack{mn\mu\nu\\1-m,n,1-\mu,\nu}} = ig[m(1-\mu)+\mu(1-m)]\,, \tag{4.4e}$$

$$M_{\substack{mn\mu\nu\\m,1-n,\mu,1-\nu}} = -ig[n(1-\nu)+\nu(1-n)]\,, \tag{4.4f}$$

and zero everywhere else.

For the computation of the spectrum, we need two more correlators and equations than in the two coupled HOs (see Fig. 3.1). In Fig. 4.2 we can see a scheme of this finite set of correlators (left) and mean values (right), labelled with the indices $\{\eta\} = \{m,n,\mu,\nu\}$. The coherent (through g) and incoherent (through $P_{E1,E2}$) links between the various correlators, given by the regression matrix, are shown with arrows (see a detail explanation of the figure in the caption). This simple graph becomes infinite for the JCM (see Fig. 5.11). Here, thanks to the saturation of both modes, being 2LSs, we obtain a simple equation,

$$\partial_\tau \mathbf{v}(t,t+\tau) = -\mathbf{M}_1\mathbf{v}(t,t+\tau)\,, \tag{4.5}$$

for the correlators

$$\mathbf{v}(t,t+\tau) = \begin{pmatrix} \langle\sigma_1^\dagger(t)\sigma_1(t+\tau)\rangle \\ \langle\sigma_1^\dagger(t)\sigma_2(t+\tau)\rangle \\ \langle\sigma_1^\dagger(t)\sigma_1^\dagger\sigma_1\sigma_2(t+\tau)\rangle \\ \langle\sigma_1^\dagger(t)\sigma_1\sigma_2^\dagger\sigma_2(t+\tau)\rangle \end{pmatrix} \tag{4.6}$$

with the matrix

$$\mathbf{M}_1 = \begin{pmatrix} i\omega_{E1}+\frac{\Gamma_1}{2} & ig & -2ig & 0 \\ ig & i\omega_{E2}+\frac{\Gamma_2}{2} & 0 & -2ig \\ 0 & -P_{E1} & i\omega_{E2}+\Gamma_1+\frac{\Gamma_2}{2} & -ig \\ -P_{E2} & 0 & -ig & i\omega_{E1}+\Gamma_2+\frac{\Gamma_1}{2} \end{pmatrix}. \tag{4.7}$$

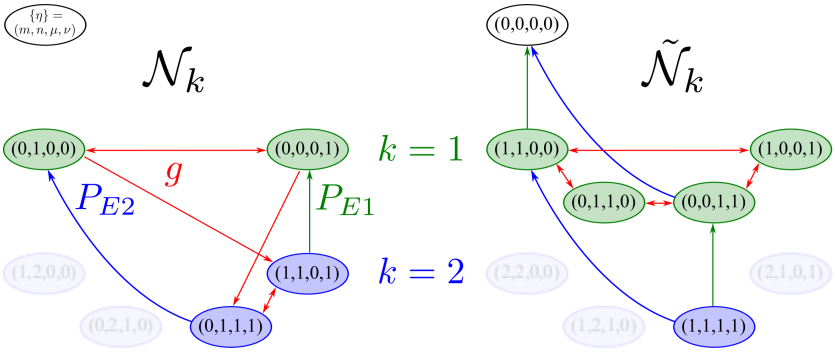

Figure 4.2: Chain of correlators—indexed by $\{\eta\} = (m,n,\mu,\nu)$—linked by the Hamiltonian dynamics with pump and decay for two coupled 2LS. On the left (resp., right), the set $\bigcup_k \mathcal{N}_k$ (resp., $\bigcup_k \tilde{\mathcal{N}}_k$) involved in the equations of the two-time (resp., single-time) correlators. In green are shown the first manifolds $\mathcal{N}_1$ and $\tilde{\mathcal{N}}_1$ that correspond to the LM (see Fig. 3.1), and in blue, the second manifold $\mathcal{N}_2$ and $\tilde{\mathcal{N}}_2$. The equation of motion $\langle \sigma_1^\dagger(t) C_{\{\eta\}}(t+\tau)\rangle$ with $\eta \in \mathcal{N}_k$ requires for its initial value the correlator $\langle C_{\{\tilde{\eta}\}}\rangle$ with $\{\tilde{\eta}\} \in \tilde{\mathcal{N}}_k$ defined from $\{\eta\} = (m,n,\mu,\nu)$ by $\{\tilde{\eta}\} = (m+1,n,\mu,\nu)$, as seen on the diagram. The thick red arrows indicate which elements are linked by the coherent (SC) dynamics, through the coupling strenght g, while the green/blue thin arrows show the connections due to the incoherent QD pumpings. The sense of the arrows indicates which element is "calling" which in its equations. The self-coupling of each node to itself is not shown. This is where $\omega_{E1,E2}$ and $\Gamma_{1,2}$ enter. These links are obtained from the rules in Eqs. (4.4), that result in the matrices $\mathbf{M}_1$ and $\mathbf{M}_0$. The number of correlators needed to compute the spectrum is truncated naturally (with four elements) thanks to the saturation of the 2LSs.

At low excitation, this system is reduced to the LM, where only the first two correlators and columns/rows of $\mathbf{M}_1$ remain. The general solution (for positive τ), $\mathbf{v}(t,t+\tau) = e^{-\mathbf{M}_1\tau}\mathbf{v}(t,t)$, leads to a correlator of the form:

$$\langle \sigma_1^\dagger(t)\sigma_1(t+\tau)\rangle = \sum_p^4 (l_p(t) + ik_p(t)) e^{-i\omega_p\tau} e^{-\frac{\gamma_p}{2}\tau}. \tag{4.8}$$

The coefficients $l_p(t)$ and $k_p(t)$ depend on the dynamics of the mean values,

$$\mathbf{v}(t,t) = \begin{pmatrix} \langle \sigma_1^\dagger\sigma_1\rangle(t) \\ \langle \sigma_1^\dagger\sigma_2\rangle(t) \\ \langle \sigma_1^\dagger\sigma_1^\dagger\sigma_1\sigma_2\rangle(t) \\ \langle \sigma_1^\dagger\sigma_1\sigma_2^\dagger\sigma_2\rangle(t) \end{pmatrix} = \begin{pmatrix} n_1(t) \\ n_{12}(t) \\ 0 \\ n_B(t) \end{pmatrix}. \tag{4.9}$$

Here, we have introduced some notation in order to highlight the meaning of each quantity: $n_i \in \mathbb{R}$ (for $i = 1,2$) are the probabilities of having each dot excited (1 or 2), independently of the other dot's state. $n_B \in \mathbb{R}$ is the probability that both dots are excited. If the QDs were uncoupled, we would have $n_B = n_1 n_2$. The quantity $n_{12} \in \mathbb{C}$ is the coherence between the dots due to the direct coupling. The

third mean value of vector $\mathbf{v}$, $\langle\sigma_1^\dagger\sigma_1^\dagger\sigma_1\sigma_2\rangle$, is zero due to the fact that each dot can only guest one exciton and, therefore, $\sigma_1^\dagger\sigma_1^\dagger = 0$ when the operators are applied at the same time. This simplifies the algebra as only three elements of the first row in matrix $e^{-\mathbf{M}_1\tau}$ need to be computed in order to obtain the correlator of Eq. (4.8).

Note that n_B is also the population of state $|B\rangle$ (see Fig. 4.1). The population of the intermediate state $|Ei\rangle$, and also the probabilities of having only dot i excited, is given by $n_{Ei} = n_i - n_B$. The population of the ground state is given by $n_G = 1 - n_1 - n_2 + n_B$. The last interesting averages are the excitation of each dot, n_1 or n_2, and the total excitation in the system, $n_1 + n_2$.

In order to insert these average quantities in the expression for the spectrum, they must be, either time integrated in the SE case to give $\mathbf{v}^{\mathrm{SE}} = \int_0^\infty \mathbf{v}(t,t)dt$ (and the coefficients $l_p^{\mathrm{SE}}, k_p^{\mathrm{SE}}$) or computed directly in the SS to give $\mathbf{v}^{\mathrm{SS}} = \lim_{t\to\infty}\mathbf{v}(t,t)$ (and the coefficients $l_p^{\mathrm{SS}}, k_p^{\mathrm{SS}}$). The normalized spectra for the direct emission of dot 1 follows from our general expression

$$S_1(\omega) = \frac{1}{\pi}\sum_{p=1}^{4}\left[L_p\frac{\frac{\gamma_p}{2}}{\left(\frac{\gamma_p}{2}\right)^2+(\omega-\omega_p)^2} - K_p\frac{\omega-\omega_p}{\left(\frac{\gamma_p}{2}\right)^2+(\omega-\omega_p)^2}\right], \qquad (4.10)$$

with $L_p = l_p/n_1$, $K_p = k_p/n_1$ being the normalized coefficients in the SE or SS case.

4.2.1 Mean values

The mean values of interest can be found through the quantum regression formula, applied on the set of correlators from the first and second manifolds $\tilde{\mathscr{N}}_{k\leq 2}$ (see Fig. 4.2) with $\Omega_1 = 1$ and the corresponding regression matrices. As in the LM, the correlators in $\tilde{\mathscr{N}}_1$ can be obtained independently solving the Eq. (3.6) with the same regression matrix $\mathbf{M}_0$ and pumping term $\mathbf{p}$ as in Eq. (3.7), only changing indexes $a,b \to E1,E2$ and with the fermionic parameters, $\Gamma_{a,b} \to \Gamma_{1,2}$. The solutions for n_1, n_2 and n_{12} are, therefore, given by the equivalent expressions of the LM. On the other hand, n_B, that belongs to $\tilde{\mathscr{N}}_2$, finds its expression separately, only in terms of n_1 and n_2, through the equation

$$\frac{dn_B(t)}{dt} = -4\Gamma_+ n_B(t) + P_{E2}n_1(t) + P_{E1}n_2(t)\,. \qquad (4.11)$$

In the SE, Eqs. (3.10)–(3.11) apply for an initial state with averages

$$n_1^0 \equiv n_1(0) \in [0,1], \quad n_2^0 \equiv n_2(0) \in [0,1], \quad \text{and} \quad n_{12}^0 \equiv n_{12}(0)\,. \qquad (4.12)$$

n_B gets in the SE case decoupled and simply decays from its initial value: $n_B(t) = e^{-4\gamma_+ t}n_B^0$. This is not the same result as with coupled bosons: even in the decay

from the state $|B\rangle = |1,1\rangle$, the population $\rho_{1,1}$ can oscillate as a result of the exchange with the other states that are available in the second manifold ($|2,0\rangle$ and $|0,2\rangle$). The fact that some mean values undergo analogous dynamics than in the LM, does not imply that the populations of the states do as well. This is because the mean values do not have the same meaning in terms of populations in both models. For instance, n_1 has not the same expression in the example of the decay from $|B\rangle = |1,1\rangle$: in the 2LSs $n_1 = n_{E1} + n_B = \rho_{1,0} + \rho_{1,1}$ while for the HOs $n_a = \rho_{1,0} + \rho_{1,1} + 2\rho_{2,0}$.

In the SS, the mean values of $\tilde{\mathscr{N}_1}$ can be written in terms of effective pump and decay parameters, as in the LM, but now with the fermionic statistics:

$$n_i^{\mathrm{SS}} = \frac{P_i^{\mathrm{eff}}}{\gamma_i^{\mathrm{eff}} + P_i^{\mathrm{eff}}} \quad (i = 1,2)\,, \tag{4.13a}$$

$$n_{12}^{\mathrm{SS}} = \frac{2g^{\mathrm{eff}}}{\Gamma_1^{\mathrm{eff}} + \Gamma_2^{\mathrm{eff}}} \frac{\gamma_{E1}P_{E2} - \gamma_{E2}P_{E1}}{\Gamma_1\Gamma_2}\, e^{i\phi}\,, \tag{4.13b}$$

$$P_i^{\mathrm{eff}} = P_i + \frac{Q_i}{\Gamma_1 + \Gamma_2}(P_{E1} + P_{E2})\,, \quad \gamma_i^{\mathrm{eff}} = \gamma_i + \frac{Q_i}{\Gamma_1 + \Gamma_2}(\gamma_{E1} + \gamma_{E2})\,, \tag{4.13c}$$

and with the corresponding Purcell rate $Q_1 = 4(g^{\mathrm{eff}})^2/\Gamma_2$, the effective coupling strength at nonzero detuning $g^{\mathrm{eff}} = g/\sqrt{1 + \left(\frac{\Delta/2}{\Gamma_+}\right)^2}$ and the phase $\phi = \arctan\left(\frac{\Gamma_+}{\Delta/2}\right)$. The only mean value that is missing to complete all SS non-vanishing ones is n_{B}, that takes a simple intuitive form in the SS,

$$n_{\mathrm{B}}^{\mathrm{SS}} = \frac{n_1^{\mathrm{SS}}P_{E2} + n_2^{\mathrm{SS}}P_{E1}}{\Gamma_1 + \Gamma_2}\,. \tag{4.14}$$

Note the difference with the equivalent n_B^{SS} for bosons, $\langle a^\dagger a b^\dagger b\rangle^{\mathrm{SS}}$, in Eq. (3.73). Mathematically, it comes from the fact that $\langle a^\dagger a b^\dagger b\rangle^{\mathrm{SS}}$ depends on other correlators of $\tilde{\mathscr{N}_2}$, as we explained in Sec. 3.6, while n_B^{SS} does not (see Fig. 4.2).

In the most general case, with pump and decay, from the initial to the steady state, also the transient dynamics of the mean values are given by the equivalent expressions from coupled bosons, Eq. (3.75). The general $n_B(t)$ must be found by solving Eq. (4.11). We can conclude from this, as we did for the LM, that the one-time dynamics are ruled by the exact fermionic counterpart of the (half) Rabi frequency in Eq. (3.12), that we will refer to as R^{1TD}. In a naive approximation to the problem, following from the abundant similarities with the LM, one could imagine that the definitions of WC and SC regimes stem from the real part of $R_0^{\mathrm{1TD}} = R^{\mathrm{1TD}}(\Delta = 0)$, being zero or not. However, we will see that this is not the case whenever both pump and decay are taken into account. The one-time dynamics seem to disconnect completely from the more involved SC/WC distinction that we will find solving the two-time dynamics.

4.2.2 Spectrum at resonance in the Steady State

The general expressions for the spectrum and correlator find a simple analytic solution at resonance, $\omega_{E1} = \omega_{E2}$, and in the SS under incoherent continuous pump. In what follows, we refer always to such situation and therefore drop the SS label. The four complex coefficients,

$$l_1 + ik_1 = \frac{1}{16Rz_1}\Big\{\Big[2(2z_1 + i\Gamma_2)(R - i\Gamma_-) + a_1\Big]n_1 + a_2 n_2 + 2g\Big[-\frac{P_{E1}}{\Gamma_+}(2z_1 + i\Gamma_2) + 2(R + z_1 + i\Gamma_+)\Big]n_{12}\Big\}, \tag{4.15a}$$

$$l_2 + ik_2 = \frac{1}{16Rz_2}\Big\{\Big[2(2z_2 + i\Gamma_2)(R + i\Gamma_-) - a_1\Big]n_1 - a_2 n_2 + 2g\Big[\frac{P_{E1}}{\Gamma_+}(2z_2 + i\Gamma_2) + 2(R - z_2 - i\Gamma_+)\Big]n_{12}\Big\}, \tag{4.15b}$$

$$l_3 + ik_3 = \frac{1}{16Rz_1}\Big\{\Big[2(2z_1 - i\Gamma_2)(R - i\Gamma_-) - a_1\Big]n_1 - a_2 n_2 + 2g\Big[-\frac{P_{E1}}{\Gamma_+}(2z_1 - i\Gamma_2) - 2(R - z_1 + i\Gamma_+)\Big]n_{12}\Big\}, \tag{4.15c}$$

$$l_4 + ik_4 = \frac{1}{16Rz_2}\Big\{\Big[2(2z_2 - i\Gamma_2)(R + i\Gamma_-) + a_1\Big]n_1 + a_2 n_2 + 2g\Big[\frac{P_{E1}}{\Gamma_+}(2z_2 - i\Gamma_2) - 2(R + z_2 - i\Gamma_+)\Big]n_{12}\Big\}, \tag{4.15d}$$

with the new definitions

$$a_1 = \frac{g^2}{\Gamma_+^2}[4\Gamma_+^2 + 2P_{E1}(P_{E2} - 2\Gamma_+) - P_{E2}\Gamma_1], \quad a_2 = \frac{g^2}{\Gamma_+^2}P_{E1}(P_{E1} - \gamma_{E1}), \tag{4.16}$$

and the corresponding frequencies and decay rates

$$\frac{\gamma_1}{2} + i\omega_1 = 2\Gamma_+ + iz_1, \qquad \frac{\gamma_2}{2} + i\omega_2 = 2\Gamma_+ + iz_2, \tag{4.17a}$$

$$\frac{\gamma_3}{2} + i\omega_3 = 2\Gamma_+ - iz_1, \qquad \frac{\gamma_4}{2} + i\omega_4 = 2\Gamma_+ - iz_2, \tag{4.17b}$$

are all given in terms of two complex parameters,

$$z_{1,2} = \sqrt{(D^s g)^2 - (\Gamma_+ \mp iR)^2}. \tag{4.18}$$

D^s is a real positive quantity, between 0 and $\sqrt{2}$, given by

$$D^s = \frac{\sqrt{(\gamma_{E1}P_{E2} + \gamma_{E2}P_{E1})/2}}{\Gamma_+} \tag{4.19}$$

that speaks of the *degree of symmetry* in the system. For example, it is one when all parameters are equal, $\gamma_{E1} = \gamma_{E2} = P_{E1} = P_{E2}$, and zero if one of the parameters is much larger than the others. The renormalized coupling,

$$G = D^s g\,, \tag{4.20}$$

reaches its maximum when the parameters are such that $D^s = \sqrt{2}$. The enhancement by 2 is related to cooperative behavior of two coupled modes, similarly to the superradiance of 2 atoms of the Dicke model (Chapter 6) or the renormalization by n in the JCM for a manifold with n photons (Chapter 5).

The last and main parameter appearing in the previous expressions is

$$R = \sqrt{g^2 - (D^s g)^2 - \Gamma_-^2}\,. \tag{4.21}$$

This is the true analog of the (half) Rabi frequency, R_0, in the LM [Eq. (3.31)]. We refer to it by R and not by R_0^{2TD}, as it would correspond to the two-time related quantity at resonance, for simplicity of notation. At vanishing pump, the renormalized coupling converges to g, and both R and R_0^{1TD} converge exactly to R_0 (LM).

The normalized spectra for the direct emission of dot 1 follows from Eq. (4.10) with the coefficients we just obtained. It is composed of four peaks with positions and broadenings given respectively by the real and imaginary parts of z_1 and z_2. These latter parameters are valid also in the SE case by only setting the pumping rates to zero. Fig. 4.3 is an example of the spectrum $S_1(\omega)$ we have constructed (in solid black), with its four peaks, each of them a combination of Lorentzian and dispersive parts.

4.3 Strong and Weak coupling at resonance

The criteria for strong coupling is based, as in the other cases we study in this work, on the splitting of the bare excitonic energies (degenerate at resonance $\omega_{E1} = \omega_{E2} = 0$) into dressed states. This is manifested in the appearance of oscillations in the two-time correlators and a splitting of the peaks that compose their spectrum. The four peaks are always positioned symmetrically in two pairs around the bare energy ($\omega_p \neq 0$ for all p). From Eq. (4.17), we know that ω_p are given by $\pm\Re(z_{1,2})$. Therefore,

$$\Re(z_{1,2}) \neq 0 \tag{4.22}$$

is the mathematical condition for SC in this system. Given that there are two different parameters z_1 and z_2 on which the condition relies, the SC/WC distinction

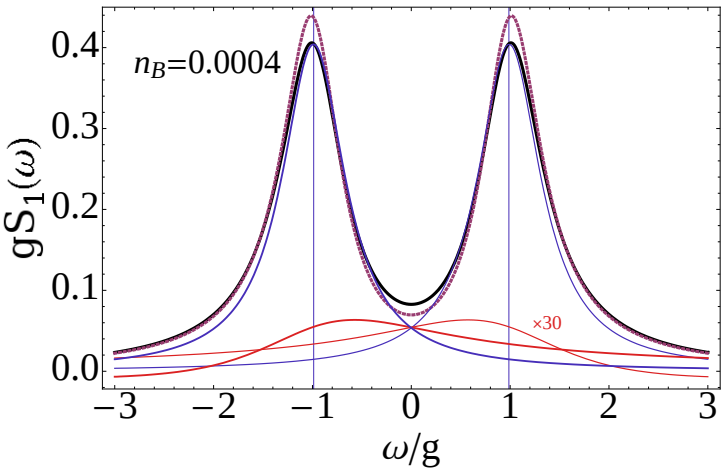

Figure 4.3: Direct emission spectrum from QD 1 (thick solid black line) in the SC regime ($\gamma_{E1} = g$ and $\gamma_{E2} = g/2$) for the SS under vanishing pump ($P_{E1} = 0.02g$ and $P_{E2} = 0.01g$). The four peaks that compose the spectra are plotted with a thin blue line (lower transitions 1, 4) and with a thin red line (upper transitions 2, 3). The equivalent spectra in the LM is plotted with a dashed purple line for comparison. Due to the low pump, the doubly excited state $|B\rangle$ is almost empty and the emission from upper transitions very weak (magnified $\times 30$ to be visible). This is the linear regime where all models for two coupled modes converge.

that sufficed with bosons must be extended to cover new possibilities. Instead of one relevant parameter, Γ_-/g, as was the case of the LM, the type of coupling between two 2LSs, depends on a set of three parameters

$$\{\Gamma_-/g\,,\Gamma_+/g\,,G/g = D^s\}\,. \tag{4.23}$$

4.3.1 Vanishing pump (and SE) case in the manifold picture

Only in the case of vanishing pump, that corresponds as well to the SE situation, the simple SC/WC classification holds. In this limit, we recover the familiar expression for the half Rabi frequency $R, R^{1\mathrm{TD}} \to R_0 = \sqrt{g^2 - \gamma_-^2}$ [as in Eq. (3.31)]. The parameters simplify to $z_{1,2} \to \sqrt{(R_0 \pm i\gamma_+)^2}$ and the associated condition for SC reduce to R_0 being real, or more explicitly $g > |\gamma_-|$, as in the LM. In SC the positions and broadenings of the four peaks reduce to

$$\frac{\gamma_1}{2} + i\omega_1 = \gamma_+ + iR_0\,, \qquad \frac{\gamma_2}{2} + i\omega_2 = 3\gamma_+ + iR_0\,, \tag{4.24a}$$

$$\frac{\gamma_3}{2} + i\omega_3 = 3\gamma_+ - iR_0\,, \qquad \frac{\gamma_4}{2} + i\omega_4 = \gamma_+ - iR_0\,. \tag{4.24b}$$

The two pairs of peaks $p = 1,4$ and $p = 2,3$ sit on the same points although they have different broadenings. This means that all peaks undergo the transition

into WC simultaneously, when $R_0 \to i|R_0|$ and both $z_{1,2} \to |\gamma_+ \pm |R_0||i$ become imaginary, giving

$$\omega_p = 0\,, \quad p = 1,2,3,4\,, \tag{4.25a}$$

$$\frac{\gamma_1}{2} = \gamma_+ - |R_0|\,, \quad \frac{\gamma_2}{2} = \gamma_+ + |R_0|\,, \tag{4.25b}$$

$$\frac{\gamma_3}{2} = 3\gamma_+ - |R_0|\,, \quad \frac{\gamma_4}{2} = 3\gamma_+ + |R_0|\,, \tag{4.25c}$$

since $\gamma_+ > |R_0|$ in WC regime. The four peaks collapse into four Lorentzians at the origin with four different broadenings. The transition $SC \to WC$ is not smooth in the sense that, for instance, peak 2 takes the place of 4 (as well, 4 of 3 and 3 of 2 as we show bellow). But this is simply a sign that the dressed states disappear in WC. In any case, all observables behave smoothly in the transition (as in the LM).

It it important to note that, as a result of the two pairs of peaks sitting always on the same two frequencies, the final spectra can only be either a single peak or a doublet, being both shapes possible in SC or WC regimes (as in the LM and for the same reasons).

The manifold picture (see Section 2.5.2) gives a very intuitive derivation and interpretation of the results in this limit. We consider the non-Hermitian Hamiltonian $H_{\text{n.h.}}$ that results from making the substitution $\omega_{E1,E2} \to \omega_{E1,E2} - i\gamma_{E1,E2}/2$ in Eq. (4.1), in order to include the decay of the modes. Diagonalizing the Hamiltonian in the first manifold [as with the two HOs, see Eq. (2.57) and discussions related in Chapter 3], we obtain

$$H_{\text{n.h.}} = E_{\text{G}}\,|G\rangle\langle G| + E_{\text{U}}\,|U\rangle\langle U| + E_{\text{L}}\,|L\rangle\langle L| + E_{\text{B}}\,|B\rangle\langle B| \tag{4.26}$$

with dressed complex energies

$$E_{\text{G}} = 0\,, \quad E_{\substack{\text{U}\\\text{L}}} = \omega_{E1} - i\frac{\gamma_{E1}+\gamma_{E2}}{4} \pm R_0\,, \quad E_{\text{B}} = 2\omega_{E1} - i\frac{\gamma_{E1}+\gamma_{E2}}{2}\,. \tag{4.27}$$

Applying Eq. (2.99) between the energies in Eq. (4.27), leads to the positions and broadenings of Eq. (4.24)–(4.25) in the way that we now explain. In Fig. 4.1(a) we can see the four possible transitions in the manifold picture: one can check that

- the lower transitions (in blue), from $|U\rangle$ and $|L\rangle$, coincide, respectively, with the expressions for peaks 1 and 4 in SC, Eq. (4.24) and 1 and and 2 in WC, Eq. (4.25);
- the upper transitions (in red), towards $|L\rangle$ and $|U\rangle$, coincide with the expressions for peaks 2 and 3 in SC, Eq. (4.24) and 3 and and 4 in WC, Eq. (4.25).

The upper transitions have a larger broadening than the lower due to the addition of the uncertainties in energy of the levels involved, brought by the spontaneous decay. This is also the case in the LM, if we consider the individual transitions, in terms of the states inside each manifold. But, in the end, the resulting SE from an initial state takes place, not only at the same two energies, but also with the same brodenings, regardless the manifold of origin. The spectral shape (the Rabi doublet) is manifold independent. The inhomogeneity in the broadenings for coupled QDs, makes a difference in the SE spectra out of the linear regime (with manifolds $k > 1$ involved). The spectra, like the populations, is different in both models if the initial state is that of the second manifold, $|B\rangle$ (or $|1,1\rangle$), because in the LM there are two more states in the same manifold to couple with, than for the 2LSs.

On the other hand, the SS case in the limit of vanishing pump is exactly the linear regime, where only the vacuum and first manifold are populated. The spectra in this limit converges with the LM and also it can be analyzed in terms of manifolds by extension. For instance, the spectrum in Fig. (4.3) corresponds to SC for vanishing pump, for $\gamma_{E1} = g$ and $\gamma_{E2} = g/2$. The lower transition peaks, in blue, dominate over the broader and weak upper peaks, in red, and as a result, the splitting in dressed modes is visible in the observed spectrum, in black. We now use this configuration in what follows to explore the effect of the incoherent continuous pump.

4.3.2 The effect of the pump and the SC/WC phase space

The different regions that can appear when the incoherent continuous pump is turned on (situation (b) in Fig. 4.2), are plotted in Fig. 4.4 as a function of the pumping rates. All the possibilities are defined in terms of $\Re(z_1)$ and $\Re(z_2)$ being zero or not. The conditions arising are linked to R (that can only be real or pure imaginary) although not so straight forwardly as in the absence of pump.

The most extended region is the standard *(first order) strong coupling* (FSC, in light blue), which includes the SC regime in the absence of pump. It is characterized by

$$R = |R| \in \mathbb{R} \quad \Leftrightarrow \quad G^2 > g^2 - \Gamma_-^2 \,, \tag{4.28}$$

from what follows that $z_1 = z_2^*$, and therefore $\Re(z_1) = \Re(z_1) \neq 0$. Note that this requires

$$g > \frac{|\Gamma_-|}{\sqrt{|1-(D^s)^2|}} \,. \tag{4.29}$$

The two pairs of peaks 1, 4 and 2, 3 are placed one on top of each other although they are differently broadened [see the spectra of Fig. 4.3 and of Fig. 4.5(a) and

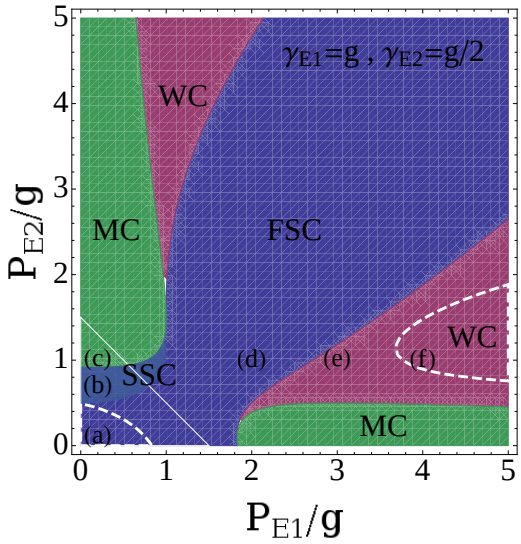

Figure 4.4: Phase space of the SS strong/weak coupling regimes as a function of pump for $\gamma_{E1} = g$ and $\gamma_{E2} = g/2$. In strong coupling (SC, blue), one can distinguish two regions, the more extended first order (FSC, dark blue) and the second order (SSC, light blue) strong coupling . The weak coupling regime (WC) is shaded in purple and the mixed coupling regime (MC), with two transitions in SC and two in WC, in green. The white solid line delimits the region (bellow) where the SS is reached in the LM, always in SC for these decay parameters. The dashed white lines enclose the two regions where two peaks can be resolved in the direct emission of the first QD, $S_1(\omega)$. One falls in SC and the other in WC. Six points are marked with letters (a)–(f) for a latter analysis.

(d)]. In this region, $D^s < 1$, so it is not possible to reach the maximum coupling and splitting of the lines given by $\sqrt{2}g$.

In Figs. 4.6(a) and (b) we track the broadenings and positions of the four peaks (1 and 4 in blue and 2 and 3 in red) as a function of pump, through the SC region of Fig 4.4, on the line $P_{E2} = P_{E1}/2$. Following them from zero pump, where the manifold picture is exact, the four peaks can be easily associated with the lower and upper transitions of Fig. 4.1, and that is why we use the same color code. The dressed states $|U\rangle$ and $|L\rangle$ exist but with energies $\omega_{E1} \pm \Re(z_1)$, both affected equally by decoherence.

By construction, the resulting spectra in this regime can only be a doublet [Fig. 4.5(a)] or a single peak [Fig. 4.5(d)], depending on the magnitude of the broadening of the peaks (that always increases with pump and decay) against the splitting of the lines (that always decreases). As in the LM, observing a doublet in the spectra is not granted in SC, but here the tendency is always the same: the lower the pump and the decay, the better the resolution of the splitting.

The second situation, the Rabi frequency being imaginary,

$$R = i|R| \quad \Leftrightarrow \quad G^2 > g^2 - \Gamma_-^2 \,, \tag{4.30}$$

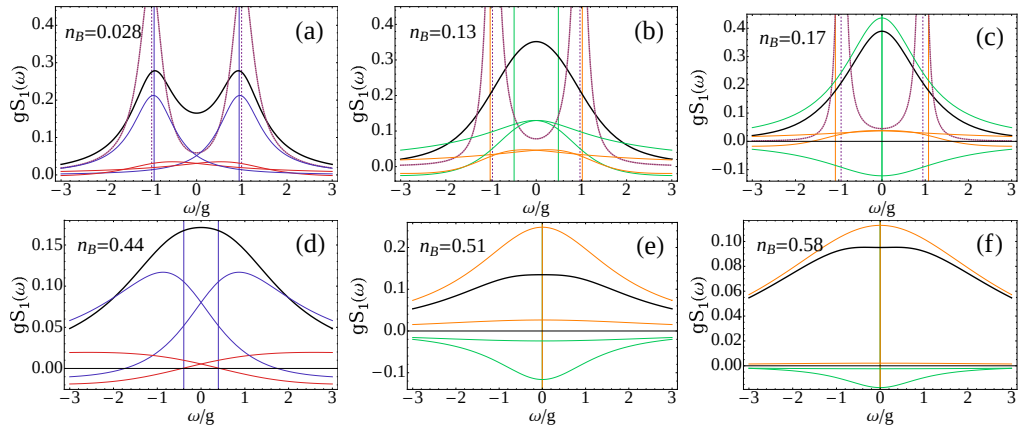

Figure 4.5: A set of spectra for $\gamma_{E1} = g$ and $\gamma_{E2} = g/2$ sampling all the different regions of Fig 4.4. The pump parameters of each plot are marked with their corresponding letter (a)–(f) in the phase space plot 4.4. The final spectral line (in thick solid black) is decomposed into two pairs of symmetric peaks (thin red-blue or green-orange) in SC and four peaks centered at zero in WC. The positions of these peaks are marked with vertical lines of the corresponding colors. The LM spectra (purple dashed), always in SC, is composed of only two peaks marked also with vertical lines for comparison.

opens three possibilities, that constitute the three remaining regions in Fig. 4.4. In what follows we assume condition Eq. (4.30) and add new conditions to define the three such regions.

The *weak coupling* regime (WC, in purple) is characterized by

$$z_1 = i|z_1| \neq z_2 = i|z_2| \quad \Leftrightarrow \quad G < |\Gamma_+ - |R|| \tag{4.31}$$

and therefore $\Re(z_1) = \Re(z_1) = 0$. Note that condition (4.31) is not analytical in terms of the relevant parameters of Eq. (4.23). The four peaks are placed at the origin with four different broadenings. Again, this does not mean that the resulting spectra is always one peak [as in Fig. 4.5(e)], it can be a doublet when a thin negative Lorentzian carves a hole in a positive Lorentzian, due to the interference between the modes [as in Fig. 4.5(f)]. The dressed states $|U\rangle$ and $|L\rangle$ have collapsed in energy to ω_{E1}.

Up to here, we have studied the SC and WC as they appeared defined in the LM. We find a new region of SC, when both parameters $z_{1,2}$ are real and

$$z_1 = |z_1| < z_2 = |z_2| \quad \Leftrightarrow \quad G > |\Gamma_+ + |R||\,. \tag{4.32}$$

We call it *second order strong coupling* regime (SSC, colored in a lighter blue in the phase space). Here, the broadenings of the four peaks are equal, $\gamma_p/2 = 2\Gamma_+$, but the positions of the pairs of peaks are different, $\omega_{1,4} = \pm|z_1|$ and $\omega_{2,3} = \pm|z_2|$. The reason is that the bare energies of the modes undergo a *second order*

anticrossing induced by the interplay between coupling, pump and decay. The energies of the dressed states are affected differently by decoherence, up to the point that we should consider new eigenstates. In Fig. 4.1(c), we have plotted these states, $|I\rangle$ and $|O\rangle$, that have energies not splitted symmetrically around ω_{E1}, but rather at $+|z_1|$ (giving rise to the *inner peaks*, in green) and $-|z_2|$ (giving rise to the *outer peaks*, in orange).

We can see how peak broadenings and positions change when going from FSC to SSC in Fig. 4.6(c)–(d). In this case, we track the peaks varying P_{E2} for fixed P_{E1}, moving from the points (a) to (c) in the phase space. The first vertical line marks the border between the two kinds of SC, with the opening of a "bubble" for the positions ω_1 and ω_2 (that were equal in the FSC region), and the convergence of all the broadenings. The spectrum we choose from this region, Fig. 4.5(b), features a single peak despite the subtle underlying structure. In principle, quadruplets and triplets can form out of the four peaks. However, the broadenings and contributions of the dispersive parts (K_p) are too large to let the fine splittings emerge clearly. The spectra in this region are singlets and doublets but we will see in Sec. 4.4 with other examples, that they can be very distorted, undoubtably betraying the multi peaked structure.

The last new region in Fig. 4.4, appears when z_1 is imaginary and z_2 real, or equivalently,

$$z_1 = i|z_1|\,, \quad z_2 = |z_2| \quad \Leftrightarrow \quad |\Gamma_+ - |R|| < G < |\Gamma_+ + |R||\,. \tag{4.33}$$

This is a *mixed coupling* regime (MC, colored in green in the phase space) where the two inner peaks, 1 and 4, have collapsed at the origin in WC, and so has the associated eigenstate $|I\rangle$. The two outer peaks, 2 and 3, are still splitted and so is $|O\rangle$. The spectrum in Fig. 4.5(c) is an example of this region, too broadened to reveal its structure. Again, although a triplet seems possible, distorted singlets are the only outcome in the best of cases due to the broadening and dispersive parts. In Fig. 4.6(c)–(d) we can see the transition from SSC into MC, at the second vertical line.

The manifold picture successfully associates the peaks that compose the spectrum of emission to transitions between the levels. In order to understand better some features of the spectra of the SS under incoherent pump in the different regions we have defined, we will now push the manifold method, adequate for vanishing pump, a bit further. Note that, in this system, the pumping mechanism is of the same nature than the decay, due to the saturation of both QDs and the symmetry in the scheme of levels that they form. The master equation is symmetrical under exchange of the pump and the decay ($\gamma_{Ei} \leftrightarrow P_{Ei}$) when the the two levels of both 2LS are inverted ($G \leftrightarrow B$ and $E1 \leftrightarrow E2$), that is, pictorially, when the structure of levels and transitions in Fig. 4.2(b) are rotated 180^{o} or, mathematically, when the rising and lowering operators are inverted. Consequently, the

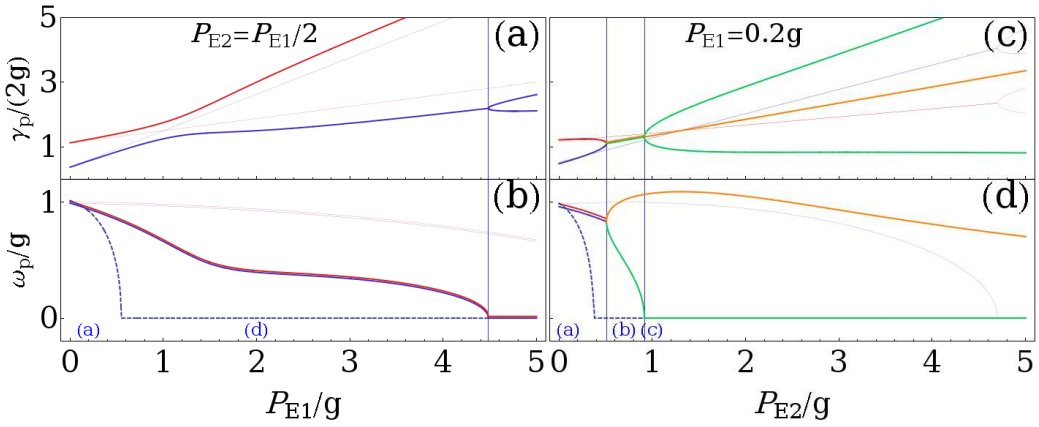

Figure 4.6: Broadenings (a), (c), and positions (b), (d) of the lines that compose the spectra as a function of pump for the decay parameters $\gamma_{E1} = g$ and $\gamma_{E2} = g/2$. In the plots of the first column, the pump P_{E1} varies with $P_{E2} = P_{E1}/2$, moving in the phase space of Fig 4.4 from point (a) to (d). The vertical line shows the crossing from FSC to WC. In the plots of the second column, the pump P_{E2} varies with $P_{E1} = 0.2g$, moving in the phase space of Fig 4.4 from point (a) to (c). The vertical lines show the crossing from FSC to SSC and finally to MC. In all the plots, the thick solid lines are the exact results [Eqs. (4.17)] while the thin ones are the approximated results from the manifold method [that follow from Eqs. (4.34)]. The dashed blue line represents the splitting as it is resolved in the final spectrum (4.10). The code of colors (red-blue and orange-green) corresponds to that of the transitions in Fig. 4.1 and the associated peaks in Fig. 4.5.

parameters z_1, z_2 and R, and also the populations of all the levels, are symmetric in the same way, as it happens with just one 2LS (see Sec. 2.5.1). In other systems we study in this manuscript, like the LM, the JCM or simply the single HO, the effect of the pump extends upwards to an infinite number of manifolds while the decay cannot bring the system lower than the ground state. There is no natural truncation for the pump (that ultimately leads to a divergence), as there is for the decay. But with coupled 2LSs, state $|B\rangle$ is the top counterpart of $|G\rangle$, undergoing a saturation when pump or decay is large, respectively. This implies, for instance, that the spectra in the limit of vanishing decay is exactly the same as that of vanishing pump and that in such case we can also apply the manifold method to obtain the right positions and broadenings as a function of pump, in the same way we did as a function of decay only. We only have to take into account the mentioned symmetry consistently. As long as the dynamics move upwards or downwards only, even when intermediate states are coupled, the manifold method is suitable.

The manifold diagonalization breaks, however, in the presence of both non-negligible pump and decay. If we combine their effects in the non-Hermitian

Hamiltonian as

$$E_{\mathrm{G}} = -i\frac{P_{E1}+P_{E2}}{2}, \quad E_{\substack{\mathrm{U}\\\mathrm{L}}} = \omega_{E1} - i\frac{\Gamma_1+\Gamma_2}{4} \pm R_0^{1\mathrm{TR}}, \quad E_{\mathrm{B}} = 2\omega_{E1} - i\frac{\gamma_{E1}+\gamma_{E2}}{2}, \tag{4.34}$$

we do not obtain the right results of four, in principle different, peaks but rather the standard pairing with

$$\frac{\gamma_{1,4}}{2} + i\omega_{1,4} = \gamma_+ \pm iR_0^{1\mathrm{TR}} + \frac{3}{4}(P_{E1}+P_{E2}), \tag{4.35a}$$

$$\frac{\gamma_{2,3}}{2} + i\omega_{2,3} = 3\gamma_+ \pm i(R_0^{1\mathrm{TR}})^* + \frac{1}{4}(P_{E1}+P_{E2}). \tag{4.35b}$$

These expressions bring us back to the naive association of SC with $\Re(R_0^{1\mathrm{TR}}) \neq 0$ that we discussed Sec. 4.2.1. It is obvious that only $R_0^{1\mathrm{TR}} = \sqrt{g^2-\Gamma_-^2}$, to describe the splitting between the dressed states, cannot give the variety of situations than the two parameters $z_{1,2}$ give. But there are other fundamental differences. One is the renormalization of the coupling constant into G, due to the interplay of pump and decay. Another one is made more clear when comparing $z_{1,2} = \sqrt{G^2-(\Gamma_- \mp iR)^2}$ (at resonance) with $R^{1\mathrm{TR}} = \sqrt{g^2-(\Gamma_- + i\frac{\Delta}{2})^2}$ (out of resonance). The Rabi R is acting as a *complex detuning* for $z_{1,2}$, like Δ for $R^{1\mathrm{TR}}$. When R is real (in FSC), it behaves like a normal real detuning, pushing the all positions outwards in the same way (see Fig. 3.2). However, if R is imaginary, it induces a difference between the real parts of z_1 and z_2 when they exist (SSC and MC), giving rise to a second order anticrossing.

Let us look now, for instance, at the positions and brodenings in Figs. 4.6(a) and (b). In thin lines (with the usual color code) we can see the approximate values from Eq. (4.35). Not only they deviate quantitatively from the exact values, but they are also qualitatively wrong giving too late the transition into WC and a crossing of the broadenings when they really repel and stay one above the other. The joined presence of coupling, decay and pump has a more complicated effect than simply bringing the excitations up and down the levels of Fig. 4.1. The positions and broadenings are also connected with the populations. For example, the anticrossing of the broadenings takes place at the same point where the populations of the intermediate states reach a maximum and state B starts to be the most populated. By manifold reasoning, the lower transitions would have larger broadening than the upper, increasing the pump after this point. However, the emptying of levels G and $E1$, $E2$ seems to decelerate this intuitive tendency. Even more dramatic is the divergence between the approximate and the exact positions and broadenings in Figs. 4.6(c) and (d). Eqs. (4.35) cannot reproduce the second anticrossing, as we said.

4.4 Some examples

In this Section we will look more closely into the populations and spectral features of a two cases of interest: that of the effective enhancement of the coupling, $g \leq G \leq \sqrt{2}g$, and that of a detrimental, $0 \leq G \leq g$.

4.4.1 Optimally symmetrical cases: $g < G \leq \sqrt{2}g$

As a first example, we study the situation where the parameters are equal only in a crossed way: $P_{E1}/g = \gamma_{E2}/g$ and $P_{E2}/g = \gamma_{E1}/g$. The system has a total input that is equal to the total output, $P_{\rm TOT} = \gamma_{\rm TOT}$, and also equal effective decoherence rates, $\Gamma_1 = \Gamma_2$, and, therefore, equal Purcell rates, $Q_1 = Q_2$. This is a very special situation where the symmetry is not total but it exist between the effective rates and there is a total compensation of the flows with the exterior. It leads to $1 < D^s < \sqrt{2}$ and a positive renormalization of the coupling strenght, from g to $G > g$. This is a very unexpected effect to be completely induced by decoherence, more precisely, by the optimal interplay between dissipation and incoherent pump. Interestingly, the present configuration of parameters, that can make the coupling more effective, is not accessible in the LM where Γ_+ vanishes and the system does not have SS. In the LM nothing seems to indicate that the coupling gets renormalized at resonance, decoherence has the only effect of diminishing the splitting of the dressed states ($g \to \sqrt{g^2 - \Gamma_-^2}$).

In Fig. 4.7 we have plotted the phase space of SC as a function of $P_{E1}/g = \gamma_{E2}/g$ and $P_{E2}/g = \gamma_{E1}/g$ with the usual color code. This configuration is in FSC only when all parameters are equal, $D^s = 1$, (blue line) and *total symmetry* is recovered. Otherwise, the possibility of reaching all other coupling regimes opens as the coupling is effectively improved $G < g$. The SSC and MC regions are linked to the absence of total symmetry. In the inset we can see that, as a consequence of this special configuration, the system is richer in spectral shapes than the previous one studied. The lineshape can be a doublet (area in white), a distorted doublet (light grey), a distorted singlet (dark grey) and a singlet (black), as listed in Table 4.1, although it never reaches a triplet or quadruplet form.

The Y-axis in Fig. 4.7, with $P_{E1} = \gamma_{E2} = \gamma$ and $P_{E2} = \gamma_{E1} = 0$, is interesting enough with all the possible regions and lineshapes, to be analyzed in more detail. This is the limit of maximum renormalization of the coupling, $G = \sqrt{2}g$ ($D^s = \sqrt{2}$), where the populations and mean values read

$$n_2 = \frac{1}{2+x^2}\,, \quad n_1 = 1 - n_2\,, \quad n_B = \frac{1/2}{2+x^2} \neq n_1 n_2\,, \quad n_{12} = -i\frac{x/\sqrt{2}}{2+x^2}\,, \quad (4.36)$$

with $x = P_{E1}/G = \gamma_{E2}/G$. The two QDs are sharing one excitation only. The Rabi

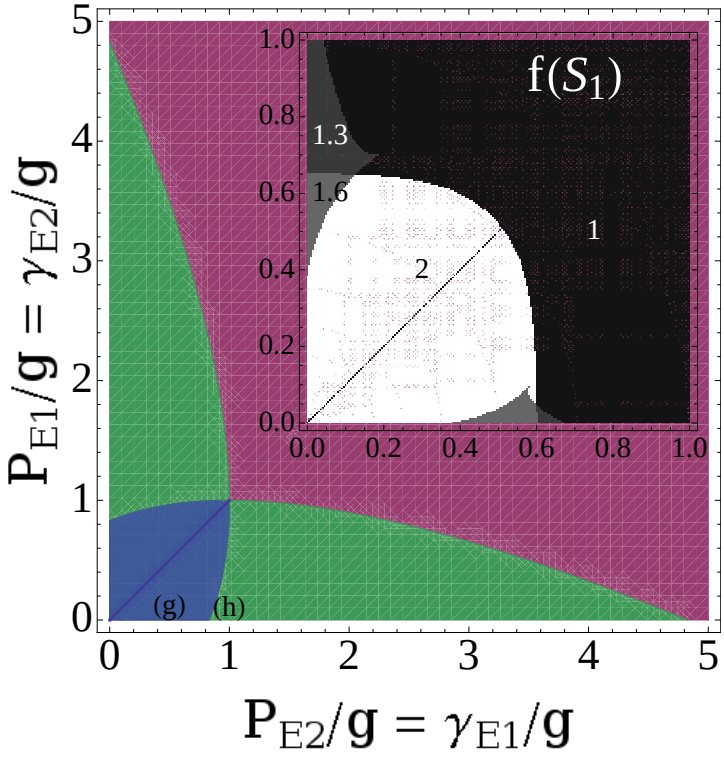

Figure 4.7: Phase space of FSC/SSC/MC/WC as function of $P_{E1}/g = \gamma_{E2}/g$ and $P_{E2}/g = \gamma_{E1}/g$. The color code is that of Fig. 4.4. In inset, the possible lineshapes of $S_1(\omega)$: a doublet (in white), a distorted doublet (light grey), a distorted singlet (dark grey) and a singlet (black), as in Table 4.1.

also simplifies to $R = ig$, because $\Gamma_- = 0$, and $z_{1,2} = \sqrt{G^2 - (g \pm \frac{\gamma}{2})^2}$. In Fig. 4.8, we can see all these magnitudes in the different regimes.

In the limit $x \ll 1$, there is FSC with all the levels equally populated ($n_1 = n_2 = 1/2$, $n_b = 1/4$) and $n_{12} = -ix/\sqrt{2}$. Soon the SSC opens a bubble in the eigenenergies with the splitting of inner and outer peaks. The transition into MC, with the collapse of the inner peaks, takes place at $\gamma = 2(\sqrt{2}-1)g$, and into WC, closing the bubble, at $\gamma = 2(\sqrt{2}+1)g$. The maximum of $z_2 = \sqrt{2}g$ (in orange) takes place at $\gamma = 2g$, when the coherence $|n_{12}| = 1/4$ is maximum. This is a special point where the splitting of the dressed mode is the largest possible, $2\sqrt{2}g$, even though the final lineshape is a singlet. Finally, when the coupling becomes very weak, $x \gg 1$, the first dot saturates and $n_2 = n_B = n_{12} = 0$.

The spectra acquires interesting lineshapes: a doublet in SSC that gets distorted towards a quadruplet in Fig. 4.8(g), and then towards a triplet in (h), as the inner peaks close. Before reaching WC the spectra has become a plain singlet. The way to distinguish mathematically the different possible shapes is explained in Table 4.1.

Lineshape	L_1	L_2	$L_1 \times L_2$	$f(S_1)$
singlet	1	2	2	1
distorted singlet	1	6	6	1.3
distorted doublet	3	8	24	1.6
doublet	3	4	12	2
triplet	5	6	30	3
quadruplet	7	8	56	4

Table 4.1: Correspondence between the lineshape of the spectrum and the value of functional $f(S_1)$. A lineshape can be defined by the product $L_1 \times L_2$: L_1 (L_2) is the number of times that $S_1(\omega)$ changes slope (concavity), that is, the number of real solutions to the equation $dS_1/d\omega = 0$ ($d^2S_1/d\omega^2 = 0$).

4.4.2 Detrimentally symmetrical cases: $0 < G \leq g$

Two equal QDs create a symmetric system of levels in the "horizontal" sense: $\gamma_{E1} = \gamma_{E2} = \gamma$ and $P_{E1} = P_{E2} = P$ ($\Gamma_1 = \Gamma_2$ but $\gamma_{\rm TOT} \neq P_{\rm TOT}$). Effectively, the populations behave as if the two dots were uncoupled

$$n_1 = n_2 = \frac{P}{\gamma + P}, \quad n_B = n_1 n_2, \quad n_{12} = 0, \tag{4.37}$$

although the system is always in strong coupling (FSC) with

$$R = \frac{|\gamma - P|}{\gamma + P} g, \tag{4.38}$$

and $D^s = 2\sqrt{\gamma P}/(\gamma + P)$. If $P \gg \gamma$, or the other way around, the symmetry in the "vertical" sense is completely broken and $D^s = 0$.

The second possibility is the case $\gamma_{E1} = P_{E1}$ and $\gamma_{E2} = P_{E2}$ ($\Gamma_1 \neq \Gamma_2$ but $\gamma_{\rm TOT} = P_{\rm TOT}$), which is symmetrical in the vertical sense. This is equivalent to both 2LS in a thermal bath of infinite temperature, so that pump and decay become equivalent. Now $D^s = 2\sqrt{\gamma_{E1}\gamma_{E2}}/(\gamma_{E1} + \gamma_{E2})$ and the populations are also effectively uncoupled, $n_1 = n_2 = 1/2$, $n_B = n_1 n_2$, $n_{12} = 0$. The Rabi reads

$$R = \frac{|\Gamma_-|}{\Gamma_+} \sqrt{g^2 - \Gamma_+^2}, \tag{4.39}$$

and gives the conditions for SC/WC regions in terms of Γ_+. If $\gamma_{E1} \gg \gamma_{E2}$ or the other way around, the symmetry in the "horizontal" sense is broken and $D^s = 0$.

In the particular case that all the parameters are equal to γ, the symmetry is perfect in all senses ($D^s = 1$). Again, all the levels are equally populated ($n_1 = n_2 = 1/2$, $n_B = 1/4$) and uncoupled ($n_{12} = 0$) but the Rabi vanishes. The SC/WC regimes become conventional with $z_{1,2} = \sqrt{g^2 - \gamma^2}$. Some asymmetry in the parameters is needed to reach the SSC and MC regimes.

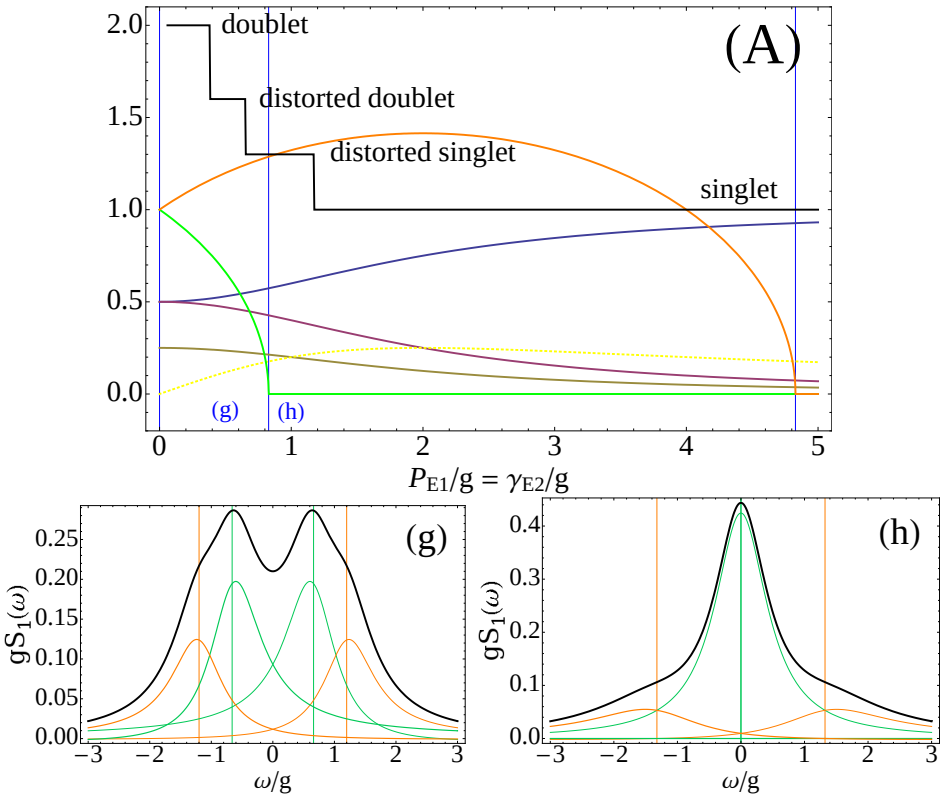

Figure 4.8: (A) Various magnitudes (ω_1 in green, ω_2 in orange, n_1 in blue, n_2 in purple, n_B in brown, $|n_{12}|$ in dashed yellow) as function of $P_{E1}/g = \gamma_{E2}/g$, for $P_{E2} = \gamma_{E1} = 0$. The vertical lines mark the transitions from from SC (at 0) to SSC, to MC, to WC, also clear from the evolution of the "bubble" in positions. The function $f(S_1)$ (in black) tracks the lineshape of the spectra as coded in Table 4.1. The most interesting lineshapes, that can only appear in SSC and MC, are the distorted quadruplet (h) and singlet (g), for parameters marked in plot (A). The total spectra (in black) is decomposed in inner (green) and outer (orange) peaks coming from the transitions in Fig. 4.1(c).

4.5 Second order correlation function

In order to obtain the correlator $\langle\sigma_1^\dagger(t)\sigma_1^\dagger(t+\tau)\sigma_1(t+\tau)\sigma_1(t)\rangle$, and $g_1^{(2)}(\tau)$, but also the cross correlator $\langle\sigma_1^\dagger(t)\sigma_2^\dagger(t+\tau)\sigma_2(t+\tau)\sigma_1(t)\rangle$ to compute $g_{12}^{(2)}(\tau)$, we can proceed as in Sec. 3.6. Once more, the quantum regression formula in Eq. (2.116), for the general set of operators $C_{\{m,n,\mu,\nu\}} = \sigma_1^{\dagger m}\sigma_1^n\sigma_2^{\dagger\mu}\sigma_2^\nu$, is the same as that used to compute the mean values. We solve the same equations, the only difference as compared with the expressions for the LM are the steady state

vectors,

$$\mathbf{w}^{\mathrm{SS}} = \begin{pmatrix} 0 \\ n_B \\ 0 \\ 0 \end{pmatrix}, \quad \mathbf{f}^{\mathrm{SS}} = \mathbf{w}^{\mathrm{SS}} - \mathbf{u}^{\mathrm{SS}} n_1^{\mathrm{SS}} = -\begin{pmatrix} n_1^2 \\ n_1 n_2 - n_B \\ n_{12} n_1 \\ n_{12}^* n_1 \end{pmatrix}. \tag{4.40}$$

The general solutions for the correlators in the SS for $\tau > 0$ are:

$$g_1^{(2)}(\tau) = 1 + \frac{[e^{-\mathbf{M}_0 \tau} \mathbf{f}^{\mathrm{SS}}]_1}{n_1^2}, \tag{4.41a}$$

$$g_{12}^{(2)}(\tau) = \frac{n_B}{n_2} + \frac{[e^{-\mathbf{M}_0 \tau} \mathbf{f}^{\mathrm{SS}}]_2}{n_1 n_2} \tag{4.41b}$$

where $[\mathbf{x}]_1$ means that we take the first element of the vector $\mathbf{x}$. At zero delay we have, $g_1^{(2)}(\tau = 0) = 0$ and $g_{12}^{(2)}(\tau = 0) = n_B/(n_1 n_2)$, and at infinite delay, $g_1^{(2)}(\tau \to \infty) \to 1$ and $g_{12}^{(2)}(\tau \to \infty) \to n_B/n_2$. As it corresponds to fermions, the emission presents *antibunching*, that is, the second photon cannot be emitted at the same time as the first one, but in a posterior emission, $g^{(2)}(0) < g^{(2)}(\tau)$.

4.6 Conclusions

In this Chapter, I have presented the counterpart for two two-level systems of the general formalism developed in Chapter 3, valid in both cases of SE and SS emission. I have focused on the resonant SS case, where an analytical solution exists and new regimes of coupling appear as compared with the LM.

The main results of this Chapter are to be found in Eqs. (4.10) and (4.15)–(4.21) that provide the analytical expression for the emission spectra. With decay and pump, the criteria for SC/WC does not rely on the analogous of the LM Rabi frequency but on the two generalized parameters $z_{1,2}$. The new set of relevant constants grows from Γ_-/g alone in the LM, to $\Gamma_-/g\,, \Gamma_+/g\,, D^s$.

The phase space in Fig. 4.4 is a good summary of all the possible regimes. FSC is the standard SC with two symmetrically splitted dressed modes and two doublets sitting on top of each other forming the spectra (a singlet or doublet depending on the resolution). SSC is specific to this system and corresponds to asymmetric dressed modes: the spectra is composed of two differently positioned doublets and this can result in distorted doublets and singlets (Fig. 4.8). In the same way, MC is when one of the dressed modes goes into WC, and can result in a distorted singlet. WC has also the standard definition, of no dressed states, and manifestation, four peaks at the bare energy of the modes. One or two peaks can

be observed at resonance in all the regimes although only at SSC distorted doublets (almost quadruplets) can appear, and only at SSC and MC distorted singlets (almost triplets). The appearance of these regimes and lineshapes is induced by decoherence and some asymmetry in the parameters, $D^s \neq 1$. It is linked to an enhancement of the coupling of up to $\sqrt{2}g$.

Chapter 5

One quantum dot in a microcavity: nonlinear models

Contents

In this Chapter, we study, semi-analytically, light-matter coupling with nonlinearities. We solve the anharmonic oscillator (weakly interacting excitons) and its coupling to a second harmonic oscillator (one cavity mode) and the Jaynes-Cummings model (small quantum dot in a cavity). We analyze the properties of emission of all these descriptions in the presence of decoherence (dissipation and incoherent pump). Most of the results presented here have been published in the references 3, 10 and 14 from the list on Page 225.

5.1 Introduction

In absence of nonlinearity or saturation of some sort, the quantum case is equivalent to the classical one (see, for instance, the work by Rudin & Reinecke (1999)). In particular, the PL spectrum exhibits a Rabi doublet at resonance, which can be equally well accounted for by a purely classical model, as was shown by Zhu et al. (1990). There is therefore a strong incentive to evidence nonlinear deviations and attribute them to quantum effects. Numerous proposals and experiments can be found in the literature on the topic: Schneebeli et al. (2008), Steiner et al. (2008), Srinivasan & Painter (2007), Press et al. (2007), Kroner et al. (2008).

With QDs in microcavities, two types of strong nonlinearities are expected, both associated to the active material, i.e., the excitons. The first one comes from Coulomb repulsion of the charged particles, and is the one investigated in Secs. 5.2 and 5.3, in the case where it is comparable to the coupling strength or decaying rate. In Sec. 5.2 we first study isolated excitons with interactions, in an anharmonic oscillator model (AO), in order to understand the implications of interactions alone. In Sec. 5.3 we add such interactions to the linear model (LM) and investigate their effect on the strong coupling (SC) physics and spectra. We have in mind large dots (or microcavity polaritons), where excitons still behave as weakly interacting bosons. In this context, Pauli exclusion (the second nonlinearity we refer to) can be taken into account phenomenologically by a phase-space filling effect that screens the exciton-photon interaction, as it has been done before by Hanamura (1970), Schmitt-Rink et al. (1985) or Ĭmamoḡlu (1998). This results in loss of strong-coupling and we therefore focus on the intermediate regime in these two first sections, where such renormalization of the coupling strength can be neglected. We prefer to take into account Pauli exclusion, and the saturation induced, separately in Sec. 5.4. It arises from the fermionic character of the particles that compose the exciton (electrons and holes) as it has been pointed out by Combescot & Betbeder-Matibet (2004) among others. The model by definition to study fermionic saturation is the Jaynes-Cummings model (JCM) that we introduced in Sec. 2.3 which consist in the coupling of an harmonic oscillator (AO) and a two-level system (2LS). With this separate analysis of the nonlinearities in dissipative and incoherently pumped light-matter systems, we can conclude in Sec. 5.5 which feature in the spectra of emission can be attributed to which effect.

As usual, in this Chapter, we neglect the spin-degree of freedom, in particular the sign-dependent interaction between same and opposite-spins excitons, respectively. This allows us to focus on nonlinear deviations and neglecting more complicated correlations effects of the multi-excitons complexes such as formations of bound pairs or molecules that would give rise to bipolaritons, as was shown by Ivanov et al. (1998), Ivanov et al. (2004) or Gotoh et al. (2005). Experimentally, this could be realized by using a circularly polarized pump.

5.2 The anharmonic oscillator

In Chapter 2 we introduced the Hamiltonian (2.69) of the AO, that includes exciton-exciton interactions when the excitons can still be considered as bosons. Then, interactions manifest as additional energy cost for the multiply occupied states. The total Hamiltonian for uncoupled interacting excitons is

$$H = \omega_b b^\dagger b + \frac{U}{2} b^\dagger b^\dagger b b \,, \tag{5.1}$$

with U being positive and $U \ll \omega_b$ for weakly repulsive excitons. The steady state of the system under pump and decay (in a thermal bath) is the same (thermal state with $n_b = P_b/(\gamma_b - P_b)$) as the harmonic case, as has been shown for example by Scully & Zubairy (2002). The complete dissipative time dynamics has also been obtained analytically, for example by Milburn & Holmes (1986). However, in our approach, we concentrate on the correlators and power spectra computed from the master equation (2.74) (only for the exciton b) thanks to the quantum regression formula, as we described in Chapter 2. The results we obtain are physically valid when $U \ll \omega_b$ and the approximations made to derive the master equation hold, as was argued by Alicki (1989). We restrict the discussion to such limits.

In this Section, we see how the simple Hamiltonian spectral structure given by Eq. (2.93) turns into a more complex expression that cannot easily be found analytically.

5.2.1 First order correlation function and power spectrum

The set of operators that are needed to compute the correlator of interest, $\langle b^\dagger(t) b(t+\tau)\rangle$, are the most general set $\{C_{\{m,n\}} = b^{\dagger m} b^n\}$, differently than for the harmonic oscillator in Section 2.6. The regression matrix M is defined by the following rules:

$$M_{\substack{mn \\ mn}} = i\omega_b(m-n) + i\frac{U}{2}[m(m-1) - n(n-1)] - (m+n)\frac{\gamma_b - P_b}{2} \,, \tag{5.2a}$$

$$M_{\substack{mn \\ m+1,n+1}} = iU(m-n) \,, \tag{5.2b}$$

$$M_{\substack{mn \\ m-1,n-1}} = P_b mn \,. \tag{5.2c}$$

This gives rise to an infinite set of coupled equations for any general correlator. $\langle b^\dagger(t) b(t+\tau)\rangle$, is linked to all correlators of the kind $C_n(t,t+\tau) = \langle b^\dagger(t)(b^{\dagger n-1} b^n)(t+\tau)\rangle$ with $n = 1, 2, \ldots$ (see Fig. 5.1), through the general equation:

$$\frac{d}{d\tau} C_n(t,t+\tau) = -\left[i\omega_b + i(n-1)U + (2n-1)\frac{\Gamma_b}{2}\right] C_n(t,t+\tau) \tag{5.3a}$$

$$- iUC_{n+1}(t,t+\tau) + n(n-1)P_b C_{n-1}(t,t+\tau) \,. \tag{5.3b}$$

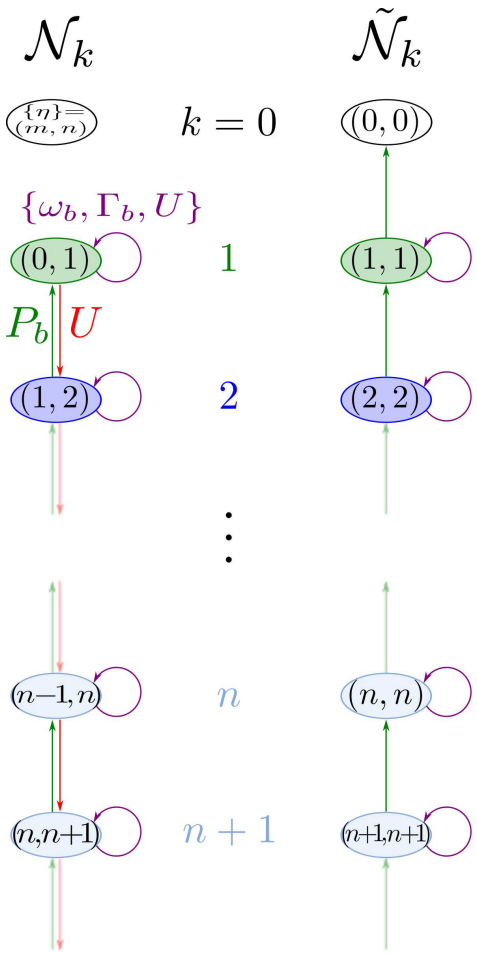

Figure 5.1: Chain of correlators—indexed by $\{\eta\}=(m,n)$—linked by the Hamiltonian dynamics with pump and decay for one AO. On the left (resp., right), the set $\mathscr{N}_k$ (resp., $\tilde{\mathscr{N}}_k$) involved in the equations of the two-time (resp., single-time) correlators. In green is shown the first manifold. The equation of motion $\langle b^\dagger(t)C_{\{\eta\}}(t+\tau)\rangle$ with $\eta\in\mathscr{N}_1$ requires for its initial value the correlator $\langle C_{\{\tilde{\eta}\}}\rangle$ with $\{\tilde{\eta}\}\in\tilde{\mathscr{N}}_1$ defined from $\{\eta\}=(m,n)$ by $\{\tilde{\eta}\}=(m+1,n)$, as seen on the diagram. The arrows show the connections due to the incoherent pumpings P_b (in green) and the interactions (in red). The sense of the arrows indicates which element is "calling" which in its equations. The self-coupling of each node to itself is shown in violet circular arrow (affected by ω_b, Γ_b and U). These links are obtained from the rules in Eq. (5.2a). The dimension of the manifolds is always one. A manifold k is only linked directly to $k\pm1$ in this model.

$\Gamma_b = \gamma_b - P_b$ is the effective bosonic broadenings. Also here, we can write the general equation in a matricial form, $d\mathbf{v}(t,\tau)/d\tau = -\mathbf{M}_1\mathbf{v}(t,\tau)$ where $\mathbf{v}$ is the vector of the ordered correlators $C_n(t,t+\tau)$ ($n = 1,2,\ldots$) and $\mathbf{M}_1$ the corresponding nondiagonal regression matrix extracted from Eq. (5.3). Finally, we integrate to $C_n(t,t+\tau) = e^{-\mathbf{M}_1\tau}C_n(t,t)$. The initial average values for the correlators $C_n(t,t) = \langle b^{\dagger n}b^n\rangle(t)$ can be found through the density matrix,

$$C_n(t,t) = \sum_{j=n}^{\infty}\frac{j!}{(j-n)!}\rho_{jj}(t)\,, \tag{5.4}$$

or applying again the quantum regression formula. The second set of equations,

$$\frac{d}{dt}C_n(t) = -n\Gamma_b C_n(t,t) + n^2 P_b C_{n-1}(t,t)\,, \tag{5.5}$$

are easily solved in the two cases we are interested in. The steady state (SS) is, as we said, the thermal state [Eqs. (2.34)-(2.35)] for which $C_n^{\mathrm{SS}} = n!n_b^n$ and $n_b = P_b/\Gamma_b$. The spontaneous decay (SE) from an initial state defined by $C_n^0 = \langle b^{\dagger n}b^n\rangle(0)$ gives simply $C_n^{\mathrm{SE}}(t,t) = e^{-n\gamma_b t}C_n^0$. In both cases, the mean one time values do not depend on the interactions. They are the same than for the harmonic oscillator.

SE analytical spectrum

The correlators $C_n(t,t+\tau)$ cannot be found analytically in the general case with pump because the Hilbert space is infinite ($n \in [1,\infty)$). The formula (2.108) of the spectra must be kept in general terms for the SS emission. The SE case truncates naturally the Hilbert space as the dynamics of decay only involves states with less number of excitations than the initial one ($n_{\max}$). Therefore, the solution can be obtained analytically for the correlator of interest,

$$C_1^{\mathrm{SE}}(t,\tau) = e^{-(\omega_b+\gamma_b/2)\tau}\sum_{n=1}^{n_{\max}}\frac{1}{(n-1)!}\Big[\frac{U}{U-i\gamma_b}(e^{-(iU+\gamma_b)\tau}-1)\Big]^{n-1}C_n^{\mathrm{SE}}(t,t)\,, \tag{5.6}$$

and its spectrum. The parameters that define the Lorentzian and dispersive lineshapes and their weight for each peak $p = 1,2,\ldots,n_{\max}$ in the expression (2.108) are

$$\omega_p = \omega_b + (p-1)U\,, \quad \gamma_p = (2p-1)\gamma_b\,, \tag{5.7a}$$

$$L_p^{\mathrm{SE}}(t) = \frac{(-1)^{p-1}}{(p-1)!}\sum_{n=p}^{n_{\max}}\Big(\frac{-U}{U^2+\gamma_b^2}\Big)^{n-1}\frac{\Re[(U+i\gamma_b)^{n-1}]}{(n-p-2)!}\frac{C_n^0}{nn_b^0}\,, \tag{5.7b}$$

$$K_p^{\mathrm{SE}}(t) = \frac{(-1)^{p-1}}{(p-1)!}\sum_{n=p}^{n_{\max}}\Big(\frac{-U}{U^2+\gamma_b^2}\Big)^{n-1}\frac{\Im[(U+i\gamma_b)^{n-1}]}{(n-p-2)!}\frac{C_n^0}{nn_b^0}\,. \tag{5.7c}$$

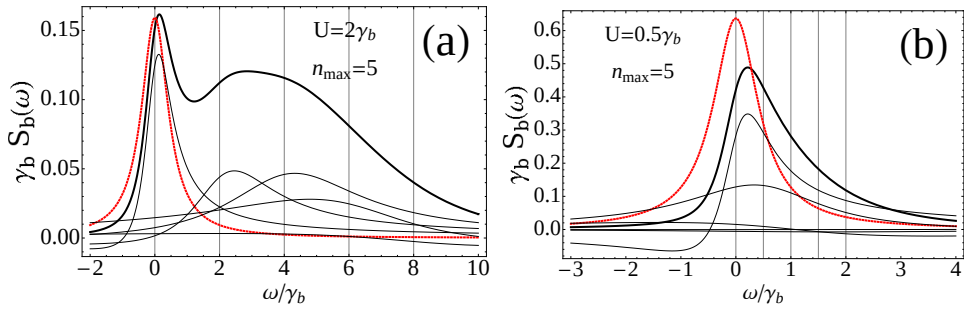

Figure 5.2: SE spectra of emission of the AO (thick black line) from the state $|5\rangle$ as compared to the HO emission (a Lorentzian in dashed red). Large interactions (a) help resolving the five peaks of each transition (thin lines) in the de-excitation process, while small interactions (b) give rise to a broad asymmetric peak. The position of the individual peaks are marked with vertical lines at $(p-1)U$. γ_b is the unit here and $\omega_b = 0$ is the reference energy.

The positions and broadenings are reproduced by the manifold method of Sec. 2.5.2, meaning that we can associate each individual peak p with the transitions from the manifold with p to $p-1$ excitations. The peak p is weighted in the total spectra by L_p and K_p, which are a sum of contributions from the dynamics of all the states above the ones of the transition, that is, those from p to $n_{\max}$. The only line that remains at ω_b is that corresponding to the decay from the first manifold, the linear regime with $p = 1$. The rest of lines are *blue-shifted* for each manifold p, from ω_b (HO) to $\omega_b + (p-1)U$ and they are broadened from γ_b to $\gamma_b + 2(p-1)\gamma_b$ (the higher the manifold, the broader the peak as compare to the HO), as we can see in Fig. 5.2 (thin black lines). We consider $\omega_b = 0$ as the reference energy from now on.

For large interactions, Fig. 5.2(a), the individual transitions can be resolved, while if they are not very large ($U < \gamma_b$), they stick together forming a broad asymmetric peak at the origin, as in Fig. 5.2(b). The asymmetry may result also in an additional effective blueshift, noticeable if we compare with the Lorentzian symmetric emission of the HO (in dashed red).

Spectrum in the Steady State

When the pump is taken into account and the spectra computed in the SS, the situation changes, as we can see in Fig. 5.3, and there are several regimes appearing. Plot (a) corresponds the most to the "quantum" regime, with low pump ($P_b < \gamma_b$), so that only the first manifolds are probed, and large interactions ($U > \gamma_b, P_b$), so that the individual transitions are distinguishable. In this regime, where the individual peaks can be well resolved, each peak narrows with pump, behaving like a *multimode laser*. The larger the interactions, the more separated and narrower the

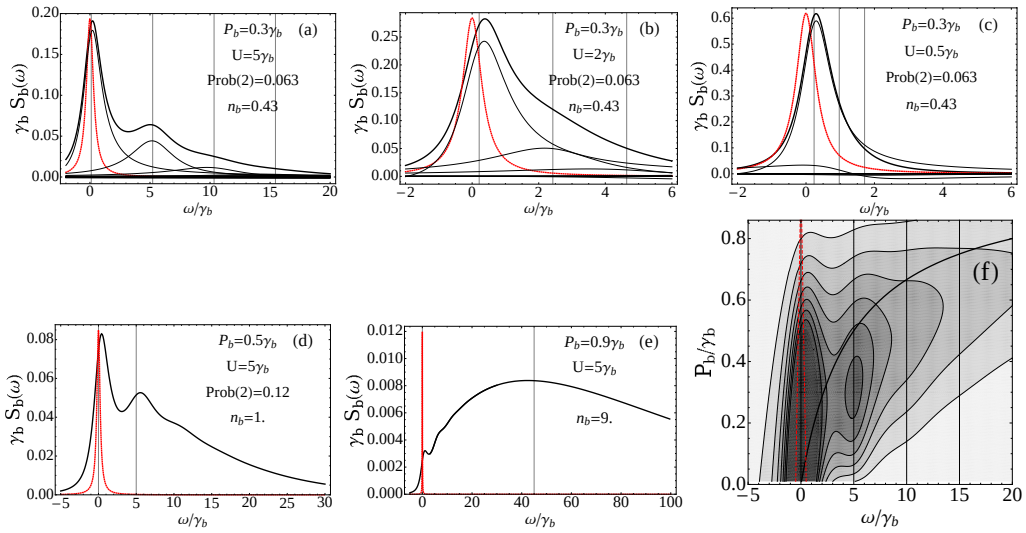

Figure 5.3: SS spectra of emission of the AO (thick black line) as compared to the HO emission (a Lorentzian in dashed red) for the parameters in inset (all in units of γ_b). In the first row (a)–(c) we fix the pumping to $P_b = 0.3\gamma_b$ and decrease the interactions, loosing in resolution of the second and third manifold peaks (thin lines) and recovering the Lorentzian lineshape. The shifted positions of the peaks are marked with vertical lines in order to compare with the SE positions $(p-1)U$. In the second row (d)–(f), we fix the interactions to a large number, $U = 5\gamma_b$, and increase the pump in order to achieve $n_b > 1$ (*lasing regime*). High manifold transitions melt into a broad shoulder for the AO while the HO Lorentzian, narrows with $\Gamma_b = \gamma_b - P_b$. The shoulder is placed approximately at Un_b evidencing a transition from a "quantum" (with resolved individual transition) to a "classical" (a mean field broad peak) regime. (f) Contour plot of this effect as a function of pump (large emission in black). The peak positions $(p-1)U$ (vertical thin lines), the ever narrowing Lorentzian $\pm\Gamma_b/2$ (dashed red) and the value of n_bU (black thick line), are plotted for comparison. HO and AO populations diverge in the same way as pump approaches γ_b but their spectra is qualitatively very different, the first one narrowing and the latter effectively broadening and blueshifting. γ_b is the unit here and $\omega_b = 0$ is the reference energy.

peaks are and the less interference between them exist.

When the pump is of the order of the decay [Fig. 5.3(a)–(d)], the individual peaks from the different manifold transitions (centered at the vertical guide lines) are further shifted from the SE positions $(p-1)U$ due to the pump/decay interplay. If the interactions are large, still the peaks can be resolved, but when they are small, the peaks start to overlap and interfere (they grow a dissipative contribution) resulting in a broad shoulder on the right side of the central linear peak $p = 1$. They end up forming a distorted asymmetrical Lorentzian when $U < \gamma_b$. Therefore, decreasing interactions at low pump induces a transition from the "quantum" to "classical" regime in the sense that, even with $n_b \ll 1$, without interactions, the system turns into an HO.

The second possibility to induce the quantum to classical transitions, is to increase pump, as it is done in the Fig. 5.3(d)–(f). For the HO (dashed red lines), the effective linewidth can only decrease with pump as $\Gamma_b = \gamma_b - P_b$ (this is a bosonic signature). Its population, the same as the AO in this model, reaches $n_b = 1$ when $P_b = 0.5\gamma_b$. Although for a thermal mixture the vacuum is always the most probable state, at this point one can say that there is an "inversion" of the population: the probability to have excitons in the SS (given by $1 - P_b/\gamma_b$) overcomes the probability of vacuum (given by P_b/γ_b), as in the 2LS. The HO starts "lasing" with a noticeable narrowing of the linewidth if pump is further increased. For the AO, $P_b = 0.5\gamma_b$ is also the point at which the second to first manifold transition energy, $(p-1)U$ with $p = 2$, is the same as the mean transition energy, $n_b U$ [vertical line in Fig. 5.3(d)]. This means that manifolds of excitations ($p > 1$) start to behave as an ensemble of emitters with inhomogeneous broadenings. Two lines can be resolved, the broad envelope of an increasing number of peaks from transitions $p > 1$, and the first manifold transition $p = 1$, corresponding to the linear regime. The broad emission peak is placed approximately at the mean manifold energy $n_b U$, while the linear peak is at 0. Fig. 5.3(e) shows an example of high pump, where this transition has taken place and the linear peak has been almost swallowed by the mean field of manifold emissions. The result is a blueshifted peak at $n_b U$ with a broadening of the order of $n_b U$ as well. Increasing pump or interactions in the AO has a "saturation" effect, as pump does in the two-level system (2LS). There, as we know, $P_\sigma = 0.5\gamma_\sigma$ is also the point of population inversion and also the broadening increases as $\Gamma_\sigma = \gamma_\sigma + P_\sigma = n_\sigma P_\sigma$. The transition can be seen in all its detail in the contour plot of Fig. 5.3(f). The well distinguished peak $p = 2$ at $\omega = 5\gamma_b$, melts into the mean field peak at around $P_b \approx 0.5\gamma_b$. The mean field peak blueshifts then following $n_b U$ (the black bending line) and becoming soon more important than the linear peak $p = 1$.

It is interesting to note that for $P_b > 0.5\gamma_b$ (classical regime) the quantum regression formula expressed in terms of correlators, becomes numerically unstable and infinite precision is needed to obtain a solution for an adequate truncation. The best way to compute the spectra here is applying Eq. (2.111). The fact that this method is blind to the peak structure (that betrays a quantized structure), is already telling us that the best description of the system is not anymore in terms of manifolds of correlators but rather some mean field approximation. The truncation that Eq. (2.108) involves is of a different nature than that of Eq. (2.111), for the same $n_{\max}$. The first one takes place in the Hilbert space of correlators and therefore requires that all averages $\langle b^{\dagger n} b^n \rangle = n! n_b^n$ with $n > n_{\max}$ are dispensable. The second truncation, takes place in the Hilbert space of states and therefore requires that all the populations $\rho_{nn} = (1+n_b)^{-(1+n)} n_b^n$ with $n > n_{\max}$ are negligible. In order to understand the implications of this difference, we plot in Fig. 5.4 the average values $\langle b^{\dagger n} b^n \rangle$, in (a), and SS populations ρ_{nn}, in (b), as a function of n,

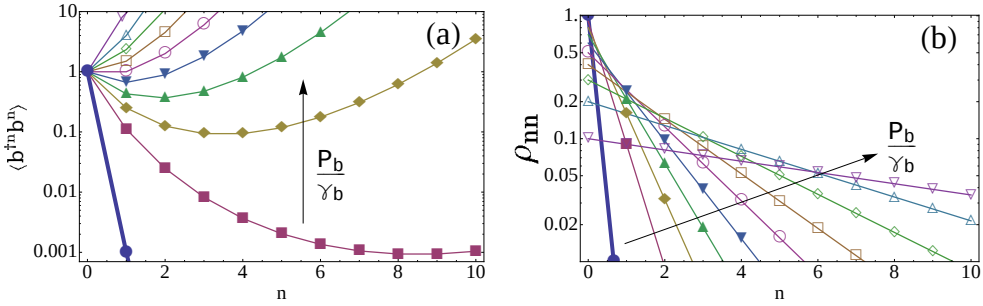

Figure 5.4: Comparison between the truncation of the QRF in the Hilbert space of correlators (a) and in the Hilbert space of states (b), equal for both HO and AO. In (a), respectively (b), we plot the average values $\langle b^{\dagger n} b^n \rangle$ (SS populations ρ_{nn}) as a function of n, for the whole range of physical P_b/γ_b. Pump increases in the sense of the arrow as $P_b/\gamma_b = 0.001, 0.1, 0.2, \ldots, 0.9$.

for the whole range of physical parameters $P_b/\gamma_b \in [0,1)$.

We can see that the truncation imposed on the density matrix is always safe, as long as the $n_{\max}$ is taken high enough ($n_{\max} \approx 10$ for $P_b < 0.8\gamma_b$, for instance), because thermal populations decrease always with n. The problem of using Eq. (2.111) to compute the spectra, however, is the high computational cost, as we already pointed out. On the other hand, the truncation in correlators looks only safe at vanishing pump (the thick curve) as it is the only one that does not grow up again at some n. In fact, the criteria to find $n_{\max}$, so that one can safely neglect the correlators with $n > n_{\max}$, is a bit more complicated than looking at this graph. The best criteria is simply that the solution does not change when increasing the truncation. However, Fig. 5.4 is representative of the increasing precision that one must use to solve the system as the pump is increased. The sooner the mean values $\langle b^{\dagger n} b^n \rangle$ start to increase with n (it does always increase at some n for $P_b \neq 0$), the more difficult for the final result is to converge into the finite solution. We will find again this kind of increasing numerical complexity in the JCM as we cross to its classical regime.

5.3 Linear model with excitonic interactions

In the previous Section, I have shown how, even for bosonic excitons, a multiplet structure and some fermionic signatures arise in the emission spectrum when intra-dot exciton-exciton interaction is accounted for. In this Section, we will study how these interactions change the spectral properties of the linear model that we studied in Chapter 3 in a quantum regime. The results, that we obtain in the steady state only, are not analytical anymore as in the previous Section. We describe light-matter interaction in a large QD including exciton-exciton interactions with the Hamiltonian

$$H = \omega_a a^\dagger a + \omega_b b^\dagger b + g(a^\dagger b + a b^\dagger) + \frac{U}{2} b^\dagger b^\dagger b b \,. \tag{5.8}$$

The model couples an HO (photons) with an AO (excitons). In this Section, g is the unit and $\omega_b = 0$ the reference energy. Let us start by diagonalizing Hamiltonian (5.8) by manifolds, in the spirit of Eq. (2.68). The structure of eigenenergies at resonance is sketched in Fig. 5.5 up to a maximum of two excitations (i.e., up to the second manifold) for three different cases. First, the bare levels corresponding to non-interacting and uncoupled (or weakly-coupled) modes ($g = 0$, $U = 0$). Second, the eigenenergies arising from the coupling ($g \neq 0$, $U = 0$), as we studied them in Chapter 2 and 3, and finally, the blueshifted lines that result from including the interactions ($g \neq 0$, $U \neq 0$). All the levels but those in the manifold $n = 1$, involving only one particle, change with the interactions because of the excitonic part of their corresponding eigenvectors. In order to keep track of the excitonic character of each level, in Fig. 5.6, we plot the excitonic component of the eigenvectors of manifold $n = 2$ and their corresponding eigenenergies as a function of the interaction U. We can see that, starting from a situation completely symmetric between the photonic and excitonic fractions, the higher level gets more and more excitonic-like with U and blueshifts strongly. The other two energy levels are only slightly affected, as follows from their more photonic character. This characterization of the levels, which also depends on the detuning, plays an important role when identifying the spectral lines, as we show in the following sections.

5.3.1 Spectra of emission with the manifold method

In order to obtain an intuitive picture on the optical spectrum of our system, as we have done with the other models, we first study the allowed transitions between the possible energy levels with the manifold method at vanishing pump. The energy bare levels of Fig. 5.5 acquire an imaginary part ($\omega_{a,b} \to \omega_{a,b} - i\gamma_{a,b}/2$) and we diagonalize again, applying the formula $i[E_k - (E_{k-1})^*] = i\omega_p + \gamma_p/2$ to obtain positions and broadenings associated to each transition. We consider the amplitude of probability, $I_a^{k\to k-1}$, for the processes of annihilation of a photon, that

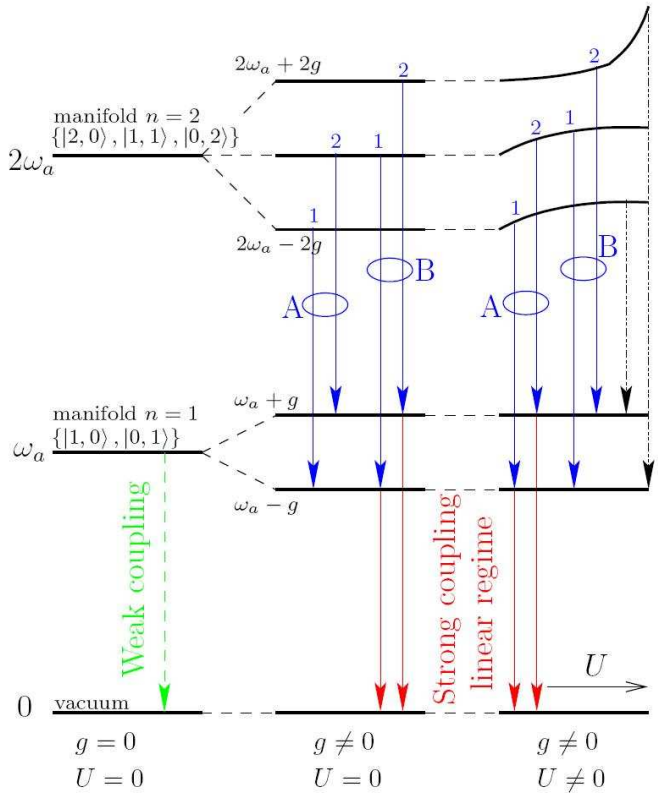

Figure 5.5: Energy levels of the eigenstates of the light-matter coupling Hamiltonian with interactions, Eq. (5.8) up to the second manifold (two excitations) at resonance ($\Delta = 0$), left panel for weak (or no-) coupling ($g = 0$), central and right panel in strong-coupling, with right panel also including interactions U varying on the x axis. The transitions between levels account for the spectral features. Red lines correspond to the vacuum Rabi doublet, that turns into a singlet in WC regime (transitions in green). Blue lines superimpose to the Rabi doublet when higher manifolds are probed. Without interactions, $U = 0$, these transitions are not distinguishable in the spectra. Transitions $2 \rightarrow 1$ in presence of interactions are plotted in Fig. 5.7 as a function of the detuning and U. New qualitative features appear thanks to the interactions. Black dashed lines are new transitions previously forbidden, although they remain weak.

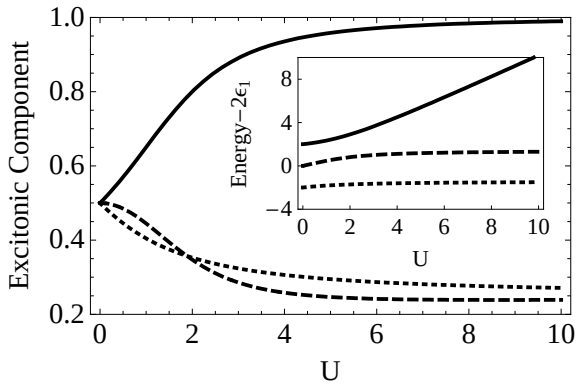

Figure 5.6: Excitonic component at resonance of the eigenvectors of H, corresponding to the three energy levels of the manifold $n = 2$ (see Fig. 5.5) as a function of the interaction strenght U. Varying the detuning also changes the character of the lines. In inset are plotted the exact corresponding eigenenergies as a function of U, that are sketched in the right-upper part of Fig. 5.5.

is, the transitions corresponding to the normal mode emission, as in Eq. (2.100). We know from previous results that, if the coupling and interactions are strong enough, the contribution of each transition to the optical spectrum $S_a(\omega)$ can be approximated by an independent Lorentzian weighted by the probability of its initial state times the amplitude of probability of the transition. The results are plotted for transitions between manifolds 2 and 1 only, as a function of the non-linearity strength U in Fig. 5.7(a) and as a function of the detuning in Fig. 5.7(b). In the latter case, the exciton bare energy is kept constant, equal to zero, while the cavity mode is brought in or out of resonance with the exciton. As I explained in Chapter 1, detuning is varied experimentally through a variety of techniques, like changing temperature or applying a magnetic field (shifting the energy of the dot with negligible perturbation on the cavity) or growing a thin film (shifting the cavity mode energy without affecting the dot). In Fig. 5.7(b) we see the intensity, width and location of spectral individual lines for smooth changes in the detuning.

Peaks appearing in Fig. 5.7(a) correspond to the transitions plotted in Fig. 5.5. They are labelled in blue: lower lines are the transitions "A" and upper lines the transitions "B". Comparing with the linear Rabi doublet, which is superimposed in red, we observe the aforementioned blueshift of both groups of lines, as it happened in the AO of previous Section. It is more important for the exciton-like mode (especially line B-2 at resonance when $U \gg g$) while the photon-like mode has a better resolved fine-structure splitting. At various detunings [Fig. 5.7(b)], complicated structures are found with crossing or anticrossing of the lines, as shown on the figure. Lines with the same bare-excitation (photon or exciton) character cross, whereas lines of a different character exhibit anticrossing. At

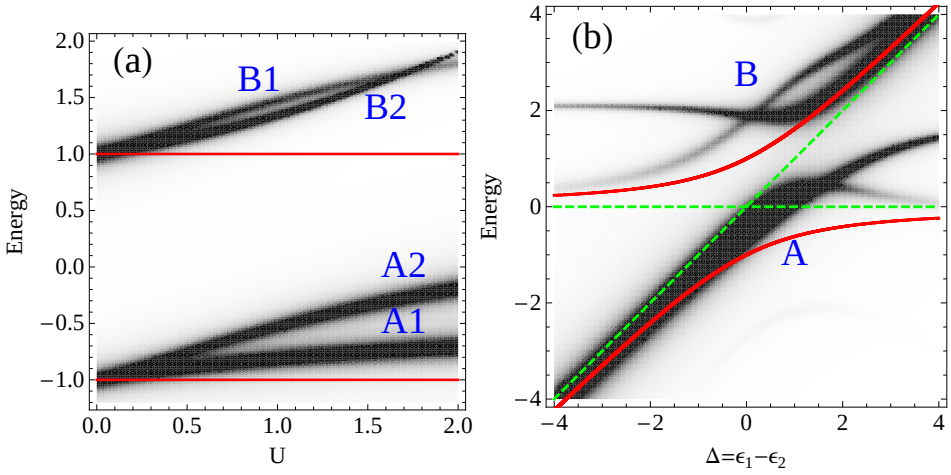

Figure 5.7: Cavity emission spectra of transitions between manifolds $2 \to 1$: (a) Resonant case as a function of interactions U. (b) Case of fixed interactions ($U = 2$) as a function of Δ. The non-interacting case $U = 0$, where only linear Rabi doublet arises, is also shown (red superimposed lines) as well as the bare cavity and excitonic lines (dashed green lines). Lines are labelled in blue corresponding to the transitions of Fig. 5.5. Parameters in both plots are: $\omega_b = 0$, $\gamma_a = 0.1g$, $\gamma_b = 0.01g$, all in units of $g = 1$.

large detunings, the bare photon and exciton modes (in green) are recovered but with an additional blueshifted bare exciton line.

Satellite peaks arise at very low and high energies from transitions that are forbidden in the LM. They enter the dynamics through nonlinear channels opened by the interactions. The dashed arrows in the right panel of Fig. 5.5 represent these two transitions, with two excitons as the initial state that release one excitation and leave one photon as the final state. They appear dimly in Fig. 5.7.

Here, as in the previous models, the manifold method allows an understanding of the composition of the spectra, as illustrated in Fig. 5.7 where the spectral lines have been labelled according to their corresponding transitions in Fig. 5.5. From this overall picture, the excitonic fraction is clearly associated to the blueshift.

5.3.2 Spectra of emission with the quantum regression formula

In order to actually know which transitions are relevant and to what extent, we solve the usual complete master equation (2.74) for dissipative coupled modes under incoherent continuous pump. In this case, we will obtain the spectra $S_a(\omega)$ with the density matrix formalism, applying Eq. (2.111).

First, we obtain the steady state elements $\rho_{ij}^{(\mathrm{SS})}$ of the system. The labels i and j index the whole Hilbert space, namely, in our case of two oscillators, $i =$

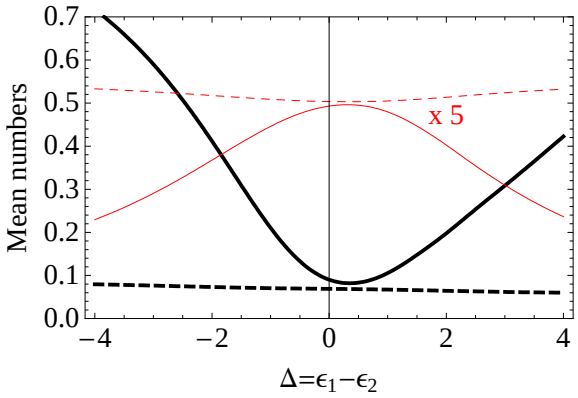

Figure 5.8: Mean number of photons (dashed line) and excitons (solid line) as a function of Δ, for the case of cavity pumping ($P_a = P$, $P_b = 0$) in thin red ($\times 5$) and electronic pumping ($P_a = 0$, $P_b = P$) in thick black. Regardless of the detuning, an approximately constant and equal population is obtained for the cavity intensity, due to the balance between the effective coupling-strenght and the exciton-population. An asymmetry is observed with detuning due to the interactions that bring the exciton closer or further to resonance with the cavity mode. Parameters: $\omega_b = 0$, $U = 2g$, $\gamma_a = 0.1g$, $\gamma_b = 0.01g$, $P = 0.01$.

$\{mn\}$ and $j = \{\mu\nu\}$. As a result, $M_{ij,kl}$ is a $n_{\max}^4 \times n_{\max}^4$ matrix where $n_{\max}$ is the truncation of each oscillator's Hilbert space. In the computations, we have checked that the results were independent of this truncation once it is taken large enough. In Eq. (2.111), A and B are the creation and destruction operators of the transitions so in the case of cavity (normal) emission, where $A = a^\dagger$ and $B = a$, we have $A_{mn;\mu\nu} = \sqrt{\mu+1}\delta_{n\nu}\delta_{m,\mu+1}$ and $B_{mn;\mu\nu} = \sqrt{\mu}\delta_{n\nu}\delta_{m,\mu-1}$.

Again, the drawback of this method is the high computational cost to obtain M and invert it for each point of the spectra. Therefore, we present here the spectra at low pump, after probing the first steps of the quantized energy levels, which presents only small deviations from the LM. We use pumping rates of $0.01g$, yielding average number of excitations of the order $\langle n_{a,b}\rangle \approx 0.1$ with probability to have two excitons of the order of 0.01. For these figures, a truncation at the fourth manifold ($n_{\max} = 3$) is enough to ensure convergence of the results. The other parameters are fixed to the following values, motivated by experiments: $g = 1$ provides the unit (experimental figures are of the order of tens of μeV), $\gamma_a = 0.1g$, $\gamma_b = 0.01g$ and $U = 2g$.

Mean numbers of excitons and photons are plotted in Fig. 5.8, for the two cases of cavity (only) and electronic (only) pumping. Close to resonance, $\Delta \approx 0$, both pumping yield approximately equal exciton and photon populations (note that the cavity pumping case has been magnified by a factor five). Detuning the modes results in a collapse (cavity pumping) or increase (electronic pumping) of the exciton population, as could be expected. Regardless of the kind of pumping,

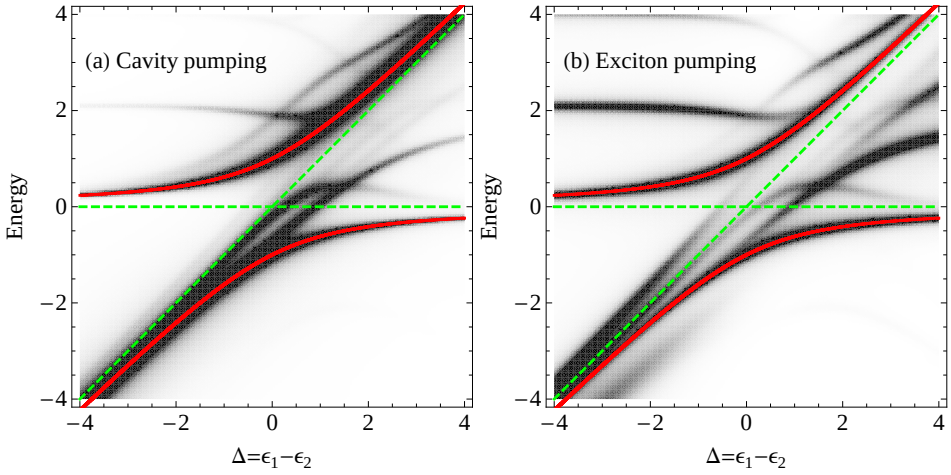

Figure 5.9: Cavity emission spectrum as a function of detuning Δ. The $U = 0$ case, which corresponds to the linear Rabi doublet, is shown in solid red and the bare exciton ($\omega_b = 0$) cavity ($\omega_a = \Delta$) lines in dashed green. The probability of having more than two excitons is very low, mostly contributions from transitions $1 \to 0$ ($p = 1$, vacuum-Rabi) and $2 \to 1$ ($p = 2$) appear. For high positive detuning, Coulomb interactions generate additional peaks close to $\omega_b + (p-1)U$. Peaks originated from transitions $3 \to 2$ ($p = 3$) appear, although with a very small intensity, due to the non-zero probability to have three excitons in the system. All energies are in units of g. Parameters: $\omega_b = 0$, $U = 2g$, $\gamma_a = 0.1g$, $\gamma_b = 0.01g$, $P = 0.01g$.

however, the cavity population is approximately constant. In the cavity pumping case, this is because the exciton gets decoupled and thus the cavity is pumped at a constant rate (one can actually see a small increase in its population). In the electronic pumping case, this is because although the coupling decreases, the exciton population increases in proportion so as to feed the cavity with a constant flux of photons. In both cases, an asymmetry is notable with detuning, because the interactions bring the cavity and the exciton modes closer or further from resonance, respectively, coupling them more efficiently for positive detuning and therefore allowing a larger production of excitons in that case. As a result, the nonlinear branches, $p > 1$, of the actual spectra, for positive and negative detunings, shown in Fig. 5.9, are not exactly as those shown in Fig. 5.7(b). The blueshifted peak is more clearly seen in the positive detuning case thanks to this exciton population asymmetry with detuning. However, an excellent qualitative agreement is obtained with the manifold method, if one superimpose the vacuum Rabi doublet to the lines arising from higher manifolds. Depending on the pumping scheme—cavity (a) or exciton (b)—only quantitative features are changed that consist mainly in different linewidths and intensities of the branches, that are otherwise well accounted for by the manifold method (see also Fig. 5.10). While

comparing Figs. 5.9(a) and (b), it should be borne in mind how the total population changes with detuning, as shown in Fig. 5.8. For this reason, panel (b) has a more complex structure, but this is due to the higher manifolds that can be reached with the electronic pumping. It is in fact possible to identify the $3 \rightarrow 2$ contribution by extracting the lines in Fig. 5.9 that do not appear in Fig. 5.7(b). These lines are clearly weaker due to the very low (but not vanishing) probability to have three excitons in the system. The transitions from even higher manifolds are too improbable to be seen in the spectra for the pumping considered here. The main differences between the two pumping schemes, if equal populations can be considered by adjusting the pumping, are therefore to be found in the linewidth and intensities of the lines. The positions of these lines embeds the most precious indications on the physical system.

In Fig. 5.10, spectra are displayed for particular detunings, in solid black for the case of electronic pumping, and thin red for cavity pumping. The electronic pumping, the most relevant case experimentally, yields the most interesting spectral shape. On top of the vacuum Rabi doublet, the interactions produce additional peaks that are clearly associated to the exciton at large detunings [panels (a) and (e)]. Three peaks, E1, E2 and E3 are obtained that correspond to one, two and three excitons coupling to the cavity mode, respectively. As these are brought in resonance with the cavity mode, the vacuum Rabi doublet dominates (essentially because the efficient coherent coupling collapses the exciton population) and satellite peaks are observed, that betray the quantum nature of the system, as the emission originates from transitions between quantized manifolds. In the absence of interactions (LM), the linear Rabi doublet is always observed independently of the total number of particles. Therefore, interactions are useful to evidence a quantum behavior linked to quantized energy transfers, in the spirit of such experiments as those used with atoms by Brune et al. (1996) in cavity to demonstrate quantization of the light field. Here, nonlinear features are observed directly in the optical spectrum, whereas in Brune et al. (1996), time-resolved measurements were used to probe anharmonic oscillations of the Rabi flops. This represents a notable experimental advantage, as measurements with cw incoherent pumping are typically easier to perform than time-resolved spectroscopy.

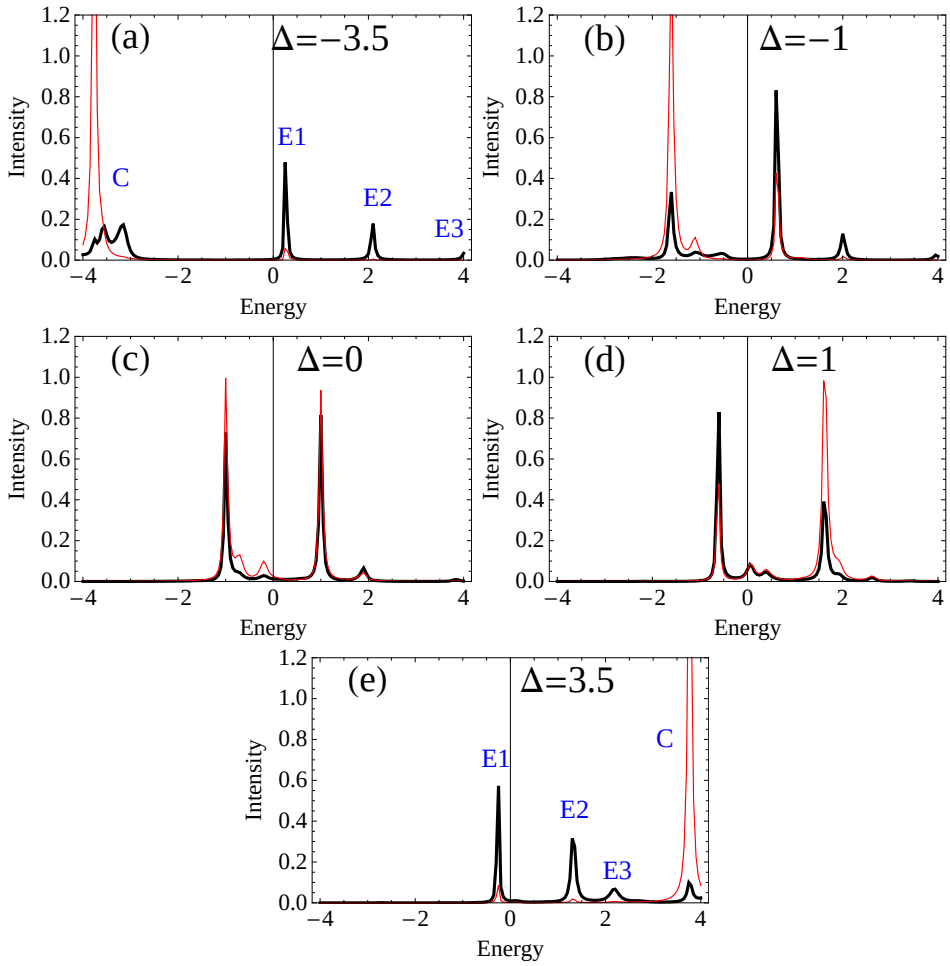

Figure 5.10: Spectra for different detunings corresponding to vertical "cuts" in Fig 5.9. Both cases, of cavity pumping ($P_a = P$, $P_b = 0$) and electronic pumping ($P_a = 0$, $P_b = P$), are represented in thin red and thick black respectively. At very large detunings [(a) and (e)], multiple excitons occupancy is observed through the peaks E1, E2, E3. Close to resonance, these result in satellites surrounding the linear vacuum Rabi doublet, that dominates because populations collapse at resonance. Parameters: $\omega_b = 0$, $U = 2g$, $\gamma_a = 0.1g$, $\gamma_b = 0.01g$, $P = 0.01g$.

5.4 The Jaynes-Cummings model

In this Section, we study saturation effects due to Pauli blocking. The material excitation follows Fermi statistics and the coupling to light is described by the Jaynes-Cummings model (JCM), that we write here again

$$H = \omega_a a^\dagger a + \omega_\sigma \sigma^\dagger \sigma + g(a^\dagger \sigma + a\sigma^\dagger) \tag{5.9}$$

Such an innocent looking Hamiltonian, with the only addition of dissipation, has been the object of numberless investigations. Analytical solutions are tricky to find already in this case, and remain uncovered for most mechanisms of excitation. SE from a given initial state has been overly privileged as the case of study, starting by the work of Sanchez-Mondragon et al. (1983). Even when the emitter was modelled as a two-level system, the JCM was commonly reduced to the LM by considering a single excitation as the initial state. This is the approximation made in many papers: Carmichael et al. (1989), Andreani et al. (1999), Cui & Raymer (2006), Auffèves et al. (2008), Inoue et al. (2008), etc. Other even more numerous works considered the excitation scheme at the same (Hamiltonian) level as the coupling, that is, they probe the system with coherent pumping: Mollow (1969), Savage (1989), Freedhoff & Quang (1994), Clemens & Rice (2000), Barchielli & Pero (2002), Florescu (2006), Bienert et al. (2007), etc. There has been less considerations for the luminescence spectra under incoherent pumping, although there exist some very interesting works on one-atom lasing, like those by Löffler et al. (1997), Clemens et al. (2004), Karlovich & Kilin (2007) and Karlovich & Kilin (2008), and some on one QD in a microcavity, like that of Perea et al. (2004). In the atomic literature, Löffler et al. (1997) have considered spectral shapes for the one-atom laser at resonance by numerical integration of the master equation and in this context have obtained some of the lineshapes of the best system that we study below. Karlovich & Kilin (2008) concentrated on strong coupling at resonance and low pump.

One of the most important current task of the SC physics in semiconductors is the quantitative description of the experiment with a theory that can provide statistical estimates to the data, in particular intervals of confidence for the fitting parameters. In this respect, there would be little need for fitting an experiment that would produce a clear observation of the Jaynes-Cummings energy levels, which is a strong qualitative effect. But no such structures have been observed so far and the deviations from a linear Rabi doublet, like those found by Hennessy et al. (2007), have been understood as non fundamental features of the problem. The most likely reason for this lack of crushing observations of the quantum regime in the PL lineshapes is that the best systems currently available in semiconductors are still beyond the range of parameters that allows the quantum features to neatly dominate. Instead, they are still at a stage where it is easy to overlook more feeble

indications, as shall be seen in what follows for less ideal systems that are closer to the experimental situation of today. Another possible reason is that the models are not suitable and a QD cannot be described by a simple two-level system. Then more involved theories should take over, with, e.g., full account for electron and hole band structures and correlations, as those of Feldtmann et al. (2006), Gies et al. (2007) or Schneebeli et al. (2008). However, if a simpler theory is successful, notwithstanding the interest of its more elaborate and complete counterpart, it clearly facilitates the understanding and putting the system to useful applications (especially in a quantum information processing context). At present, there is more element of chance left in the research for quantum SC than is actually necessary. If a quantitative description of even a "negative experiment" (not reporting a triplet or quadruplet) could be provided, this would help tracking and probably even direct the progress towards the ultimate goal: a fully understood and controlled SC in the quantum regime.

In this Section, we shall not focus on the difference between the spontaneous emission (SE) of an initial state in absence of any pumping, and the steady state (SS) established in presence of this pumping, as we did with other models. SS is the most relevant case for the experimental configuration that we have in mind, while SE is amply studied in the literature. Rather than contrasting the SE/SS results, we shall therefore contrast the boson/fermion cases. For this reason and for concision, we shall not use the "SS" superscript and assume that which of the SE/SS case is assumed is clear from context or from the presence of the time variable t.

In the LM, the quantum state of the system is not by itself an interesting quantity as most of its features are contained in its reduced density matrices, that are simply and in all cases thermal states with effective temperatures specified by the mean populations of the modes n_a and n_b. For this reason, $g^{(2)}$, that measures the fluctuations in the photon numbers, does not contain any new information. In the Fermion case however, $g^{(2)}$ becomes nontrivial, because the saturation of the dot provides a nonlinearity in the system that can produce various types of statistics, from the coherent Poisson distributions, encountered in lasers (where the nonlinearity is provided by the feedback and laser gain), to Fock-state statistics, with antibunching, exhibited by systems with a quantum state that has no classical counterpart. The fluctuations in particle numbers influence the spectral shape. The full statistics itself is most conveniently obtained from the master equation with elements $\rho_{mi;nj}$ for m, n photons and i, j exciton ($m,n \in \mathbb{N}$, $i,j \in \{0,1\}$). The distribution function of the photon number is simply $\mathrm{p}[n] = \rho_{n,0;n,0} + \rho_{n,1;n,1}$.

Rather than to consider the equations of motion for the matrix elements, it is clearer and more efficient to consider only elements that are nonzero in the steady

state,

$$\mathrm{p}_0[n] = \rho_{n,0;n,0}\,, \quad \mathrm{p}_1[n] = \rho_{n,1;n,1} \quad \text{and} \quad \mathrm{q}[n] = \rho_{n,0;n-1,1}\,. \tag{5.10}$$

They correspond to, respectively, the probability to have n photons, with (p_1), or without (p_0), exciton, and the coherence element between the states $|n,0\rangle$ and $|n-1,1\rangle$, linked by the SC Hamiltonian. Both p_0 and p_1 are real. It is convenient to separate q into its real and imaginary parts, $\mathrm{q}[n] = \mathrm{q}_\mathrm{r}[n] + i\mathrm{q}_\mathrm{i}[n]$ as they play different roles in the dynamics. The equations for these quantities, derived from Schrödinger equation for the Liouvillian (2.74), read:

$$\begin{aligned}
\frac{d\mathrm{p}_0[n]}{dt} =& -\big((\gamma_a+P_a)n+P_a+P_\sigma\big)\mathrm{p}_0[n] + \gamma_a(n+1)\mathrm{p}_0[n+1] + P_a n\mathrm{p}_0[n-1] \\
&+ \gamma_\sigma \mathrm{p}_1[n] - 2g\sqrt{n}\mathrm{q}_\mathrm{i}[n]\,, && \text{(5.11a)}\\
\frac{d\mathrm{p}_1[n]}{dt} =& -\big((\gamma_a+P_a)n+P_a+\gamma_\sigma\big)\mathrm{p}_1[n] + \gamma_a(n+1)\mathrm{p}_1[n+1] + P_a n\mathrm{p}_1[n-1] \\
&+ P_\sigma \mathrm{p}_0[n] + 2g\sqrt{n+1}\mathrm{q}_\mathrm{i}[n+1]\,, && \text{(5.11b)}\\
\frac{d\mathrm{q}_\mathrm{i}[n]}{dt} =& -\Big((\gamma_a+P_a)n - \frac{\gamma_a-P_a}{2} + \frac{\gamma_\sigma+P_\sigma}{2}\Big)\mathrm{q}_\mathrm{i}[n] \\
&+ \gamma_a\sqrt{(n+1)n}\mathrm{q}_\mathrm{i}[n+1] + P_a\sqrt{(n-1)n}\mathrm{q}_\mathrm{i}[n-1] \\
&+ g\sqrt{n}(\mathrm{p}_0[n] - \mathrm{p}_1[n-1]) - \Delta\,\mathrm{q}_\mathrm{r}[n]\,, && \text{(5.11c)}\\
\frac{d\mathrm{q}_\mathrm{r}[n]}{dt} =& -\Big((\gamma_a+P_a)n - \frac{\gamma_a-P_a}{2} + \frac{\gamma_\sigma+P_\sigma}{2}\Big)\mathrm{q}_\mathrm{r}[n] \\
&+ \gamma_a\sqrt{(n+1)n}\mathrm{q}_\mathrm{r}[n+1] + P_a\sqrt{(n-1)n}\mathrm{q}_\mathrm{r}[n-1] + \Delta\,\mathrm{q}_\mathrm{i}[n]\,. && \text{(5.11d)}
\end{aligned}$$

Note that, in the steady state, Eqs. (5.11) are detailed-balance type of equations. The conditional photon statistics with and without the exciton are similar, and coupled through the imaginary part of the q distribution (that is not a probability). At resonance, the real part of the coherence distribution, q_r, gets decoupled and vanishes in the steady state. As a result, only Eqs. (5.11a)–(5.11c) need to be solved. When g vanishes, q_i does not couple the two modes anymore, and their statistics become thermal like in the boson case. Through the off-diagonal elements q_i, the photon density matrix can vary between Poissonian, thermal (superpoissonian) and subpoissonian distributions.

The rest of the Chapter is organized as follows. In Section 5.4.1, we provide the expressions for all—and only those—correlation functions that enter the problem, making it as computationally efficient as possible for an exact treatment. We provide a decomposition of the final spectra in terms of transitions of the dressed states, which gives a clear physical picture of the problem. In Section 5.4.2, we give the analytical expressions for the position and broadening of the resonances

of the system at vanishing pumping. Weighting these resonances by the self-consistent dynamics of the system established by finite pumping and decay, gives the final spectral shape. We discuss in particular the notion of SC that varies from manifold to manifold, rather than holding for the entire system as a whole. In Section 5.4.3, we consider three particular points representative of the experimental situation, plus one point beyond what is currently available. We first discuss their behavior in terms of population and statistical fluctuations as imposed from the pumping conditions. In Section 5.4.4, we give the backbone of the final spectra at nonvanishing excitations. This is the numerical counterpart of Section 5.4.2, in the presence of arbitrary pumping. In Section 5.4.5, we present spectral shapes for the three points in a variety of configuration and compare them to each other. In Section 5.4.6, we investigate the situation at nonzero detuning, which is a case of particular importance in semiconductor physics.

5.4.1 First order correlation function and power spectrum

In the LM, the symmetry $a \leftrightarrow b$ allowed to focus exclusively on the cavity-emission without loss of generality, as the direct exciton emission could be obtained from the cavity emission by interchanging parameters. Here, the exciton (fermion) and photon (boson) are intrinsically different, and no simple relationship links them. They must therefore be computed independently. In order to apply the QRF (2.102), four indices are required to label the closing operators, namely $\{\eta\} = (mn\mu\nu)$ in $C_{\{\eta\}} = a^{\dagger m} a^n \sigma^{\dagger \mu} \sigma^\nu$ with $m, n \in \mathbb{N}$ and $\mu, \nu \in \{0,1\}$. The links established between them by the Liouvillian dynamics are given the rules:

$$M_{\substack{mn\mu\nu \\ mn\mu\nu}} = i\omega_a(m-n) + i\omega_\sigma(\mu-\nu) - \frac{\gamma_a - P_a}{2}(m+n) - \frac{\gamma_\sigma + P_\sigma}{2}(\mu+\nu)\,, \tag{5.12a}$$

$$M_{\substack{mn\mu\nu \\ m-1,n-1,\mu\nu}} = P_a mn\,, \quad M_{\substack{mn\mu\nu \\ mn,1-\mu,1-\nu}} = P_\sigma \mu\nu\,, \tag{5.12b}$$

$$M_{\substack{mn\mu\nu \\ m-1,n,1-\mu,\nu}} = M^*_{\substack{nm\nu\mu \\ n,m-1,\nu,1-\mu}} = igm(1-\mu)\,, \tag{5.12c}$$

$$M_{\substack{mn\mu\nu \\ m,n+1,\mu,1-\nu}} = M^*_{\substack{nm\nu\mu \\ n+1,m,1-\nu,\mu}} = -ig\nu\,, \tag{5.12d}$$

$$M_{\substack{mn\mu\nu \\ m,n+1,1-\mu,\nu}} = M^*_{\substack{nm\nu\mu \\ n+1,m,\nu,1-\mu}} = 2ig\nu(1-\mu)\,, \tag{5.12e}$$

and zero everywhere else. We are interested in $\Omega_1 = c^\dagger$ with $c = a$ and $\{\eta_a\} = (0,1,0,0)$ on the one hand, to get the equation for $\langle a^\dagger(t)a(t+\tau)\rangle$ that will provide the cavity emission spectrum, and $c = \sigma$ with $\{\eta_\sigma\} = (0,0,0,1)$ on the other hand, to get the equation for $\langle \sigma^\dagger(t)\sigma(t+\tau)\rangle$ for the QD direct emission spectrum.

Contrary to the LM, this procedure leads to an infinite set of coupled equations. The equations for both $\langle a^\dagger(t)C_{(0,1,0,0)}(t+\tau)\rangle$ and $\langle \sigma^\dagger(t)C_{(0,0,0,1)}(t+\tau)\rangle$ involve the same family of closing operators $C_{\{\eta\}}$, namely with $\eta \in \bigcup_{k\geq 1}\mathscr{N}_k$ where $\mathscr{N}_1 = \{(0,1,0,0),(0,0,0,1)\}$ the manifold of the boson case, and for $k>1$:

$$\mathscr{N}_k = \{(k-1,k,0,0),(k-1,k-1,0,1),(k-2,k,1,0),(k-2,k-1,1,1)\}. \quad (5.13)$$

The links between the various correlators tracked through the indices $\{\eta\}$, are shown in Fig. 5.11. To solve the differential equations of motion, the initial value of each correlator is also required, e.g., $\langle a^\dagger(t)a(t+\tau)\rangle$ demands $\langle (a^\dagger a)(t)\rangle$, etc. The initial values of $\langle a(t)C_{\{\eta\}}(t+\tau)\rangle$ (resp., $\langle \sigma(t)C_{\{\eta\}}(t+\tau)\rangle$) can be conveniently computed within the same formalism, recurring to $\Omega_1 = 1$ and $C_{\{\tilde{\eta}\}}$ with $\{\tilde{\eta}\} = \{m+1, n\mu\nu\}$ (resp., $\{mn, \mu+1, \nu\}$). This allows to compute also the single-time dynamics $\langle C_{\{\tilde{\eta}\}}(t)\rangle$, and their steady state, from the same tools used as for the two-time dynamics through the QRF. The indices $\{\tilde{\eta}\}$ required for the single-time correlators form a set—that we call $\tilde{\mathscr{N}} = \bigcup_{k\geq 1}\tilde{\mathscr{N}}_k$—that is disjoint from $\bigcup_{k\geq 1}\mathscr{N}_k$, required for the two-times dynamics. The set $\tilde{\mathscr{N}}$ has—beside the constant term $\{\eta_0\} = (0,0,0,0)$—two more elements for the lower manifold (of the LM). This is because $\{\eta_a\} = (0,1,0,0)$ and $\{\eta_\sigma\} = (0,0,0,1)$ invoke $(1,1,0,0)$ and $(1,0,0,1)$ for the cavity spectrum on the one hand, and $(0,1,1,0)$ and $(0,0,1,1)$ for the exciton emission on the other. At higher orders $k>1$, all two-times correlators $\mathscr{N}_k$ otherwise depend on the same four single-time correlators $\tilde{\mathscr{N}}_k$. Independently of which spectrum one wishes to compute, these four elements $(1,1,0,0)$, $(1,0,0,1)$, $(0,1,1,0)$ and $(0,0,1,1)$ of $\tilde{\mathscr{N}}_1$ are needed in all cases as they are linked to each other, as shown in Fig. 5.11.

In the figure, only the type of coupling—coherent, through g, or incoherent, through the pumpings $P_{a,\sigma}$—has been represented. Weighting coefficients are given by Eqs. (5.12). Of particular relevance is the self-coupling of each correlator to itself, not shown on the figure for clarity. Its coefficient, Eq. (5.12a), lets enter $\gamma_{a,\sigma}$ that do not otherwise couple any one correlator to any of the others. This makes it possible to describe decay, at vanishing pump, with the manifold method by simply providing an imaginary part to the Energy in Eq. (5.9). The incoherent pumping, on the other hand, establishes a new set of connections between correlators. Note, however, that at the exception of $\{\eta_0\}$, the pumping does not enlarge the sets $\bigcup\mathscr{N}_k$, $\bigcup\tilde{\mathscr{N}}_k$: the structure remains the same (also, technically, the computational complexity is identical), only with the correlators affecting each other differently. The addition of $\{\eta_0\}$ by the pumping terms bring the same additional physics in the boson and fermion cases: it imposes a self-consistent steady state over a freely chosen initial condition. In the LM, the pumping had otherwise only a direct influence in renormalizing the self-coupling of each correlator. In the JCM, it brings direct modifications to the Hamiltonian coherent dynamics. But its

contribution to the self-coupling is also important, and gives rise to an interesting fermionic opposition to the bosonic effects as seen in Eq. (5.12a) in the effective linewidth:

$$\Gamma_a = \gamma_a - P_a\,, \qquad \Gamma_\sigma = \gamma_\sigma + P_\sigma\,. \tag{5.14}$$

For later convenience, we also define:

$$\Gamma_\pm = \frac{\Gamma_a \pm \Gamma_b}{4}\,. \tag{5.15}$$

Eq. (5.14), reminds us that, whereas the incoherent cavity pumping narrows the linewidth, as a manifestation of its boson character, the incoherent exciton pumping broadens it. This opposite tendencies, participating together in the dynamics, bear a capital importance for the lineshapes, as narrow lines favor the observation of a structure, whereas broadening hinders it. On the other hand, the cavity incoherent pumping always results in a thermal distribution of photons with large fluctuations of the particle numbers, that brings inhomogeneous broadening, whereas the exciton pumping can grow a Poisson-like distribution with little fluctuations. Both types of pumping, however, ultimately bring decoherence to the dynamics and induce the transition into WC, with the lines composing the spectrum collapsing into one. Putting all these effects together, there is an optimum configuration of pumpings where particle fluctuations compensate for the broadening of the interesting lines, enhancing their resolution in the spectrum, as we shall see when we discuss the results below.

As there is no finite closure relation, some truncation is in order. We will adopt the same scheme as for the AO, where a maximum of $n_{\max}$ excitation(s) (photon plus excitons) is considered at the $n_{\max}$th order, thereby truncating by manifolds of correlators, which is the most relevant picture. This means that the last manifold considered in Fig. 5.11 is $\mathscr{N}_{\max}$, the one with mean values indexes that fit $(m+n+\mu+\nu)/2 = n_{\max}$. The exact result is recovered in the limit $n_{\max} \to \infty$. As seen in Fig. 5.11, the number $s_{\rm t}$ of two-time correlators from $\mathscr{N}$ up to order $n_{\max}$ is $s_{\rm t} = 4n_{\max} - 2$ and the number of mean values from $\tilde{\mathscr{N}}$ is $4n_{\max}$. The problem is therefore computationally linear in the number of excitations, and as such is as simple as it could be for a quantum system. The general case consists in a linear system of $s_{\rm t}$ coupled differential equations, whose matrix of coefficients [specified by Eqs. (5.12)] is, in the basis of $C_{\{\eta\}}$, a $s_{\rm t} \times s_{\rm t}$ square matrix that we denote $\mathbf{M}$. With these definitions, the quantum regression theorem becomes:

$$\partial_\tau \mathbf{v}_c(t,t+\tau) = \mathbf{M}\mathbf{v}_c(t,t+\tau) \tag{5.16}$$

where $\mathbf{v}_c(t,t+\tau) = \langle c^\dagger(t)\mathbf{C}_{\{\eta\}}(t+\tau)\rangle$. Explicitly, for the lower manifolds, e.g.,

for $c = a$:

$$\mathbf{C}_{\{\eta\}} = \begin{pmatrix} C_{(0,1,0,0)} \\ C_{(0,0,0,1)} \\ C_{(1,2,0,0)} \\ C_{(1,1,0,1)} \\ C_{(0,2,1,0)} \\ \vdots \end{pmatrix} \quad \text{and} \quad \mathbf{v}_a(t,t+\tau) = \begin{pmatrix} \langle a^\dagger(t)a(t+\tau)\rangle \\ \langle a^\dagger(t)\sigma(t+\tau)\rangle \\ \langle a^\dagger(t)(a^\dagger a^2)(t+\tau)\rangle \\ \langle a^\dagger(t)(a^\dagger a\sigma)(t+\tau)\rangle \\ \langle a^\dagger(t)(a^2\sigma^\dagger)(t+\tau)\rangle \\ \vdots \end{pmatrix} . \quad (5.17)$$

The ordering of the correlators is arbitrary. We fix it to that of Fig. 5.11, as seen in Eq. (5.17). With this convention, the indices of the two correlators of interests are:

$$i_a = 1, \quad i_\sigma = 2 . \quad (5.18)$$

To solve Eq. (5.16), we introduce the matrix $\mathbf{E}$ of normalized eigenvectors of $\mathbf{M}$, and $-\mathbf{D}$ the diagonal matrix of eigenvalues:

$$-\mathbf{D} = \mathbf{E}^{-1}\mathbf{M}\mathbf{E} . \quad (5.19)$$

The formal solution is given by $\mathbf{v}_c(t,t+\tau) = \mathbf{E}e^{-\mathbf{D}\tau}\mathbf{E}^{-1}\mathbf{v}_c(t,t)$. Integration of $\int e^{(-\mathbf{D}+i\omega)\tau}d\tau$ and application of the Wiener-Khintchine formula yield for the i_ath and i_σth rows of $\mathbf{v}_c$ the emission spectra of the cavity, $S_a = \frac{1}{\pi n_a}\Re\int\langle a^\dagger(t)a(t+\tau)\rangle e^{i\omega\tau}d\tau$, and of the direct exciton emission, $S_\sigma = \frac{1}{\pi n_\sigma}\Re\int\langle\sigma^\dagger(t)\sigma(t+\tau)\rangle e^{i\omega\tau}d\tau$, respectively. We find, to order $n_{\max}$:

$$S_c(\omega) = \frac{1}{\pi}\Re\sum_{p=1}^{s_t}\frac{L^c_{i_c p} + iK^c_{i_c p}}{D_p - i\omega} , \quad c = a,\sigma , \quad (5.20)$$

where $L^c_{i_c p}$ and $K^c_{i_c p}$ are given by the real and the imaginary part, respectively, of $[\mathbf{E}]_{i_c p}[\mathbf{E}^{-1}\mathbf{v}_c(t,t)]_p/n_c$:

$$L^c_{i_c p} + iK^c_{i_c p} = \frac{1}{n_c}[\mathbf{E}]_{i_c p}\sum_{q=1}^{s_t}[\mathbf{E}^{-1}]_{pq}[\mathbf{v}_c(t,t)]_q , \quad 1 \le p \le s_t , \quad (5.21)$$

and $D_p = [\mathbf{D}]_{pp}$ (when we refer to elements of a matrix or a vector by its indices, we enclose it with square brackets to distinguish from labelling indices). Further defining γ_p and ω_p as the real and imaginary parts, respectively, of D_p

$$\gamma_p + i\omega_p = D_p , \quad (5.22)$$

we can write Eq. (5.20) in a less concise but more transparent way. To all orders, it reads:

$$S_c(\omega) = \frac{1}{\pi}\lim_{n_{\max}\to\infty}\sum_{p=1}^{s_t}\left(L^c_{i_c p}\frac{\gamma_p}{(\omega-\omega_p)^2+\gamma_p^2} - K^c_{i_c p}\frac{\omega-\omega_p}{(\omega-\omega_p)^2+\gamma_p^2}\right) . \quad (5.23)$$

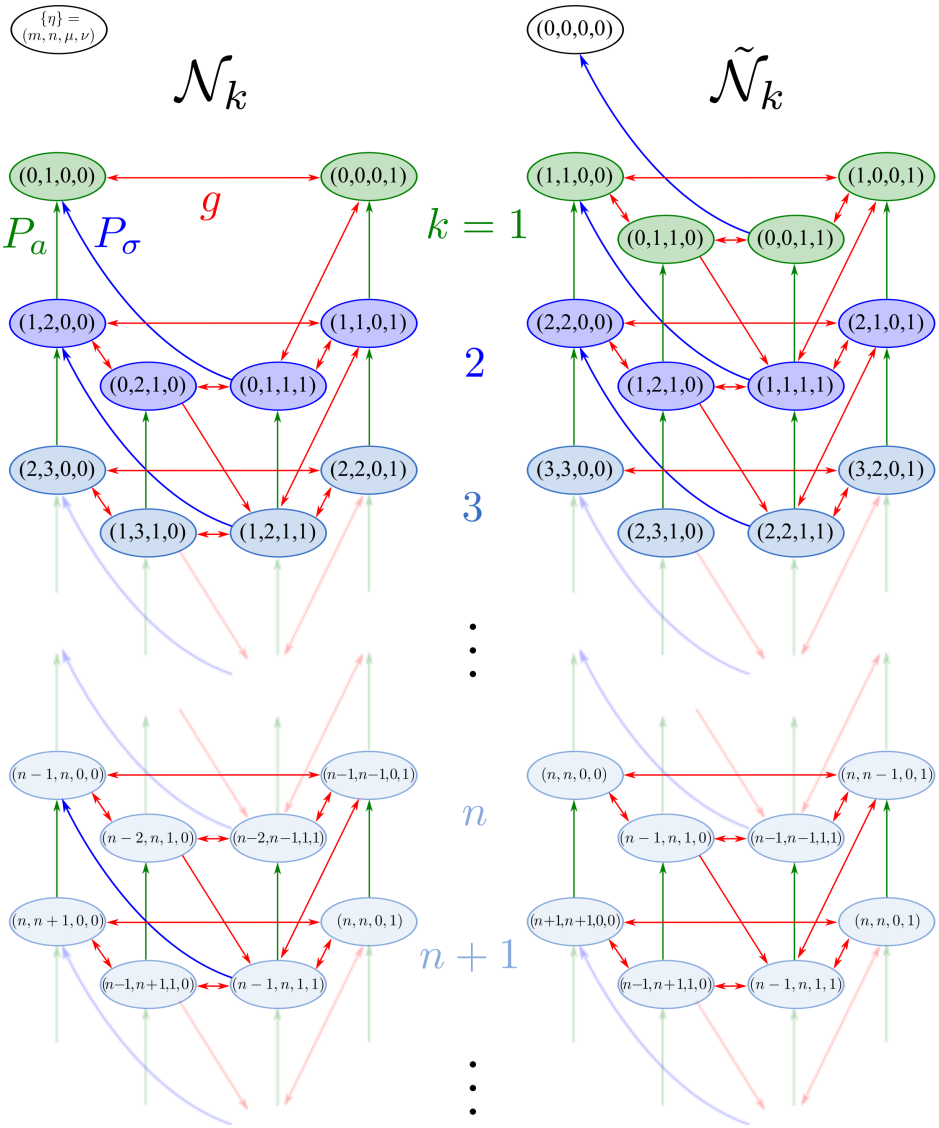

Figure 5.11: Chain of correlators—indexed by $\{\eta\} = (m,n,\mu,\nu)$—linked by the dissipative Jaynes-Cummings dynamics. On the left (resp., right), the set $\bigcup_k \mathscr{N}_k$ (resp., $\bigcup_k \tilde{\mathscr{N}}_k$) involved in the equations of the two-time (resp., single-time) correlators. In green are shown the first manifolds $\mathscr{N}_1$ and $\tilde{\mathscr{N}}_1$ that correspond to the LM, and in increasingly lighter shades of blues, the higher manifolds $\mathscr{N}_k$ and $\tilde{\mathscr{N}}_k$. The equation of motion $\langle a^\dagger(t) C_{\{\eta\}}(t+\tau)\rangle$ (resp. $\langle \sigma^\dagger(t) C_{\{\eta\}}(t+\tau)\rangle$) with $\eta \in \mathscr{N}_k$ requires for its initial value the correlator $\langle C_{\{\tilde{\eta}\}}\rangle$ with $\{\tilde{\eta}\} \in \tilde{\mathscr{N}}_k$ defined from $\{\eta\} = (m,n,\mu,\nu)$ by $\{\tilde{\eta}\} = (m+1,n,\mu,\nu)$ (resp. $(m,n,\mu+1,\nu)$), as seen on the diagram. The red arrows indicate which elements are linked by the coherent (SC) dynamics, through the coupling strenght g, while the green/blue arrows show the connections due to the incoherent cavity/exciton pumpings, respectively. The self-coupling of each node to itself is not shown. This is where $\omega_{a,\sigma}$ and $\gamma_{a,\sigma}$ enter.

The lineshape, as in all the models we have studied in this thesis, is composed of a series of Lorentzian and Dispersive parts, whose positions and broadenings (FWHM) are specified by ω_p and $2\gamma_p$, cf. Eq. (5.22), and which are weighted by the coefficients $L^c_{i_c p}$ and $K^c_{i_c p}$, cf. Eq. (5.21). The former pertain to the structure of the spectral shape as inherited from the Jaynes-Cummings energy levels. They are, as such, independent of the channel of detection (cavity or direct exciton emission). We devote Section 5.4.2 to them. The latter reflect the quantum state that has been realized in the system under the interplay of pumping and decay. They determine which lines actually appear in the spectra, and with which intensity. Naturally, the channel of emission is a crucial element in this case. We devote Section 5.4.3 to this aspect of the problem.

5.4.2 Vanishing pump case in the manifold picture

In this Section, we discuss the series of parameters ω_p and γ_p that in the luminescence spectrum, Eq. (5.23), determine the position and the broadening (HWHM) of the lines, respectively, in both the cavity and the direct exciton emission. The case of vanishing pumping is fundamental, as it corresponds to the textbook Jaynes-Cummings results with the spontaneous emission of an initial state. It serves as the skeleton for the general case with arbitrary pumping and supports the general physical picture. Finally, it admits analytical results. We therefore begin with the case where $P_a, P_\sigma \ll \gamma_a, \gamma_\sigma$. The eigenvalues of the matrix of regression $\mathbf{M}$, are grouped into manifolds. There are two for the first manifold, given by:

$$D_{\frac{1}{2}} = \Gamma_+ + i\Big(\omega_a - \frac{\Delta}{2} \mp \sqrt{g^2 - \Big(\Gamma_- + i\frac{\Delta}{2}\Big)^2}\Big)\,, \tag{5.24}$$

and four for each manifold of higher order $k > 1$, given by, for $4k-5 \leq p \leq 4k-2$:

$$D_p = \Gamma_k + i\Big(\omega_a + \mathrm{sgn}\big(p-(8k-7)/2\big)R_k + (-1)^p R^*_{k-1}\Big)\,, \tag{5.25}$$

($\mathrm{sgn}(x)$ is defined as 0 for $x = 0$ and $x/|x|$ otherwise), in terms of the kth-*manifold (half) Rabi splitting*:

$$R_k = \sqrt{(\sqrt{k}g)^2 - \Big(\Gamma_- + i\frac{\Delta}{2}\Big)^2}\,, \tag{5.26}$$

and of the kth-*manifold (half) broadening*:

$$\Gamma_k = (2k-3)\Gamma_- + (2k-1)\Gamma_+ = (k-1)\gamma_a + \frac{\gamma_\sigma}{2}\,. \tag{5.27}$$

For each manifold, we have defined the D_p in order by increasing value of the line position ω_p.

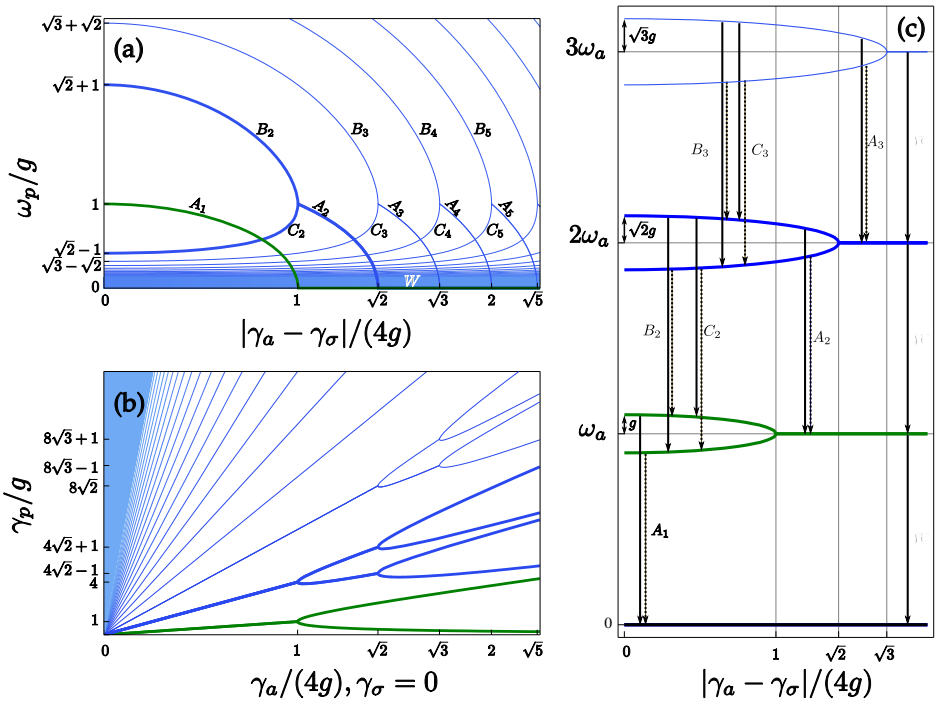

Figure 5.12: Spectral structure of the JCM at resonance and without pumping. (a) Positions ω_p of the lines in the luminescence spectrum. Only energies higher than ω_a are shown (not their symmetric below ω_a). We take $\omega_a = 0$ as the reference energy. In green (thick), the first manifold, and in increasing shades of blue, the successive higher manifolds which form a pattern of branch-coupling curves that define different orders of SC. (b) Half-Width at Half Maximum (HWHM) γ_p of the lines (with $\gamma_\sigma = 0$). In both (a) and (b), the blue filled region results from the accumulation of the countable-infinite vanishing lines. (c) Eigenenergies of the Jaynes-Cummings Hamiltonian with decay as an imaginary part of the bare energies (the *Jaynes-Cummings ladder*). This provides a clear physical picture of panel (a) where the peaks positions arise from the difference of energy between lines of two successive manifolds. Lines A_k of (a) stem from the emission from manifold k in SC into manifold $k-1$ in WC (or vacuum). Lines B_k and C_k stem from the emission between the two manifolds in SC. Solid lines are those plotted in (a), dotted lines produce the symmetric lines, not shown. The horizontal line W at 0 in (a) arises from decay between two manifolds in WC. Scheme (c) also reproduces the broadening of the lines (b) with the sum of the imaginary parts of the eigenenergies involved in the transition.

According to Eq. (5.22), these provide the position ω_p of the line and its half-broadening γ_p through their imaginary and real parts. Γ_k is always real, so contributes in all cases to γ_p only. R_k is (at resonance) either pure real, or pure imaginary, and similarly to the LM or the two coupled 2LSs, this is what defines SC. This corresponds to an oscillatory or damped field dynamics of the two-time correlators within manifold k, which lead us to the formal definition: WC and SC of order n are defined as the regime where the complex Rabi frequency at resonance, Eq. (5.26), is pure imaginary (WC) or real (SC). The criterion for nth order SC is therefore:

$$g > |\Gamma_-|/\sqrt{n}\,. \tag{5.28}$$

SC is achieved more easily, given the system parameters (g and $\gamma_{a,\sigma}$), with an increasing photon-field intensity that enhances the effective coupling strength. The lower the SC order, the stronger the coupling. This corresponds to the nth manifold (and all above) being in SC (aided by the cavity photons), while the $n-1$ manifolds below are in WC. First order is therefore the one where all manifolds are in SC. Eq. (5.28) includes the standard SC of the LM and 2LSs, $g > |\Gamma_-|$, as the first order SC of the fermion case, that is shown in green (thick) in Fig. 5.12. The same position of the peaks $\omega_{1,2}$ and the same (half) broadenings $\gamma_{1,2}$ is also recovered (in the absence of pumping). Note that similarly to the boson case, the SC is defined by a comparison between the coupling strenght g with the *difference* of the effective broadening Γ_a and Γ_b. The sum of these play no role in this regard.

The ω_p and γ_p are plotted in Fig. 5.12(a) and 5.12(b), respectively, as function of Γ_-. Note that ω_p only depends on g and Γ_-, whereas γ_p also depends on Γ_+ (that is why we plot it for $\gamma_\sigma = 0$).

The D_p, Eq. (5.25), have a natural interpretation in terms of transitions between the manifolds of the so-called *Jaynes-Cummings ladder*. The eigenenergies of the Jaynes-Cummings Hamiltonian with decay granted as the imaginary part of the bare energies ($\omega_{a,\sigma} - i\gamma_{a,\sigma}/2$), are given by $E^k_\pm$ with

$$E^k_\pm = k\omega_a - \frac{\Delta}{2} \pm R_k - i\frac{(2k-1)\gamma_a + \gamma_b}{4}\,, \tag{5.29}$$

for the kth manifold. The four possible transitions between consecutive manifolds k and $k-1$ give rise, when $k > 1$, to the four peaks we found:

$$D_{4k-5} = i[E^k_- - (E^{k-1}_+)^*]\,, \qquad D_{4k-4} = i[E^k_- - (E^{k-1}_-)^*]\,, \tag{5.30a}$$

$$D_{4k-3} = i[E^k_+ - (E^{k-1}_+)^*]\,, \qquad D_{4k-2} = i[E^k_+ - (E^{k-1}_-)^*]\,. \tag{5.30b}$$

In the case $k = 1$, only the two peaks in common with the LM arise, $D_{1,2} = iE^1_\mp$, given respectively by Eqs. (5.30a) and (5.30b) with $E^0 = 0$.

The ladder is shown (at resonance) in Fig. 5.12(c). Let us discuss it in connection with our definition of SC in this system, to arbitrary n. When $\Gamma_- = 0$, each

step of the ladder is constituted by the two eigenstates of the fermion, dressed by the n cavity photons, resulting in a splitting of $2\sqrt{n}g$. This kind of renormalization already appeared in Chapter 4 when we discussed the coupled two 2LSs, that can be considered as a particular case of the JCM, where there can be no more than a photon in the system. An n-dependent splitting produces quadruplets of delta peaks with splitting of $\pm(\sqrt{n}\pm\sqrt{n-1})g$ around ω_a, as opposed to the LM where independently of the manifold, the peaks are all placed at $\pm g$ around ω_a. In a more general situation with $\Gamma_- \neq 0$, there are three possibilities for a manifold $k > 1$:

1. *Both manifold k and $k-1$ are in SC.* The two Rabi coefficients R_k and R_{k-1} are real. This is the case when

$$|\Gamma_-| \leq g\sqrt{k-1}\,. \tag{5.31}$$

   The luminescence spectra corresponds to four splitted lines $\omega_p \to \omega_a \pm (R_k \pm R_{k-1})$, coming from the four possible transitions [Eqs. (5.30), shown as B_k and C_k in Fig. 5.12(c)] between manifolds k and $k-1$. The emission from all the higher manifolds also produces four lines. They are grouped pairwise around ω_a [Fig. 5.12(a)] and all have the same broadening, contributed by Γ_k only [the single straight line in Fig. 5.12(b)].

2. *Manifold k is in SC while manifold $k-1$ is in WC.* In this case, R_k is pure imaginary (contributing to line positions) and R_{k-1} is real (contributing to broadenings). This is the case when

$$g\sqrt{k-1} < |\Gamma_-| < g\sqrt{k}\,. \tag{5.32}$$

   This corresponds to two lines $\omega_p \to \omega_a \pm R_k$ in the luminescence spectrum, coming from the two possible transitions [shown as A_k in Fig. 5.12(c)] between the SC manifold k and the WC manifold $k-1$. Each of them is doubly degenerated. The two contributions at a given ω_p have two distinct broadenings $\gamma_p \to \Gamma_k \pm |R_{k-1}|$ around Γ_k. [cf. Fig. 5.12(b)]. The final lineshapes of the two lines A_2 is the same. In this region, all the emission from the higher manifolds produce four lines and all from the lower produce only one (at ω_a), being in WC.

3. *Both manifold k and $k-1$ are in WC.* The two Rabi coefficients R_k and R_{k-1} are pure imaginary. This is the case when

$$g\sqrt{k} \leq |\Gamma_-|\,. \tag{5.33}$$

   This corresponds to only one line at $\omega_p \to \omega_a$ in the luminescence spectrum, coming from the transition from one manifold in WC to the other

[shown as W in Fig. 5.12(c)]. The line is four-time degenerated, with four contributions with different broadenings $\gamma_p \to \Gamma_k \pm (|R_k| \pm |R_{k-1}|)$, as seen in Fig. 5.12(b).

Figure 5.12 is the skeleton for the luminescence spectra—whether that of the cavity or of the direct exciton emission. It specifies at what energies can be the possible lines that constitutes the final lineshape, and what are their broadening. To compose the final result, we only require to know the weight of each of these lines.

In the SE case, the weights L_p and K_p include the integral of the single-time mean values $\mathbf{v}_a(t,t)$ over $0 \leq t < \infty$. Therefore, only those manifolds with a smaller number of excitations than the initial state can appear in the spectrum. Each of them, will be weighted by the specific dynamics of the system. The "spectral structure"—i.e., the ω_p and γ_p—depends only the system parameters (g and $\gamma_{a,\sigma}$). Therefore, in the SE case, the resulting emission spectrum is an exact mapping of the spectral structure of the Hamiltonian, Fig. 5.12.

In the SS case, the weighting of the lines also depends on which quantum state is realized, this time under the balance of pumping and decay. But the excitation scheme also changes the spectral structure of Fig. 5.12. When the pumping parameters are small, the changes will mainly be perturbations of the present picture and most concepts will still hold, such as the definition of SC, Eq. (5.28) for nonzero $P_{a,\sigma}$ in (5.15). However, when the pump parameters are comparable to the decay parameters, the manifold picture in terms of Hamiltonian eigenenergies breaks, as it happen for the two coupled 2LS in Chapter 4. The underlying spectral structure must be computed numerically for each specific probing of the system with P_a and P_σ. It can still be possible to identify the origin of the lines with the manifold transitions by plotting their position ω_p as a function of the pumps, starting from the analytic limit. SC of each manifold can be associated to the existence of peaks positioned at $\omega_p \neq \omega_a, \omega_\sigma$. We address this problem in next Sections.

5.4.3 Population and Statistics

To know which features of the spectral structure dominate and which are negligible, one needs to know what is the quantum state of the system. In the LM, it was enough to know the average photon (n_a) and exciton (n_b) numbers, and the off-diagonal element $n_{ab} = \langle a^\dagger b \rangle$. In the two 2LS, only one more averaged quantity, n_B, was necessary. In the most general case of the fermion system, a countably infinite number of parameters are required for the exact lineshape, as in the LM with interactions or the AO. The new order of complexity brought by the fermion system is illustrated for even the simplest observable. Instead of a closed relationship that provides, e.g., the populations in terms of the system parameters and

pumping rates, only relations between observables can be obtained in the general case. For instance, for the populations:

$$\Gamma_a n_a + \Gamma_\sigma n_\sigma = P_a + P_\sigma \,. \tag{5.34}$$

This expression is formally the same as for the coupling of two bosonic modes. The differences are in the effective dissipation parameter $\Gamma_\sigma = \gamma_\sigma + P_\sigma$ (instead of the bosonic one, $\gamma_b - P_b$) and the constrain of the exciton population, $0 \leq n_\sigma \leq 1$. One solution of Eq. (5.34) is $n_a^{\text{th}} = P_a/\Gamma_a$ and $n_\sigma^{\text{th}} = P_\sigma/\Gamma_\sigma$, which corresponds to the case $g = 0$, where each mode reaches its thermal steady state independently (Bose/Fermi distributions, depending on the mode statistics). With coupling $g \neq 0$, we can only derive some analytical limits and bounds. For example, when $\gamma_a = P_a$, one sees from Eq. (5.34) that $n_\sigma = (P_\sigma + P_a)/\Gamma_\sigma$, with the condition for the cavity pump $P_a \leq \gamma_\sigma$ (since $n_\sigma \leq 1$). If only the dot is pumped, $n_\sigma = n_\sigma^{\text{th}}$, and if both P_a, $\gamma_a = 0$ then, also $n_a = n_a^{\text{th}} = P_\sigma/(\gamma_\sigma - P_\sigma)$ with the same temperature. As, in this case, P_σ must be strictly smaller than γ_σ, the exciton population $n_\sigma \leq 1/2$ prevents an inversion of population, as is well known for a two-level system.

When $\gamma_a > P_a$, we get the following bounds for the cavity populations in terms of the system and pumping parameters:

$$\frac{P_a - \gamma_\sigma}{\gamma_a - P_a} \leq n_a \leq \frac{P_a + P_\sigma}{\gamma_a - P_a} \,. \tag{5.35}$$

When $P_\sigma = \gamma_\sigma = 0$, the cavity is in thermal equilibrium with its bath, $n_a = n_a^{\text{th}}$, and with the dot $n_\sigma = P_a/(\gamma_a + P_a)$. In this case, the pump is limited by $P_a < \gamma_a$, and again $n_\sigma \leq 1/2$. Again, the inversion of population cannot take place putting the system in contact with only one thermal bath. In all these situations where an analytic expression for the population is obtained, the detuning between cavity and dot does not affect the final steady state, although it determines, together with the coupling strength, the time that it takes to reach it. An interesting limiting case where inversion can happen, is that where γ_σ and P_a are negligible, then $n_a = P_\sigma(1 - n_\sigma)/\gamma_a$. When the pump is low and $n_\sigma < 1$, n_a grows with pumping, but when the dot starts to saturate and $n_\sigma \to 1$ the cavity population starts to quench towards $n_a \to 0$, as described by Benson & Yamamoto (1999). Here, all values of P_σ bring the system into a steady state as n_a cannot diverge. However, if we allow some cavity pumping, given that a does not saturate, P_a is bounded. A rough guess of this boundary is, in the most general case:

$$P_a < \max(\gamma_a, \gamma_\sigma) \,. \tag{5.36}$$

If Eq. (5.36) is not fulfilled, the system diverges, as more particles are injected at all times by the incoherent cavity pumping than are lost by decay. Numerical evidence suggests that the actual maximum value of P_a depends on P_σ. To

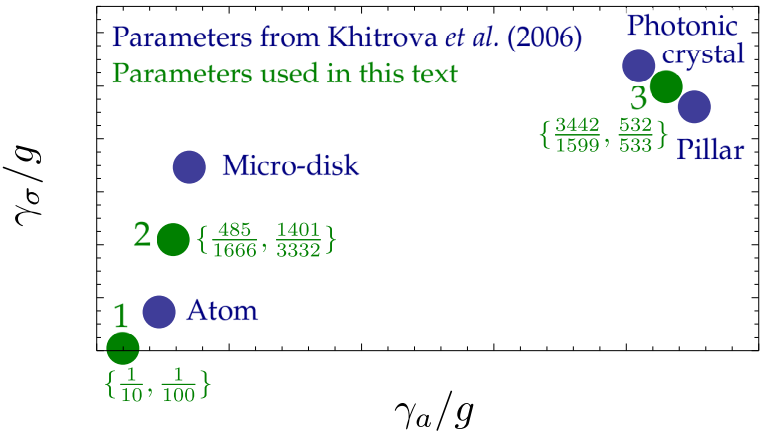

Figure 5.13: Blue points give the decay rates for the cavity and quantum dot estimated by Khitrova et al. (2006) for four references systems having achieved SC at this time: photonic crystals and pillar microcavities nearby point 3, microdisks and atomic systems nearby point 2. In Green, the three sets of parameters used in this text. Points 2 and 3 average over their two nearest neighbors and represent these systems. Point 1 represents a very good system in very strong coupling, that might be realizable in the near future. Parameters are fractions because numerical computations have been done to arbitrary precisions (with the values given).

some given order n_t, divergence typically arises much before condition (5.36) is reached, although it is difficult to know if a lower physical limit has been reached or if the order of truncation was not high enough.

The second order correlator $g^{(2)}$ at zero delay can be expressed as a function of n_a only:

$$g^{(2)} = \Big[g^2\big((n_a+1)(P_a^2+P_\sigma^2) - n_a(\gamma_a+\gamma_\sigma)^2 + P_a(\gamma_a+\Gamma_\sigma+P_\sigma+6n_a\Gamma_\sigma) + P_\sigma(\gamma_a+\gamma_\sigma-2n_a\gamma_a)\big) + (P_a-n_a\Gamma_a)\Gamma_\sigma(4\Gamma_+^2+\Delta^2)\Big] \Big/ 2g^2n_a^2\Gamma_a\Gamma_\sigma\,. \quad (5.37)$$

Obtaining the expression for the nth order correlator and setting it to zero would provide an approximate (of order n) closed relation for n_a. We shall not pursue this line of research that becomes very heavy.

As an overall representation of the typical systems that arise in real and desired experiments, we consider three configurations, shown in Fig. (5.13), scattered in order to give a rough representative picture of the overall possibilities, around parameters estimated by Khitrova et al. (2006). Point 1 corresponds to the best system of our selection, in the sense that its decay rates are very small ($\gamma_a = g/10$, $\gamma_\sigma = g/100$), and the quantum (Hamiltonian) dynamics dominates largely the system. It is a system still outside of the experimental reach. Point 3 on the other hand corresponds to a cavity with important dissipations, that, following our analysis below, precludes the observation of any neat structure attributable to the underly-

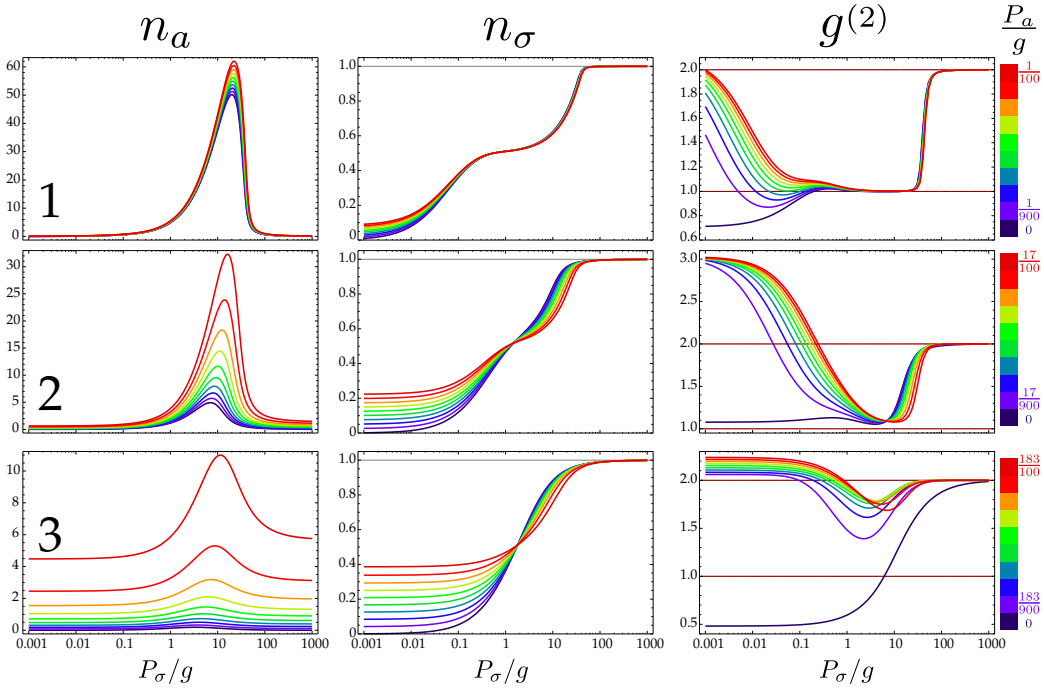

Figure 5.14: Populations and statistics of the points marked 1, 2 and 3 in Fig. 5.13. Each row shows the triplet n_a (1st column), n_σ (2nd) and $g^{(2)}(0)$ (3rd) for a given point (nth row corresponds to point n). All plots share the same x-axis in log-scale of P_σ/g ranging from 10^{-3} to 10^3. All y-axis are rescaled to its specific graph, at the exception of n_σ which is always between 0 and 1. The color code corresponds to different values of P_a. Each color code applies to its row and is given in the last column. The qualitative behavior is roughly the same for all points: there is a peak in n_a that is subsequently quenched as the dot gets saturated. In $g^{(2)}$, there is on the other hand, a local minimum of fluctuations that can be brought to the Poissonian limit of 1 (allowing for a lasing region) and maintained over a large plateau in good cavities.

ing Fermi statistics. According to numerical fitting of the experiment, real structures might even be suffering higher dissipation rates (see Sec. 3.5). Point 2 represents other lead systems of the SC physics, that we will show can presents strong departure from the linear regime, in particular conditions that we will emphasize. The best semiconductor system from Fig. 5.13 is realized with microdisks, thanks to the exceedingly good cavity factors. We shall not enter into specific discussion of the advantages and inconvenient of the respective realizations and the accuracy of these estimations. From now on, we shall refer to this set of parameters as that of "reference points", keeping in mind that points 1 and 2 in particular represent systems that we will refer to as a "good system" and a "more realistic system", respectively.

In Fig. 5.14, the three observable of main interest for a physical understanding of the system that we have just discussed—n_a, n_σ and $g^{(2)}$—are obtained nu-

merically for the three reference points. Electronic pumping is varied from, for all practical purposes, vanishing ($10^{-3}g$) to infinite ($10^{3}g$) values. Various cavity pumpings are investigated and represented by the color code from no-cavity pumping (dark blue) to high, near diverging, cavity pumping (red), through the color spectrum. We checked numerically that these results satisfy Eq. (5.34). The overall behavior is mainly known, for instance the characteristic increase till a maximum and subsequent decrease of n_a with P_σ has been predicted in a system of QD coupled to a microsphere by Benson & Yamamoto (1999). This phenomenon of so-called *self-quenching* is due to the excitation impairing the coherent coupling of the dot with the cavity: bringing in an exciton too early disrupts the interaction between the exciton-photon pair formed from the previous exciton. Therefore the pumping rate should not overcome significantly the coherent dynamics. Too high electronic pumping forces the QD to remain in its excited state and thereby prevents it from populating the cavity. In this case the cavity population returns to zero while the exciton population (or probability for the QD to be excited) is forced to one. This effect appeared as well in the two 2LSs, with the quenching of the direct emission when the dots saturated with the excitonic pump. The cavity pumping brings an interesting extension to this mechanism. First there is no quenching for the pumping of bosons that, on the contrary, have a natural tendency to accumulate and lead to a divergence. Therefore the limiting values for n_a when $P_\sigma \to 0$ or $P_\sigma \to \infty$ are not zero, as in the previously reported self-quenching scenario. They also happen to be different:

$$n_a^< \equiv n_a(P_\sigma = 0) = \frac{P_a - \gamma_\sigma n_\sigma}{\gamma_a - P_a}\,, \tag{5.38a}$$

$$n_a^> \equiv \lim_{P_\sigma \to \infty} n_a = \frac{P_a}{\gamma_a - P_a}\,, \tag{5.38b}$$

and therefore satisfy $n_a^< < n_a^>$. Eq. (5.38b) follows from the decoupled thermal values for the populations, $n_\sigma \to P_\sigma/(P_\sigma + \gamma_\sigma)$, and corresponds to a passive cavity where the quenched dot does not contribute at all. In this case, the emission spectrum of the system is expected to converge to

$$S_a(\omega) = \frac{1}{\pi}\frac{\Gamma_a/2}{(\omega - \omega_a)^2 + (\Gamma_a/2)^2}\,, \tag{5.39}$$

for the cavity, and $S_\sigma(\omega) = 0$ for the dot. The other limit when $P_\sigma = 0$, shows the deleterious effect of the dot on cavity population. The dot fully enters the dynamics contrary to the quenched case where it is subtracted from it.

In different works by Mu & Savage (1992), Ginzel et al. (1993), Jones et al. (1999), Karlovich & Kilin (2001) or Kozlovskii & Oraevskii (1999), important application of SC for single-atom lasing were found for good cavities 1 and 2, where

the coupling $g \gg \gamma_a, \gamma_b$ is strong enough. Lasing can occur when the pumping is also large enough to overcome the total losses, $P_\sigma \gg \gamma_a, \gamma_\sigma$. Setting P_a, $\gamma_\sigma = 0$, Eqs. (5.11) can be approximately reduced to one for the total probability $\mathrm{p}[n]$, as it has been shown by Scully & Zubairy (2002) or Benson & Yamamoto (1999):

$$\partial_t \mathrm{p}[n] = \gamma_a(n+1)\mathrm{p}[n+1] - \Big(\gamma_a n + \frac{l_G(n+1)}{1+l_S/l_G(n+1)}\Big)\mathrm{p}[n] + \frac{l_G n}{1+l_S/l_G n}\mathrm{p}[n-1] \tag{5.40}$$

The parameters that characterize the laser are the gain $l_G = 4g^2/P_\sigma$ and the self saturation $l_S = 8g^2 l_G/P_\sigma^2$. Far above threshold ($n_a l_S/l_G \gg 1$), the statistics are Poissonian, $g^{(2)} = 1$, with a large intensity in the emission, $n_a = P_\sigma/(2\gamma_a)$, and half filling of the dot, $n_\sigma = 0.5$. However, this analytic limit from the standard laser theory is not able to reproduce the self-quenching effect induced by the incoherent pump, nor the subpoissonian region ($g^{(2)} < 1$) where quantum effects are prone to appear. The validity of the laser theory is restricted to the narrow region, $\gamma_a \ll P_\sigma \ll \gamma_\sigma^{\mathrm{P}}$, where $\gamma_\sigma^{\mathrm{P}} = 4g^2/\gamma_a$ is the boundary for the self-quenching. In the weak coupling regime, $\gamma_\sigma^{\mathrm{P}}$ is the well known Purcell enhanced spontaneous decay rate of an exciton through the cavity mode. In the strongly coupled system, it can be similarly understood as the rate at which an exciton transforms into a photon. If the excitons are injected at a higher rate, there is no time for such a coherent exchange to take place and populate the cavity with photons. Fig. 5.14 shows that lasing can be achieved with system 1 in the corresponding region of pump. Here, we will solve the system exactly, covering this regime and all the other possible ones with the full quantum equations of motion.

The effect of cavity pumping depends strongly on the experimental situation. In the case of an exceedingly good system, P_a has little effect as soon as the exciton pumping is important, $P_\sigma > \gamma_a$. Cavity pumping becomes important again in a system like 2, where it enhances significantly the output power, with the price of superpoissonian statistics ($g^{(2)} > 1$). With a poorer system like point 3, some lasing effect can be found with the aid of the cavity pump: there is a nonlinear increase of n_a and $g^{(2)}$ approaches 1 for $g < P_\sigma < 10g$. However, the weaker the coupling, the weaker this effect until it disappears completely for decay rates outside the range plotted in Fig. 5.13. In all cases, the self-quenching leads finally to a thermal mixture of photons ($g^{(2)} = 2$) and WC at large pumping.

5.4.4 Weights and Renormalization

To give a complete picture of the spectral structure, that we have obtained analytically in Section 5.4.2, we need to consider how this limiting case of vanishing pumpings evolves with finite pumping. Here again, we have to turn to numerical results.

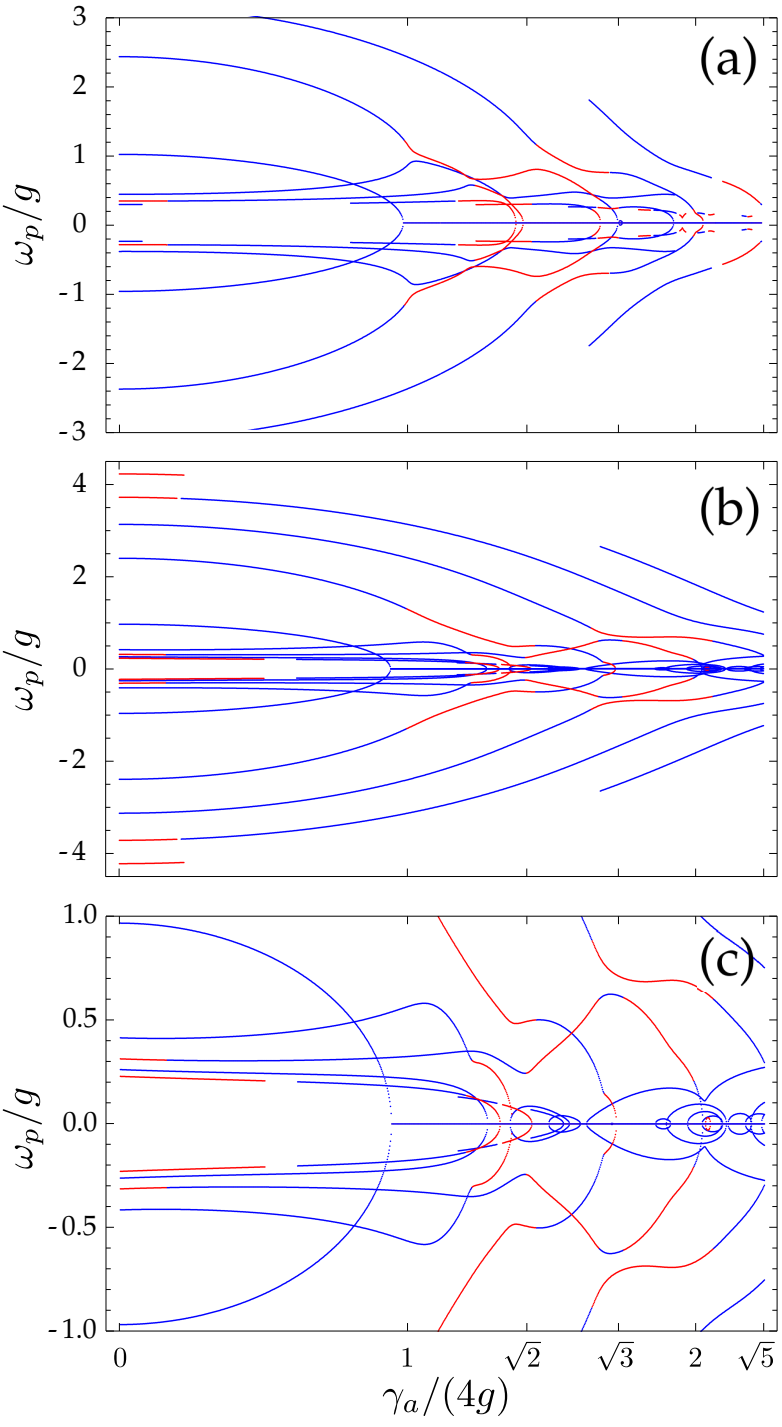

Figure 5.15: Spectral structure in the cavity emission of the Jaynes-Cummings model as a function of γ_a/g, with some electronic pumping ($\Delta = 0$, $\gamma_\sigma = 0$, $P_a = 0$, $\omega_a = 0$). Panel (a) is for $P_\sigma = g/50$ and (b)-(c) for $P_\sigma = g/10$. Panel (c) is a zoom on the central peaks of the entire picture (b). In blue (resp., red) are the peaks with $L_p^a > 0$ (resp., $L_p^a < 0$).

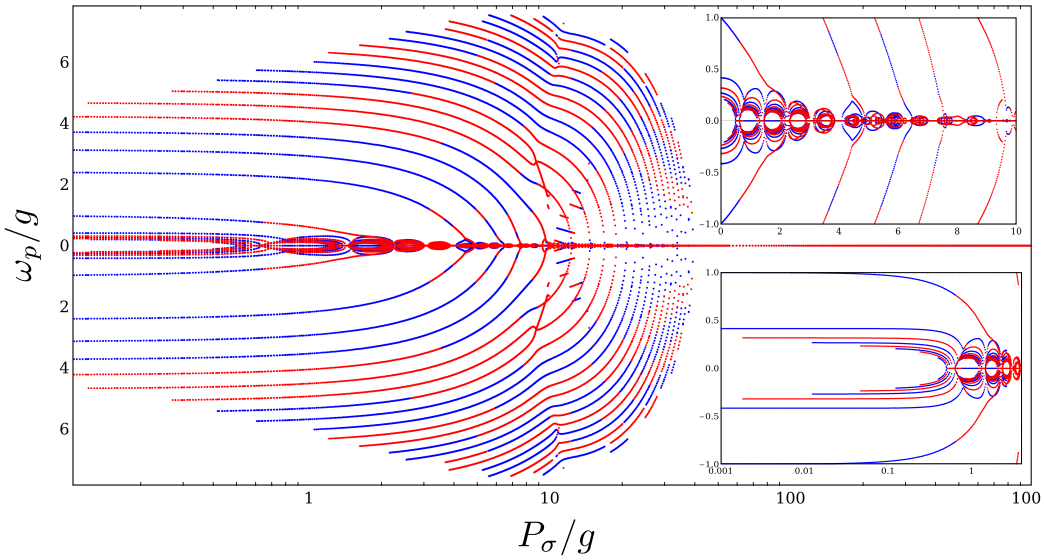

Figure 5.16: Spectral structure in the cavity emission at resonance as a function of P_σ/g for Point 2 ($\Delta = 0$, $P_a = 0$, $\omega_a = 0$). In insets, we zoom over the central peaks and the region $0 \leq P_\sigma \leq g$ (upper) and $0 \leq P_\sigma \leq 10g$ (lower), showing the complex structures that arise. In blue (resp., red) are the peaks with $L_p^a > 0$ (resp., $L_p^a < 0$). At sufficiently high pumping, all eigenvalues have collapse to zero, defining an extreme case of *weak coupling*.

Two cases of finite pumpings are shown in Fig. 5.15 for the finite pumping counterpart of Fig. 5.12(a), namely $P_\sigma = g/50$, (a), and $P_\sigma = g/10$, (b) and (c). We take $\omega_a = 0$ as the reference energy for the remaining of this text. Panel (a) shows how the limiting case ($P_\sigma \ll g$) is weighted and deviates rather lightly from the analytical result. The computation has been made to truncation order $n_t = 50$ and we checked that it had converged with other truncation orders giving exactly the same result. In the figure, only ω_p whose weighting in the cavity emission L_p^a (Lorentzian part) is nonzero are shown, although most of them are very small. If we plot only those with $|L_p^a| \geq 0.01$, only the usual *vacuum Rabi doublet* (in green in Fig. 5.12) would remain. In addition of the weight, also the degeneracy (number of peaks) at a given resonance should be taken into account to quantify the intensity of emission at a particular energy. This information is not apparent in the figures, where we only show in Blue or Red the cases of positive or negative, respectively, weighting. In some cases, many peaks superimpose with opposite signs, possibly cancelling each other. We plot negative values last so that a blue line corresponds to a region of only positive values, while a red line may come on top of a blue line. This figure gives nevertheless an insightful image of the underlying energy structure and how they contribute to the final spectrum as an

addition of many emitting (or interfering) events. In (b) we show a case of higher pumping, with the same principal information to be found in the mapping of the eigenvalues. The characteristic branch-coupling of the JCM, still easily identifiable in Fig. 5.15(a), has vanished, and lines of external peaks directly collapse toward the center. A zoom of the central part, panel (c), shows the considerable complexity of the inner peaks, forming "bubbles" around the central line, due to intensity-aided SC fighting against increasing dissipation that ultimately overtakes. This is the counterpart of the second order and mixed coupling regimes in the SC phase space of 2LSs, where bubbles could form as a result of new asymmetric eigenstates ($|I\rangle$ and $|O\rangle$) appearing in the system.

The origin of the lines can be better understood if we plot them as a function of pumping, as we commented in Section 5.4.2. In Fig. 5.16, the same weighted peak positions ω_p are shown (with the same color code) for Point 2 as electronic pumping is varied from $10^{-3}g$ to $10^3 g$ ($P_a = 0$). This last picture supports the idea that quantum effects (such as subpoissonian statistics, Fig. 5.14) are observed at small pumpings, with optimal range being roughly $P_\sigma < 0.5g$, where only the lowest manifolds are probed. This is the range of pumping where the Jaynes-Cummings manifold structure is still close to that without pump. Further pumping pushes the lines to collapse, starting by the vacuum Rabi splitting which closes, evidencing the loss of the first order SC at $P_\sigma \approx 4g$. Here again we observe this phenomenon of bubbling, with a sequence of lines opening and collapsing, that makes it impossible to specify the exact pump at which the transition takes place. From this point, SC is lost manifold by manifold similarly to the case where γ_a was increased. When $P_\sigma \approx 40g$, all lines have collapsed onto the center and will remain so at higher pumpings. The dot saturates and the cavity empties with thermal photons in a WC regime.

In these conditions, either from Fig. 5.15(b)-(c) or Fig. 5.16, a general definition of Strong-Coupling in presence of pumping is obviously very complex and remains to be established.

5.4.5 Luminescence Spectra at Resonance

Now we have all the ingredients to present the final result: the spectral shapes of the system in a broad range of configurations and parameters. We cannot give a comprehensive picture as any set of parameters is by itself unique, but will instead illustrate the main trends, using specifically for that purposes the three reference points of Fig. 5.13. They give a good account of the general case and one can extrapolate from these particular cases how another configuration will behave. To get exact results for a given point, numerical computations must be undertaken.

From now on, we shall represent in Blue the spectra that correspond to cavity emission and in Violet those that correspond to direct exciton emission. The main

conclusions, based on semi-analytical results, are different for different points or family of points.

Point 1: very good systems and the incoherent Mollow triplet

Point 1, is best suited to explore quantum effects. Its spectral shape is unambiguously evidencing transitions in the Jaynes-Cummings ladder, as shown in Fig. 5.17 with a clear "Jaynes-Cummings fork" (a quadruplet). The outer peaks at ± 1 are the conventional vacuum Rabi doublet, whereas the two inner peaks correspond to higher transitions in the ladder. Observation of a transition from outer to inner peaks with pumping such as shown in Fig. 5.17 would be a compelling evidence of a quantum exciton in SC with the cavity. Fig. 5.18 shows another multiplet structure of this kind for Point 1. The intensity of emission is presented in log-scale and for a broader range of frequencies, so that small features can be revealed. Transitions from up to the third manifold can be explicitly identified. The decay from the second manifold, that manifests distinctly with peaks labelled 2 (although it also contributes to peaks labelled 0), is already weak but still might be identifiable in an experimental PL measurement. Higher transitions have decreasing strenght. This can be checked with the probability to have n photons in the cavity, $\mathrm{p}(n)$, computed from Eqs. (5.11). Whenever the mean number n_a is low (as is the case here), this probability is maximum for the vacuum ($\mathrm{p}(n) > \mathrm{p}(n+1)$ for all n), independently of the nature of the photon distribution (sub, super or Poissonian). Only when $n_a = 1$, in the best of cases (for a Poissonian distribution), does this trend start to invert and $\mathrm{p}(1) = \mathrm{p}(0)$. This makes it impossible, even in the very good system of Point 1, to probe clearly and independently transitions between manifolds higher than 3, as their weak two outer peaks (approximately at $\pm(\sqrt{n}+\sqrt{n-1})$) are completely hidden by the broadening. A stronger manifestation of nonlinear emission is to be found in the pool of pairs of inner peaks from all high-manifold transitions (labelled 0 in Fig. 5.19), at approximately $\pm(\sqrt{n}-\sqrt{n-1})$. Not only the inner peaks coming from different manifolds are close enough to sum up, but also they are more intense than their outer counterparts. This can be easily understood by looking at the probability, I_c, of transition between eigenstates $|\pm, n\rangle$ through the emission of a photon, $c = a$, or an exciton, $c = \sigma$. This probability, $\mathrm{I}_c^{(i\to f)} \propto |\langle f|\, c\, |i\rangle|^2$, estimates the relative intensity of the peaks depending on the initial, $|i\rangle$, and final, $|f\rangle$, states of the transition and on the channel of emission, $c = a, \sigma$. A discussion in terms of the eigenstates of the Hamiltonian is still valid in the regime of Point 1 (very good system) at very low pump. At resonance, neglecting pumps and decays, the eigenstates for manifold n, are $|n, \pm\rangle = (|n, 0\rangle \pm |n-1, 1\rangle)/\sqrt{2}$. The outer peaks arise from transitions between eigenstates of different kind, $|n, \pm\rangle \to |n-1, \mp\rangle$, while the inner peaks arise from transitions between eigenstates of the same kind,

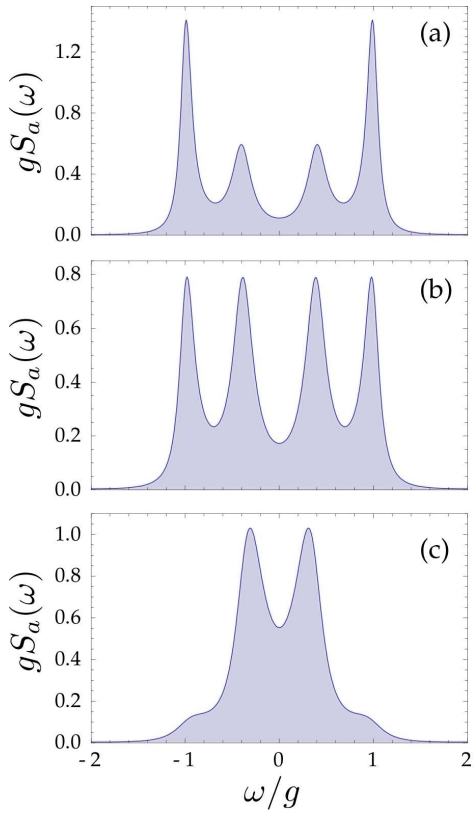

Figure 5.17: Jaynes-Cummings forks as they appear in the luminescence spectrum of a QD in a microcavity with system parameters given by Point 1 of Fig. 5.13 and for pumping rates $(P_a, P_\sigma)/g$ given by (a), $(0, 0.057)$; (b), $(0.002, 0.087)$ and (c), $(0.001, 0.27)$. The two outer peaks at ± 1 correspond to the vacuum Rabi doublet. Inner peaks correspond to transitions with states of more than one excitation. Although the underlying structure is the same, many variations of the actual lineshapes can be obtained.

$|n,\pm\rangle \rightarrow |n-1,\pm\rangle$. Their probability amplitudes in the cavity emission,

$$\mathrm{I}_a^{(\pm\rightarrow\mp)} \propto |\langle n-1,\mp|\, a\, |n,\pm\rangle|^2 = |\sqrt{n}-\sqrt{n-1}|^2/4\,, \tag{5.41a}$$

$$\mathrm{I}_a^{(\pm\rightarrow\pm)} \propto |\langle n-1,\pm|\, a\, |n,\pm\rangle|^2 = |\sqrt{n}+\sqrt{n-1}|^2/4\,, \tag{5.41b}$$

evidence the predominance of the inner peaks versus the outer ones, given that one expect the same weighting of both transitions from the dynamics of the system. The doublet formed by the inner peaks is therefore strong and clearly identifiable in an experiment. On the other hand, in the direct exciton emission, the counterparts of Eqs. (5.41) are manifold-independent and equal for both the inner and

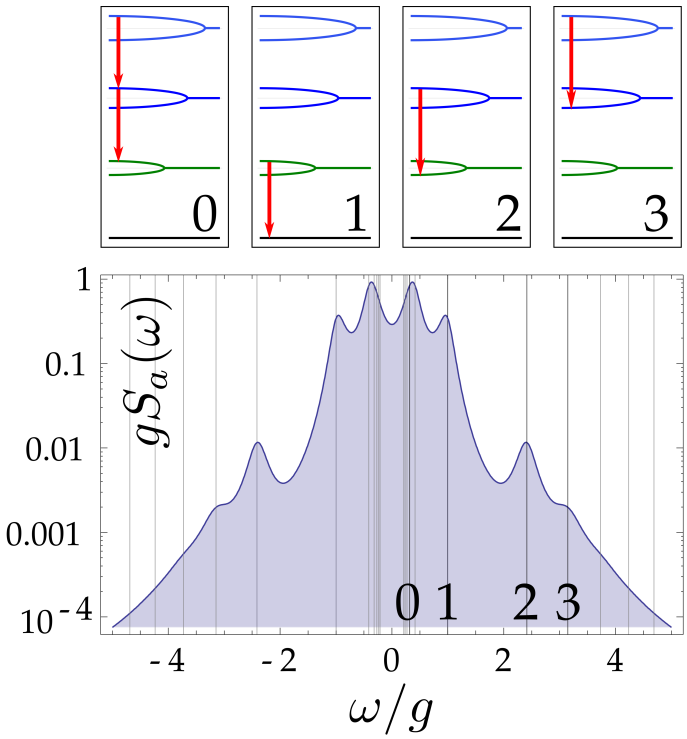

Figure 5.18: Expanded view in logarithmic scale of a spectrum similar to those of Fig. 5.17, this time with $(P_a, P_\sigma)/g = (0.002, 0.076)$. Transitions up to the third manifold (shown in insets) are resolvable. Others are lost in the broadening. The transition energies of the Jaynes-Cummings ladder are shown by vertical lines (up to the third manifold). The Rabi peaks that corresponds to transitions from the first manifold to vacuum (line 1) is in this case dominated by higher transitions that accumulate close to the center (line 0).

outer peaks:

$$\mathrm{I}_\sigma^{(\pm\to\mp)} \propto |\langle n-1,\mp|\,\sigma\,|n,\pm\rangle|^2 = 1/4\,, \tag{5.42a}$$

$$\mathrm{I}_\sigma^{(\pm\to\pm)} \propto |\langle n-1,\pm|\,\sigma\,|n,\pm\rangle|^2 = 1/4\,. \tag{5.42b}$$

In this case, therefore, one can expect similar strength of transitions for both the inner and outer peaks with a richer multiplet structure for the direct exciton emission.

In Fig. 5.19, we give an overview of the PL spectra as P_σ is varied from very small to very large values. For point 1, as we already noted, the cavity pumping plays a relatively minor quantitative role. Therefore we only show two cases, of no-cavity pumping (first row) and high-cavity pumping (second row). As can be seen, there is no strong difference from one spectra with no cavity pumping to its counterpart with large cavity pumping. Third row shows the direct exciton emission that, with no cavity pumping, corresponds to the first row. Indeed, one

can observe the richer multiplet structure up to $P_\sigma \approx 0.5g$ in the direct exciton emission, whereas only inner peaks are neatly manifest in the cavity emission. This region corresponds to a quantum regime with a few quanta of excitations (and subpoissonian particle number distribution, $g^{(2)} < 1$) giving rise to clearly resolvable peaks, attributable to the Hamiltonian manifolds. Therefore, a good system (high Q and g) and a good QD (two-level) emitter suffice to easily and clearly observe quantum effects. There is no need of pumping harder than it has been done in present systems so far.

In the region $g < P_\sigma < 30g$, the photon fluctuations are those of a coherent, classical state, $g^{(2)} = 1$. Increasing pumping with the intention to penetrate further into the nonlinearity, merely collapses the multiplet structure into a single line, as far as cavity emission is concerned. However, this does not mean that the system is in weak coupling. In the direct exciton emission, the rich SC fine structure has turned into a *Mollow triplet*, like the one found by Mollow (1969), that we discuss in depth below. In this region, the first manifolds have crossed to WC but higher manifolds retain SC, bringing the system into lasing. At this point, a change of realm should be performed favoring a classical description, as we already pointed out with the AO. A last transition into thermal light and WC, due to saturation and self-quenching, takes place at $P_\sigma \approx 30g$ that leads to a single central peak in the spectra.

In Fig. 5.20, we take a closer look into Fig. 5.19 in the region of the loss of the doublet of inner peaks with increasing electronic pumping, where the system starts to cross from the quantum to the classical regime. In the cavity emission, the doublet of inner peaks collapses into a single line that is going to narrow as the system lases. At the same time, a strikingly richer structure and regime transition is observed in the direct exciton emission. As the peaks are more clearly resolved as explained before [cf. Eqs. (5.41) and (5.42)], the "melting" of the Jaynes-Cummings ladder into a classical structure is better tracked down. Indeed, as pumping is increased, broadening of these lines starts to unite them together into an emerging structure of a much less reduced complexity, namely a triplet. This is completely equivalent to the transition from quantum to classical AO that we studied in Sec. 5.2. In Fig. 5.21, we provide another zoom of the overall picture given by Fig. 5.19, this time for the direct exciton emission exclusively. First three rows show the evolution with electronic pumping P_σ (values in inset) over a wide range of frequencies, up to $\pm 15g$, while the three last rows show the very same spectra, with a one-to-one mapping with previous rows, only in the range of frequencies $\pm 3g$. The transition manifests to different scales, with a rich fine multiplet structure in the quantum regime, as seen in the zoomed-in region, to a monolithic triplet at higher pumpings, as seen in the enlarged region. On the right, spectra are superimposed to follow their evolution with pumping. The two broad satellites peaks, at approximately $\pm 2\sqrt{n_a}$ (in the AO the broad peak was placed at

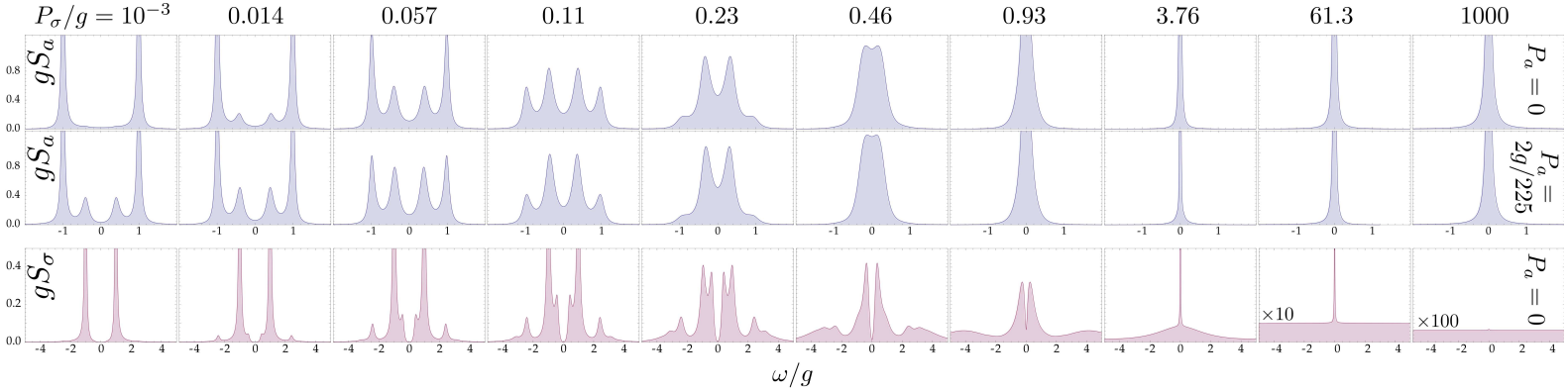

Figure 5.19: Point 1 of Fig. 5.13. Spectral emission over a wide range of electronic pumping P_σ/g from 10^{-3} to 10^3 showing the three main regimes: multiplet emission, lasing and quenching. Cavity pumping only affects quantitatively the main features of the emission in this case of very strong coupling, so a small set is shown as representative enough: two upper rows (blue) correspond to cavity emission for no and large cavity pumping, respectively, and lower row (violet) to the direct exciton emission for no cavity pumping. The Jaynes-Cummings fork is clearly resolved at small P_σ ($< 0.2g$) and is enhanced by the cavity pumping. At higher electronic pumping ($P_\sigma \approx 0.5g$), the multiplet structure collapses into a dominant doublet of inner peaks while the vacuum Rabi peaks melt into its shoulders. Then the system is brought into lasing ($g < P_\sigma < 30g$) and is finally quenched ($P_\sigma > 30g$).

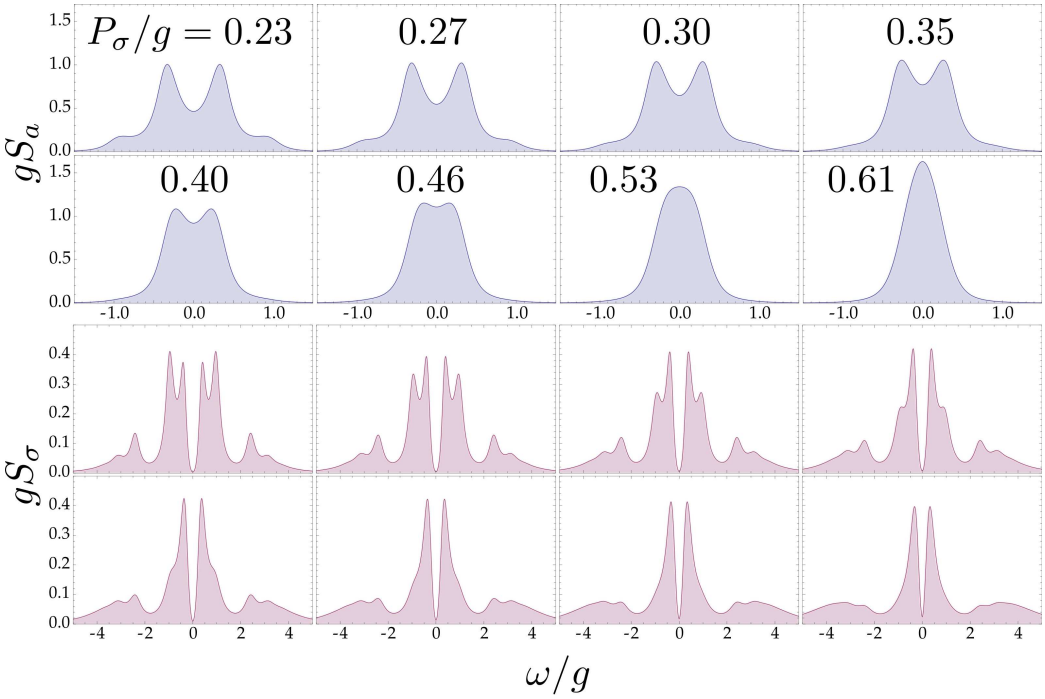

Figure 5.20: Point 1 of Fig. 5.13. Details of the loss of the multiplet structure with increasing exciton pumping and zero cavity pumping. The two upper rows (blue) correspond to the cavity emission $S_a(\omega)$ and the two lower (violet) to the exciton direct emission $S_\sigma(\omega)$. The spectral structure is richer in the exciton spectra that develops a Mollow triplet-like emission.

$n_b U$), drift apart from the main central one with increasing excitation, and in this sense behave as expected from a Mollow triplet. Various deviations are however observed, of a more or less striking character. The most astonishing feature is the emergence of a very sharp and narrow peak in the center, that has been plotted with its total intensity on the right panel to give a sense of its magnitude. It is clearly seen in the zoomed-region how this peak arises on top of the broad mountain of inner peaks, surviving the collapse of the fine structure in the classical regime. This thin central resonance appears when a large truncation is needed. It is a sum of many contributing peaks centered at zero, most of them with very small intensities. This region therefore shows all the signs of a transition from a quantum to a classical system. At low pumping, the inner peaks of all quadruplets coming from low order manifolds are placed approximately at $\pm(\sqrt{n}-\sqrt{n-1}) \neq 0$. Even when they are summed up to produce the total spectrum, the nonlinear doublet is still resolved. At around $P_\sigma \approx 1.5g$, manifolds high enough are excited so that for them $\pm(\sqrt{n}-\sqrt{n-1}) \approx 0$. This is a feature of a classical field resulting in a Mollow triplet. Note that nothing of this sort is observed in the cavity emission. The Mollow triplet, whether in atomic physics with coherent excitation or

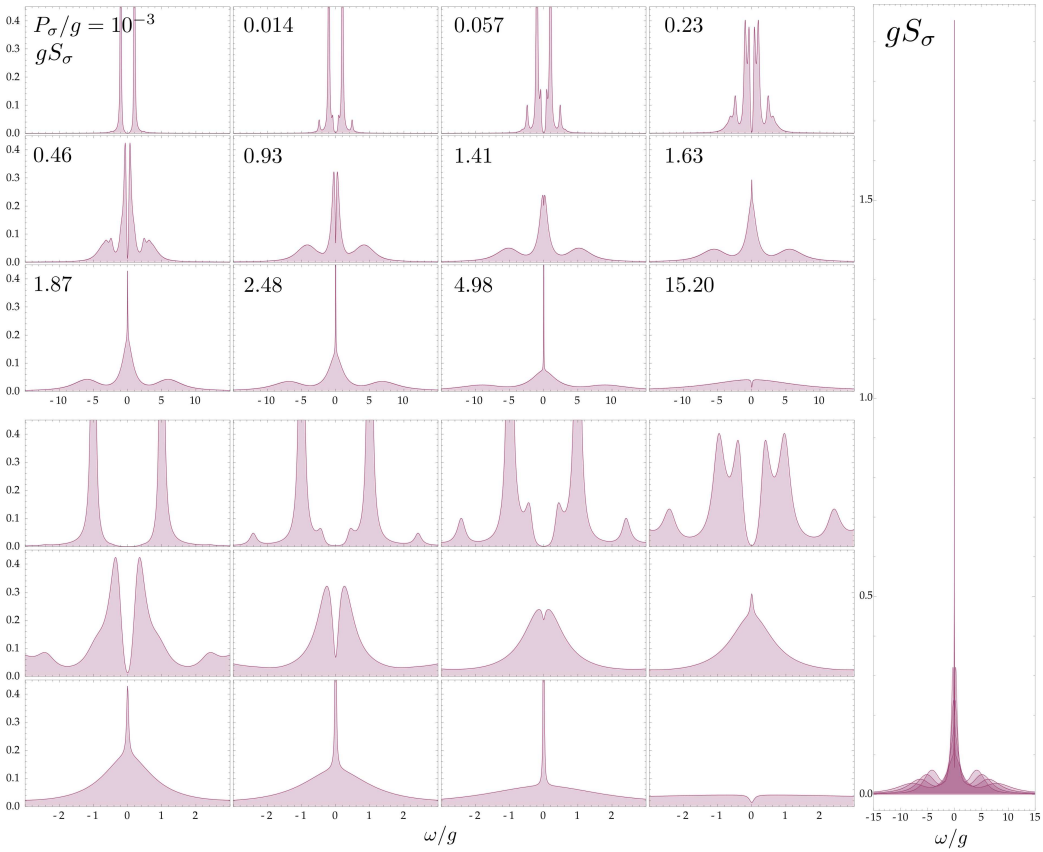

Figure 5.21: Point 1 of Fig. 5.13. Incoherent Mollow triplets are observed in the exciton direct emission with broad satellite peaks at approximately $\pm 2\sqrt{n_a}$ and a strong narrow central peak taking over a narrow resonance. Three upper rows show the spectra over the interval $|\omega| \leq 15g$ allowing to see the satellites. Three lower rows are the same in the window $|\omega| \leq 3g$, allowing to see the narrow resonance and peak that sit at the origin. Values of the electronic pumping are given in the frame of the first three rows. Cavity pumping is zero but influences very little the Mollow triplets. Rightmost figure superposes various spectra at increasing electronic pumping, showing the drift and broadening of the satellites, and putting to scale the very strong coherent feature at the origin. The incoherent Mollow triplet appears thus very differently from its counterpart under coherent excitation.

in semiconductor physics with incoherent pumping, is a feature of the quantum emitter itself, when it is directly probed. There is therefore a strong motivation here to detect leak emission of semiconductor structures. The overall features of this "incoherent Mollow triplet" differ from its counterpart namesake in the strong asymmetry of the satellites and their increased broadenings with pumping.

In order to appreciate more precisely the structure of the Mollow triplet and how it emerges from the quantum regime, we consider a even better system than Point 1: γ_a of the order of 10^{-3}, 10^{-2} and $\gamma_\sigma = 0$. With very small pumping

rates, in Fig 5.22 we can see the very sharp (owing to the small decay rates) individual lines from each transition. In the plot of the cavity emission, Fig 5.22(a), we have marked each peak with its corresponding transition between two quantized, dressed states of the JC Hamiltonian. These peaks correspond one-to-one with those of the exciton emission, that are, as we just explained, weighted differently. In both cases, the Rabi doublet dominates strongly over the other peaks. In Fig. 5.22(a), for instance, the peaks at ± 1 extend for about 9 times higher than is shown, and already the outer transitions are barely noticeable. This is because the pumping is small and so also the probability of having more than one photon in the cavity (it is in this configuration of about 10% to have 2 photons, see Fig. 5.25). One could spectrally resolve the window $[-g/2, g/2]$ over a long integration time and obtain the multiplet structure of nonlinear inner peaks, with spacings $\{\sqrt{n+1}-\sqrt{n}, n>1\}$ (in units of g), observing direct manifestation of single photons renormalizing the quantum field. Or one could increase pumping (as we do later) or use a cavity with smaller lifetime. In this case, less peaks of the JC transitions are observable because of broadenings mixing them together, dephasing and, again, reduced probabilities for the excited states, but the balance between them is better. In Fig. 5.23, where γ_a is now $g/100$, the vacuum Rabi doublet (marked R) is dominated by the nonlinear inner peaks in the cavity emission, and a large sequence of peaks is resolved in the exciton emission.

Going back to the case of Fig. 5.22, but increasing pumping, we observe the effect of climbing higher the Jaynes-Cummings ladder. Results are shown in Fig. 5.24 in logarithmic scale, so that small features are magnified. First row is Fig. 5.22 again but in log-scale, so that the effect of this mathematical magnifying glass can be appreciated. Also, we plot over the wider range $[-15g, 10g]$. Note how the fourth outer peak, that was not visible on the linear scale, is now comfortably revealed with another three peaks at still higher energies. As pumping is increased, we observe that the strong Rabi doublet is receding behind nonlinear features, with more manifolds indeed being probed, with their corresponding transitions clearly observed (one can track up to the 19th manifold in the last row). This demonstrates obvious quantization in a system with a large number of photons. The distribution of photons in these three cases is given in Fig. 5.25, going from a thermal-like, mostly dominated by vacuum, distribution, to coherent-like, peaked distribution stabilizing a large number of particles in the system. At the same time, note the cumulative effect of all the side peaks from the higher manifolds excitations, absorbing all quantum transitions into a background that is building up shoulders, with the overall structure of a triplet. This is the mechanism through which the system bridges from a quantum to a classical system with the Mollow triplet. These are obtained this time, both in the cavity and the exciton emission, but much more so in the latter.

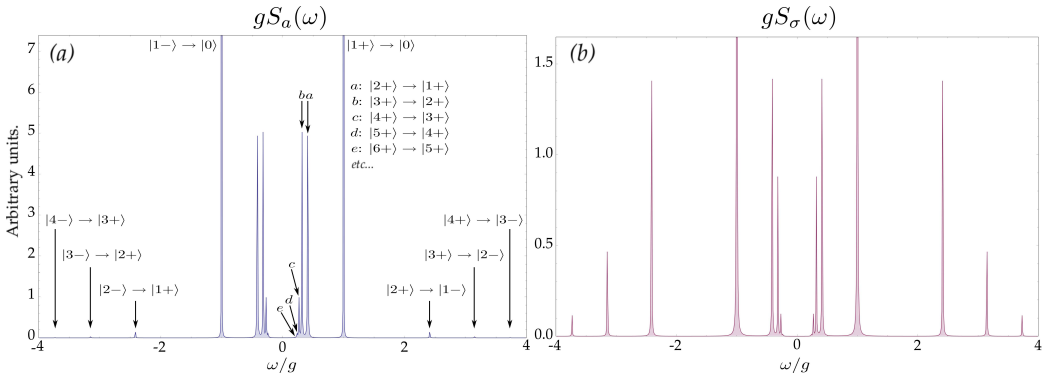

Figure 5.22: Fine structure of the "light-matter molecule": emission spectra in the cavity (a) and direct exciton emission (b) of the strongly-coupled system with $(\gamma_a, \gamma_\sigma)/g = (10^{-3}, 0)$ at $P_\sigma/g = 10^{-3}$.

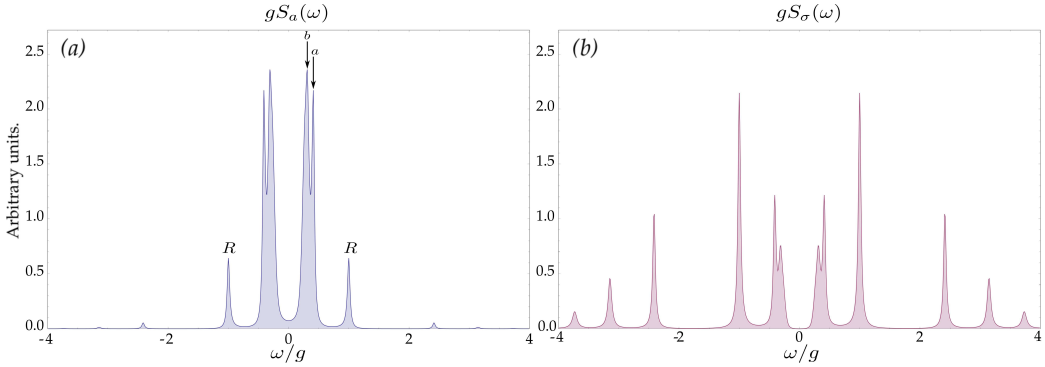

Figure 5.23: Same as Fig. 5.22 but now with $\gamma_a/g = 10^{-2}$. Less peaks are resolved because of broadening but nonlinear peaks (a, b) are neatly observable. In fact, now inner nonlinear peaks dominate in the cavity emission (the vacuum Rabi peaks are denoted R). In the exciton direct emission, the Rabi doublet remains the strongest.

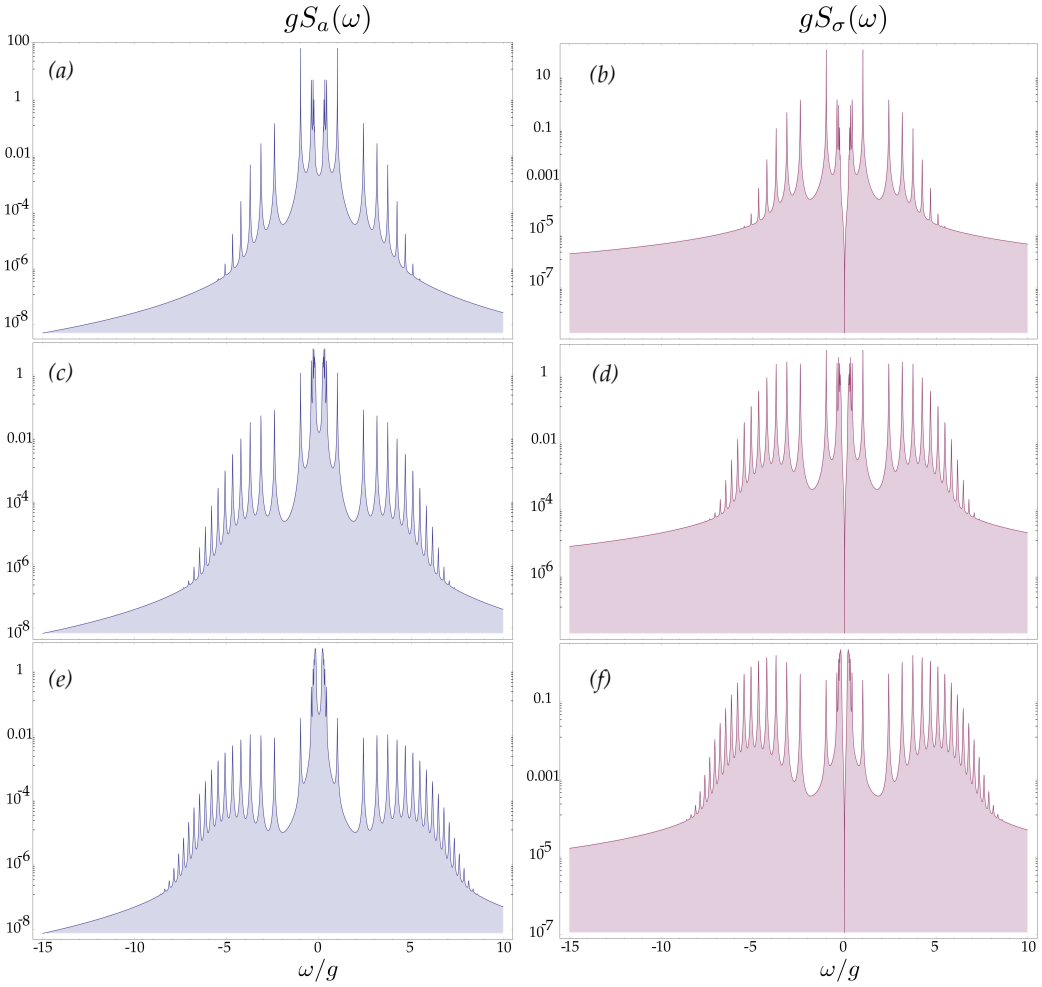

Figure 5.24: Spectra of emission in log-scales as a function of pumping P_σ/g, for 10^{-3} (upper row), 5×10^{-3} (middle) and 10^{-2} (lower row).

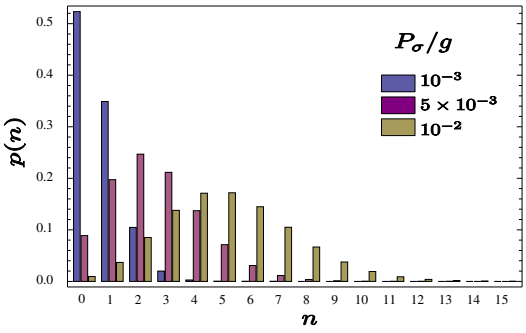

Figure 5.25: Probability $p(n)$ of having n photon(s) in the cavity, for the three cases shown on Fig. 5.24. Quite independently of the distribution of photon numbers in the cavity, field-quantization is obvious.

Point 2: Good systems, the nonlinear doublet and role of cavity pumping

In Fig. 5.26, we show for Point 2 a similar overall picture as Fig. 5.19 does for Point 1. Point 2 has larger dissipation and to current estimates, corresponds more closely to the best systems available at the time of writing. As opposed to Point 1, a small cavity pumping has a strong influence on the result, so we display more cases, namely those that range from no cavity pumping (first row) to large cavity pumping ($P_a = g/5$, 4th row) with two intermediate cases showing the transfer of the emission from the vacuum Rabi doublet to the inner peaks arising from transitions between higher manifolds.

The fifth row shows the corresponding direct exciton emission, for the extreme cases of no (1st row) and highest (4th) cavity pumping. The cavity pumping has the important role of revealing the quantum nonlinearity of the system, that was obvious for reference point 1 in any case but is now invisible in the first row, where at increasing electronic pumping, the vacuum Rabi doublet undergoes a rather dull collapse. The same spectra could be expected from a linear (bosonic) model, in the appropriate range of parameters. This is particularly evident in Fig. 5.27 where three cases of cavity pumping (none, intermediate, and large) are shown for various electronic pumping, both for the cavity and direct emission. Outer lines correspond to zero and inner lines to larger cavity pumping. Note how the intermediate cavity pumping cases display obvious deviation from a bosonic model, that has essentially the shape of a doublet of Lorentzian peaks (with a dispersive correction that has little bearing on the qualitative aspect of the final result). Cavity pumping literally unravels the nonlinearity. The case of intermediate pumping is the most determining in this aspect as far as cavity emission is concerned, while higher cavity pumpings are more favorable for uncovering quantum features from the direct exciton emission. This is mainly for two reasons. One has to do with the influence of what effective quantum state is realized in the system, that we will discuss in more details in connection with the third reference point. The other being the excitation of higher manifolds from the Jaynes-Cummings ladder, that are now less accessible because of the larger dissipation rates. Note how the disappearance of the vacuum Rabi doublet with increasing P_σ (with no cavity pumping), is of a different character than for Point 1, where higher P_σ resulted in an excitation of the upper manifolds and a transfer of the dynamics higher in the Jaynes-Cummings ladder, whereas in this case it essentially results in a competition between only the first and second manifold transitions. Cavity pumping can help climbing the ladder with no prejudice to broadening. Finally, even if blurry resolution or statistical noise of an actual experiment would cast doubt on the presence of a quadruplet in such a structure, the transfer with increasing cavity pumping of the emission from outer (vacuum Rabi) to inner peaks (from the second manifold transitions in this case) makes it clear that the underlying statistics is of a Fermi rather than of a

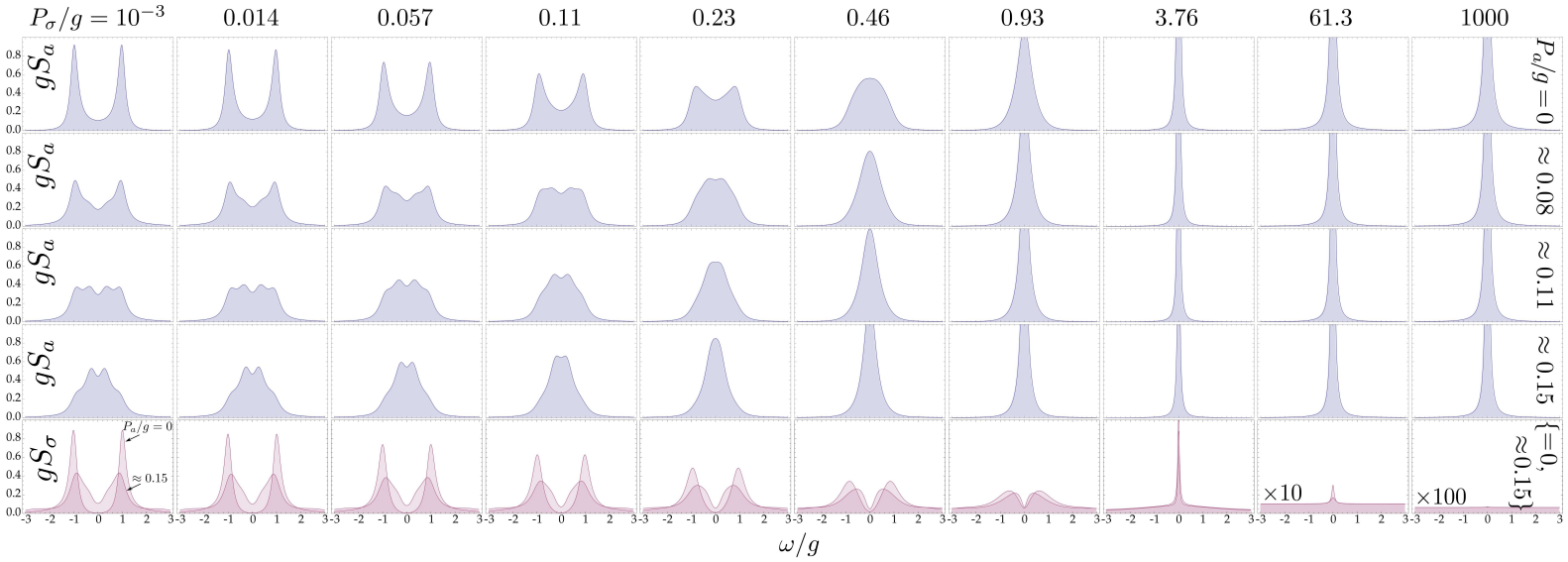

Figure 5.26: Same as Fig. 5.19 over the same range of P_σ, but for Point 2 of Fig. 5.13. In this case, cavity pumping has a strong influence on the cavity luminescence spectra, so we show more cases, namely $P_a/g = 0$ (upper row), ≈ 0.08 (second), ≈ 0.11 (third) and ≈ 0.15 (fourth) as well as the exciton direct emission spectra S_σ in the fifth columns with two cases of cavity pumping, $P_a/g = 0$ (outer peaks) and ≈ 0.15, corresponding to first and fourth rows of the cavity emission. Exciton spectra are less qualitatively affected by the cavity pumping. With electronic pumping only, no particular feature is observed in the cavity emission. In this case, cavity pumping makes a huge difference by revealing the underlying Jaynes-Cummings ladder.

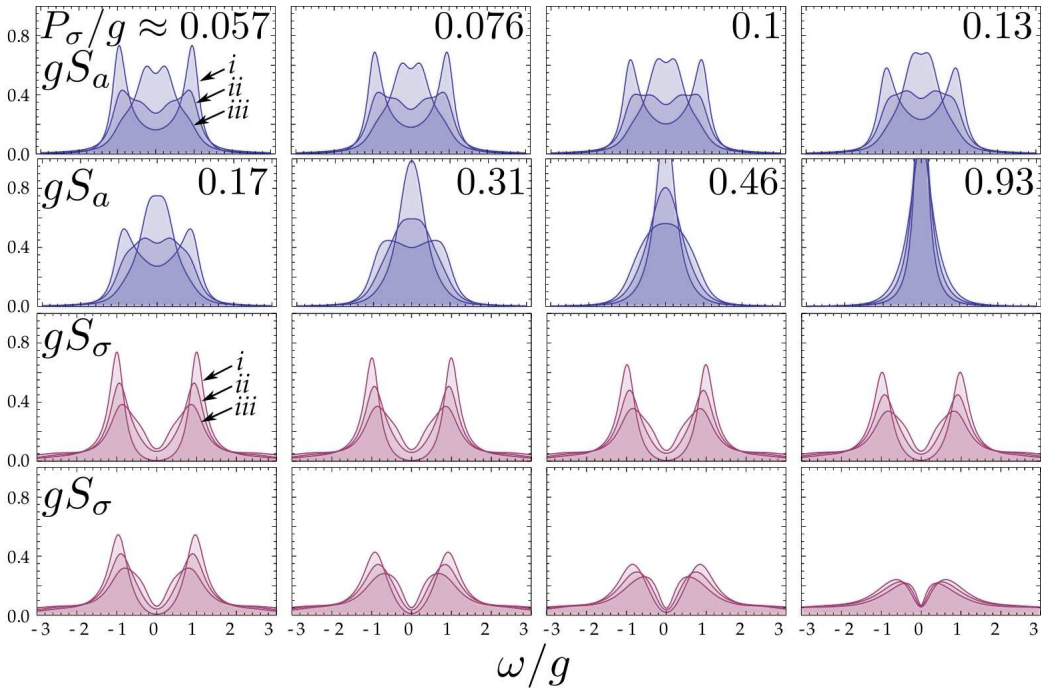

Figure 5.27: Point 2 of Fig. 5.13. Details of the loss of the multiplet structure with increasing exciton pumping. Two upper rows (blue) correspond to the cavity emission $S_a(\omega)$ and two lower (violet) to the corresponding exciton direct emission $S_\sigma(\omega)$ for $P_a/g = 0$ (*i*), ≈ 0.076 (*ii*) and ≈ 0.15 (*iii*) (higher pumping corresponds to innermost peaks). Cavity pumping is essential in such a system to reveal the Fermionic nature of the QD emitter.

Bose character. In Fig. 5.28, we show the case $P_\sigma = 10^{-3}g$ for such an increasing cavity pumping for a detailed appreciation of the previous statement. A very close look might still suggest that the case $P_a = 0$ (outer peaks) still has a small deviation from the linear model that would betray, in a very finely resolved experiment, its non-bosonic or nonlinear character. Counter to intuition, this is better seen for vanishing electronic pumping, as otherwise the lines are broadened according to Eq. (5.14) and this dampens the inner nonlinear peaks. Note, on the other hand, how cavity pumping unambiguously settles the issue.

Point 3: decoherence and saturation

Finally, we turn to point 3 of Fig. 5.13, i.e., to the case with high dissipation rates. In this case, as shown in Fig. 5.29, the Jaynes-Cummings structure is not probed and the spectra are mere doublets closing in the WC. A small cavity pumping again helps to resolve them. The main physics at work here is the one that has been amply detailed in Chapter 3, in the LM, namely, the effective quantum state

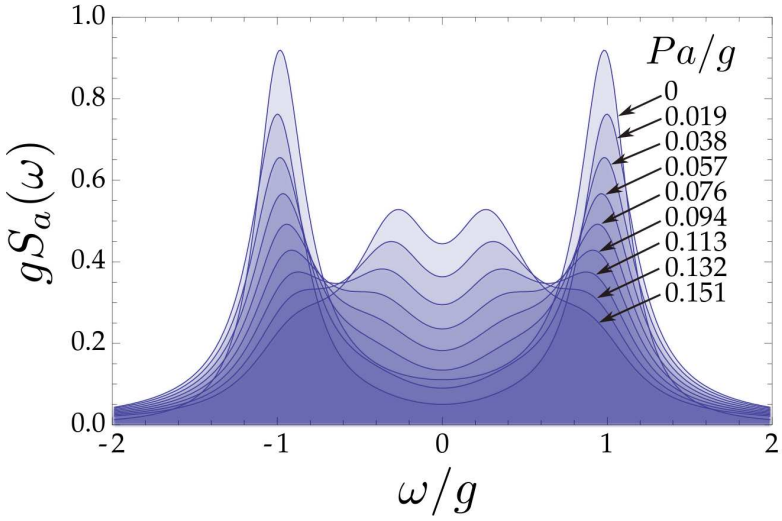

Figure 5.28: Detail of $S_a(\omega)$ for Point 2 of Fig. 5.13 at vanishing P_σ for the values of P_a/g indicated (higher pumpings correspond to innermost peaks). In a reasonably good QD–cavity system, strong deviations from the linear regime are observed in the emission spectrum, revealing the Jaynes-Cummings fork. The quantum features are made more obvious by increasing the cavity pumping, with a neat renormalization of the dominant doublet even if the quadruplet cannot be resolved experimentally.

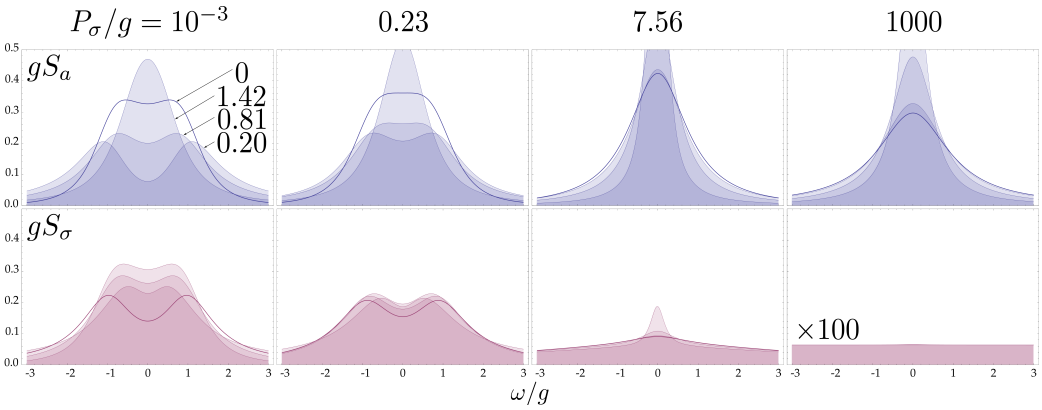

Figure 5.29: Point 3 of Fig. 5.13. Spectral emission for the indicated electronic pumping P_σ/g: 10^{-3} (1st column), ≈ 0.23 (2nd), ≈ 7.56 (3rd, lasing) and 1000 (4th, quenching), for $P_a/g = 0$ (thick line with no coloring), ≈ 0.20, ≈ 0.81 and ≈ 1.42 as indicated in the top left panel, and similarly for others (apart from the case $P_a = 0$, inner peaks corresponds to higher pumpings). In this system, broadening is always too high to allow any manifestation of the underlying Jaynes-Cummings structure. The structure could be mistaken for a bosonic system (or the other way around). Specially, cavity pumping helps observation of the vacuum Rabi doublet in the same way as of the linear Rabi doublet for the LM (see Fig. 5.30.

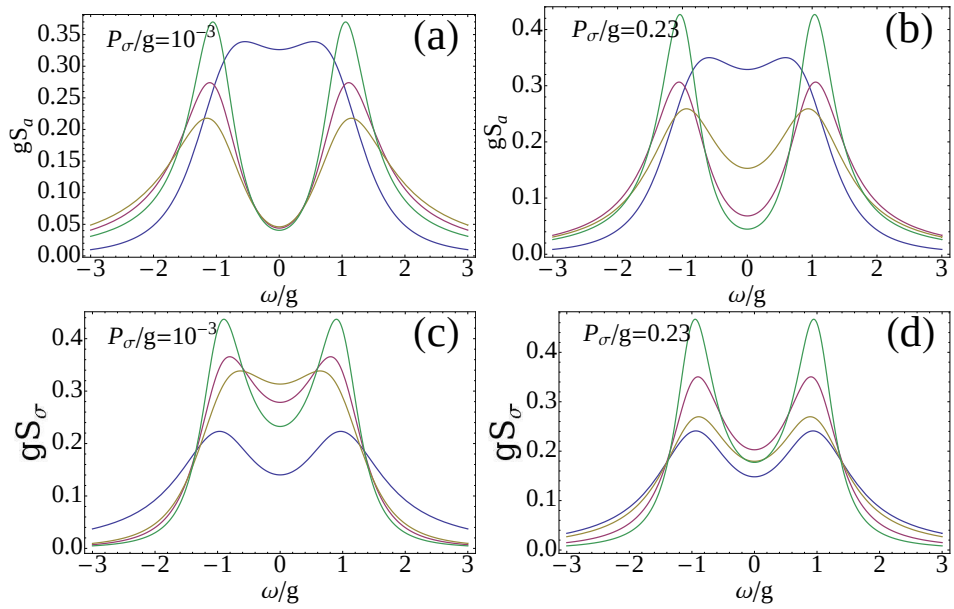

Figure 5.30: Linear model spectra for the system in Point 3 of Fig. 5.13. (a)–(b) correspond to cavity spectra and (c)–(d) to exciton spectra. The pumpings vary as in the two first columns of Fig. 5.29 for comparison with the JCM. The color code goes: blue, purple, brown and green, from low to high P_a.

realized in the system by the interplay of pumpings and decay. In Fig. 5.30 we plot the LM spectra for the pumping cases that lead to a SS, for comparison with the first two columns in Fig. 5.29. The LM is always in SC for these $\gamma_{a,b}/g$, and leads to a Rabi doublet in both channels of emission at all pumpings that is much better resolved in the presence of cavity pumping P_a. In both models, therefore, photon-like quantum state has dispersive corrections that push apart the dressed states (Lorentzians) and therefore enhances the visibility and splitting of the lines.

Although the spectral features found in this system are those of the LM (doublet/singlet), the actual spectra differ greatly out of the linear regime. Increasing P_a further brings the JCM into WC with a singlet in the emission, while it cannot induce such transition in the LM, that remains a doublet and in SC.

A fundamental difference between the models is that the bosonic pumps P_a, P_b, always reduce the total broadening of the lines (Γ_+) while P_σ increases it. The contribution of pump to the line positions differs greatly from the bosons, as not only P_σ carries a different sign but also this contribution depends on the manifold. The statistics make also an important difference. Opposite to the wide variety of photon distributions found with a fermion model, cavity and exciton are always in a thermal state for bosons, without quenching or really lasing. The issue of the underlying statistics could therefore be settled in photon-counting experiment.

Fig. 5.14 shows that such systems (especially when $\gamma_a \gg 1$ and $\gamma_\sigma \to 0$) have the advantage over better cavities that at low electronic pumping and *vanishing* cavity pumping, the system generates antibunched light, suitable for single-photon emitters (though not on demand).

5.4.6 Luminescence spectra with detuning

In semiconductors, the detuning between bare modes is a parameter that can easily be varied and which provides useful information of the SC physics. Strong coupling is better studied at resonance, and detuning is mainly used to help locate it, by finding the point where anticrossing is maximum and level repulsion stationary. In a fitting analysis of an experiment, it brings a lot of additional data at the cost of only one additional fitting parameter. In the Fermion case, it also has the benefit of uncovering new qualitative behavior of the PL lineshapes, that are strongly restricted by symmetry at resonance.

Fig. 5.31 shows the vanishing pumping case of ω_p in Eq. (5.22) with detuning, i.e., the imaginary part of Eq. (5.24) for the first row that corresponds to the first manifold (also, the boson case) and of Eq. (5.25) for the second and third rows, that corresponds to the second and third manifold, respectively. Fourth row is a superposition of all manifolds up to the 15th one. Detuning is varied in columns, from no detuning (first column) to twice the coupling strength (fifth column). Negative detunings are symmetric with respect to the x axis.

The line opening is common to all manifolds, but note the different behavior of the first manifold (linear or boson case) and higher manifolds: in the first case, one line collapses towards the center (on the cavity mode) while the other recedes away, towards the exciton mode. In the nonlinear case, there is up to four lines, and outer lines are both repelled away while inner lines get both attracted towards the cavity mode, at the center. As we discussed, the total doublet of inner peaks is intense and will dominate. For cases with high dissipation, there is little or no particular insights to be gained from detuning, as, again, most features are lost in broadening. We restrict out attention to Points 1 and 2 in what follows. In Fig. 5.32, PL with detuning are shown for Point 1 in panels (a)–(d) and for Point 2 in panel (e). Panel (d) is a magnified view of panel (a). It is seen clearly how the doublet of inner peaks essentially remains fixed at its resonance position independently of the exciton position. Only at very high detunings does the doublet collapse onto the center. The vacuum Rabi doublet however appears as an anticrossing of the exciton bare mode with the doublet of inner peaks (that eventually becomes the cavity bare mode). Panel (a) is at small electronic pumping and (b), (c) at ten time larger electronic pumping (both no cavity pumping), for the cavity and direct exciton emission, respectively. Again, lower electronic pumping is more prone to reveal rich quantum features. In panel (b) only the inner non-

linear doublet is visible, with a transfer of the emission intensity from one peak (essentially fixed) to the other. The resonance case is plotted in the third panel on first row (third row for the exciton emission) of Fig. 5.20. The linear Rabi doublet, which trace is seen faintly undergoing anticrossing with the pinned central peaks, provides small shoulders. In general, PL with detuning in the Fermi case shows a very characteristic behavior, that cannot be mistaken with a conventional (bosonic) anticrossing experiment.

In panel (e), the case of a more realistic system is shown with detuning. The pinning of the inner peaks is less obvious in this case, although if one draws a vertical line at the resonance, through the minimum of the doublet, one observes that this minimum is fixed. As a result, triplets are obtained in the cavity emission spectra, that are of a very distinct nature than the Mollow triplet observed in the side (exciton) emission of Point 1. The triplets involving the nonlinear doublet are a manifestation of the quantum regime overcoming broadening while the Mollow triplet is a manifestation of the lasing regime.

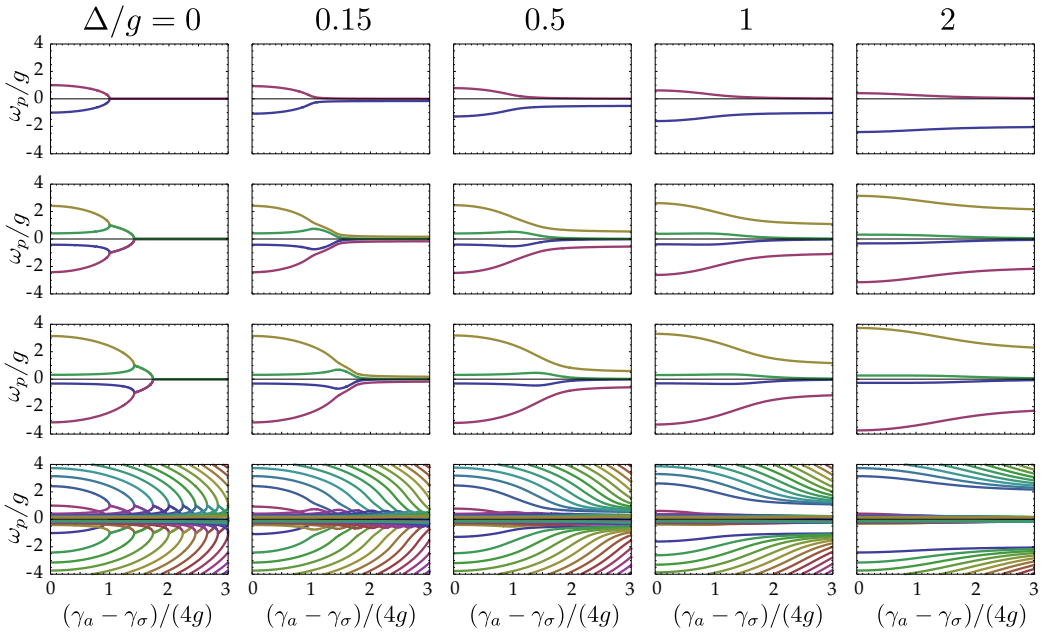

Figure 5.31: Positions ω_p/g of the lines around $\omega_a = 0$ in the luminescence spectrum with detuning and in the absence of pump. Columns correspond to various detunings, first column being the case of resonance (cf. Fig. 5.12). First three rows show in isolation the first, second and third manifold, respectively. First manifold corresponds to the bosonic or linear case. Fourth row shows all manifolds together. Left-bottom panel is detailed for positive ω_p in Fig. 5.12.

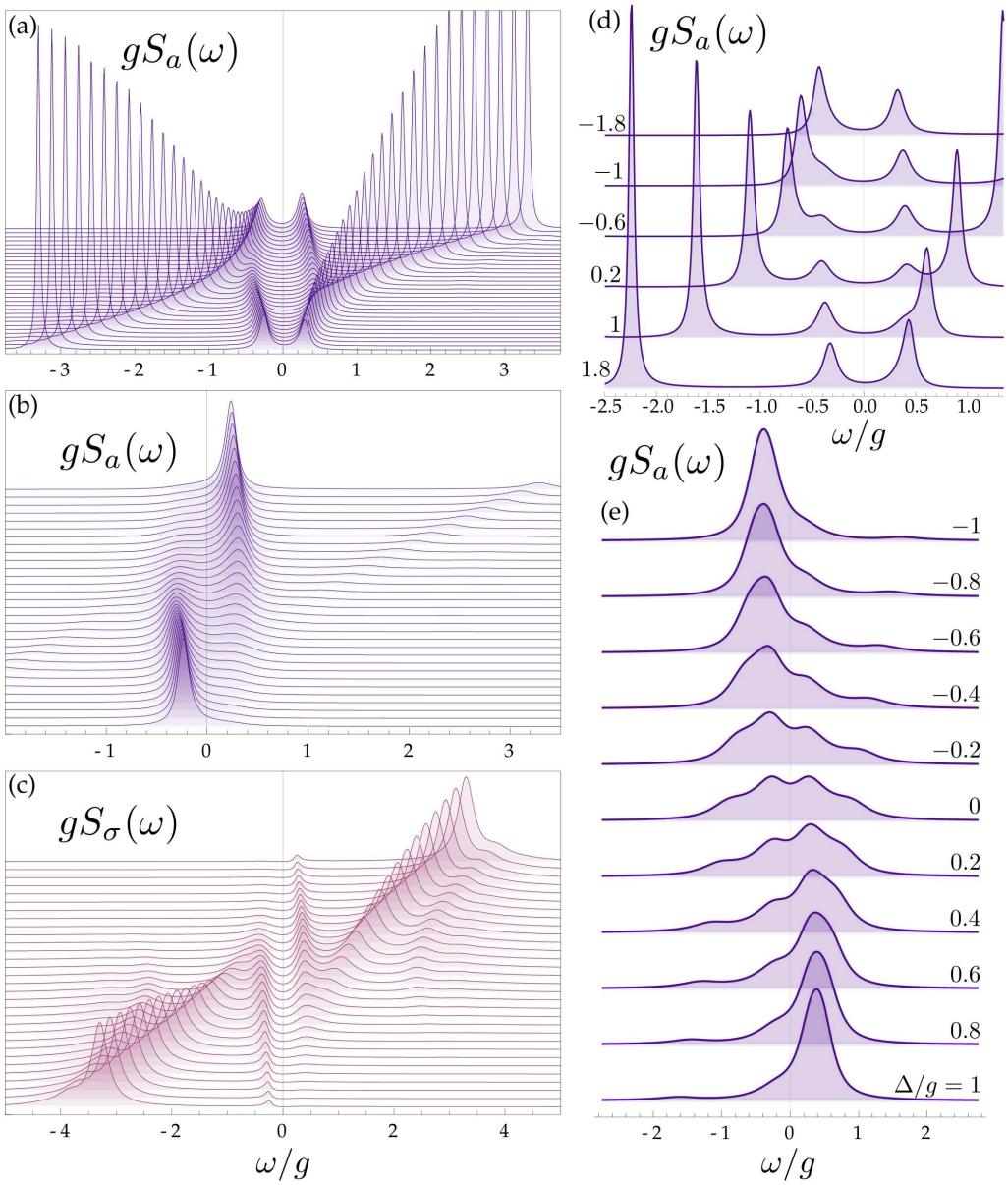

Figure 5.32: Anticrossing of the luminescence lines as detuning $\Delta = \omega_a - \omega_\sigma$ is varied. Here, $\omega_a = 0$ is fixed and the QD bare energy is tuned from below the cavity (positive detuning) to above (negative detuning). Panels (a)-(d) correspond to Point 1 and panel (e) to Point 2. (a)-(d) are at zero cavity pumping, $P_a = 0$. (a) and (d) are for $P_\sigma = 0.03g$ [(d) is a zoom of (a)] and (b)-(c) for $P_\sigma = 0.3g$. (a), (b), (d) are the cavity emission $S_a(\omega)$ and (c) the direct exciton emission $S_\sigma(\omega)$. (e) is for $P_\sigma = 10^{-3}g$ and $P_a = g/5$ (cf., 7th row, 1st column of Fig. 5.26). The nonlinear central peaks give rise to very characteristic anticrossing profiles.

5.5 Conclusions

In this Chapter, I have presented the study of nonlinearities that the excitons can bring, with different models. The main results of this Chapter are in the description of the spectra of emission for each case, that follows from the general expression (2.108), in WC or SC regimes.

In Sec. 5.2 we studied isolated interacting excitons, still considered as bosons, with the AO model. This fundamental model can be solved analytically for the SE case [Eq. (5.7)] but requires numerical computations in the SS case. The most interesting consequence of the nonlinearity then, is that the transition from a quantum (*multimode lasing*) to a classical (*mean field lasing*) regime can be easily tracked by the melting of the individual peaks (at $(p-1)U$) that compose the spectra into a broad single peak (at $n_b U$) (see Fig. 5.3). The transition can be induced by increasing the pump ("inverting" the population) or decreasing the interactions (towards the "classical" HO).

In Sec. 5.3, we coupled the AO, representing the interacting excitons, with an HO, the photons, to study the effect of nonlinearities in the LM. In this case, I have focused on the quantum regime (very low pump) of the SS case, where nonlinearities are weakly probed. In this limit, we could successfully analyze all the spectral features from the very well resolved lines, in terms of manifold transitions only. We paid special attention to the specific lines that the different kinds of pumping, excitonic or photonic, enhances in the optical emission, and how this is affected by detuning (Fig. 5.9). The spectral shapes observed are accounted mainly by the Coulomb energy bueshift on top of the vacuum Rabi doublet, with crossings and anticrossings of the lines with detuning, depending on their opposed (photon *and* exciton) or identical (photon *or* exciton) character. We can conclude in this model that the optimum experimental configuration to observe nonlinear effects in the PL spectra is at an intermediate, nonzero detuning, for instance at $\Delta \approx \pm g$. There is an asymmetry with the sign of the detuning due to the interactions that further helps in characterizing the nature of the nonlinearity (e.g., to which extent it comes from the exciton-exciton Coulomb interaction). The presence of satellites with detuning demonstrates emission from quantized manifolds, and as such is a signature of the quantum regime. The spectral drift of these lines with detuning is a useful tool to explicit the exact form of the Hamiltonian that accounts for the exciton nonlinearities.

In Sec. 5.4, we turned to the most important Hamiltonian in quantum optics, the Jaynes-Cummings model. It takes into account the saturation of the QD (considered small) due to fermionic spin effects. As in the previous Sections, manifestations of nonlinearities in the SC physics of a genuine quantum nature are no better sought at high pumpings, looking forward to large number of excitations. The quantum regime involves a few quanta only. It is achieved and better mani-

fests with low pumpings in high quality samples (see JC forks in Fig. 5.18, with well identified transitions in the Jaynes-Cummings ladder). As we did with the AO, we have tracked theoretically by increasing the pump, the crossover from a quantum to a classical regime, where the cavity can be considered a continuous field. The counterpart of a Mollow triplet is observed in this regime for the best samples, more clearly in the direct exciton emission (Fig. 5.21). It features a narrow resonance in the center of the spectrum that turns into a sharp emission line. When the Mollow triplet is fully formed, the cavity mode is in the lasing regime. The Mollow triplet is lost as the system is quenched with no return to quantum behaviors. This provides the general sequence of regimes with increasing electronic pumping for a good (strongly coupled) system: quantum regime, lasing (classical) regime and quenched (also classical but thermal) WC regime.

Again, the cavity pumping appears as an important factor to take into account. First, because of its relevance in an actual experiment, where it can arise due to secondary effects such as other dots (not in SC) emitting in the cavity, temperature, or a variety of other factors. It could conceivably also be input directly by the experimentalist. Cavity pumping has many virtues for the physics of SC in a semiconductor. Because the typical type of excitation is electronic and the typical channel of detection is photonic, SC is hampered as compared to the microwave cavity case where detection and excitation are on the same footing (both directly on the atom). A cavity pumping can help balance this situation and provide an effective photon character to the states realized in the semiconductor, enhancing or even revealing spectral structures. This phenomena manifests also in the LM and has been investigated and explained in its full detailed in Chapter 3. Also in the fermion case, cavity pumping is beneficial for the same reasons, and it can help go beyond the linear regime (with a vacuum Rabi doublet) to the nonlinear quantum regime, typically by making emerge additional quadruplets of the JCM, with a doublet of inner peaks to be sought as the strongest signature (as in Fig. 5.28).

Chapter 6

Two quantum dots in a microcavity

Contents

In this Chapter, we numerically study two two-level systems (two quantum dots or two excitons in a quantum dot) coupled only through and harmonic oscillator (cavity mode), which corresponds to the simplest realization of the Dicke model. We analyze the properties of one-photon and two-photon emission and entanglement in the presence of decoherence (dissipation and incoherent pump). The results presented here have been published in the papers 1, 2, 6, 7 of the list in Page 225, or are in preparation, 11.

6.1 Introduction

Unlike atoms, self assembled QDs are not identical to each other but present a small size inhomogeneity and are randomly distributed in the sample. This results

in a finite dispersion in the coupling to the cavity modes and in the emission frequency. The aim of this Chapter is to analyze the effect of such differences in the SS under incoherent continuous pump. In particular, we show how one can take advantage of them to understand and engineer the emission of the structure, its lasing properties, or the generation of entangled states. For this purpose, we study the case of two QDs (extensible to two excitons in a single QD), each one represented as a two-level system, and coupled to a cavity mode, as in Gywat et al. (2006) or Perea & Tejedor (2005). In this Chapter again, we are neglecting internal degrees of freedom such as carrier spin or photon polarisation, that can be achieved, for instance, by working with charged QDs.

The Chapter is organized as follows. In Section 6.2, we turn into the case where the dots are in a cavity and close to resonance with one of its modes. A new master equation is derived for two different pumping configurations. In Section 6.2.1, the potentiality of the system for entangling two equal QDs is discussed and analyzed through its tangle and entropy. In Section 6.2.2, we propose an application of this entanglement mechanism in a transport experiment with three QDs. In Section 6.2.3, the one-photon lasing properties are analyzed through the photon population and the second-order coherence.

In Section 6.3, we consider again a cavity mode strongly coupled to a single QD, but that is large enough to host two excitons (a biexciton state). This case can be described with a similar Hamiltonian than that of two QDs, but including the biexciton energy, that we present. In Section... we study the two-photon lasing properties of the system and the spectrum of emission.

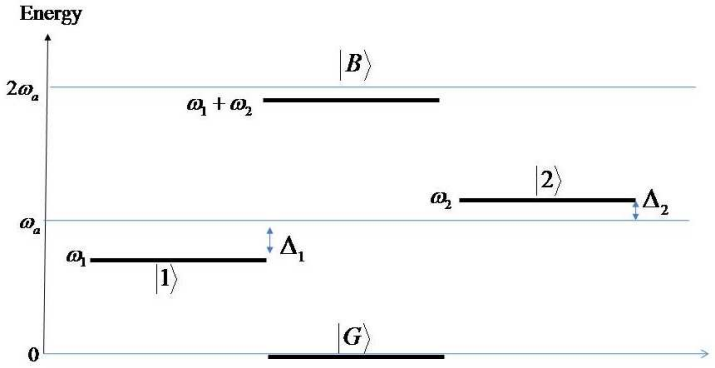

Figure 6.1: QD levels as compared to the cavity mode ω_a for Hamiltonian 6.1.

6.2 Two quantum dots in a microcavity

We consider that the two QD of Chapter 4 are not directly coupled but each of them interacts separately with the same cavity mode, with coupling strengths g_1 and g_2. In general, the modes are not at resonance but detuned a small quantity $\Delta_i = \omega_a - \omega_i$, $i = 1,2$, from the cavity mode ω_a. These four parameters $g_1 \neq g_2$ and $\Delta_1 \neq \Delta_2$ represent the experimental inhomogeneity present in the sample. The total Hamiltonian in this case is the sum of two Jaynes-Cummings Hamiltonians or the Dicke Hamiltonian for only two emitters:

$$H = \omega_a a^\dagger a + \sum_{i=1,2} [\omega_i \sigma_i^\dagger + g_i \left(a\sigma_i^\dagger + a^\dagger \sigma_i\right)]. \tag{6.1}$$

The QD levels as compared with the cavity mode are plotted in Fig. 6.1. Together with this "localized" QD basis of states, that we already introduced in Chapter 4, one can refer to the *Dicke states*, corresponding to the triplet states $\{|\mathrm{T}_{-1}\rangle = |G\rangle, |\mathrm{T}_0\rangle = \frac{1}{\sqrt{2}}(|E1\rangle + |E2\rangle), |\mathrm{T}_1\rangle = |B\rangle\}$, and to the singlet state $\{|S\rangle = \frac{1}{\sqrt{2}}(|E1\rangle - |E2\rangle)\}$. In the Dicke basis, the interaction part of H becomes:

$$H_{\mathrm{int}} = g\big(|\mathrm{T}_0\rangle\langle \mathrm{T}_{-1}| + |\mathrm{T}_1\rangle\langle \mathrm{T}_0|\big)2 + \delta g\big(|\mathrm{S}\rangle\langle \mathrm{T}_{-1}| - |\mathrm{T}_1\rangle\langle \mathrm{S}|\big)2 + \mathrm{h.c.}, \tag{6.2}$$

where $g = (g_1 + g_2)/\sqrt{2}$ and $\delta g = (g_1 - g_2)/\sqrt{2}$. Fig. 6.2 shows the corresponding level scheme, up to two excitations in the Dicke basis, with all the coherent and incoherent couplings, represented by curved and straight arrows respectively. Note that when $g_1 = g_2$, the singlet state decouples from the other ones and becomes a *dark state*. This will play an important role in what follows.

The master equation of the system includes decay for both the cavity mode and the QDs. The QD leaky parameters are set to $\gamma_1 = \gamma_2 = 5 \times 10^{-3} g$, a value

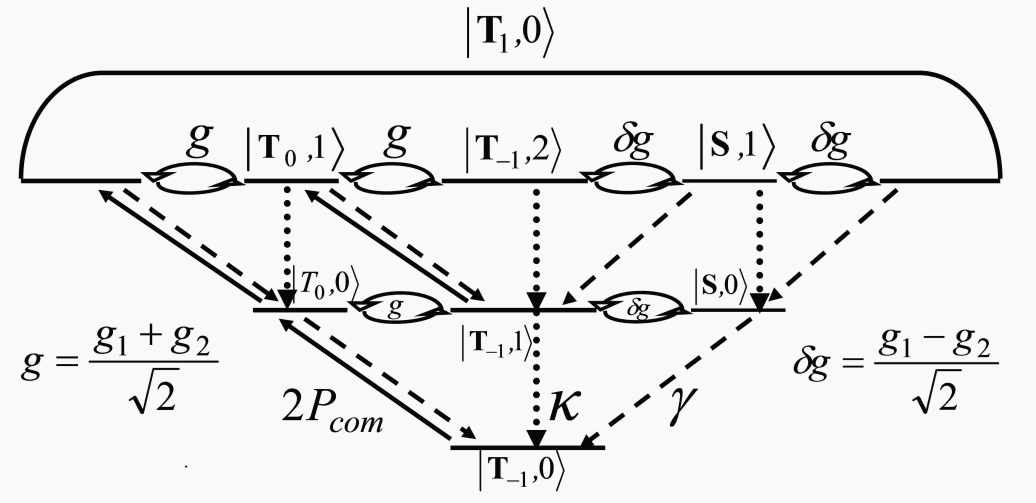

Figure 6.2: Levels of the system up to two excitations in the Dicke basis. Only the case with common pumping bath ($P_{\rm ind} = 0$) is presented here in order to illustrate the discussion to come in Sec 6.2.1. Solid lines represent the common pump which only affects the triplet subspace $|\mathrm{T}_{-1},n\rangle, |\mathrm{T}_0,n\rangle, |\mathrm{T}_1,n\rangle$ with $2P_{\rm com}$, increasing the dot excitations without changing the number of photons n. Dotted lines stand for the cavity photon decay. Dashed lines take account of the leaky modes affecting all QD levels. Finally, curved arrows show coherent couplings (g and δg) between levels.

much smaller than the typical cavity decay rates γ_a considered and experimentally achievable in general. We neglect pure dephasing of the QDs for simplicity. The pumping scheme is the most important ingredient in this work. We consider two physically different situations that we explain in what follows deriving the appropriate Lindblad terms from the microscopic approach.

First, the case where the two QDs are distinguishable in a classical (as opposed to "quantum") way for the pump excitation. Such a situation arises when both QDs are far enough from each other to be resolved and pumped independently or have very different excitation energies. This is the case when the *collection areas* around each dot—the areas of the wetting layer where free carriers are captured by the dot—are completely separated. In the following we denote by A the collection areas of the dots (considered equal for simplicity) and A_c their overlapping area. Each of the QDs couple independently to each element of its own reservoir (electrons e_{R_i}, holes h_{R_i} and phonons f_{R_i}), with coupling strengths δ_{R_i}. This is the situation encountered with atoms and that has been more systematically explored. The Hamiltonian of such a coupling reads:

$$H_{\rm pump} = \sum_{R_1} \left[\delta_{R_1} \sigma_1^\dagger e_{R_1} h_{R_1} f_{R_1}^\dagger + \text{h.c.} \right] + \sum_{R_2} \left[\delta_{R_2} \sigma_2^\dagger e_{R_2} h_{R_2} f_{R_2}^\dagger + \text{h.c.} \right]. \qquad (6.3)$$

Applying the method and approximations described in Chapter 2, Sec. 2.4, one

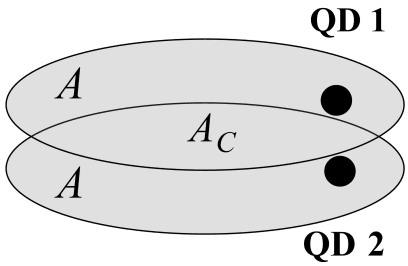

Figure 6.3: Scheme of the two QDs with their associated collection areas A which can be deformed by applying electric field as was explained by Holtz (2007) The overlapping area is called A_c. When it is nonzero and comparable to the coherence length of the excitation, cross-terms of the pump operators appear in the master equation.

arrives to two independent Lindblad terms of the form:

$$\frac{P_{\text{ind}}}{2}\sum_{i=1,2}\left(2\sigma_i^\dagger\rho\sigma_i-\sigma_i\sigma_i^\dagger\rho-\rho\sigma_i\sigma_i^\dagger\right) \tag{6.4}$$

with parameters that we expect to be proportional to the collection areas A through the average injection efficiency per unit area and unit time η. This magnitude is proportional to the number of carriers in the wetting layer that actually create an exciton in the dot. Here it is considered approximately the same for both dots. The rate can then be expressed as: $P_{\text{ind}}=\eta A$.

On the other hand, when, e.g., two identical dots are close to each other, if the coherence length of the excitation is larger than the distance between the two dots, the final state is a quantum superposition of the excited states of the QDs. This second situation of a common excitation bath has been considered by Braun (2002) keeping the coherent nature of the couplings to the bath. An analogous scheme of a common reservoir has been developed by Ficek & Tanas (2002) and by Akram et al. (2000) but for a common squeezed vacuum. It requires the QDs to be indistinguishable for the pumping mechanisms (with equal excitation energies $\omega_1=\omega_2$), the reservoir excitations—electron-hole pairs with high energy and phonons—to have a large enough coherence length to be shared by both dots, and the two collection areas to be fully overlapped ($A=A_c$). With these characteristics, there is only one common reservoir and, given that we consider equal efficiencies for the dots (the excitation always affects both dots in the same way), only symmetrical states can be pumped. The Hamiltonian now reads:

$$H_{\text{pump}}=\sum_R\left[\delta_R\left(\sigma_1^\dagger+\sigma_2^\dagger\right)e_R h_R f_R^\dagger+\text{H.c.}\right] \tag{6.5}$$

Taking into account the fact that the reservoir is common we obtain two different contributions to the master equation:

1. The first is an incoherent contribution to the dynamics given by a Lindblad term:
$$\frac{P_{\text{com}}}{2}\sum_{i,j=1,2}\left(2\sigma_i^\dagger\rho\sigma_j-\sigma_j\sigma_i^\dagger\rho-\rho\sigma_j\sigma_i^\dagger\right) \tag{6.6}$$
with rate $P_{\text{com}}=\eta A_c$.

2. The second is a direct coupling between the QDs which appears as a coherent coupling in the Hamiltonian, $H_{12}=g_{12}\left[\sigma_1^\dagger\sigma_2^- + \text{H.c.}\right]$ with g_{12} of the order of magnitude of the common pumping $g_{12}\approx 2P_{\text{com}}$. In the Dicke basis this coupling detunes the state $|\text{T}_0\rangle$ from $|\text{S}\rangle$.

In a more general and realistic case, the collection areas overlap partially in the region A_c, which contributes to the common pumping with a rate $P_{\text{com}}=\eta A_c$, while the rest of the areas $A-A_c$ contribute to the excitation of each of the QDs separately with rates $P_{\text{ind}}=\eta(A-A_c)$ (see Fig. 6.3). We define the degree of common pumping as the fraction $C=A_c/A$. Varying it between 0 and 1 interpolates between the two extreme cases of independent and common pumping. The Lindblad term of the total pumping is separated in two parts, one specific to each dot which depends on $\sigma_i^\dagger$ and another one which is invariant under QDs exchange (creates symmetrical states) and that can be expressed in terms of the operator $J^\dagger=\sigma_1^\dagger+\sigma_2^\dagger$. The total master equation of the system is now complete:

$$\frac{d\rho}{dt} = i[\rho,H]+i[\rho,H_{12}] \tag{6.7a}$$
$$+\frac{\gamma_a}{2}\mathscr{L}^a\rho+\frac{\gamma}{2}(\mathscr{L}^{\sigma_1}+\mathscr{L}^{\sigma_2})\rho \tag{6.7b}$$
$$+\frac{P_{\text{ind}}}{2}(\mathscr{L}^{\sigma_1^\dagger}+\mathscr{L}^{\sigma_2^\dagger})\rho+\frac{P_{\text{com}}}{2}\mathscr{L}^{J^\dagger}\rho \tag{6.7c}$$

As a summary, the first line describes the coherent dynamics of the two dots and the cavity including the direct QD coupling created by the common excitation bath (H_{12}). The second line describes in the usual way the losses of cavity photons and QD excitations. The third line describes the incoherent pumping written here to set apart clearly the two schemes which play an important role in our analysis: first the pumping of each dot regardless of the other, at rate P_{ind}, and then the joint pumping which distributes the excitation among the two dots as a symmetrical quantum superposition, at rate P_{com}. As proved in the next Section, one would expect this common pumping mechanism to create new correlations and coherent superposition between the dots. Taking advantage of this situation, we will show how to build up entanglement between the QD excited states. On the other hand, we find the incoherent independent pumping—that cannot increase coherence between dots—more suitable for lasing properties.

Here, we are interested in the properties of the steady state of Eq. (6.7) in the limit of strong coupling between cavity and QDs. This state was obtained in two independent and equivalent ways. First we solved the set of linear equations for the density matrix elements resulting from setting the time derivative to zero $d\rho/dt = 0$. Second, we time-integrated the master equation and waited a time long enough to reach the steady state. The solution is unique for a given set of parameters, regardless of the initial state, and both methods agreed exactly except when a singularity arises (as detailed in the next Section) which can only be reached asymptotically with the time-integrated approach.

6.2.1 Entanglement

Two degrees of freedom are entangled when the system density matrix cannot be expressed as a mixture of separable states. Besides their fundamental interest, entangled states are highly sought for applications in quantum information processing. Many such implementations might involve QDs as building blocks, as that of Awschalom et al. (2002) or Ĭmamoḡlu et al. (1999). In the following we consider the possibilities open to the system under consideration.

From the couplings that Eq. (6.7) establishes between the different levels in the local basis, it follows that the reduced density matrix for the QDs in the steady state takes the form:

$$\rho_{\mathrm{QD}}^{\mathrm{SS}} = \begin{pmatrix} \rho_{GG} & 0 & 0 & 0 \\ 0 & \rho_{11} & \rho_{12} & 0 \\ 0 & \rho_{12}^{*} & \rho_{22} & 0 \\ 0 & 0 & 0 & \rho_{BB} \end{pmatrix}. \tag{6.8}$$

Therefore, the only way to entangle the two dots is to populate the Dicke states $|\mathrm{T}_0/\mathrm{S}\rangle$ (which are two of the so-called Bell states). In a bipartite four-level system, the degree of entanglement can be quantified by the *tangle* (τ), which ranges from 0 (separable states) to 1 (maximally entangled states) [see the work by Wootters (1998)]. In order to compute τ, we need to introduce the intermediate quantities T and R, defined as:

$$T = \begin{pmatrix} 0 & 0 & 0 & -1 \\ 0 & 0 & 1 & 0 \\ 0 & 1 & 0 & 0 \\ -1 & 0 & 0 & 0 \end{pmatrix} \quad \text{and} \quad R = \rho_{\mathrm{QD}} T \rho_{\mathrm{QD}}^{*} T\,. \tag{6.9}$$

The tangle is then

$$\tau = [\max\{0, \sqrt{\lambda_1} - \sqrt{\lambda_2} - \sqrt{\lambda_3} - \sqrt{\lambda_4}\}]^2 \tag{6.10}$$

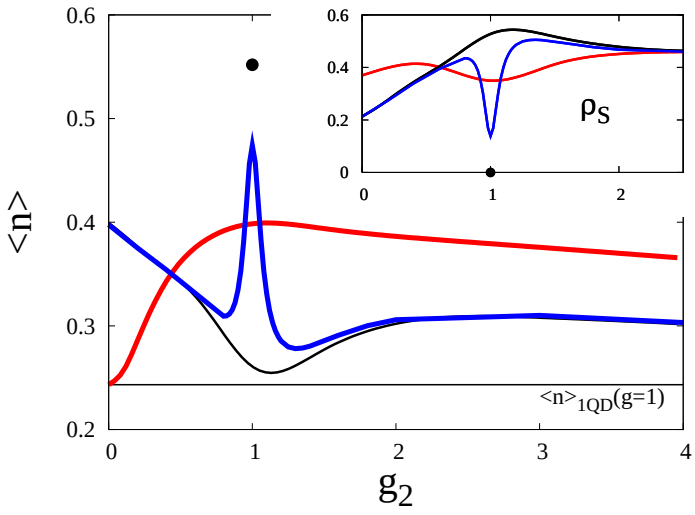

Figure 6.4: Mean number of photons $\langle n \rangle$ stored in the cavity as a function of the coupling of the second dot g_2, for $\gamma_a = g_1$, $\Delta_1 = \Delta_2 = 0$ and $P = 0.33 g_1$ (all in units of g_1). Both the cases of independent pumping only (red line, corresponding to $P_{\rm ind} = P$, $P_{\rm com} = 0$) and common pumping only (black and blue lines, with $P_{\rm ind} = 0$, $P_{\rm com} = P$), are plotted. In the latter case, the black line corresponds to $\gamma = 0$ and the blue one to $\gamma = 5 \times 10^{-3} g_1$. *Inset:* Population of the singlet state. In both plots, the black line has a discontinuity at $g_1 = g_2$. The singular value assumed by $\langle n \rangle$ and the singlet population in this case is marked by the black point.

where $\{\lambda_1, \lambda_2, \lambda_3, \lambda_4\}$ are the eigenvalues of R in decreasing order. One finds that whenever it is not zero, the tangle is given by:

$$\tau = 4(|\rho_{12}| - \sqrt{\rho_{GG}\rho_{BB}})^2 . \tag{6.11}$$

We are interested in conditions that maximize τ: these correspond to large values of the off-diagonal elements $|\rho_{12}|$ and small populations of the states $|G\rangle, |B\rangle$. Here, dissipation and pumping cause $\rho_{\rm QD}(t)$ to evolve into a mixture, with reduced coherences and nonzero occupancy of all levels. This limits the maximum tangle that can be achieved as was described by Munro et al. (2001). In order to isolate the contribution of such effect, we quantify the degree of purity of the QD states, by computing the *linear entropy*:

$$S_L = \frac{4}{3}[1 - {\rm Tr}(\rho_{\rm QD}^2)] = \frac{4}{3}[1 - (\rho_{GG}^2 + \rho_{11}^2 + \rho_{22}^2 + \rho_{BB}^2 + 2|\rho_{12}|^2)] , \tag{6.12}$$

which is 0 for a pure state, and 1 for a maximally disordered state (where the four dot states have the same probability $1/4$).

The entangling of the dots in the singlet state (rather than the triplet) is a natural way to achieve a good degree of tangle and purity at the same time, as in the limiting case where parameters for each dot are identical ($g_1 = g_2$, $\Delta_1 = \Delta_2$) the

singlet becomes a "dark state". In the case where $P_{\rm ind} = 0$, it is also decoherence free [Lidar et al. (1998)], i.e., is not affected by the decoherence introduced by the pump. When the limiting case is only approached ($g_1 \simeq g_2$), $|\mathrm{S}\rangle$ becomes coupled to the triplet-subspace by a small effective coefficient δg (see Fig. 6.2), and the population can be trapped in the singlet state (see below). As we already mentioned, equivalent trapping mechanisms have been reported when interacting with a common squeezed bath by Ficek & Tanas (2002) and Akram et al. (2000) Our proposal for achieving a high value of the tangle is based on a slight imbalance between the coupling strengths of the QDs, resulting in a very high occupation of the singlet state.

In Fig. 6.4 we plot the mean number of photons and the population of the singlet state (inset), for $\Delta_i = 0$. The first dot is in the strong coupling regime with the cavity ($\gamma_a/g_1 < 4$), whereas the second one goes from weak to strong coupling regime as a function of g_2. If the QDs are pumped independently (red line), the photon number increases with g_2, until the maximum is reached for $g_2 = g_1$. The presence of the second dot in strong interaction with the cavity increases nonlinearly the emission (see below).

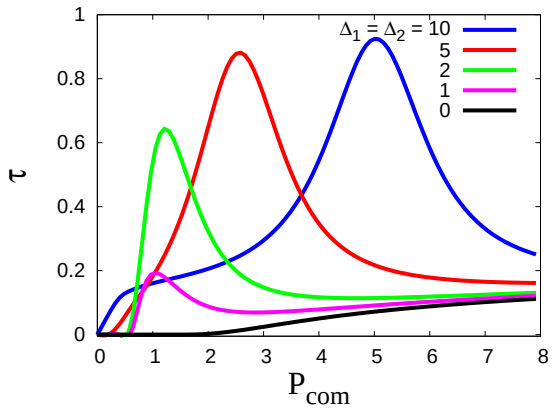

Figure 6.5: Tangle τ for various detunings, as a function of $P_{\rm com}$ (in units of g_1). Parameters: $\gamma_a = g_1$, $\gamma = 5 \times 10^{-3} g_1$, $P_{\rm ind} = 0$, $g_2 = 0.6 g_1$. The maximum tangle achieved grows with the detuning but requires a larger pumping.

On the other hand, when the pump is common, a very different behavior is observed (blue line in Fig. 6.4). First, for $g_2 = 0$, the single-QD limit is not recovered, since the cross pumping term $P_{\rm com}$ creates an effective coupling between the QDs, which induces correlation between their states even when no cavity-induced coupling is present. The other striking difference occurs for $|g_2 - g_1| \approx 0$: the photon number decreases, while the singlet population increases. Here, $\delta g \ll g$, and the singlet is almost decoupled from the dynamics (see Fig. 6.2 and the above discussion). There is a slow flow of population into the singlet state with zero pho-

tons, which also has a very long relaxation time. In the specific case $g_2 = g_1$, there is an abrupt change of the photon number, and the system turns into an effective three-level system, as the singlet is optically dark.

The strong differences between the emission of a system under independent or common pumping evidenced in Fig. 6.4 (especially when one of the dots is not coupled to the cavity or when they are coupled in a similar way) provide a simple experimental hint to discriminate them.

In the case where the only decay channel for the dot is the emission into the cavity mode ($\gamma = 0$), this behavior is singular (black in Fig. 6.4). For finite γ, the singularity is replaced by an abrupt maximum. The occupation of state $|\mathrm{T}_0\rangle$ is enhanced. However, being this state strongly coupled with the other two triplet states, the purity is not high and the tangle remains zero. Therefore, in order to increase τ, we seek for the set of parameters that maximize the singlet occupation knowing that a moderate population of triplet states does not suffice (Fig. 6.4). The best regime corresponds to small $\delta g/g$, and large ratios g/γ_a. Besides, in order to keep at a minimum the excitations of radiant states in such a configuration, the QDs must be detuned from the cavity mode. In turn, because of this detuning which weakens the dynamics, the pumping must be increased. Accordingly, we show the tangle τ for $g_2 = 0.6g_1$, $\gamma_a = g_1$, $\gamma = 5 \times 10^{-3} g_1$, as a function of the pumping P_{com}/g_1 (Fig. 6.5). Larger detunings increase the tangle, though this requires larger values of the pump as well. For very high values of the pump, the emission from the two dots gets quenched and the number of cavity photons vanishes. The population saturates between the states $|\mathrm{S},0\rangle$ and $|\mathrm{T}_1,0\rangle$ (with zero photon) and the tangle gets spoiled. There is therefore a maximum for a given detuning, as shown on Fig. 6.5 from the numerical results.

In the following we consider a detuning $\Delta = 2g_1$ between the dots and the cavity mode, so as to keep realistic values of the pump required to maximize the tangle, namely, $P_{\mathrm{com}} = 1.22g_1$ as read from the magenta line in Fig. 6.5. In Fig. 6.6, we make a systematic analysis of the steady state in terms of (a) its cavity population, (b) population of the singlet state with zero photon $|\mathrm{S},0\rangle$ (almost equal to the total population of the singlet), (c) tangle and (d) entropy, by scanning the space of relevant parameters g_2 and P_{com}, (in units of g_1) and keeping other parameters fixed to the values given above. The maximum of the tangle ($\tau = 0.64$, marked with a cross), is achieved at $g_2 = 0.6g_1$ and $P_{\mathrm{com}} = 1.22g_1$ (see Fig. 6.5). It corresponds to the minimum entropy and an increase of the population of the state $|\mathrm{S},0\rangle$, and therefore to a decrease of $\langle n \rangle$.

Entanglement between the QD excited states is not an easy magnitude to access experimentally (other than by reconstructing the QD density matrix with quantum tomography). The low number of cavity photons associated with the maximum of the tangle, and consequently the low cavity emission, can be used as an experimental indication of a high degree of entanglement.

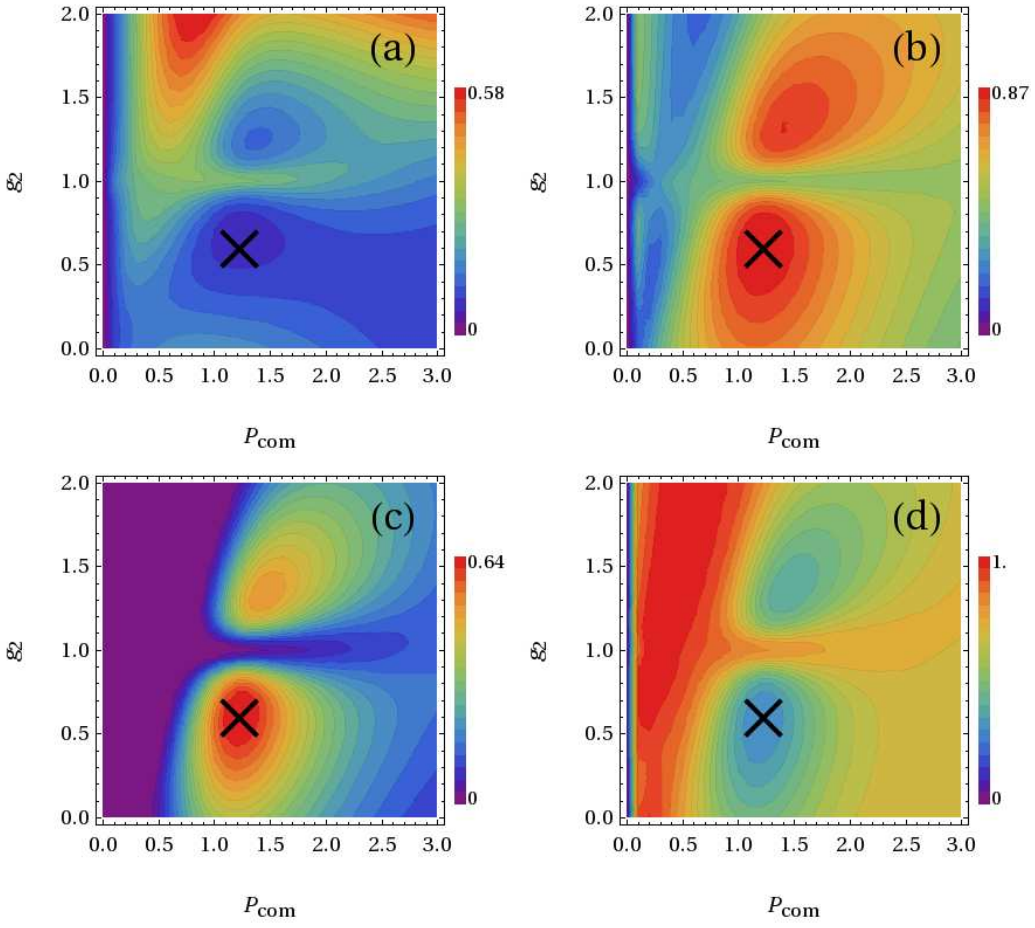

Figure 6.6: Density plots of (a) mean number of photons, (b) population of the state $|S,0\rangle$, (c) tangle and (d) entropy, all as a function of g_2 and $P_{\rm com}$ (in units of g_1). Parameters are $\gamma_a = g_1$, $\gamma = 5\times10^{-3}g_1$, $\Delta_1 = \Delta_2 = 2g_1$, $P_{\rm ind} = 0$. The maximum value for the tangle ($\tau = 0.64$) is achieved at $g_2 = 0.6g_1$ and $P_{\rm com} = 1.22g_1$ (this point is marked with a cross).

Another important feature of these plots (Fig. 6.6) is that they are not symmetric with respect to $g_2 = g_1$ and in this case, it is easier to reach the maximum tangle when the second dot coupling is smaller than the first. The sign of $g_1 - g_2$ which maximizes the tangle for a given $|g_1 - g_2|$ depends on the position of the maxima in the curves of $\langle n\rangle$ and singlet population with respect to g_2 around the singularity $g_1 = g_2$. The best case is the one which maximise the singlet population and minimize the total population.

In Fig. 6.7—the counterpart of Fig. 6.4 in the configuration under consideration, which is suitable for entanglement—these maxima are obtained for $g_2 < g_1$. Note that in Fig. 6.4 the situation is opposite. Note also that it is not needed nei-

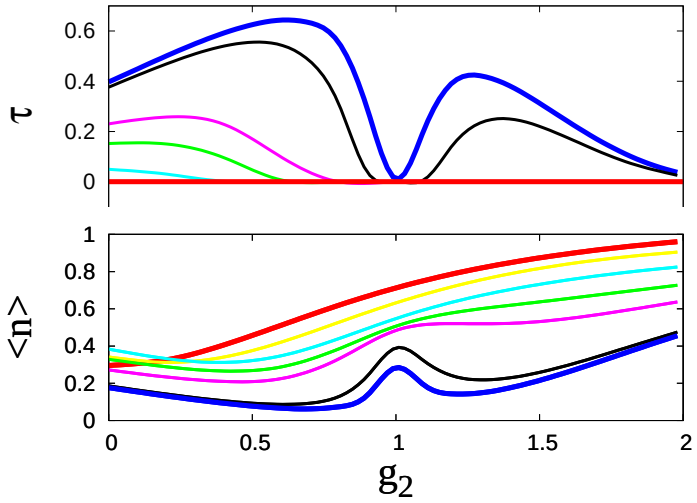

Figure 6.7: Tangle and mean number of photons as a function of g_2 (in units of g_1) for $\gamma_a = g_1$, $\Delta_1 = \Delta_2 = 2g_1$, $\gamma = 5 \times 10^{-3} g_1$, and total pump $1.22g_1$. The cases from independent pump $C = 0$ (red) to common pump $C = 1$ (dark blue) are considered. The intermediate curves correspond to $C = 0.33$ (yellow), 0.66 (light blue), 0.82 (green), 0.91 (magenta) and 0.99 (black).

ther a very strong coupling of the QDs with the cavity. Fig. 6.7 shows as well the transition from the common bath ($C = 1$) to independent ones ($C = 0$), in the case where the total pump is fixed $P_{\text{ind}} + P_{\text{com}} = 1.22g_1$. It gives an idea of the overlap needed to obtain a sizeable tangle. No tangle is obtained for an overlap less than 66%. The important overlap which is required can be obtained experimentally by application of an electric field which can squeeze the areas of two nearby QDs into each other.

6.2.2 Application in a three QD transport experiment

Before moving on to other properties of this system, we will discuss an application for the effect that we have just analyzed. It is also possible to create entanglement between the two dots when instead of being coupled to a cavity mode, they are both coupled to a third QD. In this case, instead of self assembled QD in a microcavity, we rather have in mind electrostatically defined QDs in the vacuum. Experiments on transport through these kind of QDs have recently experienced such a development that it is now possible to reproduce many of the phenomena that the field of quantum optics, involving atoms, has been exploring for many years, as it is explained for instance by Brandes (2005). In particular, state preparation and manipulation of one or more QDs is nowadays feasible by controllable external means such as gate and bias potentials plus either continuous or AC electric and/or magnetic fields. Again, each QD can be considered as a *qubit* with the

lower state $|0\rangle$ corresponding to a neutral QD and the upper state $|1\rangle$ to having one extra electron in the QD. Due to Coulomb blockade, charging the QD with more than one electron requires an energy that can be considered infinite for any practical purpose, reducing the Hilbert space to that spanned by the two mentioned states. Entanglement effects in transport through double QDs have been extensively studied by, for instance, Hayashi et al. (2003), Marquardt & Bruder (2003), Vorrath & Brandes (2003), Brandes (2005), Michaelis et al. (2006), da Silva et al. (2006) or Lambert et al. (2007). In a similar way, ours is a proposal for experimentally preparing and measuring a charge-entangled state of two QDs. Our starting point is the pioneering ideas of Michaelis et al. (2006), where the constraint of having no more than one electron in the whole system allows the population trapping in a dark-entangled state. The same configuration does not give the desired results within a regime more experimentally accessible (more than one electron in total) as we will show below. We obtain interesting results (in experimentally accessible conditions) when we add cross-terms in the incoherent pumping of the two QDs as we have seen in the previous Section. In the framework of transport, the role of the cavity is played by a third QD and both incoherent pumping of the QDs and cavity photon emission find their counterpart for the transport realization in the tunneling processes produced by the application of a bias. We will show here that, apart from all the analogies, there is an important advantage in doing transport: entanglement could be easily detected in the same setup that prepares the equivalent to the quasi-dark (entangled) state.

The three QD system is presented in Fig. 6.8(a). A two-dimensional electron gas is depleted in some regions by means of a series of gate potentials. A bias applied from the left to the right lead produces two tunneling processes: incoherent population of QDs *A* and *B* as well as electron current from QD *C* to the right lead. QDs *A* and *B* are coherently coupled to QD *C* (acting as the cavity in the previous Section). The gate-potentials V_3, V_4 and V_7 are designed to control the levels of the three *qubits*, V_2 and V_8 control the in- ($\Gamma_{\rm p}$) and out- (Γ_κ) tunneling rates while the gates V_5 and V_6 control the coherent couplings g_{AC} and g_{BC} respectively. The crucial novelty with respect to the configuration of Michaelis et al. (2006) is gate V_1. Switching on and off the V_1 gate, one can experimentally tune from a quantum mechanically distinguishable (V_1 on) to an indistinguishable (V_1 off) pumping of the two QDs *A* and *B*. Let us first see how this appears in the quantum mechanical description of the transport through the whole system and later what are the physical effects that can be tuned in this setup.

As opposed to the case with photons, where the truncation can be arbitrarily high, Coulomb blockade on each QD limits the Hilbert space to that spanned by a basis of 8 states $|n_A, n_B, n_C\rangle$ [depicted in Fig. 6.8(b)] with $n_{A,B,C} = 0, 1$. Cross term effects only occur for electrons with the same spin. We therefore consider the system under the action of an in-plane magnetic field and neglect the spin.

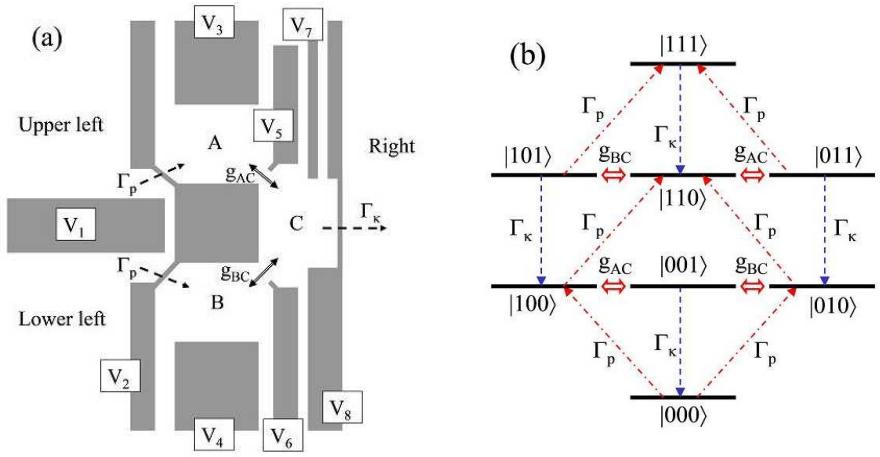

Figure 6.8: (a) Scheme of the proposed setup, with a two-dimensional electron gas depleted by 8 gate potentials V_i. V_3, V_4 and V_7 control the levels of the QDs. V_2 and V_8 control Γ_p and Γ_κ. V_5 and V_6 control g_{AC} and g_{BC}. Switching V_1 from "on" to "off" tunes the pumping of A and B from distinguishable to indistinguishable quantum mechanically. The current is induced by a bias from left to right. (b) Scheme of the dynamics in the Hilbert space spanned by $|n_A, n_B, n_C\rangle$. We simplify the plot by setting detunings to zero.

Both intra-dot Coulomb blockade and spin polarisation stand within an experimentally accessible regime. To reduce the Hilbert space to the lowest four states in Fig. 6.8(b), as is done by Michaelis et al. (2006), would require an extremely high inter-dot Coulomb repulsion, something unreasonable in a system such as the one shown in Fig. 6.8(a). The coherent part of the dynamics is controlled by the Hamiltonian:

$$H = \sum_{i=A,B} \Delta_i \sigma_i^\dagger \sigma_i + g_{iC}(\sigma_i^\dagger \sigma_C + \sigma_C^\dagger \sigma_i) \tag{6.13}$$

where σ_i, $\sigma_i^\dagger$ are this time, annihilation and creation operators of an electron in QD i. We have taken the level of the QD C as the origin of energies so that only the detunings Δ_A, Δ_B and the couplings g_{AC}, g_{BC} are relevant. The master equation is, in analogy with Eq. (6.7):

$$\frac{d\rho}{dt} = i[\rho, H] + ig_{AB}[\rho(\sigma_A^\dagger \sigma_B + \sigma_B^\dagger \sigma_A)] + \frac{\Gamma_\kappa}{2}\mathscr{L}^{\sigma_C} + \frac{\Gamma_\mathrm{p}}{2}\sum_{i=A,B}\mathscr{L}^{\sigma_i^\dagger} \tag{6.14a}$$

$$+ \frac{\gamma_d}{2}\sum_{i=1}^{8}\left(2\mathscr{P}_i\rho\mathscr{P}_i - \mathscr{P}_i\rho - \rho\mathscr{P}_i\right) \tag{6.14b}$$

$$+ \frac{\Gamma_{AB}}{2}\sum_{i\neq j}\left(2\sigma_i^\dagger\rho\sigma_j - \sigma_j\sigma_i^\dagger\rho - \rho\sigma_j\sigma_i^\dagger\right) \tag{6.14c}$$

where $\mathscr{P}_i = |n_A, n_B, n_C\rangle\langle n_A, n_B, n_C|$ ($i = 1, \ldots, 8$) is the general projector for the eight possible states in the system. In this configuration, instead of pump and decay, the incoherent part of the master equation features the in- ($\Gamma_{\rm p}$) and out- (Γ_κ) tunneling processes [Eq. (6.14a)] and pure dephasing at rate $\gamma_{\rm d}$ [Eq. (6.14b)]. There are also the two pump cross terms [Eq. (6.14c)] and their coherent direct coupling that accompanies them [Eq. (6.14a)]. They appear when the QDs A and B are pumped from the same reservoir (left lead) in a complete indistinguishable (quantum) way. In such a case, the corresponding rate of pumping is given by $\Gamma_{AB} = \Gamma_{\rm p}$. This corresponds to switching off the gate V_1. By smoothly switching it on, the upper and lower parts of the left lead separate from each other. Γ_{AB} is reduced down to the situation in which the two left reservoirs become completely independent and $\Gamma_{AB} = 0$. Cross terms in the pumping are therefore experimentally controllable. The new Förster-like direct coupling in Eq. (6.14a) contributes to enhancing the entanglement between QDs A and B. The coupling parameter is $g_{AB} = 2\Gamma_{AB}$ as derived by Ficek & Tanas (2002) in analogy with the Lamb-shift of a single two-level system. Once again, one can experimentally control this mechanism from switching on V_1, which gives $g_{AB} = 0$, to switching it off, which gives $g_{AB} = 2\Gamma_{\rm p}$.

The current flowing through the system is an easily measurable experimental quantity that plays the role of the cavity emission intensity from the previous configuration. The current is simply given by $I = \Gamma_\kappa \langle \sigma_C^\dagger \sigma_C \rangle$. In the stationary limit, the master equation (6.14) simplifies to a set of 64 linear equations, plus the normalization condition $\mathrm{Tr}(\rho) = 1$. In this finite Hilbert space, the tangle is $\tau = [\max\{0, 2(|\widetilde{\rho}_{10,01}| - \sqrt{\widetilde{\rho}_{00,00}\widetilde{\rho}_{11,11}})\}]^2$, in terms of the matrix elements of $\widetilde{\rho} = \mathrm{Tr}_C(\rho)$.

Let us discuss the results to be expected from the setup we propose. We consider that the QDs A and B are equal, $\Delta_A = \Delta_B = \Delta$, what can be achieved by adjusting independently the gates V_3 and V_4. The entanglement can be manipulated by having different couplings g_{AC} and g_{BC} as controlled by the gates V_5 and V_6. Hereafter, all the couplings and rates will be given in units of $g_{AC} = 1$.

First of all, we analyze the adequacy of truncating the Hilbert space basis to only four states as it was done by Michaelis et al. (2006). For this purpose we consider the simple case of neglecting cross-terms and estimate the total mean number of excitations in the system. For a system that is pumped with a total rate P_{tot}, decays with γ_{tot} and that has a saturation limit S, one finds [generalizing the single two-level system result in Eq. (2.53)] that the mean total number of excitations in the very strong coupling regime is given by $\langle n \rangle = SP_{\rm tot}/(P_{\rm tot} + \gamma_{\rm tot})$. In our case where $P_{tot} = 2\Gamma_p$, $\gamma_{tot} = \Gamma_\kappa$ and $S = 3$ (maximum of three electrons in the system), and in the symmetric case, $\Gamma_P = \Gamma_\kappa = \Gamma$, that we consider in what follows, the total average excitation is further simplified into $\langle n \rangle = 3 \times 2\Gamma/(2\Gamma + \Gamma) = 2$. This result, that agrees with numerical calculations, is the first indication

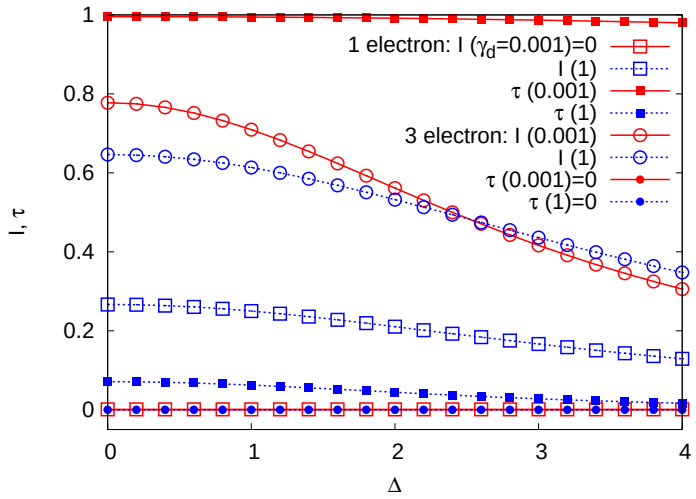

Figure 6.9: Current intensity I (empty symbols) and tangle τ (full symbols) as a function of detuning Δ when V_1 is so large that pumpings to A and B are distinguishable from each other, i.e. $\gamma_{AB} = 0$. Two different values for the dephasing are considered: $\gamma_d = 0.001$ (in solid-red) and $\gamma_d = 1$ (in dashed-blue). $\Gamma_p = \Gamma_\kappa = 2$ and $g_{BC} = 1$. Energies and rates in units of $g_{AC} = 1$. Strong Coulomb blockade is considered either inter-QD (maximum charge of 1 electron in the whole system, plotted with squares) or just intra-QD (maximum charge of 1+1+1=3 electrons, plotted with circles). Red and blue full circles coincide to zero (as the tangle in the three-electron case for all dephasing rates is zero) and therefore they appear superimposed in the plot. Also the current in the case of 1 electron and negligible dephasing ($\gamma_d = 0.001$) is zero.

of the inadequacy of truncating the Hilbert space to only one electron. Moreover, we find that the relevant magnitudes under study (I and τ) depend strongly on the truncation. Fig. 6.9 shows I and τ as a function of the detuning for two different dephasing rates, $\gamma_d = 1$ and $\gamma_d = 0.001$, both with truncation (up to one electron in the system) and without truncation (up to three electrons in the system). When truncation is not imposed, τ is always zero and entanglement is not achieved.

The approximation of keeping just one electron in the whole system that was made by Michaelis et al. (2006), forces the steady state of QDs A and B to be a singlet $|\mathrm{S}\,0\rangle = (|100\rangle - |010\rangle)/\sqrt{2}$ (with QD C in the vacuum). This implies a tangle of one and no current passing through the system if the dephasing is negligible. This is a new example of a trapping mechanism. The pumping is populating both the singlet and its symmetric counterpart, the triplet state $|\mathrm{T}\,0\rangle = (|100\rangle + |010\rangle)/\sqrt{2}$. However, when the couplings are equal $g_{AC} = g_{BC}$, the singlet is dark, does not couple to other states and finally stores all the excitation of the system in the steady state. Therefore, when more than one electron is allowed, this trapping mechanism breaks as also the states $|11n_C\rangle$ become pumped. In the absence of cross terms, the tangle drops to zero and there is current

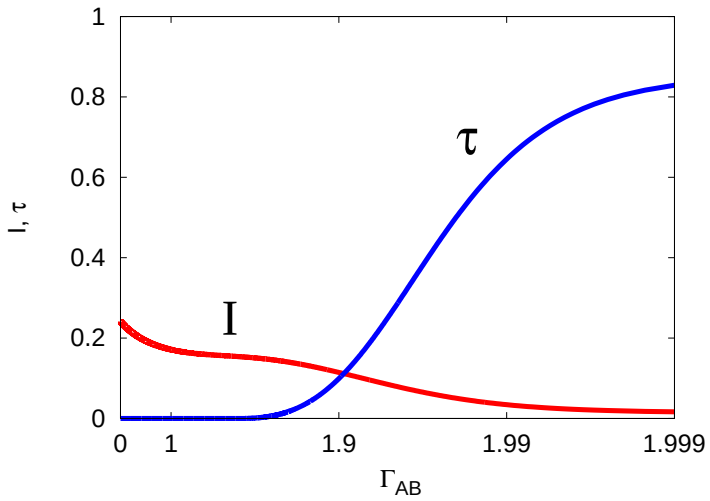

Figure 6.10: Current intensity I (in red) and tangle τ (in blue) as a function of Γ_{AB} (in logarithmic scale). This is experimentally controlled by varying V_1 from a large value (giving $\Gamma_{AB} = 0$) to zero (giving $\Gamma_{AB} = \Gamma_p$). $\Delta = 4$, $\Gamma_p = \Gamma_\kappa = 2$, $\gamma_d = 0.001$ and $g_{BC} = 0.7$ with energies and rates in units of $g_{AC} = 1$. Fast rising of τ, detectable by fast quenching of I, is due to the switching on of a quantum mechanically indistinguishable pumping. Only intra-QD Coulomb blockade is considered (maximum charge of 3 electrons).

through the system. A negative result to be drawn from Fig. 6.9 is that without cross terms, in the actual case of more than one electron, there is no entanglement to be expected experimentally.

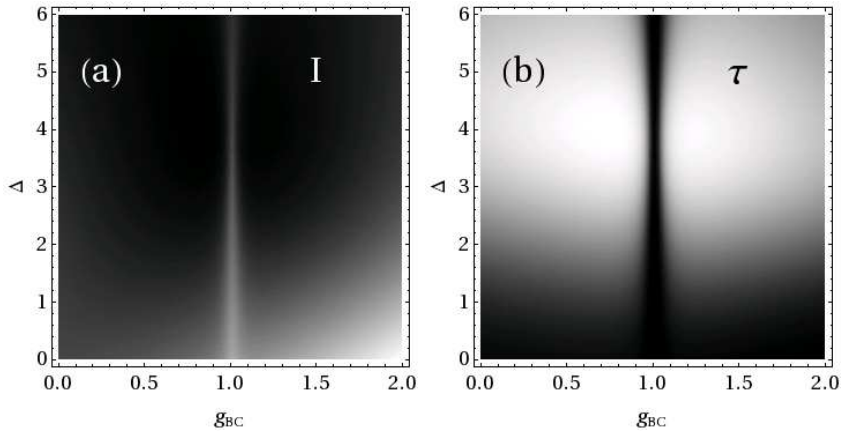

Figure 6.11: Current intensity I (a) and tangle τ (b) in density plots as a function of g_{BC} and Δ in the quantum mechanically indistinguishable case $\Gamma_{AB} = \Gamma_p$. $\Gamma_p = \Gamma_\kappa = 2$ and $\gamma_d = 0.001$. Energies and rates are in units of $g_{AC} = 1$. Bright areas correspond to maximum values of current and tangle and the dark ones to zero.

Our main finding here is the entanglement induced by cross terms in the dynamics, enhanced by the coherent coupling between A and B. Hereafter we consider the general case, i.e., without truncation to only one electron. Fig. 6.10 shows I and τ as a function of Γ_{AB} for the larger detuning $\Delta = 4$ and the lowest dephasing $\gamma_{\rm d} = 0.001$ considered in Fig. 6.9. An important fact is that now the couplings g_{AC}, g_{BC} must be slightly different (for instance $g_{BC} = 0.7$) so that the singlet is not completely dark, but a quasi-dark state weakly coupled to the rest of the system (with a coupling given by $|g_{AC} - g_{BC}|/\sqrt{2}$). When the gate V_1 is completely switched on, $\Gamma_{AB} = 0$ and, as it happened in Fig. 6.9, there is current larger than $I = 0.2$, implying no entanglement. Increasing Γ_{AB} by quenching the gate V_1 does not affect the behavior of the system until the regime where cross terms apply fully is reached. Here, when Γ_{AB} tends to $\Gamma_{\rm p}$, adding cross terms in Eq. 6.14 translates in pumping only the symmetric states (under QDs A, B exchange). Therefore the incoherent pump with cross terms neither excites the singlet nor induces decoherence of it. This fact, together with the weak link between the singlet state and the other levels, results in a slow coherent transfer of population to the singlet $|{\rm S}\ 0\rangle$, which can be described as a quasi-dark state free of decoherence, as we already showed in the previous Section. This trapping mechanism is enhanced strongly by the direct coupling g_{AB}, also induced by the cross pump. In this case, the tangle becomes close to its highest possible value of 1. The detectable manifestation is a sharp reduction of the current through the system, as QD C is practically empty. This means a clear way of entangled state preparation between QDs A and B as well as a straightforward measurement associated to its occurrence (drop of the current).

Finally, we want to show how entanglement induced by cross terms depends on the coherent part of the dynamics controlled by H. For this purpose, Fig. 6.11 presents current I (a) and tangle τ (b) as a function of the detuning Δ and the coherent coupling g_{BC} (always in units of g_{AC}). The tangle plot shows that detuning is needed to generate a high degree of entanglement. As we explained, also slightly different couplings g_{AC} and g_{BC} are necessary to create the quasi-dark state. In Fig. 6.10 we were giving results for the situation with highest tangle ($\tau = 0.85$), that is $g_{BC} = 0.7$ and $\Delta = 4$, corresponding also to lowest current ($I = 0.01$). On the other hand, for the symmetric case $g_{AC} = g_{BC}$, the singlet is completely dark and therefore there is no entanglement, as we also showed in Fig. 6.9. In this case the current is nonzero. The correlation between high tangle and negligible current and vice versa is clear from Fig. 6.11.

6.2.3 One-photon lasing

In this Section we analyze lasing properties of the system. A practical motivation is the significant improvement, as far as low threshold behavior is concerned,

recently obtained by Strauf et al. (2006) in a system having just a few (from 2 to 4) QDs embedded in a single-mode microcavity with respect to previous attempts using quantum wells or high density QDs [Slusher et al. (1993), Rohener et al. (1997), Painter et al. (1999), Ryu et al. (2000), Zhang & Hu (2003), Park et al. (2004)...]. An important finding in this Section is that the presence of a second dot in strong coupling with the cavity, even far from resonance with the cavity, changes substantially the emission of a single one.

As opposed to the previous Section, now we focus on the quantum state of the cavity photons, rather than on that of the QDs. Nevertheless, the light state depends on the coherences established between the levels of the system and therefore depends on the QD parameters. Unlike atoms, QDs can be differently detuned with respect to the cavity mode. In what follows, we therefore study the dependence on the detuning configuration of the mean photon number and of the second-order coherence function in the case of zero delay $g^{(2)}$. Only in the case where the two dots are equally detuned, one can compare the two limiting pumping schemes described previously; as mentioned above, such symmetry is a necessary condition for the common pumping bath.

Given the structure of Eq. (6.7), all off-diagonal elements of the density matrix between levels with equal QD states but different number of photons have been washed away in the steady state. As in the case of one QD in the cavity under incoherent pump (Chapter 5), the photon reduced density matrix $\rho_{\rm ph} = {\rm Tr}_{\rm QD}\rho$ is diagonal in the number of photons: it is thus impossible for the system to achieve a coherent state, with density matrix ρ_α of the form (2.23), at the steady state. However, the system can reach a mixture of number states, $\rho_{|\alpha|}$ from Eq. (2.25), with the same Poissonian distribution, as it happens for a laser much above threshold. In both cases, $\langle n\rangle = |\alpha|^2$ and $g^{(2)} = 1$.

Fixing the leaky modes to $\gamma = 5\times 10^{-3} g_1$ and the coupling constants $g_2 = g_1$, we first compare the number of photons $\langle n\rangle$ in the cases where one or two QDs are in resonance with the cavity (Fig. 6.12). Fig. 6.12 shows how the growth of the occupation number with pumping is limited by the self-quenching effect. This results in a maximum cavity population, corresponding to an optimum value of the pumping intensity. Further increase of the pumping results in a decrease of the mean number of photons and saturation of the dots. We already discussed in the previous Chapter how this effect is due to the incoherent nature of the pump, which destroys the coherences established between QDs and cavity driving the system into a thermal state ($g^{(2)} = 2$). However, we are interested in the behavior at much lower pumps, where the number of photons does not yet saturate as is the case of Strauf et al. (2006).

In the pumping range plotted in Fig. 6.12, the self-quenching region is reached only for the case of a common pumping bath (green line). Therefore, this case is the least suitable for lasing properties. There are several reasons for the enhance-

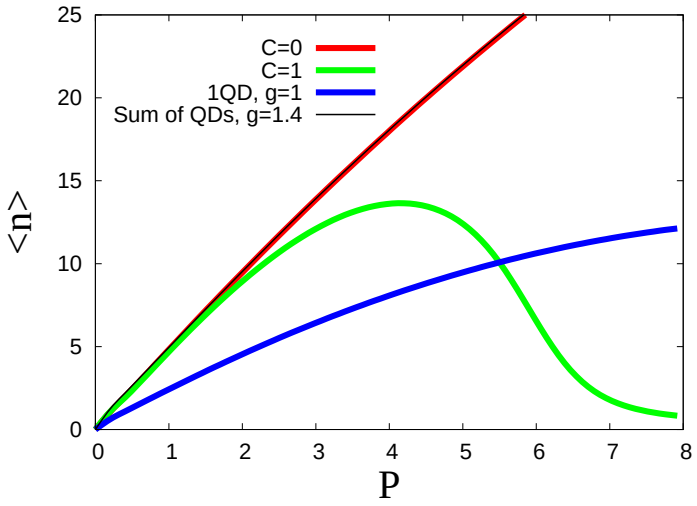

Figure 6.12: Mean number of photons stored in the cavity as a function of pumping P (in units of g_1), for $\gamma_a = 0.2g_1$, $\gamma = 5\times10^{-3}g_1$, $g_1 = g_2$. Both cases, with independent ($P_{\text{ind}} = P$ and $P_{\text{com}} = 0$, red) and common pumping ($P_{\text{ind}} = 0$ and $P_{\text{com}} = P$, green), are presented for the resonant case ($\Delta_1 = \Delta_2 = 0$). These are compared with the emission of a single QD in resonance with coupling $g = g_1$ (blue line), and the sum of emissions of two independent dots in resonance with renormalized coupling constants $g = \sqrt{2}g_1$ (black line).

ment of the self-quenching effect in this case. The first reason is that, neglecting the leaky modes, the QD system is reduced from four to three levels, diminishing the range of pump available before reaching the saturation of the ensemble. Taking into account leaky modes, the second reason is that, although $g_1 = g_2$, and thus the singlet is not coherently coupled to the triplet, the decay of state $|\mathrm{T}_1,0\rangle$ into $|\mathrm{S},0\rangle$ via those leaky modes populates the singlet, thus hindering the storage of photons. A third drawback is the presence of the coherent coupling between states $|E1\rangle$ and $|E2\rangle$, which prevents the distribution of photons from being Poissonian. The resulting distribution is a sum of the contribution of the singlet subspace (with high probabilities around zero photons) and the triplet (Poissonian like distributions as found in the other cases plotted here).

On the other hand, in the case of independent pumpings, the emission of two QDs approximately corresponds to the sum of the individual emissions with coupling constants renormalized by a factor $\sqrt{2}$. This approximation improves when both dots are close to resonance, as shown by the red curve in Fig. 6.12. The second-order coherence function is also similar at low pumping.

As the common-bath of excitations is detrimental to lasing, we now consider the case of independently and equally pumped dots only ($P_{\text{com}} = 0$, $P_{\text{ind}} = P$), where QDs are coupled uniquely through the cavity mode. Results are given in Fig. 6.13, which shows the behavior of $\langle n\rangle$ and $g^{(2)}$ as a function of the pump,

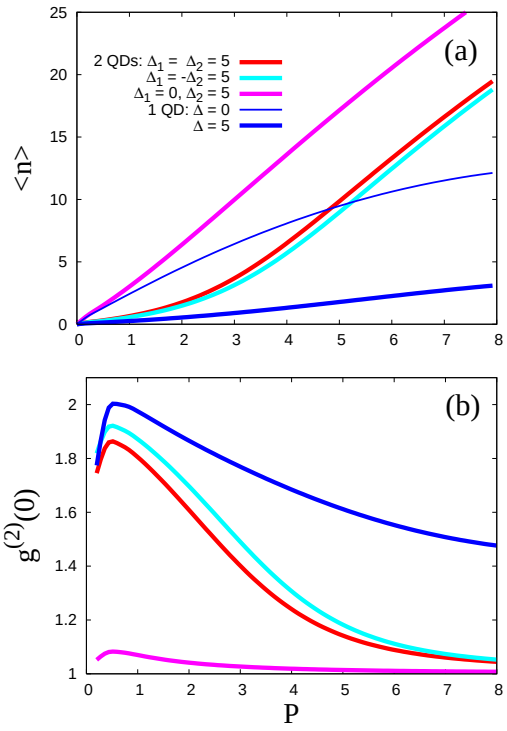

Figure 6.13: (a) Mean number of photons $\langle n \rangle$ stored in the cavity and (b) second-order coherence function $g^{(2)}$ of the cavity field, as a function of $P_{\rm ind} = P$ (in units of g_1), for $P_{\rm com} = 0$, $\gamma_a = 0.2g_1$, $\gamma = 5 \times 10^{-3} g_1$, $g_2 = g_1$. Several detuning cases are presented, with equal ($\Delta_1 = \Delta_2 = 5g_1$), opposite ($\Delta_1 = -\Delta_2 = 5g_1$) and mixed ($\Delta_1 = 0, \Delta_2 = 5g_1$) configurations. There is a qualitative change with two dots as, even when none is in resonance with the cavity mode, the threshold for lasing (with linear increase of $\langle n \rangle$ with P) is low also in the case where the single dot alone would not lase.

for different detuning configurations: equal ($\Delta_1 = \Delta_2$), opposite ($\Delta_1 = -\Delta_2$), and mixed ($\Delta_1 = 0 \neq \Delta_2$) detunings.

In the ideal case, if the QDs are in resonance (Fig. 6.12), the production of photons is very efficient, and $g^{(2)}$ is always one until the self-quenching begins. With detuning, a threshold for linear production of photons (as a function of pumping) appears, as can be seen in the figure. It occurs approximately when the pumping compensates the losses: the number of photons becomes larger than one and the stimulated exceeds the spontaneous emission. This transition into lasing is accompanied by the decrease of the second-order coherence function to a value of one [Fig. 6.13(b)], and a Poissonian distribution of the photon number. As we have seen in the previous Chapter and we can see now in this figure, lasing is also present in the case with one dot, but the threshold of the transition is considerably lowered by the presence of a second strongly coupled dot.

The optimal configurations, i.e., the ones with lowest threshold, are those where at least one of the dots is in resonance. In these case, the presence of the second dot makes a great difference even if its detuning is large. So, neglecting the role of strongly coupled QDs when they are out of resonance is not a good approximation. We can see this by comparing $\langle n \rangle$ of one QD in resonance [thin blue line in Fig. 6.13(a)] with two dots, one in resonance and the second highly detuned ($\Delta_1 = 0$ and $\Delta_2 = 5$ [magenta line in Fig.6.13(a)]. Whether the detunings are identical ($\Delta_1 = \Delta_2$) or opposite ($\Delta_1 = -\Delta_2$), makes no qualitative difference, although the two cases are not strictly equal.

In these results we find a possible explanation for the recent experimental findings of Strauf et al. (2006) on lasing with unexpected low laser thresholds and high photon production efficiency from a cavity containing a few dots out of resonance. The experimental parameters in that case are comparable to ours (with a pump threshold of $P = 0.08$meV), as well as the detunings of the dots, $\Delta_1 \approx -\Delta_2 \approx 5$meV. In our scheme, several dots result in qualitative changes of the emission, enhancing it significantly even when dots are off-resonance. In this sense, our model predicts still better cavity emission with extremely low threshold if one dot could be matched in resonance with the cavity.

6.2.4 Two-photon lasing

The last effect we consider with this configuration is the two-photon lasing. Two-photon (2P) related effects have been extensively studied, and observed in many configurations, during the past few decades. We first list here the most relevant works for our discussion.

Two-photon masers have been theoretically described by Davidovich et al. (1987), and Ashraf et al. (1990) and engineered by Brune et al. (1987). Atoms (effective three level systems) were injected in a cavity in the upper level of a transition which was 2P-resonant with the cavity mode. The state of the atoms was time-resolved and it was found that above threshold the lower state of the 2P transition was populated, evidencing the 2P de-excitation. This effect is present only for a small range of cavity detunings around the 2P resonance (2PR). The same principle applies for the case of a single few-level atom when the quality factor of the cavity, Q, is sufficiently increased.

Lewenstein et al. (1990) studied theoretically two-photon gain and lasing. This was achieved experimentally by Gauthier et al. (1992) in an ensemble of many atoms (two-level systems) strongly driven by a continuous laser. The system can undergo a 2P transition between dressed states (arising from the laser-atoms coupling) if this transition is enhanced by also coupling the atoms to a cavity mode. The 1 and 2 photon lasing regimes are switched on and off by tuning the cavity energy, taking into account the Stark shift and triggering the 2P lasing with a cw

probe. The two regimes are distinguished mainly thanks to the cavity energy at which the output intensity is enhanced. The main experimental point to claim a 2P based laser is the appearance of an extra peak in the emission at the 2PR. This peak grows on top of the one photon (1P) emission, that otherwise does not lase at this energy. In this configuration there is an intrinsic superposition of both 1 and 2P processes that, in the best of cases, can be optimized so that the 2P gain is dominant. Recently, Kubanek et al. (2008) realized experimentally a two-photon gateway with a single atom, in a similar scheme. In their experiment, dressed states appear due to the strong coupling between atom and cavity. A weak cw laser field is shined on the system providing photons that are absorbed and emitted in pairs when there is a 2PR with manifold 2 [see Fig. 5.12 (c)]. The quantity used here to evidence that such process dominates the off-resonant 1P counterpart, is the so-called *differential correlation function* at zero delay, $C^{(2)}$, which is a variation of $g^{(2)}$:

$$C^{(2)} = \langle a^{\dagger 2} a^2 \rangle - \langle n_a \rangle^2 = \langle n_a \rangle^2 (g^{(2)} - 1)\,. \tag{6.15}$$

As explained by Kubanek et al. (2008), $C^{(2)}$ reflects better the 2P versus 1P probability competition than $g^{(2)}$ and we will prefer it in this context. Another interesting quantity found in the literature (see, for instance, Koganov & Shuker (2000)), is the *Fano factor*,

$$F = \frac{\Delta n_a^2}{\langle n_a \rangle} = \langle n_a \rangle (g^{(2)} - 1) + 1 = \frac{C^{(2)}}{\langle n_a \rangle} + 1\,. \tag{6.16}$$

The two-photon dynamics has also been explored theoretically for two atoms (two two-level systems) interacting with a driving laser by Varada & Agarwal (1992) or with a cavity mode (as here) by Pathak & Agarwal (70). In both cases, the light mode was considered to be far from resonance with any of the single atom energies but close to resonance with their sum. In order to avoid the destructive interference between the two possible 2P de-excitation paths that can occur from state $|B\rangle$ (through $|E1\rangle$ or $|E2\rangle$), different ideas can be implemented. Varada & Agarwal (1992) added dipole-dipole direct interactions between the dots and a 2PR was found even for two identical atoms. The 2P absorption and spontaneous emission were characterized by their intensity at the 2PR, and also by the probability that both atoms are excited (related to the transition probability for 2P absorption). The problem of the competition with the 1P processes was not addressed in this work where it was taken for granted that the system is completely dominated by 2P processes. Pathak & Agarwal (70) removed the two-path interference by considering either two different atomic levels (different detunings $|\Delta_1| \neq |\Delta_2|$ and couplings $g_1 \neq g_2$) or two different cavity modes. The authors

concentrated on the Hamiltonian dynamics looking into 2P versus 1P Rabi oscillations of the wavefunction. Lambropoulos (1999) also considered two cavity modes, each one associated with the 1P or 2P lasing, coupled and resonant with two different atomic transitions separately. Here, an incoherent continuous pump for the atoms was considered that inverted the population of the 2P transition. A comparison of the intensity emitted in each mode allowed to quantify the 2P efficiency.

In most of the cases just described, the Stark shift induced by the off-resonant 1P exchange with the atomic levels is taken into account in order to achieve a real 2PR in the system. The 2P lasing is simply characterized by the enhancement in the intensity of the emission at the 2PR against that achieved at 1PR. This could be observed in continuous operation or thanks to time-resolved measurements of the dynamics after a probe. In the case of coherent excitation of the atoms or spontaneous emission from the excited state, the population of the atomic levels can also be a meaningful magnitude.

The configuration we are investigating is that of Pathak & Agarwal (70), in the SS under incoherent continuous pump. In this system, a 2PR can be induced when $\omega_1+\omega_2\approx 2\omega_a$. At the same time, in order to suppress one photon processes, the single exciton energies should be greatly detuned from the cavity mode. The unperturbed states $|G,n\rangle$ and $|B,n-2\rangle$ are resonant if $\Delta_1=-\Delta_2$. However in this case the two photon transition probability is zero due to destructive interference between the processes $|B,n-1\rangle\rightarrow|E1,n-1\rangle\rightarrow|G,n\rangle$ and $|B,n-1\rangle\rightarrow|E2,n-1\rangle\rightarrow|G,n\rangle$. That is, the transition probability to first order in the small parameter $g_j/|\Delta_2-\Delta_1|$,

$$T^{(1)}_{B\rightarrow G}\propto\langle G,n|H^i\frac{1}{\lambda_{B,n-2}-H^0_{12}}H^i|B,n-2\rangle=-\sqrt{n(n-1)}g_1g_2\Big(\frac{1}{\Delta_1}+\frac{1}{\Delta_2}\Big), \tag{6.17}$$

is zero in this case, even when the couplings are different. By keeping $|\Delta_1|\neq|\Delta_2|$, second order resonant 2P Rabi oscillations can become larger than the first order off-resonance 1P oscillations as detunings are increased with opposite signs. An example of such a situation is plotted in Fig. 6.14.

We evaluate the corrections at second order in perturbation theory to the two bare energies as done in the book by Cohen-Tannoudji et al. (2001), which are the so-called Stark shifts:

$$\lambda^{(2)}_{G,n}=n\big(\frac{g_1^2}{\Delta_1}+\frac{g_2^2}{\Delta_2}\big),\quad \lambda^{(2)}_{B,n-2}=-(n-1)\big(\frac{g_1^2}{\Delta_1}+\frac{g_2^2}{\Delta_2}\big). \tag{6.18}$$

The corresponding eigenenergies for the system with n excitations are $E_\alpha=n\omega_0+\lambda^0_\alpha+\lambda^2_\alpha$. The condition for resonant two-photon emission $E_{B,n-2}=E_{G,n}$ becomes

$$\Delta_1+\Delta_2=-(2n-1)(\frac{g_1^2}{\Delta_1}+\frac{g_2^2}{\Delta_2}). \tag{6.19}$$

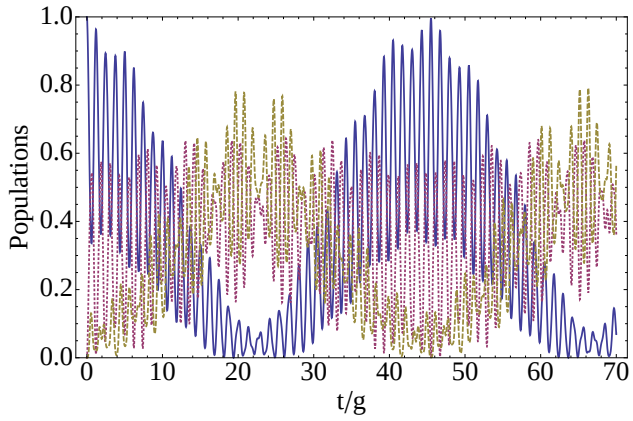

Figure 6.14: Populations of the QD levels as a function ot time with initial state $|B,0\rangle$ in the 2PR: $|B,0\rangle$ (solid-blue line), $|E,1\rangle$ (dashed-purple) and $|G,2\rangle$ (dotted-brown). The parameters are: $g_2 = 2g_1$, $\Delta_1 = 5g_1$, $\Delta_2 = -2.8g_1$. The oscillations take place in the second manifold, mainly between $|B,0\rangle$ and $|G,2\rangle$.

When this condition is satisfied the transfer of population between state $|B,n-2\rangle$ and $|G,n\rangle$ is almost perfect with negligible excitation of the intermediate states $|E1,n-1\rangle$ and $|E2,n-1\rangle$.

Already at this Hamiltonian level, it is complicated to fit the above 2PR condition while keeping large detunings to suppress the 1PR. The 2PR condition demands detunings with opposite signs whose absolute value is close to each other but still different. Therefore, either 2PR is fulfilled but with the 1PR also strongly present (for not so large a detuning as in the case of Pathak & Agarwal (70), in Fig. 6.14) either the 1PR is completely suppressed but the 2P oscillations are weak and occur very slowly as it corresponds to a 4th order effect (when detunings are large and almost equal).

Moreover, in a realistic environment, the 2PR being so weak, decoherence washes out the oscillations and this effect is not observable. Note as well that the resonance condition depends on the number of photons *n*. Therefore the two-photon emission can be efficient only for a fixed *n*. When pump and decay mechanisms drive the system, several manifolds of different number of excitations enter the dynamics and the condition can only be fulfilled partially.

6.3 One quantum dot in a cavity with a biexcitonic state

In this Section we consider the situation where up to two excitons can be created in a single QD, forming a biexciton. This is an interesting system for two-photon generation and several works exist on its coherent control through pulsed light, like that of Stufler et al. (2004) and Machnikowski (2008) or that of Flissikowski et al. (2004) and (2005). However, here we center our attention on the competition between two and one photon processes under incoherent continuous pump. With this excitation mechanism is more adequate to speak about 2P versus 1P lasing or gain, in a similar way than in the studies of Ning (2004) and Lambropoulos (1999).

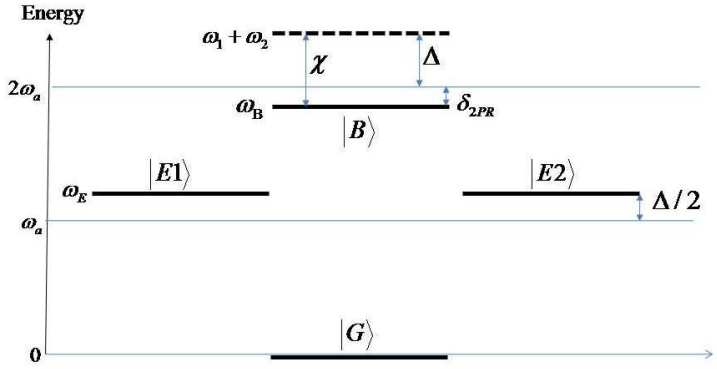

Figure 6.15: QD levels as compared to the cavity mode ω_a when the biexcitonic binding energy $\chi = \omega_1 + \omega_2 - \omega_B > 0$ is taken into account and the 2PR achieved. The two excitonic levels are considered equal in energy (to ω_E) and detuned from the cavity mode by the negative quantity $\Delta_{1,2} = \omega_a - \omega_E = -\Delta/2$. The 2PR condition $\Delta = \chi + \delta_{2\mathrm{PR}}$ is fulfilled here.

This system can be modelled with the same Hamiltonian and master equation than the two QDs in a cavity but now we must take into account that the two excitons in the biexciton configuration form a molecule with a binding energy, therefore, changing the QD level structure. This can be described with an energy correction to the Hamiltonian of Eq. (6.1) of the form

$$H_{\mathrm{B}} = -\chi \left|B\right\rangle \left\langle B\right| . \tag{6.20}$$

The biexciton binding energy defined as $\chi = \omega_1 + \omega_2 - \omega_B$, is a positive number and can be as big as one order of magnitude larger than the couplings g_1, g_2. The resulting level structure is plotted in Fig. 6.15 for the case with similar energies for the excitonic states, $\omega_1 = \omega_2 = \omega_E$, that we will analyze in what follows. In Section 6.3.1, we derive an effective Hamiltonian for large detuning, as was done

by Fernandez-Vidal et al. (2007), in order to find analytically the conditions for 1P and 2P resonances and the effective couplings associated. In Section 6.3.2, we add a continuous incoherent pump of the QD and decay. Finally, in Section 6.3.2, we compute exactly the luminescence spectrum in a truncated scheme.

6.3.1 Effective Hamiltonian close to the two-photon resonance

In order to derive an effective Hamiltonian, first, we make a change of the reference frame to the cavity frequency ω_a. The unitary operator of the transformation reads $U = e^{-i\omega_a(a^\dagger a+\sum_j \sigma_j^\dagger \sigma_j)t}$, and it is constructed such that $i\partial_t |\psi\rangle = H|\psi\rangle \xrightarrow{U} i\partial_t|\tilde{\psi}\rangle = \tilde{H}|\tilde{\psi}\rangle$ with $|\tilde{\psi}\rangle = U|\psi\rangle$ and

$$\tilde{H} = UHU^\dagger - iU\partial_t U^\dagger = H_0 + H_{\text{int}} \tag{6.21}$$

where

$$H_0 = \frac{\Delta+\varepsilon}{2}\sigma_1^\dagger\sigma_1 + \frac{\Delta-\varepsilon}{2}\sigma_2^\dagger\sigma_2 - \chi|B\rangle\langle B| \tag{6.22a}$$

$$H_{\text{int}} = \sum_{j=1,2} g_j(\sigma_j^\dagger a + a^\dagger\sigma_j). \tag{6.22b}$$

Here, we have introduced the detunings

$$\varepsilon = -(\Delta_1-\Delta_2), \quad \Delta = -(\Delta_1+\Delta_2), \tag{6.23a}$$

$$\delta = \Delta - \chi = \omega_B - 2\omega_a. \tag{6.23b}$$

In order to study the new 2PR condition and the strength of the effective coupling that it induces, we take the limit $|\Delta| \gg g_j, |\delta|, |\varepsilon|$, where the 2PR can be achieved and 1PR suppressed. An effective Hamiltonian can be obtained,$H_{\text{eff}} = H_{\text{eff},2P} + H_{\text{eff},0P}$, within perturbation theory up to second order, which decouples the subspaces $\mathscr{H}_{2\text{P}} = \{|G,n\rangle, |B,n-2\rangle\}$ (with two photon exchange between states) and $\mathscr{H}_{0\text{P}} = \{|E1,n\rangle, |E2,n\rangle\}$ (with no photon exchange). The effective Hamiltonian for the two photon exchange at fixed excitation number n is given by

$$H^n_{\text{eff},2\text{P}} = \lambda_{Gn}S_nS_n^\dagger + \lambda_{Bn-2}S_n^\dagger S_n + g_{\text{eff}}\sqrt{n(n-1)}(S_n^\dagger + S_n) \tag{6.24}$$

with $S_n = |G,n\rangle\langle B,n-2|$ and the renormalized eigenenergies/coupling constant

$$\lambda_{Gn} = -2n\frac{g_1^2+g_2^2}{\Delta}, \tag{6.25a}$$

$$\lambda_{Bn-2} = \delta - 2(n-1)\frac{g_1^2+g_2^2}{\Delta},, \tag{6.25b}$$

$$g_{\text{eff}} = -4\frac{g_1g_2}{\Delta}. \tag{6.25c}$$

The two photon resonant condition $\lambda_{Gn} = \lambda_{Bn-2}$, or in terms of detunings,

$$\delta_{\mathrm{2PR}} = -2\frac{g_1^2 + g_2^2}{\Delta}\,, \tag{6.26}$$

is independent of the manifold, that is, of the number of photons in the cavity. When this condition is satisfied (for the cavity mode placed at $\omega_a^{\mathrm{2PR}} = (\omega_B - \delta_{\mathrm{2PR}})/2$), the Hamiltonian is that of an effective two-photon exchange through the operator $S = |G\rangle\langle B|$:

$$H_{\mathrm{eff,2P}} = \delta a^\dagger a + 2\delta S^\dagger S + g_{\mathrm{eff}}(a^{\dagger 2} S + S^\dagger a^2)\,. \tag{6.27}$$

Similarly, one can determine the effective Hamiltonian in the subspace $\mathscr{H}_{0\mathrm{P}}$. In this subspace there is no exchange of energy between QD and cavity and no photon is involved in their Rabi oscillations. The only oscillations taking place in this system when Eq. (6.26) is satisfied and detuning Δ is infinite, are those of two photons. Moreover, as the two subspaces $\mathscr{H}_{0\mathrm{P}}$ and $\mathscr{H}_{2\mathrm{P}}$ are effectively decoupled in this limit, if the system is initiated in a biexcitonic or ground state, only $\mathscr{H}_{2\mathrm{P}}$ will be populated dominating the dynamics.

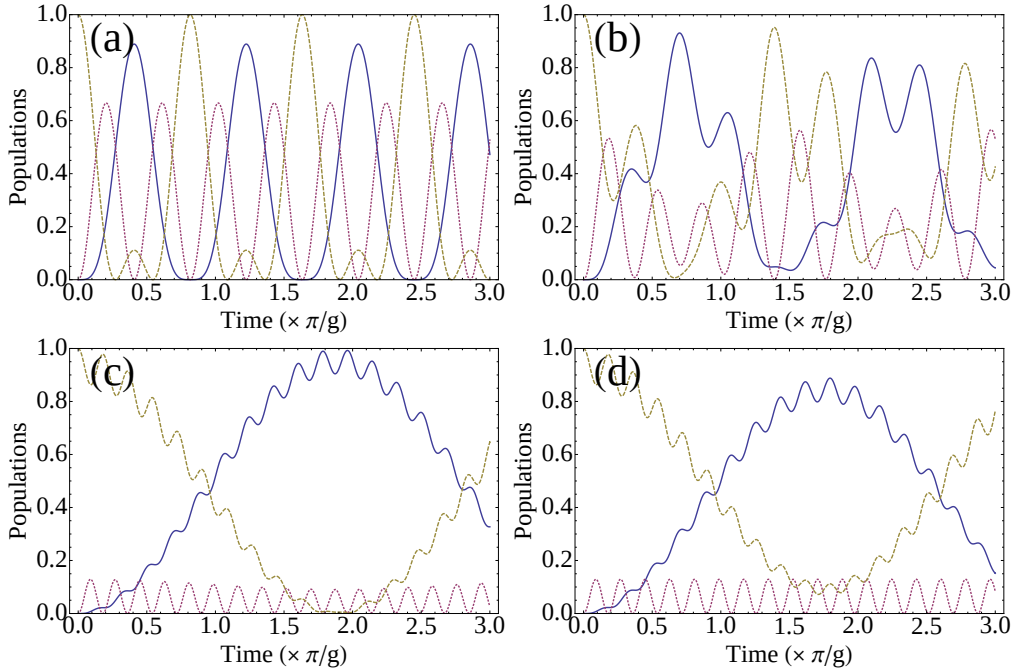

Figure 6.16: Populations of the QD levels as a function ot time with initial state $|G,2\rangle$: $|B,0\rangle$ (solid-blue line), $|E,1\rangle$ (dashed-purple) and $|G,2\rangle$ (dotted-brown). The parameters for each case are: (a) $\Delta = 0$, $\chi = 0$, (b) $\Delta = 5g$, $\chi = \Delta - \delta_{\mathrm{2PR}}$, (c) $\Delta = 20g$, $\chi = \Delta - \delta_{\mathrm{2PR}}$, (d) $\Delta = 20g$, $\chi = \Delta$.

However, for intermediate values of $|\Delta|$, in general all the QD levels get populated and 1P oscillations between the subspaces $\mathscr{H}_{2\mathrm{P}}$ and $\mathscr{H}_{0\mathrm{P}}$ also take place. Keeping in mind the effective physics that we just obtained, let us analyze the possible situations depending on the exciton detuning Δ and the biexciton binding energy χ by plotting the Rabi oscillations of the total Hamiltonian. We consider the dynamics inside the manifold with two excitations given by the states $\{|G,2\rangle, |E1,1\rangle, |E2,1\rangle, |B,0\rangle\}$. The population of each of these states, $|j\rangle$, from the initial state $|G,2\rangle$, is given by $\rho_j(t) = |\langle j| e^{-iHt} |G,2\rangle|^2$. We suppose that the coupling constants and detunings of the two excitons are equal ($g_1 = g_2 = g$, $\Delta_1 = \Delta_2 = -\Delta/2$ and $\varepsilon = 0$). In Fig. 6.16, population of $|B,0\rangle$ is plotted in solid-blue lines, $|G,2\rangle$ in dotted-brown, and the sum of the populations of $|E1,1\rangle$ and $|E1,2\rangle$ in dashed-purple. The last magnitude ($\rho_{E,1}$) is the total population in the subspace $\mathscr{H}_{0\mathrm{P}}$ and it can only interact through 1P exchange with the other subspace. Therefore, its oscillations are all the 1P oscillations occurring in the system. On the other hand, oscillations in populations $\rho_{G,2}$ or $\rho_{B,0}$ are a mixture of 1P and 2P exchange, only those clearly *between* $\rho_{G,2}$ and $\rho_{B,0}$ are purely 2P like.

The first case in Fig. 6.16-(a) is that of complete resonance between all QD states and the cavity ($\Delta = 0$ and $\chi = 0$). All states 1P-oscillate and there are no 2P oscillations due to the destructive interference. When the binding energy of the biexciton is introduced and the 2P resonance condition achieved, 2P oscillations appear already at small detuning, $\Delta = 5g$, in Fig. 6.16-(b). The coupling strength in the second manifold for identical excitons is renormalized twice by a factor $\sqrt{2}$ (i.e., by 2), having as a result a period for the 1P oscillations of $T_{1P} \approx \pi/(2g)$. 2P oscillations are slower as the Rabi frequency is given by g_{eff} and therefore $T_{2\mathrm{P}} \approx |\Delta|/2T_{1P}$. In this case, it is clear also in the plot that for each 2P oscillations between $\rho_{B,0}$ and $\rho_{G,2}$, three 1P oscillations take place in $\rho_{E,1}$. The amplitude of the oscillations is inversely related to the detuning between the cavity mode and the transition involved. 2P oscillations occur almost with maximum amplitude while 1P ones (off-resonance by $\Delta/2$) never do. This features are enhanced if the excitonic detuning is increased (keeping the 2P resonance condition) as we can see in Fig. 6.16-(c) where $\Delta = 20g$. Note that the amplitude of the oscillations is practically 1 because we obtain the 2P resonance condition computing and taking into account the Stark shift of the cavity mode due to the presence of the non-resonant excitons. If this shift is not included in the derivation, a naive 2P condition would be simply $\Delta = \chi$. This would still lead to enhanced 2P oscillations but with a reduced amplitude, as can be seen in Fig. 6.16-(d).

We can conclude from the previous discussion that the larger Δ, the stronger the 2P oscillations and the more suppressed the 1P oscillations. At a large enough value of Δ, the result would be the same as using the effective Hamiltonian (where $\rho_E \to 0$ for this initial condition). The problem associated with increasing Δ, as discussed in more details in the following sections, is that the effective coupling

also becomes weaker and the cavity must be extremely good to observe such a slow dynamics.

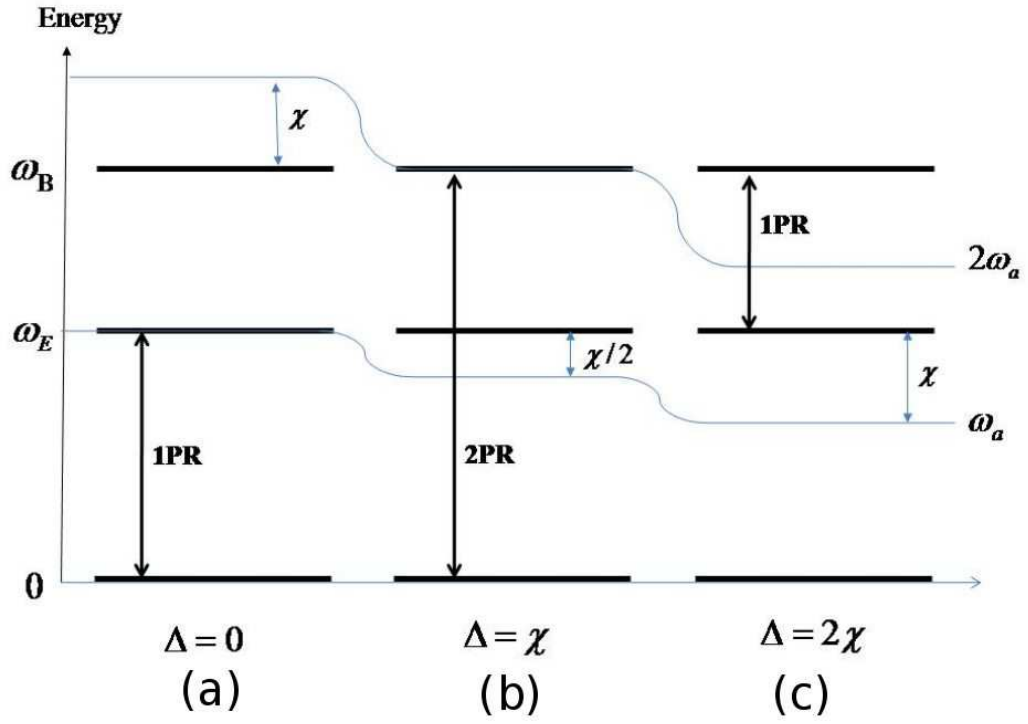

Figure 6.17: QD levels as compared to the cavity mode with a biexcitonic energy of $\chi = 20g$. When the cavity mode changes its energy, the situation changes from (a) to (c). In case (a) with $\Delta = 0$ ($\omega_a = \omega_E = \omega_B - \omega_E + \chi$), there a 1P resonance between $|G\rangle$ and $|E\rangle$ only and no 2PR ($2\omega_a = \omega_B + \chi$). In case (b) with $\Delta = 20g$, there is no 1PR ($\omega_a = \omega_E - 10g = -(\omega_B - \omega_E) - 10g$) but the system is close to 2PR ($2\omega_a = \omega_B$). In case (c) with $\Delta = 2\chi$ ($\omega_a = \omega_B - \omega_E = \omega_E - \chi$), there a 1P resonance between $|E\rangle$ and $|B\rangle$ only and again no 2PR ($2\omega_a = \omega_B - \chi$). In this simple scheme the Stark shift is not considered explicitly nor plotted.

Getting closer to the experimental situation, we fix the QD energy levels $\omega_1 = \omega_2 = \omega_E$ and choose a reasonable value for the biexciton energy $\chi = 20g$. We will not speak explicitly the Stark shift in what follows in order to simplify the discussion (writing approximate expressions for the resonance conditions) but it is included for a completely efficient 2PR resonance.

The transition between 1PR and 2PR can be evidenced by tuning the cavity from $\omega_a \approx \omega_E$ to $2\omega_a \approx \omega_B$. The QD levels corresponding to both cases are plotted in Fig. 6.17-(a) and (b) respectively. The evolution of populations in the manifold with two excitations is again shown in Fig. 6.18 in order to appreciate the qualitative change in the dynamics when tuning the cavity mode. In Fig. 6.18(a), we can see the oscillations in the configuration of Fig. 6.17(a) that correspond to

1P exchange only between states $|G,2\rangle$ and $|E,1\rangle$. The oscillations in the other extreme configuration of Fig. 6.17(b) are plotted in Fig. 6.16-(d). The intermediate cases where the QD transitions are not in resonance with the energy of 1 nor 2 photons, are those in Fig. 6.18-(b) and (c). We can see that 2P oscillations appear clearly only when the cavity is brought very close to the 2PR condition ($\Delta \approx \chi$). This can be also seen in a more precise way in Fig. 6.19-(a), where we plot the amplitude of the oscillations in the populations as a function of detuning Δ. The broad peak sitting at $\Delta = 0$ affects only populations ρ_G and ρ_E, while at $\Delta \approx \chi$ the peak is very narrow and affects populations ρ_G and ρ_B. The first one corresponds to a 1PR and the second to the 2PR.

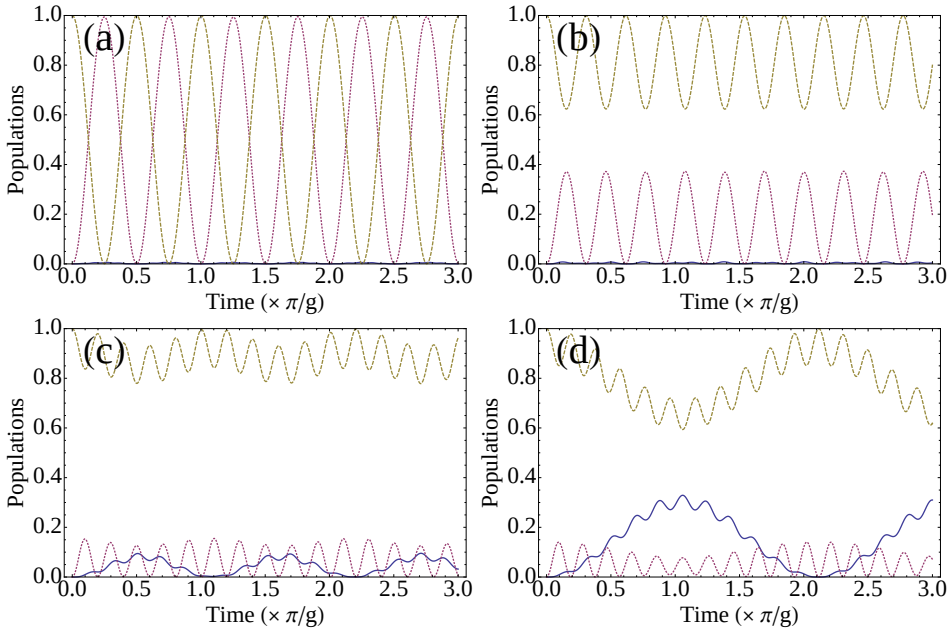

Figure 6.18: Populations of the QD levels as a function ot time with initial state $|G,2\rangle$: $|B,0\rangle$ (solid-blue line), $|E,1\rangle$ (dashed-purple) and $|G,2\rangle$ (dotted-brown). In all cases the QD levels and biexciton energy are fixed with $\chi = 20g$ while the cavity mode changes from 1PR in (a) $\Delta = 0$ towards 2PR: (b) $\Delta = 10g$ (c) $\Delta = 18g$, (d) $\Delta = 19g$. The perfect 2PR, corresponding to case (b) in Fig. 6.17, can be seen in Fig. 6.16-(c).

Note that if the cavity energy is further tuned down to $\Delta \approx 2\chi$ (see Fig. 6.17-(c)), the 1P resonance is again satisfied for the transition between states $|E\rangle$ and $|B\rangle$. In order to see this oscillations at the Hamiltonian level, the system must be initiated in other state than $|G,2\rangle$. That is, a higher excitation intensity is needed to see this second 1PR. In Fig. 6.19-(b), the amplitude of oscillations for the initial state $|B,0\rangle$, shows a third broad peak at $\Delta \approx 2\chi$ affecting only populations ρ_E and ρ_B. This is the second 1PR. The 2PR also manifests in this configuration in the same way as starting with $|G,2\rangle$. Finally, if the initial state is a superposition

of both cases ($(|G,2\rangle + |B,0\rangle)/\sqrt{2}$), the dynamics resulting is a superposition of the previous two cases, where we can see the three resonances with less sharp transitions among them.

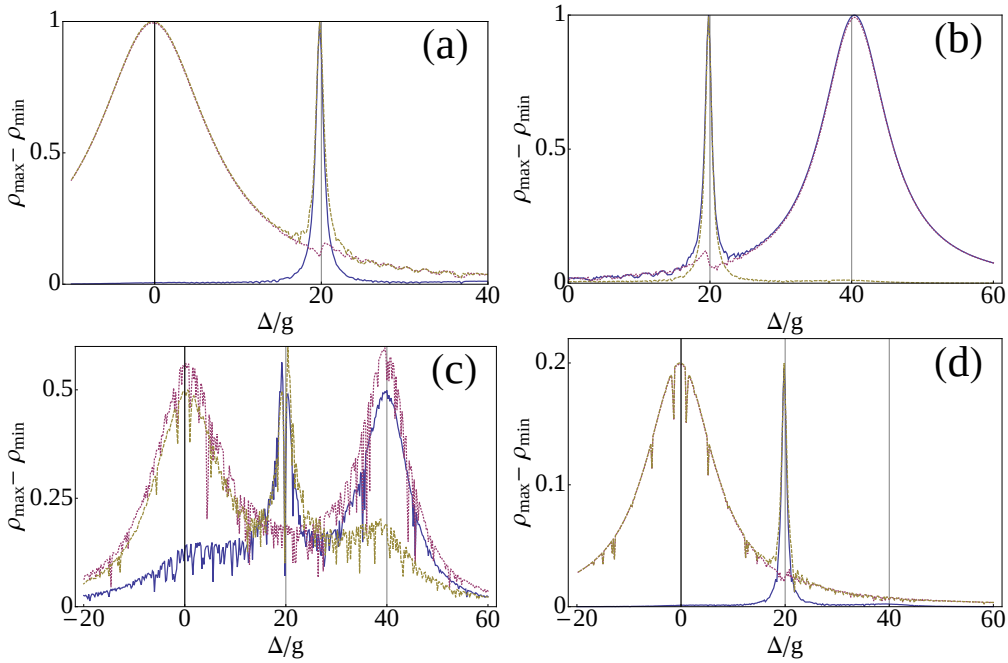

Figure 6.19: Amplitude of oscillation of populations of the states of the manifold with two excitations when tuning the cavity energy (changing detuning Δ): $|B,0\rangle$ (solid-blue line), $|E,1\rangle$ (dashed-purple) and $|G,2\rangle$ (dotted-brown). Biexciton energy is fixed to $\chi = 20g$. Plot (a) corresponds to oscillations from an initial state $|G,2\rangle$, (b) from $|B,0\rangle$, (c) from $(|G,2\rangle + |B,0\rangle)/\sqrt{2}$ and (d) from a mixture with 40% of $|B,0\rangle$ and 20% of each of the other states. Depending on the case, the peaks corresponding to 1PR can be seen at $\Delta \approx 0$ (oscillations between $|G\rangle$ and $|E\rangle$) or at $\Delta \approx 2\chi$ (between $|E\rangle$ and $|G\rangle$). The peak of 2PR manifests in all cases at $\Delta \approx \chi$.

6.3.2 Two-photon lasing

The analysis of the system in terms of the coherent Hamiltonian dynamics is essential in order to characterize the configurations where there is resonance with the cavity mode and the strength of the couplings giving rise to 1P and 2P oscillations. However, the efficiency and actual possibility of 2P lasing versus 1P lasing or simply against the decoherence, must be investigated taking into account pump and decay with the master equation

$$\frac{d\rho}{dt} = i[\rho,H] + \frac{\gamma_a}{2}\mathscr{L}^a\rho + \frac{\gamma}{2}(\mathscr{L}^{\sigma_1} + \mathscr{L}^{\sigma_2})\rho + \frac{P}{2}(\mathscr{L}^{\sigma_1^\dagger} + \mathscr{L}^{\sigma_2^\dagger})\rho\,. \qquad (6.28)$$

As we know, one of the effects of pump and decay on the Hamiltonian dynamics analyzed in the previous Section, is to averaging out the Rabi oscillations from the density matrix elements and in particular from the populations of all the states. The steady state can only be represented by a mixture of all the possible final outcomes. Different manifolds of excitation are involved in the dynamics and the mixture of states with some probability. It is no longer possible to observe the 1P/2P oscillations in the average populations. However, the 1PR and 2PR are still an intrinsic feature of the system and can be studied in the spirit of Fig. 6.19. When tuning the cavity mode over the 1PR-2PR transitions, the intensity of the emission $\langle n \rangle$ and the two-photon sensitive quantities $g^{(2)}$ and $C^{(2)}$, change dramatically as we can see in Fig. 6.20-(a) (in solid-blue, dashed-purple and dashed-brown lines respectively). Here, we kept the previous configuration for the QD levels ($\chi = 20g$) and some reasonable parameters for pump and decay ($\gamma_a = 0.2g$, $\gamma = 0.05g$ and $P = 3g$). The resonant energies (where the intensity increases) are approximately the same as those given by the Hamiltonian analysis in the case where the initial state is closer to the biexciton (see Fig. 6.19-(b) and 6.19-(d)). Let us discuss these results in more detail.

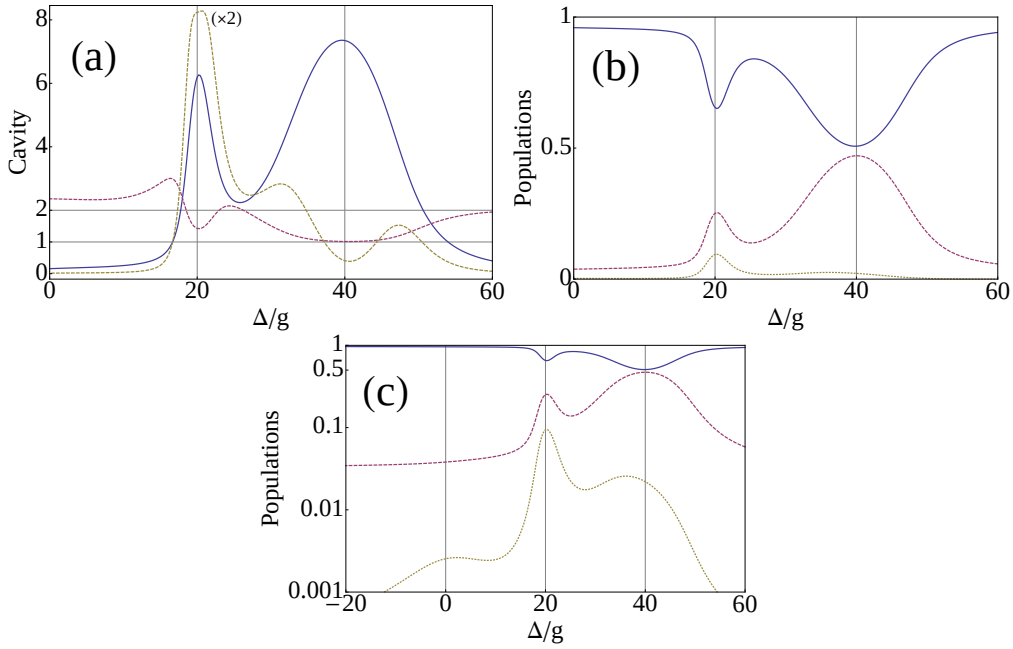

Figure 6.20: Steady state properties of the system as a function of the cavity detuning Δ for a biexciton energy of $\chi = 20g$ (see Fig. 6.17). (a) Mean value of photons $\langle n \rangle$ in the cavity (solid-blue line), $g^{(2)}(0)$ (dashed-purple) and $C^{(2)}(0)$ (dashed-brown). (b) Populations of the states: $|B\rangle$ (solid-blue), $|E\rangle$ (dashed-purple) and $|G\rangle$ (dotted-brown). The peak corresponding to 1PR can be seen at $\Delta = 2\chi$ (between $|E\rangle$ and $|B\rangle$) and that of 2PR at $\Delta = \chi$. In a logarithmic scale (c), also the 1PR at $\Delta = 0$ (between $|G\rangle$ and $|E\rangle$)

When the cavity mode is close to a resonance with some excitonic transition, the system can enter a lasing regime, where $\langle n \rangle > 1$ and $g^{(2)} \approx 1$ as we have already seen. This depends on the strength of the couplings, either g for *1P lasing* or the effective coupling g_{eff} for *2P lasing*, relatively to the decoherence in the system. If the cavity is good enough $\gamma_a \ll g$ (like in the case under study), the excitations created inside can be sustained for a long time thanks to the light-matter exchange allowing for an efficient storage of photons. Also the QD must be far from saturation (in the biexciton in this case) or self-quenching.

In Fig. 6.20-(a) it is clear from the increase in $\langle n \rangle$ and decrease in $g^{(2)}$ towards one, that both resonances bring the system into a lasing regime. The 2PR is less efficient as the coupling associated is weaker ($g_{\text{eff}} = 0.2g$) than in the case of the 1PR (g with two excitonic states involved). This manifests in three ways: the maximum intensity achieved at 2PR resonance is lower, the state is less Poissonian-like ($g^{(2)} = 1.42$ for 2PR and 1 for 1PR) and the width of the lasing regime in terms of the detuning Δ is much narrower. When the detuning brings the cavity mode too far from any QD level, $\langle n \rangle$ decays, no lasing is produced and $g^{(2)}$ becomes 2. We can see a clear transition between the two lasing regimes although the two peaks overlap and none is purely 1P or 2P lasing. Moreover, $C^{(2)}$ decreases towards zero close to $\Delta \approx 2\chi$ evidencing 1P exchange while it is enhanced around $\Delta \approx \chi$ evidencing 2P exchange.

In order to understand up to which extent the 2P lasing regime is dominated by 2P dynamics, in Fig. 6.20-(b) we plot the total populations of states $|B\rangle$ (solid-blue line), $|G\rangle$ (dotted-brown) and $|E\rangle$ (dashed-purple) as a function of detuning. Out of any excitonic resonance, the biexciton state is saturated by the pump. The transition into 2PR and 1P lasing is evidenced by the deviation from this saturation ($\rho_B = 1$). This is why resonances excited in Fig. 6.20 are basically those of Fig. 6.19-(b) and 6.19-(d) where the coherent dynamics started from biexcitonic states. The other QD states populated through the interplay with the biexciton, are the levels involved in each lasing regime, as it was the case with the Rabi oscillations. At $\Delta = 2\chi = 40g$, only $|E\rangle$ and $|B\rangle$ are involved. This implies that the dynamics are driven by 1P processes only.

On the other hand, at $\Delta = \chi = 20g$, not only $|G\rangle$ and $|B\rangle$ participate, which would imply a 2P dynamics, but also $|E\rangle$. The dynamics inside $\mathscr{H}_{0\text{P}}$ alone does not populate the cavity (as we could see in the derivation of the effective Hamiltonian), but this subspace can exchange 1P with states $|G\rangle$ and $|B\rangle$ separately even being so far from the 1PR (the same far for both transitions $|G\rangle$-$|E\rangle$ and $|E\rangle$-$|B\rangle$). At the 2PR, this 1P exchange is inefficient, as we know, by it results in some contribution, not negligible in this case. Therefore, the 2PR does not lead to 2P dynamics exclusively in general, as there will always be some weak non-resonant 1P process still present. In this case, the transition $|B\rangle$ and $|E\rangle$ is the one providing single photons as the ground state is less probably occupied. We can conclude that

the population of the ground state ρ_G is another good magnitude to identify the 2P versus 1P lasing at the 2PR.

Finally, at $\Delta = 0$, some signature of the 1PR with the transition $|G\rangle$ and $|E\rangle$ is expected. It appears in the logarithmic plot of the population ρ_G, Fig. 6.20-(c), as a small perturbation. For a case with stronger coupling (smaller γ_a) and less pumping (less saturation) this resonance would be more evident.

This discussion leads us the problem of maximizing the 2P processes so that there is a truly 2P laser operating in some clearly defined regime. There are the following points to take into account:

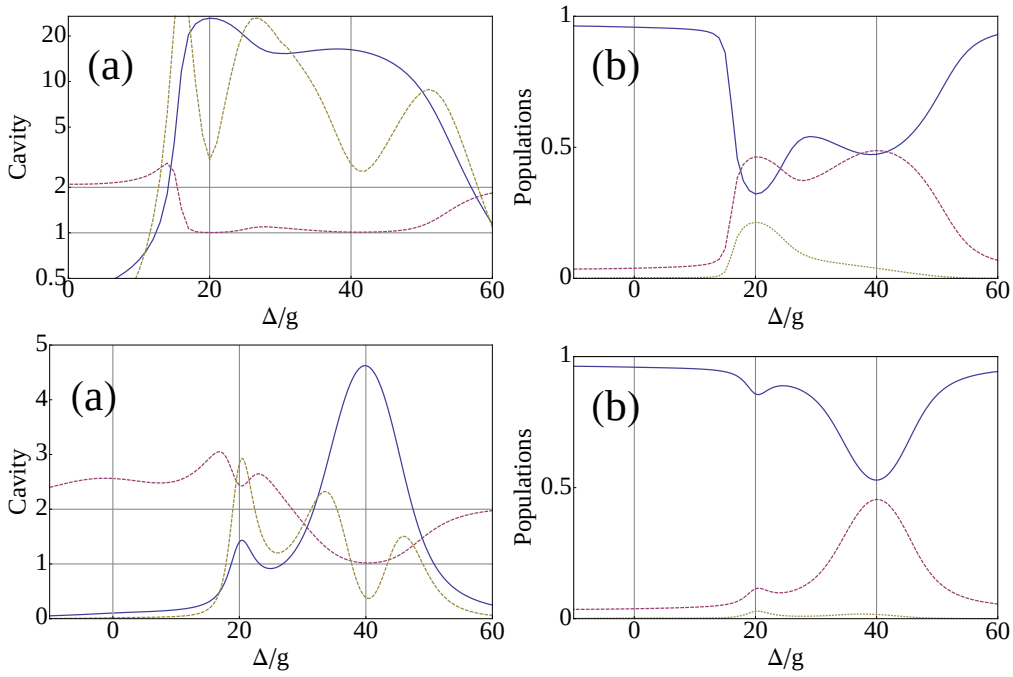

Figure 6.21: Same as Fig. 6.20 for a better cavity with $\gamma_a = 0.1g$ (upper) and for a worse cavity with $\gamma_a = 0.3g$ (lower).

(1) The system should be in strong 2P-coupling which means a large coupling g together with a good cavity so that $\gamma_a < 4g_{\text{eff}}$ for detunings Δ as large as needed. However the cavity should not be so good that even at large detuning for the 1PR, the system is still sensitive to it and therefore the 2P lasing gets polluted with single photons. We can see this effect in Fig. 6.21 where the cavity quality is improved (upper figures) or worse (lower ones). In the first case, the lasing is more efficient but both for 1P and 2P processes making it so that the separation is not clear enough. In the second case, the separation between the two regimes is larger but the 2P resonance does not lead to lasing ($g^{(2)} > 2$).

(2) The pump P should be not so strong that the system saturates for all detun-

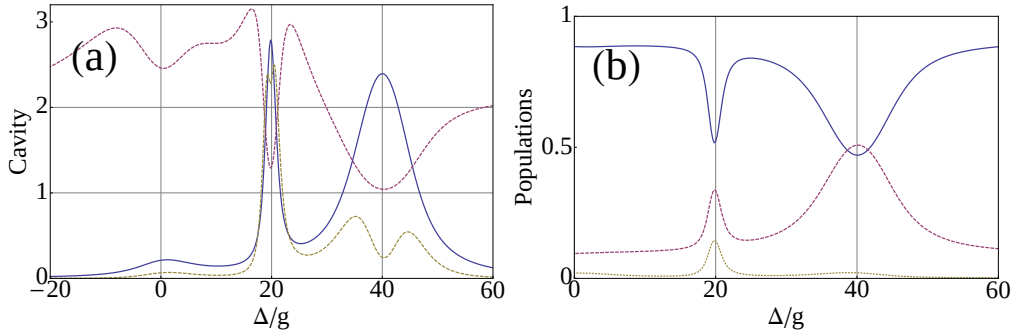

Figure 6.22: Same as Fig. 6.20 for less pumping $P = g$.

ings, quenching the production of photons at resonance. But it should be strong enough so that in the vicinity of the 2PR, and in particular in the transition from 2P to 1P lasing, the biexciton is populated and the probability to be in excitonic states (that involve 0P or 1P processes) is low. This makes the transition clearer experimentally and makes the lasing regimes purely 1P or 2P.

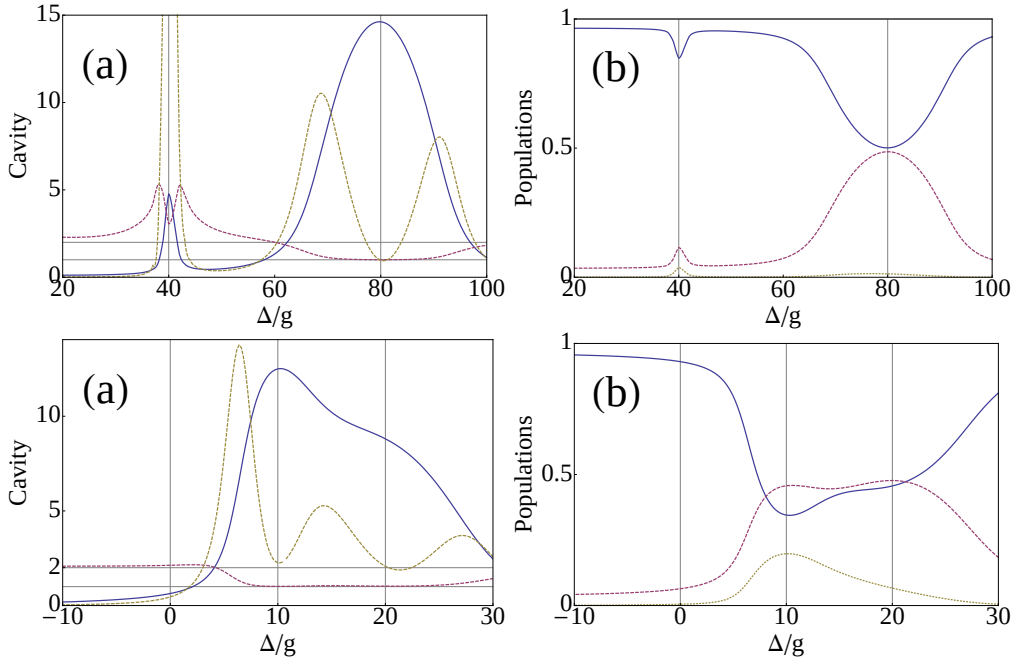

Figure 6.23: Same as Fig. 6.20 for a system with more biexciton binding energy $\chi = 40g$ but also better cavity $\gamma_a = 0.1g$ (upper) and simply with less biexciton energy $\chi = 10g$.

(3) The binding energy χ should be large enough so that the 1P and 2P lasing regions (resonances) are far from each other and can be resolved and considered independently. The 2P lasing efficiency is reduced in this case, but the character

of the emission seems to be more defined (see how $C^{(2)}$ in upper Fig. 6.23-(a) is large and distinct around $\Delta \approx \chi$). χ cannot be so large, however, that the effective coupling becomes negligible at the 2PR. We can see in lower Fig. 6.21 the effect of reducing the biexciton binding energy to $\chi = 10g$. The effective 2P coupling is stronger and therefore at the 2PR ($\Delta = 10g$) the lasing is more intense with $g^{(2)} = 1$, but the two lasing regions are superimposed making it impossible to assert that the system is dominated by 2P processes.

All these effects together could be summarized in the conditions for the best system: A large biexcitonic extra energy χ balanced with a reasonable good cavity. The optimum pumping depends on the goal. More efficient lasing requires high pumping while a more quantum 2P emission happens at low pump.

6.3.3 Spectra of emission

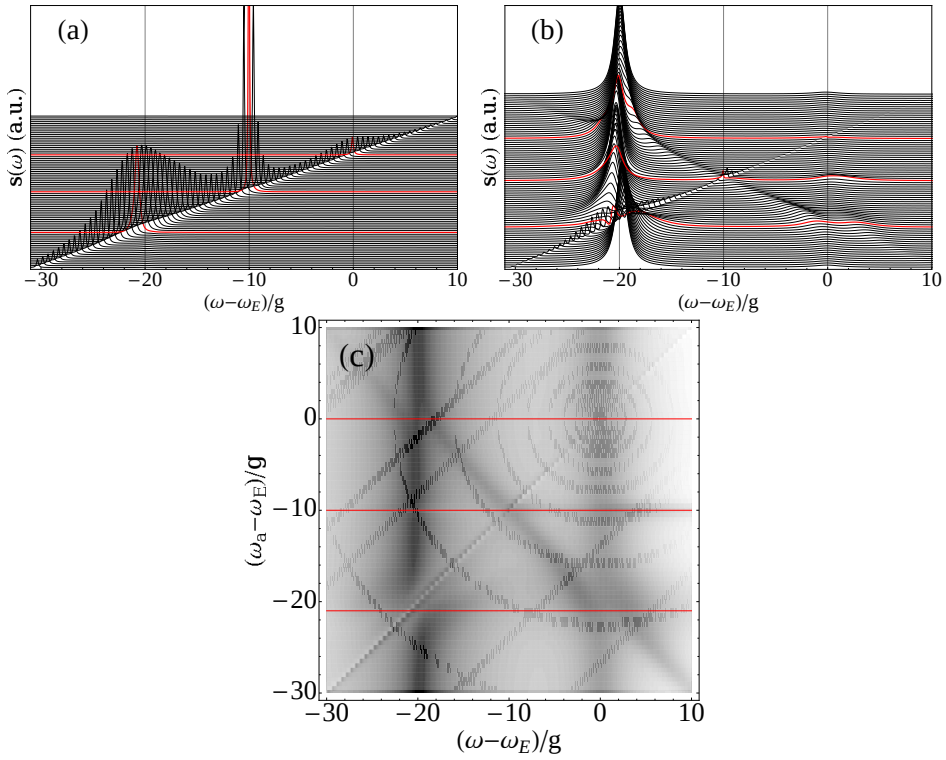

Figure 6.24: Set of (a) cavity and (b) excitonic spectra for the same parameters as in Fig. 6.22 varying the cavity energy also in the same rage of energies. The contour plot for the exciton emission is plotted in (c) in order to appreciate the anticrossings between cavity and QD modes. The cases corresponding to the three resonances are highlighted in thick red (from top to bottom): $\Delta = 0$ (1PR), $\Delta = 20g$ (2PR) and $\Delta = 40g$ (1PR). (We recall that $\omega_a - \omega_E = -\Delta/2$)

The last relevant magnitude we consider that can be measured experimentally, is the (normalized) power spectrum $S_c(\omega)$ of both the cavity ($c = a$) and the excitonic direct emission ($c = \sigma$) in the steady state. The computation of the spectra in this case involves correlators of the kind $\langle c^\dagger(t^{\rm ss})[a^{\dagger m}a^n\sigma_1^{\dagger\mu_1}\sigma_1^{\nu_1}\sigma_2^{\dagger\mu_2}\sigma_2^{\nu_2}](t^{\rm ss}+\tau)\rangle$ at all orders in the photonic indexes m, n. The fermionic ones μ_i, ν_i can only take values 0, 1. They in turn require as initial conditions at $\tau = 0$, mean values in the steady state ($t^{\rm ss}$) of the form $\langle c^\dagger a^{\dagger m}a^n\sigma_1^{\dagger\mu_1}\sigma_1^{\nu_1}\sigma_2^{\dagger\mu_2}\sigma_2^{\nu_2}\rangle^{\rm ss}$ that can be found applying again the quantum regression theorem, in a more efficient way than using the density matrix obtained in the previous Section. A truncation in the photonic indexes m, n is needed again to close the equations. The number of correlators needed to obtain $\langle c^\dagger(t)c(t+\tau)\rangle$ goes like $16N_{\rm t}$ where $N_{\rm t}$ is the maximum value that m, n are allowed to take. Truncation must be good enough so that the result is independent of it. As in the previous cases, the spectra is of the form of Eq. (2.108), a sum of $16N_{\rm t}$ peaks composed of a Lorentzian and a Dispersive part.

In Fig. 6.24 we put together a set of cavity (a) and excitonic (b) spectra for various detunings between the cavity and the exciton mode, varying in the same range as in Fig. (6.22). They are not normalized, so that the total integrated spectra is the total intensity of the emission. The cavity spectra is clearly dominated by the emission at the cavity energy, that moves in diagonal from left bottom to right-top corners of the plots. At each of the three resonances the cavity emission is enhanced (thick red lines), and notably more at the 2PR (middle one at $\Delta = \chi = 20g$). The lasing behavior of the cavity emission is very different to the direct excitonic one [Fig. 6.24(b)], where one can learn more on the level structure. The QD frequencies pin some of the emission at $\omega = \omega_E$ (lowest transition) but mostly at $\omega = \omega_E - \chi$ (highest one), due to the little contribution of the ground state to the 1P dynamics [see Fig. 6.22(b)]. There are some line anticrossings and interference patterns around the resonant points giving away the SC physics that we discussed in previous Chapters, only now displaying more complicated structures. This is better appreciated in the contour plot of Fig. 6.24(c).

6.4 Conclusions

In this Chapter, I have shown some SS properties of two QDs in a microcavity under incoherent continuous pump, considering them as two-level system. Most of the results are numerically obtained, due to the complexity of the system.

In Sec. 6.2, I discussed a model where the QDs are pumped either in an independent or in a common fashion. I have shown that the general case is a mixture of the two kinds of pumping which is determined mainly by geometrical factors but can be increased one way or the other, for instance by applying an external electric field. In the case where the dots are essentially excited through the common pump-

ing, quantum interferences in the dots alter significantly the dynamics and yield singularities or abrupt features in the steady state populations. For suitable sets of parameters, which include different couplings between cavity and dots, the system can be brought to a regime where the singlet state, $|\mathrm{S}\rangle = (|E1\rangle - |E2\rangle)/\sqrt{2}$, is predominantly occupied. This provides good values of the tangle, despite the incoherent and continuous nature of the pumping (Fig. 6.6).

After these positive results, we propose a quantum transport experiment for preparing and measuring in the SS a charge-entangled state of two non-interacting QDs. Each QD is coherently coupled to a third one, playing the role of the cavity in the previous scheme. The coherent trapping mechanism that creates the entanglement can be switched on and off by means of a gate potential. This allows both state preparation and entanglement detection by simply measuring the total current (Fig. 6.10).

In the case where the dots in the cavity are essentially pumped independently, the presence of a largely detuned or weakly coupled dot changes qualitatively the dynamics of a near resonant, strongly coupled dot. In view of its lasing properties, the system therefore acquires a low stimulated emission threshold resulting in efficient cavity population with Poissonian distribution, even when both dots are detuned from the cavity mode (Fig. 6.13). This is qualitatively different from a model with isolated dots which emission would scale with their number, especially at nonzero detuning.

In Sec. 6.3, we finally studied two-photon lasing considering a single QD in a microcavity but that can contain a biexcitonic bounded state and therefore can be described by a similar Hamiltonian and master equation than the two small dots in the cavity. The biexcitonic binding energy allows for a two photon resonance while the one photon processes are largely suppressed. We studied the feasibility of a two-photon correlated emission under the incoherent pump and decay and obtained positive results measurable through the properties of the emitted light (Fig. 6.20 and 6.24). For this system, some analytical expressions have been derived at a Hamiltonian perturbative level, like the effective coupling and Stark shifts, Eq. (6.25).

Conclusions (*Conclusiones*)

Spanish *(Castellano)*

En esta tésis, he descrito teóricamente la interacción entre luz y materia en presencia de decoherencia para uno o dos puntos cuánticos (QDs) en una microcavidad.

El observable experimental principal que he estudiado es el espectro de fotoluminescencia. He aplicado un método general que permite descomponer las curvas de emisión en transiciones individuales entre diferentes estados del sistema. Con esta información he podido identificar sin ambiguedad los estados vestidos (*polaritones*) en el espectro, y caracterizar diferentes regímenes según la fuerza del acoplo. Cada línea espectral está compuesta por por una parte Lorentziana, que corresponde a la emisión pura del polariton, y una parte dispersiva, que corresponde a la interferencia entre differentes emisiones de polaritones, que se solapan en energía como resultado de la decoherencia.

Los elementos básicos que he usado para modelizar los modos excitónico y bosónico son el oscilador armónico (HO) para bosones, el oscilador anarmónico (AO) para bosones interactuantes, y el sistema de dos niveles (2LS) para ferminones. Su acoplo (g) da lugar a los modelos fundamentales de cQED que hemos analizado en detalle: el regimen lineal de bajo bombeo, así como el acoplo de excitones y fotones en un QD grande (de dos modos bosónicos), se describe con el modelo lineal (LM). Para excitones interactuantes, hemos extendido este modelo añadiendo interacciones anarmónicas al excitón. El estudio ha culminado con el modelo de Jaynes-Cummings (JCM) que describe la interacción totalmente cuantizada de luz (HO) y materia (2LS). Es adecuado para QDs pequeños donde los efectos fermiónicos se manifiestan. Otro modelo fundamental que nos ha ayudado a comprender mejor el JCM, es el acoplo de dos 2LSs.

Para estudiar el acoplo fuerte (SC) de estos sistemas y sus propiedades de emisión en un contexto realista, nos hemos referido a dos situaciones físicas: la emisión espontánea del sistema desde un estado inicial general (SE) y, con mayor relevancia, la emisión en el estado de equilibrio conducido por bombeo continuo e incoherente (SS). El SE representa los mecanismos de excitación que son de naturaleza coherente (Hamiltoniana) y no traen decoherencia al sistema. La única

fuente de decoherencia es la disipación, lo que hace posible resolver la dinámica de manera analítica en todos los casos. He presentado el SE como el punto de partida para el estudio de las propiedades del SS, ya que revela la estructura en manifolds del sistema en el límite de bajo bombeo. El caso del SS solo se puede resolver analíticamente en el LM y para los dos 2LSs, aunque el método que hemos utilizado para calcular espectros permite obtener expresiones semi-analíticas en el resto de casos no lineales.

Para todas estas configuraciones, he estudiado diferentes regímenes que surgen de la competencia entre acoplo y decoherencia, especialmente aquellos que se deben a la presencia del bombeo.

En el regimen lineal, o en el LM, un criterio sencillo basado en la frecuencia generalizada de Rabi determina la aparición de estados vestidos y SC. Los regímenes de SC y WC pueden ser inducidos por los bombeos de cavidad/exciton, demostrando que se trata de parámetros indispensables para el fiteo los datos experimentales de hoy en día. He mostrado como la constante de acoplo puede ser estimada erróneamente si no se tiene en cuenta el bombeo en el modelo teórico (por ejemplo usando las fórmulas del SE). El famoso dublete de Rabi solo se ovserva claramente muy adentrados en el regimen de acoplo fuerte. Si no, la contribución a los picos dispersiva o de interferencia, puede llegar a dominar colapsando el espectro en un singlete antes incluso de alcanzar el WC. El estado cuántico del sistema, dado por el bombeo y el decaimiento, determina las curvas de emisión. Añadir interacciones al LM le dota de una nolinearidad que se manifiesta incluso a bajo pump. El dublete de Rabi se vuelve asimétrico, si las interacciones son pequeñas, separándose en una estrucutra de múltiples picos, si las interacciones son del orden del acoplo y la disipación. Los picos se pueden identificar como más fotónicos o excitónicos cuando el QD y el modo de cavidad están algo fuera de resonancia.

Los dos 2LSs acoplados nos han dado algunas pistas valiosas sobre el JCM. Varios tipos de SC aparecen debido a la conjunción de bombeo y decaimiento, dando lugar a dubletes y singletes deformados. El acoplo se renormaliza, en el mejor de los casos, a $\sqrt{2}g$ debido a efectos cooperativos. El JCM, incluso en ausencia de bombeo, da lugar a una compleja estructura de estados vestidos y a una renormalización del acoplo que depende del número de fotones $\sqrt{n}g$. Un pequeño bombeo es suficiente para probar la escalera de JC y observar multipletes en el espectro, prueba por excelencia del emisor cuántico. Sin embargo, si se aumenta el bombeo para adentrase en las no linearidades, la estructura en sí misma se ve afectada por la decoherencia. En el peor de los casos, uno puede asociar comportamientos cuánticos a la transición del dublete de vacío de Rabi a los picos internos no lineales, como hemos propuesto. La transición del dublete de Rabi (regimen lineal), al tenedor de JC (regimen cuántico), al triplete de Mollow (regimen clásico de lasing), se entiende y se sigue claramente gracias a nuestra

descomposción del espectro.

English *(Inglés)*

In this thesis I described theoretically light-matter interaction in the presence of decoherence for one or two quantum dots (QDs) in a microcavity.

The main experimental observable that I studied is the photoluminescence (PL) spectrum. I applied a general method that allows to decompose the lineshapes into individual transitions between the different states of the system. With this information I was able to identify unambiguously the dressed states (*polaritons*) in the spectra, and characterize different regimes depending on the strengh of the coupling. Each spectral line is composed of a Lorenztian part, corresponding to the pure polaritonic emission, and a dispersive part, corresponding to the interference between different polariton emissions, overlapping in energy as a result of decoherence.

The basic elements I used to model the excitonic and photonic modes are the harmonic oscillator (HO) for bosons, the anharmonic oscillator (AO) for interacting bosons, and the two-level system (2LS) for fermions. Their coupling (g) gives rise to the fundamental models of cQED that we analyzed in detail: the linear regime of vanishing pump, as well as the coupling of excitons and photons in a large QD (two bosonic modes), is described by the linear model (LM). For interacting excitons, we made an extension of this model by adding anharmonic excitonic interactions. The study culminated with the Jaynes-Cummings model (JCM), that describes full field-quantization interaction of light (HO) and matter (2LS). It is adequate for small QDs where the fermionic effects are manifest. Another fundamental model that helped us undertand the more complex JCM, is the coupling of two 2LSs.

In order to study the strong coupling (SC) of these systems and their emission properties in realistic settings, we addressed two physical situations: the spontaneous emission of the system from a general initial state (SE) and, most importantly, the steady state emission under incoherent continuous pump (SS). The SE case represents all mechanisms of excitation that are coherent in nature (Hamiltonian) and do not bring decoherence to the system. The only source of decoherence is dissipation, which made it possible to solve the dynamics analytically in all cases. I presented SE as the starting point of the study of SS properties, as it provides the manifold structure of the system in the limit of vanishing pump. The SS case is only analytically solvable for the LM and two 2LSs, although the method used to compute the spectra allows for semi-analytical expressions in the rest of nonlinear cases.

For all these configurations, I studied the different regimes that stem from

the competition between coupling and decoherence, specially those due to the presence of the pump.

In the linear regime, or for the LM, a simple criteria based on the Rabi frequency determines the appearance of dressed states and SC. The SC and WC regimes can be induced by the cavity/exciton pump, proving itself to be an indispensable fitting parameter for state of the art experimental data. I showed how the coupling strenght can be wrongly estimated if the pump is missing in the theoretical model (for example, using the SE formulas). The famous Rabi doublet is only clearly observed in the very SC spectra. Otherwise, the dispersive interfering part of the peaks can take over collapsing the spectra into a singlet even before reaching WC. The quantum state of the system, given by pump and decay, determines the lineshape. Adding interactions to the LM, provides a nonlinearity that manifests even at very low pump. The Rabi doublet becomes asymetric, if the interactions are weak, and eventually splits in a multiplet structure when they are of the order of dissipation and coupling. The peaks can be identified as more excitonic or photonic when the QD and cavity modes are detuned from each other.

The two coupled 2LSs gave some useful insights on the JCM. Several kinds of SC appeared due to the interplay between pump and decay, having distorted doublets and singlets as a result. The coupling strenght gets renormalized, in the best of cases, to $\sqrt{2}g$ due to cooperative behaviors. The JCM, already at vanishing pump, gives rise to more complicated braches of dressed states and a renormalization of the coupling $\sqrt{n}g$, with n the number of photons. A small pump is enough to probe JC ladder structure, and observe multiplets in the spectra, signature of quantum emitter by excellence. However, as the pump is increased to investigate the nonlinearities, the structure itself is affected by decoherence. In the worse case, one can claim quantum behaviors by observing the transition from vacuum Rabi doublet to nonlinear inner peaks that we proposed. However, only in the very good systems, increasing the pump can lead to the observation of an incoherent Mollow triplet. The crossover from a vacuum Rabi doublet (the linear regime), to the JC fork (quantum regime), to the Mollow triplet (classical lasing regime), was clearly understood and tracked thanks to our spectra decomposition.

List of publications

Regular Journals

1. **E. del Valle**, F. P. Laussy, F. Troiani and C. Tejedor, *Entanglement and lasing with two quantum dots in a microcavity*, Phys. Rev. B **76**, 235317 (2007)

2. **E. del Valle**, F. P. Laussy and C. Tejedor, *Electrostatic control of quantum dot entanglement induced by coupling to external reservoirs*, Europhys. Lett. **80**, 57001 (2007)

3. **E. del Valle**, F. P. Laussy, F. M. de Souza and I. Shelykh, *Optical spectra of a quantum dot in a microcavity in the nonlinear regime*, Phys. Rev. B **78**, 085304 (2008)

4. F. P. Laussy, **E. del Valle** and C. Tejedor, *Strong-coupling of quantum dots in microcavities*, Phys. Rev. Lett. **101**, 083601 (2008)

5. A. Amo, D. Sanvitto, D. Ballarini, F. P. Laussy, **E. del Valle**, M. D. Martin, A. Lemaitre, J. Bloch, D. N. Krizhanovskii, M. S. Skolnick, C. Tejedor and L. Viña, *Collective fluid dynamics of a polariton condensate in a semiconductor microcavity*, Nature **457**, 291 (2009)

Conference proceedings

6. **E. del Valle**, F. Troiani, C. Tejedor, *Cavity quantum electrodynamics for two quantum dots*, AIP ICPS28 Conf. Proc. 893, 1077 (2007)

7. **E. del Valle**, F. P. Laussy, F. Troiani and C. Tejedor, *Steady state of two quantum dots in a cavity*, PLMCN7 Conf. Proc., Superlattices and Microstructures **43**, 465 (2007)

8. F. P. Laussy, **E. del Valle** and C. Tejedor, *Quantitative Description of Strong-Coupling of Quantum Dots in Microcavities*, AIP ICPS29 Conf. Proc. (2008)

Preprints

9. F. P. Laussy, **E. del Valle** and C. Tejedor, *Luminescence spectra of quantum dots in microcavities. I. Bosons*, submitted to Phys. Rev. B arXiv:0807.3194, (2008)

10. **E. del Valle**, F. P. Laussy and C. Tejedor, *Luminescence spectra of quantum dots in microcavities. II. Fermions*, submitted to Phys. Rev. B arXiv:0812.2694, (2008)

11. **E. del Valle**, S. Zipilli, A. Gonzalez-Tudela, F. P. Laussy, C. Tejedor and G. Morigi, *Two-photon gain of a quantum dot in a microcavity under incoherent continuous pump*, in preparation.

12. **E. del Valle**, *Luminescence spectra of two coupled two-level systems*, in preparation.

13. **E. del Valle**, F. P. Laussy and C. Tejedor, *Quantum regression formula and luminescence spectra of two coupled modes under incoherent continuous pumping*, submitted to AIP ICTOPON1 Conf. Proc. (2009)

14. F. P. Laussy. **E. del Valle** *Optical Spectra of the Jaynes-Cummings Ladder*, submitted to AIP ICTOPON1 Conf. Proc. (2009)

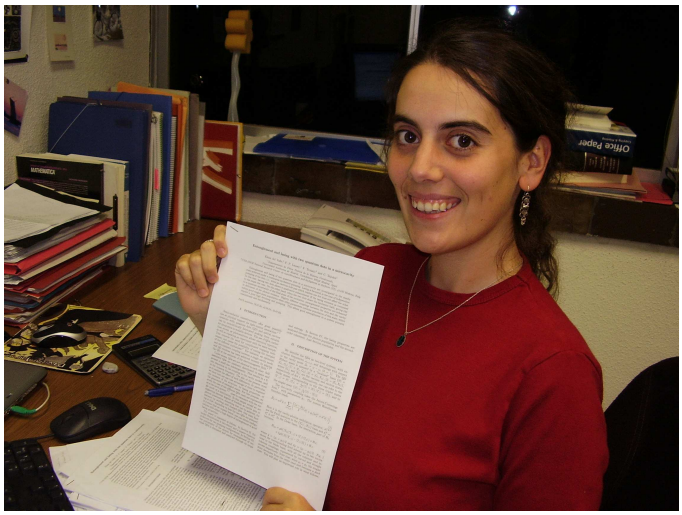

The author with the manuscript of her first published work
in an high-impact journal, on May, 22 (2007).

Bibliography

Agarwal, G. S. & Puri, R. R. (1986). Exact quantum-electrodynamics results for scattering, emission, and absorption from a rydberg atom in a cavity with arbitrary Q, *Phys. Rev. A* **33**: 1757.

Akram, U., Ficek, Z. & Swain, S. (2000). Decoherence and coherent population transfer between two coupled systems, *Phys. Rev. A* **62**: 013413.

Alicki, R. (1989). Master equations for a damped nonlinear oscillator and the validity of the markovian approximation, *Phys. Rev. A* **40**: 4077.

Amo, A., Lefrere, J., Pigeon, S., Adrados, C., Ciuti, C., Carusotto, I., Houdre, R., Giacobino, E. & Bramati, A. (2009). Observation of superfluidity of polaritons in semiconductor microcavities, *arXiv:0812.2748* .

Amo, A., Sanvitto, D., Laussy, F. P., Ballarini, D., del Valle, E., Martin, M. D., Lemaître, A., Bloch, J., Krizhanovskii, D. N., Skolnick, M. S., Tejedor, C. & Viña, L. (2009). Collective fluid dynamics of a polariton condensate in a semiconductor microcavity, *Nature* **457**: 291.

Andreani, L. C., Panzarini, G. & Gérard, J.-M. (1999). Strong-coupling regime for quantum boxes in pillar microcavities: Theory, *Phys. Rev. B* **60**: 13276.

Armani, D. K., Kippenberg, T. J., Spillane, S. M. & Vahala, K. J. (2003). Ultra-high-*q* toroid microcavity on a chip, *Nature* **421**: 925.

Ashraf, I., Gea-Banacloche, J. & Zubairy, M. S. (1990). Theory of the two-photon micromaser: Photon statistics, *Phys. Rev. A* **42**: 6704.

Auffèves, A., Besga, B., Gérard, J.-M. & Poizat, J.-P. (2008). Spontaneous emission spectrum of a two-level atom in a very-high-q cavity, *Phys. Rev. A* **77**: 063833.

Averkiev, N. S., Glazov, M. & Poddubny, A. (2008). Collective modes of quantum dot ensembles in microcavities, *arXiv:0809.3155* .

Awschalom, D. D., Loss, D. & Samarth, N. (2002). *Semiconductor spintronics and quantum, computation*, Springer.

Badolato, A., Hennessy, K., Atature, M., Dreyser, J., Hu, E., Petroff, P. M. & Ĭmamoḡlu, A. (2005). Deterministic coupling of single quantum dots to single nanocavity modes, *Science* **308**: 1158.

Barchielli, A. & Pero, N. (2002). A quantum stochastic approach to the spectrum of a two-level atom, *J. Opt. B* **4**: 272.

Barut, A. O. & Huele, J. F. V. (1996). Quantum electrodynamics based on self-energy: Lamb shift and spontaneous emission without field quantization, *Phys. Rev. A* **53**: 2816.

Bayer, M., Reinecke, T. L., Weidner, F., Larionov, A., McDonald, A. & Forchel, A. (2001). Inhibition and enhancement of the spontaneous emission of quantum dots in structured microresonators, *Phys. Rev. Lett.* **86**: 3168.

Bennett, A. J., Ellis, D. J. P., Shields, A. J., Farrer, P. A. I. & Ritchie, D. A. (2007). Observation of the purcell effect in high-index-contrast micropillars, *Appl. Phys. Lett.* **90**: 191911.

Benson, O. & Yamamoto, Y. (1999). Master-equation model of a single-quantum-dot microsphere laser, *Phys. Rev. A* **59**: 4756.

Bethe, H. A. (1947). The electromagnetic shift of energy levels, *Phys. Rev.* **72**: 339.

Bienert, M., Merkel, W. & Morigi, G. (2004). Resonance fluorescence of a trapped three-level atom, *Phys. Rev. A* **69**: 013405.

Bienert, M., Torres, J. M., Zippilli, S. & Morigi, G. (2007). Resonance fluorescence of a cold atom in a high-finesse resonator, *Phys. Rev. A* **76**: 013410.

Bishop, L. S., Chow, J. M., Koch, J., Houck, A. A., Devoret, M. H., Thuneberg, E., Girvin, S. M. & Schoelkopf, R. J. (2009). Nonlinear response of the vacuum rabi resonance, *Nature Phys.* **5**: 105.

Björk, G., Machida, S., Yamamoto, Y. & Igeta, K. (1991). Modification of spontaneous emission rate in planar dielectric microcavity structures, *Phys. Rev. A* **44**: 669.

Boca, A., Miller, R., Birnbaum, K. M., Boozer, A. D., McKeever, J. & Kimble, H. J. (2004). Observation of the vacuum rabi spectrum for one trapped atom, *Phys. Rev. Lett.* **93**: 233603.

Brandes, T. (2005). To be found, *Phys. Rep.* **408**: 315.

Braun, D. (2002). Creation of entanglement by interaction with a common heat bath, *Phys. Rev. Lett.* **89**: 277901.

Brune, M., Raimond, J. M., Goy, P., Davidovich, L. & Haroche, S. (1987). Realization of a two-photon maser oscillator, *Phys. Rev. Lett.* **59**: 1899.

Brune, M., Schmidt-Kaler, F., Maali, A., Dreyer, J., Hagley, E., Raimond, J. M. & Haroche, S. (1996). Quantum Rabi oscillation: A direct test of field quantization in a cavity, *Phys. Rev. Lett.* **76**: 1800.

Brunner, K., Bockelmann, U., Abstreiter, G., Walther, M., Böhm, G., Tränkle, G. & Weimann, G. (1992). Photoluminescence from a single gaas/algaas quantum dot, *Phys. Rev. Lett.* **69**: 3216.

Carmichael, H. J. (2002). *Statistical methods in quantum optics 1*, 2 edn, Springer.

Carmichael, H. J., Brecha, R. J., Raizen, M. G., Kimble, H. J. & Rice, P. R. (1989). Subnatural linewidth averaging for coupled atomic and cavity-mode oscillators, *Phys. Rev. A* **40**: 5516.

Carusotto, I. & Ciuti, C. (2004). Probing microcavity polariton superfluidity through resonant rayleigh scattering, *Phys. Rev. Lett.* **93**: 166401.

Casimir, H. B. (1948). On the attraction between two perfectly conducting plates, *Proc. K. Ned. Akad. Wetensch.* **51**: 793.

Chang, W.-H., Chen, W.-Y., Chang, H.-S., Hsieh, T.-P., Chyi, J.-I. & Hsu, T.-M. (2006). Efficient single-photon sources based on low-density quantum dots in photonic-crystal nanocavities, *Phys. Rev. Lett.* **96**: 117401.

Ciuti, C. (2004). Branch-entangled polariton pairs in planar microcavities and photonic wires, *Phys. Rev. B* **69**: 245304.

Ciuti, C., Schwendimann, P., Deveaud, B. & Quattropani, A. (2000). Theory of the angle-resonant polariton amplifier, *Phys. Rev. B* **62**: R4825.

Clemens, J. P. & Rice, P. R. (2000). Nonclassical effects of a driven atoms-cavity system in the presence of an arbitrary driving field and dephasing, *Phys. Rev. A* **61**: 063810.

Clemens, J. P., Rice, P. R. & Pedrotti, L. M. (2004). Spectra of single-atom lasers, *J. Opt. Soc. Am. B* **21**: 2025.

Cohen-Tannoudji, C., Dupont-Roc, J. & Grynberg, G. (2001). *Photons et atomes*, EDP Sciences.

Combescot, M. & Betbeder-Matibet, O. (2004). Scattering rates and lifetime of exact and boson excitons, *Phys. Rev. Lett.* **93**: 016403.

Cui, G. & Raymer, M. G. (2006). Emission spectra and quantum efficiency of single-photon sources in the cavity-qed strong-coupling regime, *Phys. Rev. A* **73**: 053807.

da Silva, L. G. G. V. D., Sandler, N., Ingersent, K. & Ulloa, S. E. (2006). To be found, *Phys. Rev. Lett.* **97**: 96603.

Davidovich, L., Raimond, J. M., Brune, M., & Haroche, S. (1987). Quantum theory of a two-photon micromaser, *Phys. Rev. A* **36**: 3771.

De Liberato, S., Ciuti, C. & Carusotto, I. (2007). Quantum vacuum radiation spectra from a semiconductor microcavity with a time-modulated vacuum rabi frequency, *Phys. Rev. Lett.* **98**: 103602.

del Valle, E., Laussy, F. P., Souza, F. M. & Shelykh, I. A. (2008). Optical spectra of a quantum dot in a microcavity in the nonlinear regime, *Phys. Rev. B* **78**: 085304.

Deveaud, B. (ed.) (2007). *The Physics of Semiconductor Microcavities: From Fundamentals to Nanoscale Devices*, Wiley-VCH.

Dicke, R. H. (1954). Coherence in spontaneous radiation processes, *Phys. Rev.* **93**: 99.

Diederichs, C. & Tignon, J. (2005). Design for a triply resonant vertical-emitting micro-optical parametric oscillator, *Appl. Phys. Lett.* **87**: 251107.

Diederichs, C., Tignon, J., Dasbach, G., Ciuti, C., Lemaître, A., Bloch, J., Roussignol, P. & Delalande, C. (2006). Parametric oscillation in vertical triple microcavities, *Nature* **440**: 904.

Dirac, P. A. M. (1927). The quantum theory of the emission and absorption of radiation, *Proc. Roy. Soc. London A* **114**: 243.

Eberly, J. & Wódkiewicz, K. (1977). The time-dependent physical spectrum of light, *J. Opt. Soc. Am.* **67**: 1252.

Feldtmann, T., Schneebeli, L., Kira, M. & Koch, S. W. (2006). Quantum theory of light emission from a semiconductor quantum dot, *Phys. Rev. B* **73**: 155319.

Fernandez-Vidal, S., Zippilli, S. & Morigi, G. (2007). Nonlinear optics with two trapped atoms, *Phys. Rev. A* **76**: 253829.

Ficek, Z. & Tanas, R. (2002). Entangled states and collective nonclassical effects in two-atom systems, *Phys. Rep.* **372**: 369.

Fink, J. M., Göppl, M., Baur, M., Bianchetti, R., Leek, P. J., Blais, A. & Wallraff, A. (2008). Climbing the jaynes–cummings ladder and observing its nonlinearity in a cavity qed system, *Nature* **454**: 315.

Flissikowski, T., Betke, A., Akimov, I. A. & Henneberger, F. (2004). Two-photon coherent control of a single quantum dot, *Phys. Rev. Lett.* **92**: 227401.

Flissikowski, T., Betke, A., Akimov, I. A. & Henneberger, F. (2005). Coherent control of the biexciton in a single quantum dot, *Phys. Stat. Sol. A* **202**: 383.

Florescu, L. (2006). Spectrum of a one-atom laser in photonic crystals, *Phys. Rev. A* **74**: 063828.

Freedhoff, H. & Quang, T. (1994). Ultrasharp lines in the absorption and fluorescence spectra of an atom in a cavity, *Phys. Rev. Lett.* **72**: 474.

Gardiner, G. W. (1991). *Quantum Noise*, Springer-Verlag, Berlin.

Gauthier, D. J., Wu, Q., Morin, S. E. & Mossberg, T. W. (1992). Realization of a continuous-wave, two-photon optical laser, *Phys. Rev. Lett.* **68**: 464.

Gérard, J.-M. & Gayral, G. (1999). Strong Purcell effect for InAs quantum boxes in three-dimensional solid-state microcavities, *J. Light Wave Tech.* **17**: 2089.

Gerry, C. C. & Knight, P. L. (2005). *Introductory Quantum Optics*, Cambridge University Press.

Gies, C., Wiersig, J., Lorke, M. & Jahnke, F. (2007). Semiconductor model for quantum-dot-based microcavity lasers, *Phys. Rev. A* **75**: 013803.

Ginzel, C., Briegel, H.-J., Martini, U., Englert, B.-G. & Schenzle, A. (1993). Quantum optical master equations: The one-atom laser, *Phys. Rev. A* **48**: 732.

Glauber, R. J. (1963a). Coherent and incoherent states of the radiation field, *Phys. Rev.* **131**: 2766.

Glauber, R. J. (1963b). The quantum theory of optical coherence, *Phys. Rev.* **130**: 2529.

Gotoh, H., Kamada, H., Saitoh, T., Ando, H. & Temmyo, J. (2005). Exciton absorption properties of coherently coupled exciton-biexciton systems in quantum dots, *Phys. Rev. B* **71**: 195334.

Goy, P., Raimond, J. M., Gross, M. & Haroche, S. (1983). Observation of cavity-enhanced single-atom spontaneous emission, *Phys. Rev. Lett.* **50**: 1903.

Gywat, O., Meier, F., Loss, D. & Awschalom, D. D. (2006). Dynamics of coupled qubits interacting with an off-resonant cavity, *Phys. Rev. B* **73**: 125336.

Hanamura, E. (1970). Theory of the high density exciton. i, *J. Phys. Soc. Jpn.* **29**: 50.

Hanbury Brown, R. & Twiss, R. Q. (1956). A test of a new type of stellar interferometer on Sirius, *Nature* **178**: 1046.

Haroche, S. & Kleppner, D. (1989). Cavity quantum electrodynamics, *Physics Today* **42**: 24.

Hayashi, T., Fujisawa, T., Cheong, H. D., Jeong, Y. H. & Hirayama, Y. (2003). To be found, *Phys. Rev. Lett.* **91**: 226804.

Hennessy, K., Badolato, A., Winger, M., Gerace, D., Atature, M., Gulde, S., Fălt, S., Hu, E. L. & Ĭmamoḡlu, A. (2007). Quantum nature of a strongly coupled single quantum dot–cavity system, *Nature* **445**: 896.

Holland, M., Burnett, K., Gardiner, C., Cirac, J. I. & Zoller, P. (1996). Theory of an atom laser, *Phys. Rev. A* **54**: R1757.

Holtz, P. O. (2007). Communication at the plmcn7 conference in havana.

Hopfield, J. J. (1958). Theory of the contribution of excitons to the complex dielectric constant of crystals, *Phys. Rev.* **112**: 1555.

Houdré, R., Weisbuch, C., Stanley, R. P., Oesterle, U., Pellandin, P. & Ilegems, M. (1994). Measurement of cavity-polariton dispersion curve from angle-resolved photoluminescence experiments, *Phys. Rev. Lett.* **73**: 2043.

Ĭmamoḡlu, A. (1998). Phase-space filling and stimulated scattering of composite bosons, *Phys. Rev. B* **57**: 4195R.

Ĭmamoḡlu, A., Awschalom, D. D., Burkard, G., DiVincenzo, D. P., Loss, D., Sherwin, M. & Small, A. (1999). Quantum information processing using quantum dot spins and cavity QED, *Phys. Rev. Lett.* **83**: 4204.

Inoue, J. I., Ochiai, T. & Sakoda, K. (2008). Spontaneous emission properties of a quantum dot in an ultrahigh-q cavity: Crossover from weak- to strong-coupling states and robust quantum interference, *Phys. Rev. A* **77**: 015806.

Ivanov, A. L., Borri, P., Langbein, W. & Woggon, U. (2004). Radiative corrections to the excitonic molecule state in GaAs microcavities, *Phys. Rev. B* **69**: 075312.

Ivanov, A. L., Haug, H. & Keldysh, L. V. (1998). Optics of excitonic molecules in semiconductors and semiconductor microstructures, *Phys. Rep.* **296**: 237.

Jaynes, E. & Cummings, F. (1963). Comparison of quantum and semiclassical radiation theory with application to the beam maser, *Proc. IEEE* **51**: 89.

John, S. (1987). Strong localization of photons in certain disordered dielectric superlattices, *Phys. Rev. Lett.* **58**: 2486.

Jones, B., Ghose, S., Clemens, J. P., Rice, P. R. & Pedrotti, L. M. (1999). Photon statistics of a single atom laser, *Phys. Rev. A* **60**: 3267.

Kaluzny, Y., Goy, P., Gross, M., Raimond, J. M. & Haroche, S. (1983). Observation of self-induced rabi oscillations in two-level atoms excited inside a resonant cavity: The ringing regime of superradiance, *Phys. Rev. Lett.* **51**: 1175.

Karlovich, T. B. & Kilin, S. Y. (2001). Quantum statistical properties of one-atom lasers, *Opt. Spectrosc.* **91**: 343.

Karlovich, T. B. & Kilin, S. Y. (2007). Auto-and cross-correlation functions of a one-atom laser in a regime of strong coupling, *Laser Phys.* **103**: 280.

Karlovich, T. B. & Kilin, S. Y. (2008). Fluorescence spectrum of a one-atom laser in the strong-coupling regime, *Laser Phys.* **18**: 783.

Kasprzak, J., Richard, M., Kundermann, S., Baas, A., Jeambrun, P., Keeling, J. M. J., Marchetti, F. M., Szymanska, M. H., André, R., Staehli, J. L., Savona, V., Littlewood, P. B., Deveaud, B. & Le Si Dang (2006). Bose-Einstein condensation of exciton polaritons, *Nature* **443**: 409.

Kavokin, A., Baumberg, J. J., Malpuech, G. & Laussy, F. P. (2007). *Microcavities*, Oxford University Press.

Kavokin, A. & Malpuech, G. (2003). *Cavity polaritons*, Vol. 32 of *Thin films and nanostructures*, Elsevier.

Kavokin, A. V. (2007). Exciton-polaritons in microcavities: present and future, *Appl. Phys. A* **89**: 241.

Keldysh, L. V., Kulakovskii, V. D., Reitzenstein, S., Makhonin, M. N. & Forchel, A. (2006). Interference effects in the emission spectra of qd's in high quality cavities, *Pis'ma ZhETF* **84**: 584.

Khitrova, G., Gibbs, H. M., Jahnke, F., Kira, M. & Koch, S. W. (1999). Nonlinear optics of normal-mode-coupling semiconductor microcavities, *Rev. Mod. Phys* **71**: 1591.

Khitrova, G., Gibbs, H. M., Kira, M., Koch, S. W. & Scherer, A. (2006). Vacuum Rabi splitting in semiconductors, *Nature Phys.* **2**: 81.

Kippenberg, T. J., Kalkman, J., Polman, A. & Vahala, K. J. (2006). Demonstration of an erbium-doped microdisk laser on a silicon chip, *Phys. Rev. A* **74**: 051802R.

Kiraz, A., Michler, P., Becher, C., Gayral, B., Imamoglu, A., Zhang, L., & Hu, E. (2001). Cavity-quantum electrodynamics using a single inas quantum dot in a microdisk structure, *Appl. Phys. Lett.* **78**: 3832.

Kleppner, D. (1981). Inhibited spontaneous emission, *Phys. Rev. Lett.* **47**: 233.

Koganov, G. A. & Shuker, R. (2000). Photon statistics of a ground-state-pumped laser, *Phys. Rev. A* **63**: 015802.

Kozlovskii, A. & Oraevskii, A. (1999). Sub-poissonian radiation of a one-atom two-level laser with incoherent pumping, *Sov. Phys. JETP* **88**: 666.

Krauss, T. F., Rue, R. M. D. L. & Brand, S. (1996). Two-dimensional photonic-bandgap structures operating at near-infrared wavelengths, *Nature* **383**: 699.

Kroner, M., Govorov, A. O., Remi, S., Biedermann, B., Seidl, S., Badolato, A., Petroff, P. M., Zhang, W., Barbour, R., Gerardot, B. D., Warburton, R. J. & Karrai, K. (2008). The nonlinear fano effect, *Nature* **451**: 311.

Kubanek, A., Ourjoumtsev, A., Schuster, I., Koch, M., Pinkse, P. W. H., Murr, K. & Rempe, G. (2008). Two-photon gateway in one-atom cavity quantum electrodynamics, *Phys. Rev. Lett.* **101**: 203602.

Lachs, G. (1965). Theoretical aspects of mixtures of thermal and coherent radiation, *Phys. Rev.* **138**: B1012.

Lamb Jr., W. E. (1995). Anti-photon, *Appl. Phys. B* **60**: 77.

Lamb Jr., W. E. & Retherford, R. C. (1947). Fine structure of the hydrogen atom by a microwave method, *Phys. Rev.* **72**: 241.

Lambert, N., Aguado, R. & Brandes, T. (2007). To be found, *Phys. Rev. B* **75**: 45340.

Lambropoulos, D. P. P. (1999). Competition between one- and two-photon lasing in two cavity modes, *Phys. Rev. A* **60**: 398.

Laucht, A., Hofbauer, F., Hauke, N., Angele, J., Stobbe, S., Kaniber, M., Böhm, G., Lodahl, P., Amann, M. C. & Finley, J. J. (2008). Electrical control of spontaneous emission and strong coupling for a single quantum dot, *arXiv:0810.3010v2* .

Laussy, F. P., del Valle, E. & Tejedor, C. (2008). Strong coupling of quantum dots in microcavities, *Phys. Rev. Lett.* **101**: 083601.

Laussy, F. P., Glazov, M. M., Kavokin, A., Whittaker, D. M. & Malpuech, G. (2006). Statistics of excitons in quantum dots and their effect on the optical emission spectra of microcavities, *Phys. Rev. B* **73**: 115343.

Laussy, F. P., Malpuech, G., Kavokin, A. & Bigenwald, P. (2004). Spontaneous coherence buildup in a polariton laser, *Phys. Rev. Lett.* **93**: 016402.

Laussy, F. P., Shelykh, I. A., Malpuech, G. & Kavokin, A. (2006). Effects of Bose-Einstein condensation of exciton polaritons in microcavities on the polarization of emitted light, *Phys. Rev. B* **73**: 035315.

Lax, M. (1963). Formal theory of quantum fluctuations from a driven state, *Phys. Rev.* **129**: 2342.

Lax, M. (1967). Quantum noise. x. density-matrix treatment of field and population-difference fluctuations, *Phys. Rev.* **157**: 213.

Lewenstein, M., Zhu, Y. & Mossberg, T. W. (1990). Two-photon gain and lasing in strongly driven two-level atoms, *Phys. Rev. Lett.* **64**: 3131.

Lidar, D. A., Chuang, I. L. & Whaley, K. B. (1998). Decoherence-free subspaces for quantum computation, *Phys. Rev. Lett.* **81**: 2594.

Lindblad, G. (1976). On the generators of quantum dynamical semigroups, *Commun. Math. Phys* **48**: 119.

Löffler, A., Reithmaier, J. P., Sek, G., Hofmann, C., Reitzenstein, S., Kamp, M. & Forchel, A. (2005). Semiconductor quantum dot microcavity pillars with high-quality factors and enlarged dot dimensions, *Appl. Phys. Lett.* **86**: 111105.

Löffler, M., Meyer, G. M. & Walther, H. (1997). Spectral properties of the one-atom laser, *Phys. Rev. A* **55**: 3923.

Louisell, W. H. (1973). *Quantum Statistical Properties of Radiation*, New York: Wiley.

Low, F. (1952). Natural line shape, *Phys. Rev.* **88**: 53.

Machnikowski, P. (2008). Theory of two-photon processes in quantum dots: Coherent evolution and phonon-induced dephasing, *Phys. Rev. B* **78**: 195320.

Mandel, L. & Wolf, E. (1995). *Optical coherence and quantum optics*, Cambridge University Press.

Marquardt, F. & Bruder, C. (2003). To be found, *Phys. Rev. B* **68**: 195305.

Marzin, J.-Y., Gérard, J.-M., Izraël, A., Barrier, D. & Bastard, G. (1994). Photoluminescence of single inas quantum dots obtained by self-organized growth on gaas, *Phys. Rev. Lett.* **73**: 716.

Meekhof, D. M., Monroe, C., King, B. E., Itano, W. M. & Wineland, D. J. (1996). Generation of nonclassical motional states of a trapped atom, *Phys. Rev. Lett.* **76**: 1796.

Michaelis, B., C., C. E. & Beenakker, C. W. (2006). To be found, *Europhys. Lett.* **73**: 677.

Milburn, G. J. & Holmes, C. A. (1986). Dissipative quantum and classical liouville mechanics of the anharmonic oscillator, *Phys. Rev. Lett.* **56**: 2237.

Milonni, P. W., Ackerhalt, J. R. & Smith, W. A. (1973). Interpretation of radiative corrections in spontaneous emission, *Phys. Rev. Lett.* **31**: 958.

Mollow, B. R. (1969). Power spectrum of light scattered by two-level systems, *Phys. Rev.* **188**: 1969.

Mølmer, K. (1996). Notes: Correlations functions and the quantum regression theorem.
URL: *http://www.phys.au.dk/quantop/kvanteoptik/qrtnote.pdf*

Mu, Y. & Savage, C. M. (1992). One-atom lasers, *Phys. Rev. A* **46**: 5944.

Muller, A., Flagg, E. B., Bianucci, P., Wang, X. Y., Deppe, D. G., Ma, W., Zhang, J., Salamo, G. J., Xiao, M. & Shih, C. K. (2007). Resonance fluorescence from a coherently driven semiconductor quantum dot in a cavity, *Phys. Rev. Lett.* **99**: 187402.

Muller, A., Shih, C.-K., Ahn, J., Lu, D., Gazula, D. & Deppe, D. G. (2006). High q (33 000) all-epitaxial microcavity for quantum dot vertical-cavity surface-emitting lasers and quantum light sources, *Appl. Phys. Lett.* **88**: 031107.

Munro, W. J., James, D. F. V., White, A. G. & Kwiat, P. G. (2001). Maximizing the entanglement of two mixed qubits, *Phys. Rev. A* **64**: 030302.

Nielsen, T. R., Gartner, P. & Jahnke, F. (2004). Many-body theory of carrier capture and relaxation in semiconductor quantum-dot lasers, *Phys. Rev. B* **69**: 235314.

Ning, C. Z. (2004). Two-photon lasers based on intersubband transitions in semiconductor, *Phys. Rev. Lett.* **93**: 187403.

Noda, S., Chutinan, A. & Imada, M. (2000). Trapping and emission of photons by a single defect in a photonic bandgap structure, *Nature* **407**: 608.

Noda, S., Fujita, M. & Asano, T. (2007). Spontaneous-emission control by photonic crystals and nanocavities, *Nature Photon.* **1**: 449.

Nomura, M., Ota, Y., Kumagai, N., Iwamoto, S. & Arakawa, Y. (2008). Large vacuum rabi splitting in single self-assembled quantum dot-nanocavity system, *Appl. Phys. Express* **1**: 072102.

Nosich, A. I., Smotrova, E. I., Boriskina, S. V., Benson, T. M. & Sewell, P. (2007). Trends in microdisk laser research and linear optical modelling, *Opt. Quant. Electron.* **39**: 1253.

Painter, O., Lee, R. K., Scherer, A., Yariv, A., O'Brien, J. D., Dapkus, P. D. & Kim, I. (1999). Two-dimensional photonic band-gap defect mode laser, *Science* **284**: 1819.

Park, H.-G., Kim, S.-H., Kwon, S.-H., Ju, Y.-G., Yang, J.-K., Baek, J.-H., Kim, S.-B. & Lee, Y.-H. (2004). Electrically driven single-cell photonic crystal laser, *Science* **305**: 1444.

Pathak, P. K. & Agarwal, G. S. (70). Large two-atom two-photon vacuum rabi oscillations in a high-quality cavity, *Phys. Rev. A* **043807**: 2004.

Pau, S., Björk, G., Jacobson, J., Cao, H. & Yamamoto, Y. (1995). Microcavity exciton-polariton splitting in the linear regime, *Phys. Rev. B* **51**: 14437.

Perea, J. I., Porras, D. & Tejedor, C. (2004). Dynamics of the excitations of a quantum dot in a microcavity, *Phys. Rev. B* **70**: 115304.

Perea, J. I. & Tejedor, C. (2005). Polarization entanglement visibility of photon pairs emitted by a quantum dot embedded in a microcavity, *Phys. Rev. B* **72**: 035303.

Peter, E., Senellart, P., Martrou, D., Lemaître, A., Hours, J., Gérard, J. M. & Bloch, J. (2005). Exciton-photon strong-coupling regime for a single quantum dot embedded in a microcavity, *Phys. Rev. Lett.* **95**: 067401.

Porras, D. & Tejedor, C. (2003). Linewidth of a polariton laser: Theoretical analysis of self-interaction effects, *Phys. Rev. B* **67**: 161310R.

Press, D., Götzinger, S., Reitzenstein, S., Hofmann, C., Löffler, A., Kamp, M., Forchel, A. & Yamamoto, Y. (2007). Photon antibunching from a single quantum dot-microcavity system in the strong coupling regime, *Phys. Rev. Lett.* **98**: 117402.

Purcell, E. M. (1946). Spontaneous emission probabilities at radio frequencies, *Phys. Rev.* **69**: 681.

Reithmaier, J. P., Sek, G., Löffler, A., Hofmann, C., Kuhn, S., Reitzenstein, S., Keldysh, L. V., Kulakovskii, V. D., Reinecker, T. L. & Forchel, A. (2004). Strong coupling in a single quantum dot–semiconductor microcavity system, *Nature* **432**: 197.

Reitzenstein, S., Hofmann, C., Gorbunov, A., Strauß, M., Kwon, S. H., Schneider, C., Löffler, A., Höfling, S., Kamp, M. & Forchel, A. (2007). Alas/gaas micropillar cavities with quality factors exceeding 150.000, *Appl. Phys. Lett.* **90**: 251109.

Rohener, M., Reitmaier, J. P., Forchel, A., Schaefer, F. & Zull, H. (1997). Laser emission from photonic dots, *Appl. Phys. Lett.* **71**: 488.

Rudin, S. & Reinecke, T. L. (1999). Oscillator model for vacuum rabi splitting in microcavities, *Phys. Rev. B* **59**: 10227.

Ryu, H. Y., Notomi, M., Kuramoti, E. & Segawa, T. (2000). Laser emission from quantum dots in microdisk structures, *Appl. Phys. Lett.* **77**: 184.

S. Haroche, J.-M. R. (2006). *Exploring the Quantum: Atoms, Cavities, and Photons*, Oxford University Press.

Sanchez-Mondragon, J. J., Narozhny, N. B. & Eberly, J. H. (1983). Theory of spontaneous-emission line shape in an ideal cavity, *Phys. Rev. Lett.* **51**: 550.

Sanvitto, D., Daraei, A., Tahraoui, A., Hopkinson, M., Fry, P. W., Whittaker, D. M. & Skolnick, M. S. (2005). Observation of ultrahigh quality factor in a semiconductor microcavity, *Appl. Phys. Lett.* **86**: 191109.

Savage, C. M. (1989). Resonance fluorescence spectrum of an atom strongly coupled to a cavity, *Phys. Rev. Lett.* **63**: 1376.

Savasta, S., Stefano, O. D., Savona, V. & Langbein, W. (2005). Quantum complementarity of microcavity polaritons, *Phys. Rev. Lett.* **94**: 246401.

Savvidis, P. G., Baumberg, J. J., Stevenson, R. M., Skolnick, M. S., Whittaker, D. M. & Roberts, J. S. (2000). Angle-resonant stimulated polariton amplifier, *Phys. Rev. Lett.* **84**: 1547.

Schlosshauer, M. A. & Schlosshauer-Selbach, M. (eds) (2007). *Decoherence and the Quantum-to-classical Transition*, Springer.

Schmitt-Rink, S., Chemla, D. S. & Miller, D. A. B. (1985). Theory of transient excitonic optical nonlinearities in semiconductor quantum-well structures, *Phys. Rev. B* **32**: 6601.

Schneebeli, L., Kira, M. & Koch, S. W. (2008). Characterization of strong light-matter coupling in semiconductor quantum-dot microcavities via photon-statistics spectroscopy, *Phys. Rev. Lett.* **101**: 097401.

Schuster, I., Kubanek, A., Fuhrmanek, A., Puppe, T., Pinkse, P. W. H., Murr, K. & Rempe, G. (2008). Nonlinear spectroscopy of photons bound to one atom, *Nature Phys.* **3**: 382.

Scully, M. O. & Zubairy, M. S. (2002). *Quantum optics*, Cambridge University Press.

Shore, B. W. & Knight, P. L. (1993). The jaynes-cummings model, *J. Mod. Opt.* **40**: 1195.

Skolnick, M. S., Fisher, T. A. & Whittaker, D. M. (1998). Strong coupling phenomena in quantum microcavity structures, *Semicond. Sci. Technol.* **13**: 645.

Slusher, R. E., Levi, A. F. J., Mohideen, U., McCall, S. L., Pearton, S. J. & Logan, R. A. (1993). Threshold characteristics of semiconductor microdisk lasers, *Appl. Phys. Lett.* **63**: 1310.

Solomon, G. S., Pelton, M. & Yamamoto, Y. (2001). Single-mode spontaneous emission from a single quantum dot in a three-dimensional microcavity, *Phys. Rev. Lett.* **86**: 3903.

Srinivasan, K. & Painter, O. (2007). Linear and nonlinear optical spectroscopy of a strongly coupled microdisk–quantum dot system, *Nature* **450**: 862.

Steiner, J. T., Kira, M. & Koch, S. W. (2008). Optical nonlinearities and rabi flopping of an exciton population in a semiconductor interacting with strong terahertz fields, *Phys. Rev. B* **77**: 165308.

Strauf, S., Hennessy, K., Rakher, M. T., Choi, Y. S., Badolato, A., Andreani, L. C., Hu, E. L., Petroff, P. M. & Bouwmeester, D. (2006). Self-tuned quantum dot gain in photonic crystal lasers, *Phys. Rev. Lett.* **96**: 127404.

Stufler, S., Machnikowski, P., Ester, P., Bichler, M., Axt, V. M., Kuhn, T. & Zrenner, A. (2004). Two-photon rabi oscillations in a single $in_xga_{1-x}as$/gaas quantum dot, *Phys. Rev. B* **73**: 125304.

Takahashi, Y., Hagino, H., Tanaka, Y., Song, B.-S., Asano, T. & Noda, S. (2007). High-q nanocavity with a 2ns photon lifetime, *Opt. Express* **15**: 17206.

Tanaka, Y., Asano, T. & Noda, S. (2008). Design of photonic crystal nanocavity with q-factor of $\sim 10^9$, *J. Light Wave Tech.* **26**: 1532.

Vahala, K. J. (2003). Optical microcavities, *Nature* **424**: 839.

Varada, G. V. & Agarwal, G. S. (1992). Two-photon resonance induced by the dipole-dipole interaction, *Phys. Rev. A* **45**: 6721.

Vera, C. A., Vinck-Posada, H. & Gonzalez, A. (2008). Theory of the polariton laser, *arXiv:0807.1137* .

Vorrath, T. & Brandes, T. (2003). To be found, *Phys. Rev. B* **68**: 35309.

Weisbuch, C., Nishioka, M., Ishikawa, A. & Arakawa, Y. (1992). Observation of the coupled exciton-photon mode splitting in a semiconductor quantum microcavity, *Phys. Rev. Lett.* **69**: 3314.

Weisskopf, W. & Wigner, E. (1930). Calculation of the natural line width on the basis of dirac's theory of light (as translated by j. b. sykes), *Zeitschrift für Physik* **63**: 54.

Welton, T. A. (1948). Some observable effects of the quantum-mechanical fluctuations of the electromagnetic field, *Phys. Rev.* **74**: 1157.

Whittaker, D. M., Guimaraes, P. S. S., Sanvitto, D., Vinck, H., Lam, S., Daraei, A., Timpson, J. A., Fox, A. M., Skolnick, M. S., Ho, Y.-L. D., Rarity, J. G., Hopkinson, M. & Tahraoui, A. (2007). High q modes in elliptical microcavity pillars, *Appl. Phys. Lett.* **90**: 161105.

Wiener, N. (1930). Generalized harmonic analysis, *Acta Mathematica* **55**: 117.

Wootters, W. K. (1998). Entanglement of formation of an arbitrary state of two qubits,, *Phys. Rev. Lett.* **80**: 2245.

Yablonovitch, E. (1987). Inhibited spontaneous emission in solid-state physics and electronics, *Phys. Rev. Lett.* **58**: 2059.

Yablonovitch, E. (2001). Photonic crystals: Semiconductors of light, *Sci. Am.* **285**.

Yablonovitch, E., Gmitter, T. J. & Leung, K. M. (1991). Photonic band structure: The face-centered-cubic case employing nonspherical atoms, *Phys. Rev. Lett.* **67**: 2295.

Yamaguchi, M., Asano, T. & Noda, S. (2008). Photon emission by nanocavity-enhanced quantum anti-zeno effect in solid-state cavity quantum-electrodynamics, *Opt. Express* **16**: 118067.

Yamamoto, Y. & Ĭmamog̅lu, A. (1999). *Mesoscopic Quantum Optics*, John Wiley & Sons, inc.

Yokoyama, H., Nishi, K., Anan, T., Yamada, H., Brorson, S. D. & Ippen, E. P. (1990). Enhanced spontaneous emission from gaas quantum wells in monolithic microcavities, *Appl. Phys. Lett.* **57**: 2814.

Yoshie, T., Scherer, A., Heindrickson, J., Khitrova, G., Gibbs, H. M., Rupper, G., Ell, C., Shchekin, O. B. & Deppe, D. G. (2004). Vacuum Rabi splitting with a single quantum dot in a photonic crystal nanocavity, *Nature* **432**: 200.

Zhang, L. H. & Hu, E. (2003). Lasing from ingaas quantum dots in an injection microdisk, *Appl. Phys. Lett.* **82**: 319.

Zhu, Y., Gauthier, D. J., Morin, S. E., Wu, Q., Carmichael, H. J. & Mossberg, T. W. (1990). Vacuum Rabi splitting as a feature of linear-dispersion theory: Analysis and experimental observations, *Phys. Rev. Lett.* **64**: 2499.